GRAZ UNIVERSITY OF TECHNOLOGY

DOCTORAL THESIS

MMID – Milli-Meter wave revolution beyond UHF RFID

Author:

DI Philipp F. FREIDL

Supervisor:

Prof. DI Dr. Wolfgang BÖSCH

DI Dr. Michael E. GADRINGER

A thesis submitted in fulfilment of the requirements
for the degree of Doctor of Engineering Sciences

in the

Microwave Technologies Group
Institute of Microwave and Photonic Engineering
Faculty of Electrical and Information Engineering

February 2018

Declaration of Authorship

I declare that I have authored this thesis independently, that I have not used other than the declared sources/resources, and that I have explicitly indicated all material which has been quoted either literally or by content from the sources used. The text document uploaded to TUGRAZonline is identical to the present doctoral dissertation.

Ich erkläre an Eides statt, dass ich die vorliegende Arbeit selbstständig verfasst, andere als die angegebenen Quellen/Hilfsmittel nicht benutzt, und die den benutzten Quellen wörtlich und inhaltlich entnommenen Stellen als solche kenntlich gemacht habe. Das in TUGRAZonline hochgeladene Textdokument ist mit der vorliegenden Dissertation identisch.

Signed: _____

Date: _____

"I don't think it was for reading. It was for having written."

—Sir Terry Pratchett,
Collegiate Casting-Out of Devilish Devices [1]

Abstract

MMID – Milli-Meter wave revolution beyond UHF RFID

by DI Philipp F. Freidl

The keyword Internet of Things (IoT) represents the idea of connecting more and more devices, sensors, and "things" in general in a global network. It is expected that the IoT will reach out to more than 20 billion objects within the next decade. To achieve this goal, solutions for small and low-power communication devices are required. A promising technology for these applications is mm-wave identification (MMID), which transforms the backscatter communication of RFID to mm-wave frequencies. The shift to higher frequencies allows overcoming drawbacks of existing solutions, such as limited available bandwidths and the rather larger size of the required antennas.

Within this thesis, a demonstrator of such a backscatter communication system in the E-band (60–90 GHz) was developed. The aim of the demonstrator was to provide a platform for the analysis of the technology with respect to the requirements and challenges of IoT systems. In a first step, the operational principle of a MMID system utilizing backscatter communication is derived from a signal flow graph. Based upon this derivation, a system simulation was set up. In a second step, an in-depth analysis of the transmission channel was carried out for different MMID scenarios. The data gathered in this analysis was used together with the system simulations to derive a specification for the MMID demonstrator. Based on these specifications, all relevant components of the communication system, namely the base-station, and the transponder were developed with a maximum degree of flexibility in terms of operating frequency, modulation schemes and antenna configurations. To ease the integration of the MMID system in existing applications, the demonstrator supports the standard protocol for UHF RFID applications (EPC Gen2).

TU GRAZ

Zusammenfassung

Fakultät für Elektrotechnik und Informationstechnik
Institut für Hochfrequenztechnik

Doktor der technischen Wissenschaften

MMID – Milli-Meter wave revolution beyond UHF RFID

von DI Philipp F. FREIDL

Unter Internet der Dinge (Internet of Things, IoT) versteht man die stetig voranschreitende globale Vernetzung von Geräten, Sensoren und "Dingen" im weitesten Sinne. Aktuelle Marktstudien gehen davon aus, dass das IoT innerhalb der nächsten zehn Jahre bis zu 20 Milliarden Objekte umfassen wird. Um diese Marktdurchdringung zu ermöglichen, werden platz- und vor allem stromsparende Kommunikationstechnologien benötigt. Eine vielversprechende Lösung ist die mm-Wellen Identifikation (MMID), welche das Konzept der Rückstrahlmodulation eines UHF RFID Systems auf Frequenzen im mm-Wellen Bereich anwendet. Dieser Wechsel zu sehr viel höheren Frequenzen ermöglicht es, Schwächen von aktuellen Produkten, wie zum Beispiel die limitierte verfügbare Bandbreite, oder auch die relativ großen Antennen, eliminieren.

In dieser Dissertation wurde ein Demonstrator für ein Kommunikationssystem, welches das Konzept der Rückstrahlmodulation im E-Band (60–90 GHz) umsetzt, entwickelt. Das Ziel dieses Demonstrators ist, eine Plattform für die Analyse von MMID in Bezug auf einen IoT Anwendungsfall, bereitzustellen. Hierzu wurde in einem ersten Schritt das Funktionsprinzip eines MMID Systems anhand von Signalfluss Diagrammen hergeleitet. Basierend auf dieser Herleitung wurde in Simulation des Systems aufgesetzt. In weiterer Folge wurde der Übertragungskanal anhand mehrerer MMID Anwendungsszenarien analysiert. Anhand der hierbei gewonnen Daten wurde gemeinsam mit den Simulationsergebnissen eine Spezifikation für den Demonstrator abgeleitet. Die Komponenten des MMID Systems – die Basisstation und der Transponder – wurden basierend auf dieser Spezifikation, im Hinblick auf ein Maximum an Flexibilität der Betriebsfrequenz, der Modulationsalgorithmen und der Antennenkonfigurationen, entwickelt. Um eine unkomplizierte Integration des MMID Systems in bereits bestehende Applikationen zu ermöglichen, unterstützt der vorgestellte Demonstrator das Standardprotokoll für UHF RFID (EPC Gen2).

Acknowledgements

Contents

List of Figures

List of Tables

List of Abbreviations

APDP average power delay profile

AWG arbitrary waveform generator

AWGN Additive White Gaussian Noise

BLE Bluetooth Low Energy

CIR channel impulse response

CIR channel impulse response

CTF channel transfer function

DAC digital-analog converter

EIRP effective isotropically radiated power

EPC electronic product code

FMCW frequency modulated continuous wave

FPGA fiel programmable gate array

FSPL free space path loss

IoT Internet of Things

LAN local area network

LOS line of sight

LTCC low-temperature co-fired ceramic

M2M machine-to-machine communication

MMID mm-wave identification

MPC multi path component

NFC near-field communication

P2P peer-to-peer

PAN personal area network

PC precision connector

PCB printed circuit board

PCB printed circuit board

PDP power delay profile

PDP power delay profile

PLL phased locked loop

RCS radar cross section

RFID radio frequency identification

RMSDS root-mean square delay spread

SFG signal flow graph

VCO voltage controlled oscillator

VNA vector network analyzer

VSS Visual System Simulator$^{\text{TM}}$

WLAN wireless local area networks

WPAN wireless personal area networks

Chapter 1

Introduction

The Internet of Things (IoT) is an omnipresent vision of connecting all physical devices and objects in a common network. It comprises objects with electronically readable identifiers, wireless sensor systems, and smart devices, which are interacting with their environment, and with each other. Users are given access to these objects via services and applications over the internet. The term "Internet of Things" was first introduced in 1999 to describe a system in which physical objects are connected to the internet by attached sensors [2].

The concept of networks connecting computers with sensors or actuators is relatively mature. Already in the 1970s, first applications for remote monitoring of power meters and telephone grids were introduced in the market. In the 1990s, wireless networks for monitoring and operations in industrial environments became widespread under the term machine-to-machine communication (M2M). While these deployments are generally relying on proprietary networks, the IoT utilizes a standardized and open network – the internet [3].

With the possibility to connect every device or object with each other, an enormous amount of new applications become possible. The environments for such applications include on body sensor systems, smart homes and cities, production sites and retail environments. Motivated by these new applications, market forecasts predict a total number of 24-26 billion interconnected devices by 2020 [4, 5]. Other sources expect a total economic impact of up to 11.1 trillion USD by 2025 [6].

With this enormous market potential, the IoT became a key driving force in the development of wireless communication devices.

1.1 Elements of IoT Systems

A typical IoT system pattern is presented in Figure 1.1 [7]. It comprises several nodes which are attached to, or interacting with, real world objects. They can be used to identify objects or gather information via integrated sensors. The nodes are usually wirelessly connected to a local gateway within a local area network (LAN) or a personal area network (PAN). This gateway pre-processes the data from heterogeneous nodes and ensures a certain level of security. The application service provider gathers the data from various gateways and analyzes, structures and stores the data for further usage. Applications which want to utilize the IoT can access this data via different services of the application service provider and gain access to single nodes in order to carry out their tasks.

In general, IoT systems can be described as the interaction of six main elements: identification of objects, gathering information (sensing) from and actuating with the object, communication with other nodes and services, processing of data (computation), analyzing and modeling of information (semantics), and providing access to the information (services) [8].

Identification

The identification of objects and devices is important to map them with relevant IoT services. There are many identification methods available including the widespread optical bar codes, electronic product codes (EPC) [9] or ubiquitous codes (ucode) [10]. Additionally to the identification, the addressing of objects within the network through an unique identifier is necessary. Addressing can be achieved by well known methods like IPv6 which provides an space of up to 2^{128} unique addresses [11].

Sensing and Actuating

Besides identifying, IoT nodes often provide interfaces to interact with tagged objects or devices. Sensors, which are integrated in the nodes, gather relevant data
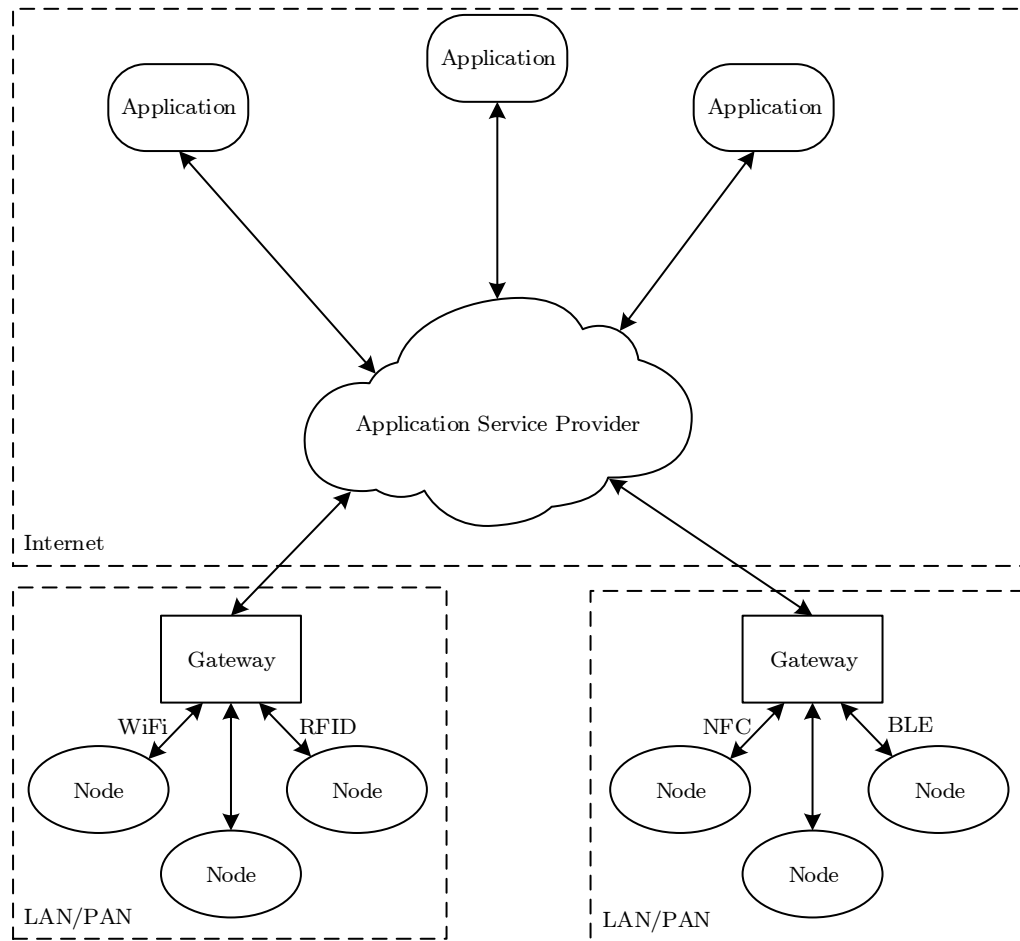
FIGURE 1.1: Typical IoT system

from their related objects and send them to a data warehouse or to databases. Additionally, actuators can be used to interact with the respective objects. Examples for such IoT nodes are smart sensors, wearable sensing devices, embedded sensors and actuators or RFID transponder.

Communication

In an IoT context, communication technologies are responsible for connecting objects with each other and with services. For most applications, these are wireless technologies such as LTE-Advanced, ZigBee, WiFi, Bluetooth or radio frequency identification (RFID) and near-field communication (NFC). Many IoT nodes require a low-power communication interface which is performing reliably in noisy environments and under multipath propagation conditions.

Computation

To process the data gathered by the IoT nodes, computational platforms and the

software running on them are required. These platforms can be generally divided into two categories: On the one side, there are local platforms which are deployed in smart devices. These devices interact with IoT nodes in their vicinity and facilitate the access to the internet. On the other side, remote or cloud platforms provide frameworks and computational power for IoT services.

Semantics

Semantics refer to the ability to extract information from an heterogeneous pool of sources (IoT nodes) and present them in a structured and standardised manner. This capability enables IoT applications to interact with a highly diverse network of objects.

Services

IoT services provide a foundation for applications which want to utilize the IoT [12]. They can be divided into four different general categories [13]: (i) Identity-related services connect real-world objects with the virtual world by identifying them, like in shipping or retail scenarios. (ii) Information aggregation services, such as smart grids, accumulate data from nodes and provide them through a standardized way to the applications. (iii) Collaborative-aware services process the data provided by the previous services in order to initiate further activities (e.g. smart homes). (iv) Ubiquitous services are the ultimate vision of the IoT and extend the collaborative-aware services to be available for everyone, everywhere at any time needed. An example for such a service is the concept of smart cities, which utilize the IoT in order to connect their assets in order to improve the quality and efficiency of its services.

1.2 Wireless Technologies for IoT

Wireless communication technologies are a key element in IoT systems as described in Section 1.1. They provide a simple and flexible connection between the nodes and the local gateway. As the nodes are often powered via a battery or wirelessly, they demand very efficient and low-power processing capabilities and communication front-ends. However, for most use cases like identification and sensing, the required data rates

are usually rather low. Additional requirements are costs, ease of integration, security, and interoperability with other technologies [14].

Many of the wireless communication technologies utilized by IoT systems operate in industrial, scientific and medical (ISM) bands [15]. While systems can operate at these bands without acquiring a license, they are limited in their transmit power according to the corresponding standards.

1.2.1 WiFi

The WiFi technology is a wide spread communication technology based on the IEEE 802.11 standard [16], which was developed as a wireless replacement for local Ethernet networks. Typically, WiFi wireless local area networks (WLAN) implement a star topology with an access point, which acts as an internet gateway, and several devices within the local network. Currently available solutions usually operate in the ISM 2.4 GHz and 5 GHz bands and offer high data rates up to 100 Mbit/s at a maximum range of up to 100 m. WiFi solutions utilizing the mm-wave ISM band at 60 GHz with data rates up to several Gbit/s are available under the term WiGig [17].

Due to the complexity of the protocol, which requires high computational efforts, and the relatively high transmission power levels, WiFi technologies are mainly suitable for smart devices like smartphones, tablets and notebooks.

1.2.2 Bluetooth

Initially, the Bluetooth technology was invented by Ericsson in 1994 as a standard for wireless data transmission in the 2.4 GHz ISM band and is now maintained by Bluetooth SIG [18]. Historically, Bluetooths main use case was the connectivity of battery powered peripheral devices, such as hands-free equipment for mobile phones. With the rise of smartphones, Bluetooth became popular for high-fidelity audio streaming, as it supports data rates up to 3 Mbit/s while maintaining a low power consumption. The range of Bluetooth wireless personal area networks (WPAN) reaches distances up to 100 m. While the standard itself supports several different network topologies, Bluetooth is mostly operated in star and peer-to-peer (P2P) configurations with a smart device acting as the internet gateway.

Under the term Bluetooth Low Energy (BLE) or Bluetooth Smart, the Bluetooth SIG released a power-efficient standard tailored for IoT nodes powered by small batteries and a life time of several years.

1.2.3   ZigBee

Among other technologies such as Z-Wave [19], or 6LoWPAN [20], ZigBee provides low-power, low-data rate WPAN technology for the 868 MHz, 915 MHz, and 2.4 GHz ISM bands based on the IEEE 802.15.4 standard [21]. It provides data rates up to 250 kbit/s and a coverage of up to 10 m. Although the standard supports a star topology, ZigBee networks usually operate in a mesh configuration. In such topologies, the data packages are relayed from one node to the next until they reach their destination node. This allows to limit the necessary transmission power while maintaining a wide coverage range of the network. Additionally, this topology allows a high scalability with thousands of nodes in a single network. To access the internet, a gateway acts as a ZigBee node and in parallel provides access to the internet over Ethernet or WiFi.

Due to its ultra-low power consumption, this technology is widely used for sensors and actuators in environments like home automation, or remote sensing.

1.2.4   RFID

RFID is an ultra-low-power communication technology in which the transponder, or node, utilizes the carrier from the base-station to transmit information via load- or backscatter-modulation [22]. These modulation technologies allow the design of passive transponders which are wirelessly powered by the base-station. This results in very cost-effective transponders which consist only of an antenna and a single integrated chip. Commercial RFID systems usually operate in ISM bands at 13.56 MHZ (HF), 868 MHz and 915 MHz (UHF), but there are also solutions which operate at much lower frequencies (125-150 kHz, LF) [23]. Additionally, there are RFID systems at 2.4 GHz and 5.6 GHz on the market. Typical reading distances for passive RFID transponders range from 10 cm for LF and HF systems up to 10 m for UHF systems. As the transponder utilizes the base-station signal for communication, RFID systems use a P2P network topology in which the base-station is used as an internet gateway.

The main focus of RFID systems is the identification of object, goods, and persons, which are equipped with a transponder. This includes application areas tracking of goods and persons, access control, toll collection, contact-less payment and machine readable travel documents [24]. However, there are transponders reported in the literature, which implement sensors on a passive RFID transponder [25–28]. These transponders extend the functionality of RFID systems from identification to sensing and actuating.

1.3 Challenges for IoT Systems

There are many considerations to be taken into account while designing an IoT system. These include privacy and security of information [29] and the compatibility of heterogeneous services [30]. From the view of the development of a communication frontend of a single IoT node, the main challenges are the interoperability of various communication standards, the miniaturization of the node dimensions, the power consumption and the costs of deployment and maintenance.

Interoperability As presented in Section 1.2, there are many different communication technologies suitable for IoT systems. These technologies have to inter-operate in order to enable a seamless integration of heterogeneous nodes within the IoT. Additionally, many of IoT enabled devices such as smartphones or tablets have a multiplicity of different communication frontend integrated in a close proximity. While some of these frontend work in similar frequency bands, the issue of interference plays an important role during the development of these devices.

Miniaturization To ease the integration process of IoT nodes on physical objects, a small physical size is important. The miniaturization can be achieved by ensuring a high degree of integration. The main challenge of the miniaturization process is to maintain the reliability and the reading range of the node at an acceptable level.

Low Power The generation of data and the transfer from one node to the next are costly in terms of power. As many of the nodes are powered by a battery, the power consumption can decrease the life time of a node significantly, which in turn increases the deployment costs. To ensure a reasonable life time, a trade-off

between the amount of data generated, processed, and transmitted, as well as the reading range and the power consumption are necessary.

Costs With the ever increasing amount of IoT systems the cost factor for deployment becomes more and more important. Due to the high amount of nodes, the price of a single node takes a big part of the overall system costs. To reduce these costs, a higher degree of integration is desirable, as it significantly reduces the expenses for the assembly.

1.4   Summary and Thesis Outline

In this chapter, an introduction into the Internet of Things and its importance for the communication industry is given. The IoT can be perceived as the concept of the seamless integration of real world objects into a large scale information network (the internet) where they can be utilized by various applications.

Section 1.1 discusses the different elements of an IoT system including identification, sensing, communication, computation, semantics and services. It can be seen that the fundamental service for IoT systems is the identification of real world objects and connect them to the virtual world through their attached IoT nodes. To connect the nodes and, therefore, the real world objects with the internet, Section 1.2 gives a brief overview on existing communication technologies which are currently used for IoT applications. The key parameters of these technologies are their transmission speed (data rate), power consumption, and access range. All presented technologies rely on gateway nodes which provide internet access to the local and personal area networks in which the IoT nodes are deployed. In Section 1.3, challenges and requirements for IoT nodes with a focus on the communication frontends are discussed. The main driver for these requirements are the costs of IoT systems in terms of deployment and operation.

A promising wireless communication technique which enables ultra-low power IoT nodes is the backscatter communication. It is successfully implemented in UHF RFID for low data-rate systems (several hundreds of kBit/s) with reasonable reading ranges up to 10 m [23]. Commercially available UHF RFID transponders provide already a very high degree of integration, with the antenna as the only external element. To target a wider range of IoT applications, a decrease of the size of the transponder, as well as utilizing less

crowded frequency ranges, would be beneficial. The miniaturization of the node, while maintaining a good efficiency of the antenna and a reasonable reading range, a shift to higher operating frequencies is required. In this sense, the exploitation of the mm-wave frequency range is attractive as it provides unlicensed broadband communication bands, such as the ISM band at 60 GHz [31]. The reduction of the wavelength of the operating frequency by a factor of 60 or more compared to UHF RFID in combination with modern integration technologies would allow the implementation of effective antennas in the package or even on the die itself. Additionally, the higher absolute bandwidth available at these frequency ranges would enable additional functionality, such as localization of the node [32]. The concept of transferring backscatter communication of UHF RFID from sub-GHz and microwave frequency ranges to mm-wave frequencies was introduced by the authors of [33] under the term mm-wave identification (MMID).

The aim of this thesis was to evaluate RFID systems operating at mm-wave frequencies, which provide the fundamental service required by the IoT – identification. To accomplish this goal, a demonstrator was build which implements the functionality of the EPC Gen2 protocol for UHF RFID [9]. The purpose of the demonstrator is to identify the advantages and limitations of RFID systems which are imposed by the mm-wave technologies.

Chapter 2 describes the architecture of a MMID system and its elements, namely the base-station and the transponder. To underline potential limitations, the link budgets for both, the up- and the downlink, are derived from a signal flow chart. Using the link budgets, the core components of the MMID system were examined in order to define a specification for the demonstrator. Additionally, a system simulation environment was implemented in a commercial simulation tool in order to support the design phase with additional data. Chapter 3 presents a detailed examination of the transmission channel including three different measurement approaches. The gathered data was evaluated using common channel models. Chapters 4 and 5 present the design and implementation of the base-station and the transponder, respectively. Based on the specifications evaluated in Chapter 2 the concepts for the design were derived. After a detailed description of the specific components, measurements of the separate building blocks are presented. In Chapter 6, the setup of the full demonstrator is documented. The demonstrator was used to evaluate the performance of the presented implementation. Appendices A

and B show the schematics of the base-stations baseband amplifier and the transponders baseband board, respectively.

1.5 Contributions

In comparison to the work of other authors on the topic of MMID, this work is to the best of the authors knowledge the first which documents the development of a fully functional MMID communication system at a target frequency within the E-band. The presented MMID system incorporates new concepts for both, the base-station and the transponder. Differently to other publications, the base-station employs a fully digital baseband generation and analysis which allows the exploration of different modulation schemes and enables new applications such as localization which integrate the identification feature of the MMID system. The concept of the transponder is the first of it's art which implements the EPC Gen2 protocol at mm-wave frequencies without the need of additional signals coming from the base-station. The system design including the base-station and the transponder, as well as measurement results were presented in [34, 35]. The analysis of the system with respect to IoT applications in [36] was awarded as the best student paper by the GAAS Association.

For the development of the MMID system a channel measurement campaign up to reading distances of 1 m was carried out. The analysis of such short-range communication channels at mm-wave frequencies was a novel contribution at the time they were accomplished. The measurement systems, as well as the result of the analysis were published in [37]. Additionally, a use-case scenario measurement campaign which includes the behavior of a user interacting with the MMID base-station was performed. The results of this campaign were analyzed in [38] and demonstrated, for the first time, the influence of a real application scenario on the transmission channel of an MMID system.

To enable the characterization of the microstrip components of the transponder a novel probe-launch for PCB applications was developed. Contrary to existing PCB probe-launches which are band limited, this new design allows un-banded measurements in a wide frequency range from DC up to 90 GHz. The launch design and its optimization was published in [39]. In [40] a detailed analysis of the measurement results were presented.

Chapter 2

MMID System

MM-Wave Identification is the transformation of the UHF RFID backscatter communication principle into the mm-wave regime [33]. Due to the shift to higher frequencies, MMID systems have two advantages: On the one side, due to the small wavelengths (from 1 cm at 30 GHz down to 1 mm at 300 GHz), the implementation of small effective antennas becomes possible. On the transponder, this reduction of the antenna dimensions allows the implementation of mm-wave antennas within the package or on the die of an integrated circuit [32]. On the base-station, then implementation of high directive and electronically steerable antenna arrays becomes feasible. This would enable the selection of a single transponder among a group by pin-pointing it. On the other side, unlicensed mm-wave communication bands such as the ISM band at 60 GHz offer a much higher bandwidth (10× to 100× higher) compared to the ISM bands available in the UHF ranges [31]. This increase in the absolute bandwidth enhances the data rates of backscatter communication based RFID systems up to several GBit/s. Furthermore, applications such as the localization of transponders using techniques such as time of flight estimation or frequency modulated continuous wave based radar, can be utilized with a high degree of accuracy [41–43].

Besides these advantages, the usage of mm-waves introduces also several challenges [31]. The wave propagation at these frequency ranges is limited by the free space path loss (FSPL), which is proportional to the square of the frequency (at 60 GHz and 1 m distance, the FSPL is 68 dB). Additionally, the ability to penetrate through obstacles is rather poor. Furthermore, the atmospheric attenuation has a maximum at 60 GHz
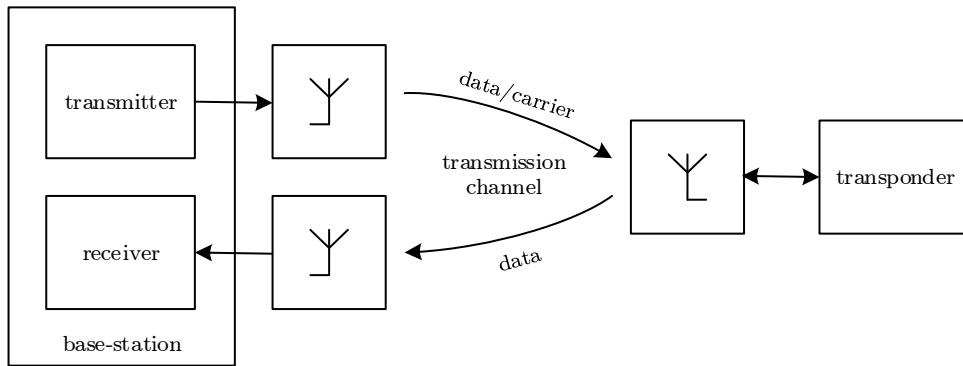
FIGURE 2.1: Basic block diagram of the MMID system with the base-station, the transmission channel, and the transponder.

(20 dB/km) due to the interaction of the propagating waves with the O_2 molecules in the air. However, for expected operating ranges of MMID systems of several meters, the effect of the atmospheric attenuation is negligible. With the decreasing wavelengths the manufacturing of microstrip components on integrated circuits as well as on printed circuit boards (PCB) becomes more complicated. Another challenge for mm-wave communication systems is – at the time of writing – the limited availability and consequently the price of mm-wave components.

2.1 System Overview

Similar to UHF RFID systems, the MMID system consists of two components, as shown if Figure 2.1: a base-station or reader, and a transponder or tag [23]. Both components interact with each other via the transmission channel, which represents the environment in which the system is operating.

In the downlink communication from the base-station to the transponder, the base-station transmits its commands via an amplitude modulated continuous wave signal. The transponder detects the data from the base-station and calculates a response. During the uplink communication from the transponder to the base-station, the transmitter of the base-station provides a continuous wave carrier which is modulated by the transponder through changing its radar cross section. The base-station retrieves the data from the transponder by detecting the the time variant reflected power.
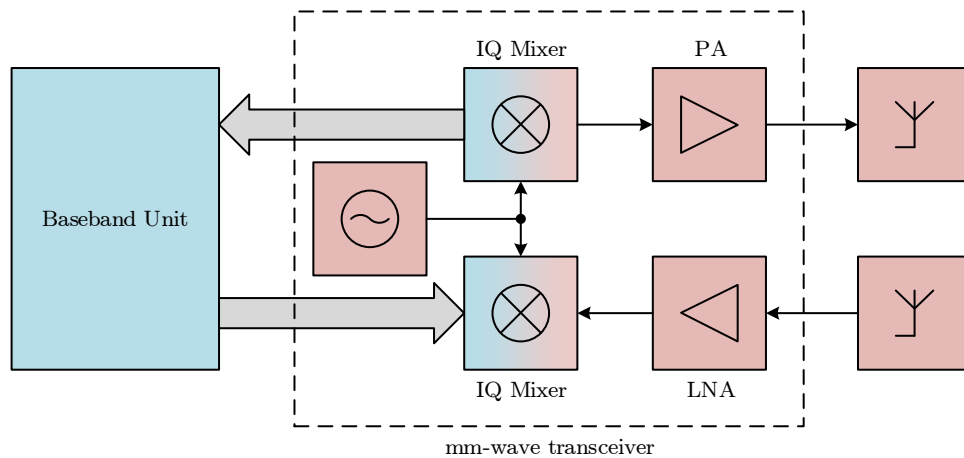
FIGURE 2.2: Basic block diagram of the MMID base-station with its core components.

During the transmission of the data and carrier over the air, the signals of the base-station and the transponder undergo the influences of the transmission channel. Thus, its characteristics are a limiting factor for the performance of MMID systems.

2.1.1 Base-Station

A possible architecture of a base-station is shown in Figure 2.2. Similar to many UHF base-stations it utilizes a direct conversion transceiver to transform the signals of the baseband unit into the mm-wave regime and vice versa. Since the base-station transmits a high power signal while receiving the backscattered response of the transponder, a bistatic configuration, with separate antennas for the transmitter and receiver, is used to ensure a maximum isolation. A detailed description of the base-station is given in Chapter 4.

2.1.2 Transponder

The MMID transponder consists of two parts as depicted in Figure 2.3: a baseband unit and a mm-wave frontend. The baseband unit processes the commands coming from the base-station, provides the data stream for the response, and controls the active components of the mm-wave frontend. The mm-wave frontend is responsible for the modulation and demodulation of the base-station signals and carrier. It comprises an antenna, a detector and modulator circuitry and a low-pass filter. In the downlink, the detector is used to provide the envelope of the signal transmitted by the base-station. In
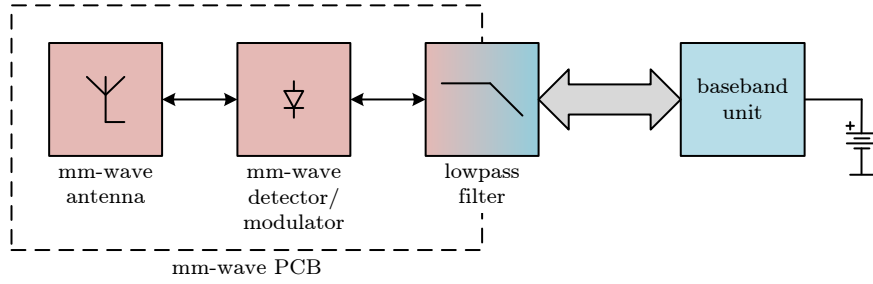
FIGURE 2.3: Basic block diagram of the MMID transponder with its core components.

order to generate the signal for the uplink transmission, several implementations for the modulator are possible. A common approach is to change the impedance provided at the feeding port of the antenna. In this way, the transponder either reflects or absorbs the signal transmitted by the base station. The design and implementation of the MMID transponder are described in Chapter 5.

2.2 Operation Priciple

To derive the potentials and limitations of a MMID system, a closer look on the dependencies between the different components is necessary [33]. Figure 2.5 illustrates the relations between the base-station, the transmission channel and the transponder using a S-Parameter block diagram for a bi-static base-station. The transmitter (TX) and receiver (RX) of the base-station are connected to its antennas which are characterized by $S_{Ant,Tx}$ and $S_{Ant,Rx}$, respectively. The transponder is modeled by its antenna $(S_{Ant,Tr})$ and the input impedance of the mm-wave frontend Z_{Tr}. The transmission channel which is connecting the base-stations transmitter and receiver with the transponder is represented by three 2-port S-Parameter blocks: One connects the base-station transmit antenna with the transponder $(S_{Tx,Tr})$. The second one connects the base-station receiver antenna with the transponder $(S_{Rx,Tr})$. The third block models the cross talk between the base-stations transmitter and receiver $(S_{Tx,Rx})$.

For the further analysis, the S-Parameter block diagram in Figure 2.4 is translated into a signal flow graph (SFG) depicted in Figure 2.5. In this representation, the input impedance Z_{Tr} of the transponders mm-wave frontend is transformed into a reflection coefficient $S_{Tr,11}$ according to (2.1).
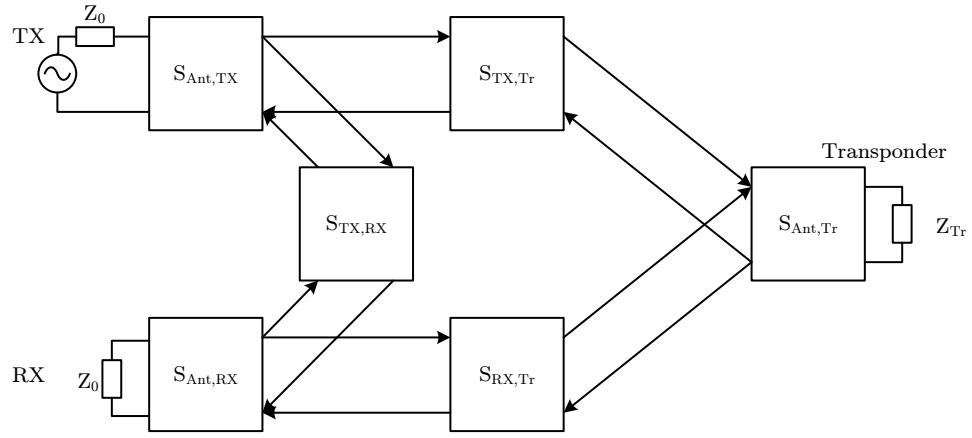
FIGURE 2.4: S-Parameter block diagram of the MMID system.
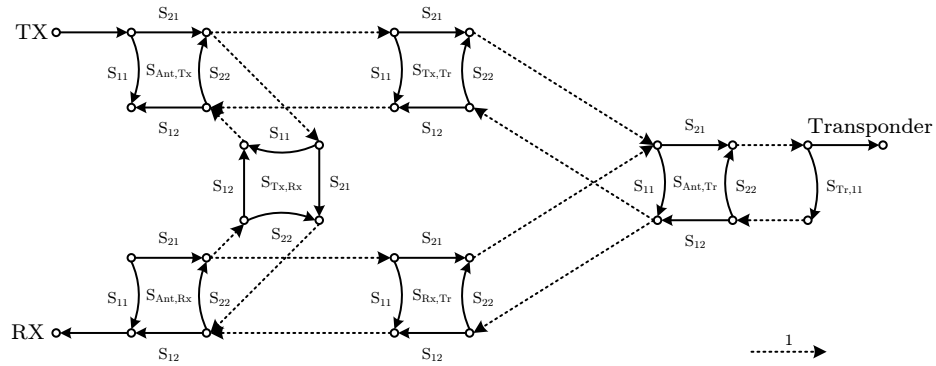
FIGURE 2.5: Signal flow graph of the MMID system.

$$S_{Tr,11} = \frac{Z_{Tr} - Z_0}{Z_{Tr} + Z_0} \tag{2.1}$$

Before deriving the transfer functions for the downlink (TX to Transponder) and backscatter uplink (TX to RX), several simplifications can be assumed:

- The base-station antennas are well matched in the desired operating frequency range. Additionally, $S_{Ant,Tx,21}$ and $S_{Ant,Rx,12}$ can incorporate the remaining matching losses by using the realized antenna gain [44]. Therefore, $S_{Ant,Tx,11}$ and $S_{Ant,Rx,11}$ can be set to 0.

- The radar cross section (RCS) of the base-station antennas is in combination with the path losses negligible. Therefore, $S_{Ant,Tx,22}$ and $S_{Ant,Rx,22}$ can be set to 0.

- The reflections from obstacles within the transmission channel can be neglected. This allows to eliminate S_{11} and S_{22} of $S_{Tx,Tr}$, $S_{Rx,Tr}$, and $S_{Tx,Rx}$.
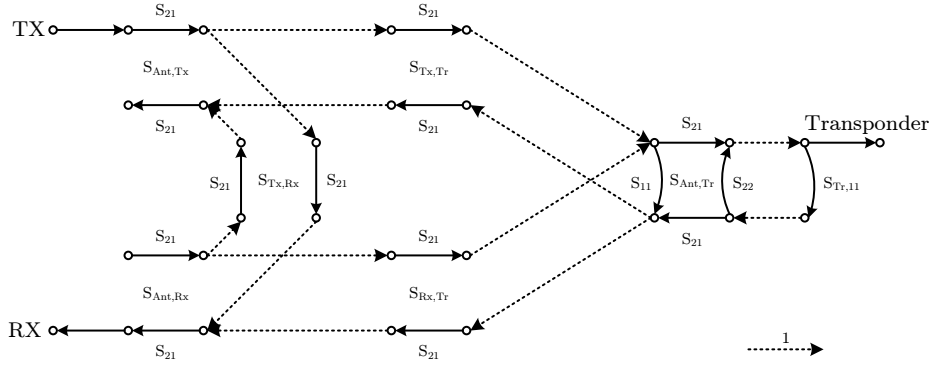
FIGURE 2.6: Simplified signal flow graph of the MMID system.
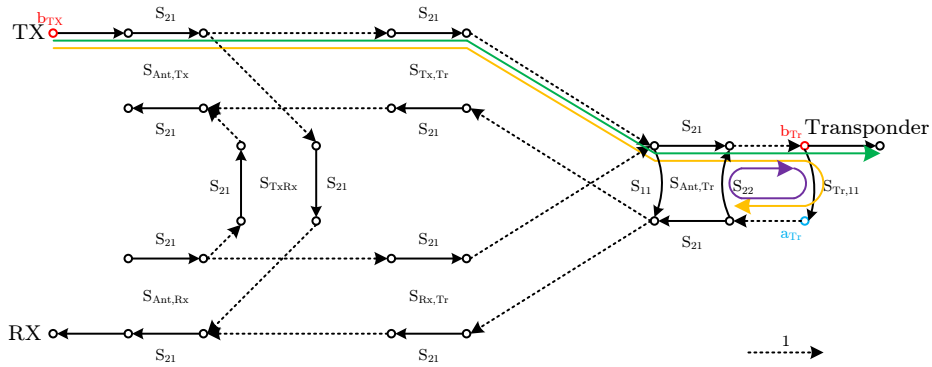
FIGURE 2.7: Signal flow graph of the downlink of the MMID system.

Taking these simplifications into account, Figure 2.5 can be reduced to Figure 2.6. In this simplified SFG, the number of loops is cut down from 19 to a single one between the antenna and the mm-wave frontend of the transponder. Based on this SFG, the transfer functions for the down- and uplink scenarios can be derived.

2.2.1 Downlink

Figure 2.7 shows the path between TX and transponder (green) and the aforementioned loop between the transponders antenna and mm-wave frontend (violet), which is touched by the path. The additional path in orange depicts the path for the power reflected by the transponder input.

The transfer function for the downlink ($\frac{b_{Tr}}{b_{TX}}$) can be therefore written as:

$$\frac{b_{Tr}}{b_{TX}} = \frac{S_{Ant,Tx,21} \cdot S_{Tx,Tr,21} \cdot S_{Ant,Tr,21}}{1 - (S_{Tr,11} \cdot S_{Ant,Tr,22})} \tag{2.2}$$
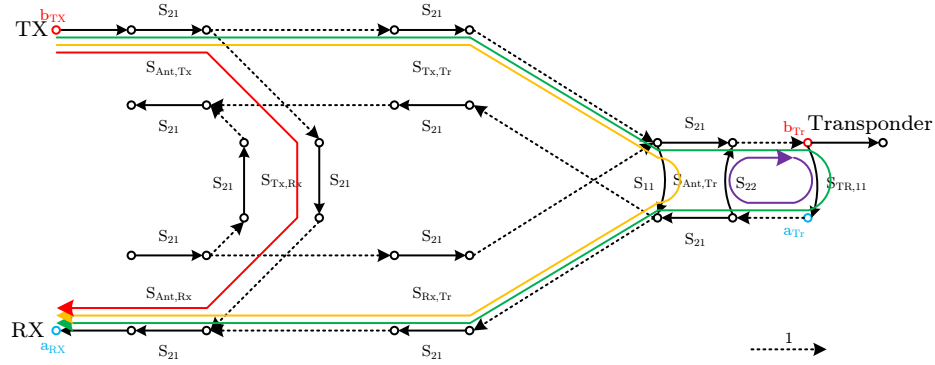
FIGURE 2.8: Signal flow graph of the uplink of the MMID system.

$$\frac{a_{Tr}}{b_{TX}} = S_{Tr,11} \cdot \frac{b_{Tr}}{b_{TX}} \tag{2.3}$$

Using (2.2) and (2.3), the power delivered into the transponder (P_{Tr}) can be calculated by:

$$P_{Tr} = \frac{1}{2} \cdot \left(|b_{Tr}|^2 - |a_{Tr}|^2 \right) = \frac{1}{2} \cdot |b_{Tr}|^2 \cdot \left(1 - |S_{Tr,11}|^2 \right) \tag{2.4}$$

$$P_{Tr} = \frac{|b_{TX}|^2}{2} \cdot |S_{Ant,Tx,21}|^2 \cdot |S_{Tx,Tr,21}|^2 \cdot |S_{Ant,Tr,21}|^2 \cdot \frac{1 - |S_{Tr,11}|^2}{|1 - (S_{Tr,11} \cdot S_{Ant,Tr,22})|^2} \tag{2.5}$$

Assuming a perfect matching between the transponder antenna and the transponder input ($S_{Ant,Tr,22} = S_{Tr,11}{}^*$), (2.5) reduces to:

$$P_{Tr} = \frac{|b_{TX}|^2}{2} \cdot |S_{Ant,Tx,21}|^2 \cdot |S_{Tx,Tr,21}|^2 \cdot |S_{Ant,Tr,21}|^2 \cdot \underbrace{\frac{1}{1 - |S_{Tr,11}|^2}}_{\text{transponder matching}} \tag{2.6}$$

The last term in (2.6) shows that for an optimum performance of the downlink of the MMID system, the transponder needs to be well matched ($S_{Tr,11} << 1$), thus maximizing the power going in to the transponders receiver.

2.2.2 Uplink

The SFG for the uplink scenario of the MMID system is depicted in Figure 2.8. It shows three possible paths from the transmitter of the base-station to its receiver: The green path is reflected by the transponders input which modulates its reflection coefficient in order to communicate with the base-station. The yellow path is reflected by the transponder antenna. The red path shows the cross-talk between the base-stations transmitter and receiver over the transmission channel.

From this SFG, the transfer function between the base-stations transmitter and receiver $(\frac{a_{RX}}{b_{TX}})$ can be derived:

$$
\begin{aligned}
\frac{a_{RX}}{b_{TX}} &= \frac{S_{Ant,TX,21} \cdot S_{TX,Tr,21} \cdot S_{Ant,Tr,21} \cdot S_{Tr,11} \cdot S_{Ant,Tr,12} \cdot S_{RX,Tr,12} \cdot S_{Ant,RX,12}}{1 - \left(S_{Tr,11} \cdot S_{Ant,Tr,22}\right)} \\
&\quad + S_{Ant,TX,21} \cdot S_{TX,Tr,21} \cdot S_{Ant,Tr,11} \cdot S_{RX,Tr,12} \cdot S_{Ant,Rx,12} \\
&\quad + S_{Ant,TX,21} \cdot S_{TX,RX,21} \cdot S_{Ant,RX,12}
\end{aligned}
\tag{2.7}
$$

During the uplink scenario, the reflection of the transponder $(S_{Tr,11})$ is switched between two states $(S'_{Tr,11}$ and $S''_{Tr,11})$ in order to modulate the base-station transmitters carrier. Assuming that the transponder switches equally between these two states with a frequency ω_{mod}, the reflection of the transponder can be split into a common-mode reflection $(S_{Tr,11,cm})$ and a modulated reflection $(S_{Tr,11,mod})$ which is shifted by the modulation frequency:

$$
\begin{aligned}
\frac{a_{Tr}}{b_{Tr}} &= \underbrace{\frac{S'_{Tr,11} + S''_{Tr,11}}{2}}_{common-mode\ reflection} + \underbrace{\frac{S'_{Tr,11} - S''_{Tr,11}}{2} \cdot \cos\left(\omega_{mod} \cdot t\right)}_{modulated\ answer} \\
&= S_{Tr,11,cm} + S_{Tr,11,mod} \cdot \cos\left(\omega_{mod} \cdot t\right)
\end{aligned}
\tag{2.8}
$$

Substituting (2.8) in (2.7) yields to:

$$
\begin{aligned}
\frac{a_{RX}}{b_{TX}} &= \underbrace{L_{TX,Tr,RX} \cdot \frac{S_{Ant,Tr,21} \cdot S_{Ant,Tr,12}}{1 - \left(S_{Tr,11} \cdot S_{Ant,Tr,22}\right)} \cdot \frac{S'_{Tr,11} - S''_{Tr,11}}{2} \cdot \cos\left(\omega_{mod} \cdot t\right)}_{transponder\ modulation} \\
&\quad + \underbrace{L_{TX,Tr,RX} \cdot \left(\frac{S_{Ant,Tr,21} \cdot S_{Ant,Tr,12}}{1 - \left(S_{Tr,11} \cdot S_{Ant,Tr,22}\right)} \cdot \frac{S'_{Tr,11} + S''_{Tr,11}}{2} + S_{Ant,Tr,11}\right)}_{transponder\ reflection} \\
&\quad + \underbrace{S_{Ant,TX,21} \cdot S_{TX,RX,21} \cdot S_{Ant,RX,12}}_{crosstalk}
\end{aligned}
\tag{2.9}
$$

Where $L_{TX,Tr,RX}$ is the round-trip loss from the base-station transmitter to the transponder to the base-station receiver as:

$$
L_{TX,Tr,RX} = S_{Ant,TX,21} \cdot S_{TX,Tr,21} \cdot S_{RX,Tr,12} \cdot S_{Ant,RX,12}
\tag{2.10}
$$

(2.9) shows that there are three components in the signal received from the base-station: the modulated answer from the transponder, the unwanted reflection from the transponder, and the cross-talk between the base-stations transmitter and receiver over the transmission channel. In order to estimate the influence of these components, each of them is separately taken into consideration. The power received by the base-station (P_{RX}) can therefore be assumed as:

$$P_{RX} = \frac{|a_{RX}|^2}{2}$$
$$\approx \frac{|b_{TX}|^2}{2} \cdot \left(\begin{array}{c} |L_{TX,Tr,RX}|^2 \cdot \frac{|S_{Ant,Tr,21}|^2 \cdot |S_{Ant,Tr,12}|^2}{|1 - S_{Tr,11} \cdot S_{Ant,Tr,22}|^2} \cdot |S_{Tr,11,mod}|^2 \cdot \cos\left(\omega_{mod} \cdot t\right) \\ + |L_{TX,Tr,RX}|^2 \cdot \left(\frac{|S_{Ant,Tr,21}|^2 \cdot |S_{Ant,Tr,12}|^2}{|1 - S_{Tr,11} \cdot S_{Ant,Tr,22}|^2} \cdot |S_{Tr,11,cm}|^2 + |S_{Ant,Tr,11}|^2 \right) \\ + |S_{Ant,TX,21}|^2 \cdot |S_{TX,Rx,21}|^2 \cdot |S_{Ant,Rx,12}|^2 \end{array} \right)$$

$$(2.11)$$

Looking at (2.11), one can see that the wanted signal (transponder modulation) and the unwanted reflection of the transponder experience the same attenuation from the round trip loss. Assuming that one reflection state of the transponder has a very good matching ($S'_{Tr,11} \approx 0$), while the other maintains a high reflectivity ($S''_{Tr,11} \approx 1$), both signals will have similar power levels at the receiver. The cross-talk between the base-station transmitter and receiver however experiences a much lower attenuation by the transmit channel (only $S_{TX,RX,21}$ compared to $S_{TX,TR,21} \cdot S_{RX,Tr,12}$). However, the wanted signal is shifted by the modulation frequency. Therefore, the maximum range of the uplink of the MMID system is limited by the dynamic range of the base-station receiver and the modulation depth of the transponder ($|S_{Tr,11,mod}|^2$), as long as the cross-talk component from the transmitter does not block the receiver.

Substituting the following definitions in (2.5) and (2.11) result in the final equation for the down- and uplink of the MMID system as shown in (2.12) and (2.13), respectively.

$\frac{|b_{TX}|^2}{2} = P_{TX}$ base-station transmit power

$|S_{Ant,TX,21}|^2 = G_{TX}$ realized gain of the base-station transmit antenna

$|S_{Ant,RX,12}|^2 = G_{RX}$ realized gain of the base-station transmit antenna

$|S_{TX,Tr,21}|^2 = L_{TX,Tr}$ transmission loss between base-station transmitter and transponder

$|S_{RX,Tr,12}|^2 = L_{RX,Tr}$ transmission loss between transponder and base-station receiver

$|S_{TX,RX,21}|^2 = L_{TX,RX}$ cross-talk between transponder and receiver of the base-station

$|S_{Ant,Tr,21}|^2 = |S_{Ant,Tr,12}|^2 = G_{Tr}$ realized gain of the transponder antenna

$|S_{Ant,Tr,11}|^2 = \sigma_{Tr}$

$S_{Ant,Tr,22} = \Gamma_{Ant,Tr}$ reflection coefficient at the transponder antenna feeding point

$S_{Tr,11} = \Gamma_{Tr,RX}$ reflection coefficient of the transponder while being in receive mode

$S_{Tr,11,cm} = \Gamma_{Tr,TX,cm}$ common-mode reflection coefficient of the transponder while being in transmit mode

$S_{Tr,11,mod} = \Gamma_{Tr,TX,mod}$ reflection modulation of the transponder while being in transmit mode

$$P_{Tr} = P_{TX} \cdot G_{TX} \cdot L_{TX,Tr} \cdot G_{Tr} \cdot \frac{1 - |\Gamma_{Tr}|^2}{|1 - \Gamma_{Tr,RX} \cdot \Gamma_{Ant,Tr}|^2} \tag{2.12}$$

$$P_{RX} = \underbrace{P_{TX} \cdot G_{TX} \cdot L_{TX,Tr} \cdot L_{RX,Tr} \cdot G_{RX} \cdot \frac{G_{Tr}^2 \cdot \Gamma_{Tr,TX,mod}|^2}{|1 - \Gamma_{Ant,Tr}} \cdot \cos\left(\omega_{mod} \cdot t\right)}_{P_{RX,mod}}$$
$$+ P_{TX} \cdot G_{TX} \cdot L_{TX,Tr} \cdot L_{RX,Tr} \cdot G_{RX} \cdot \left(\frac{G_{Tr}^2 \cdot |\Gamma_{Tr,TX,cm}|^2}{|1 - \Gamma_{Ant,Tr} \cdot \Gamma_{Tr,TX,cm}|^2} + \sigma_{Tr} \right)$$
$$+ P_{TX} \cdot G_{TX} \cdot L_{TX,RX} \cdot G_{RX} \tag{2.13}$$

2.3 Core Components

Looking at (2.12) and (2.13) one can easily identify several core components which influence the performance of the MMID system. In this section, the influences of these components on the performance and the specification of the MMID system are discussed.

Base-Station Transceiver

The base-station transceiver provides the up- and down-conversion for the baseband unit. It limits the maximum available transmission power P_{TX}. In the

uplink, the read range of the MMID system is limited by the sensitivity (P_{RX}^m) and the dynamic range ($\frac{P_{RX}^m}{P_{TX} \cdot L_{TX,RX}}$) of the receiver path.

mm-Wave Detector/Modulator Circuitry

The mm-wave detector/modulator circuitry is a critical component in both, the down- and the uplink. In the downlink scenario, the detector is responsible for demodulating the incoming signal. To ensure a maximum efficiency, the detector needs to be in an absorbing state and have a good matching towards the transponder antenna. Additionally, the detector should have a high sensitivity in order to provide a high voltage swing to the input of the baseband unit of the transponder. During the uplink communication, the modulation depth of the modulation circuitry is a critical factor. A large difference between the two reflection coefficients ($\Gamma_{Tr,TX,mod}$) is desirable.

mm-Wave PCB Manufacturing

For a best performance, an integration of the transponder on an ASIC is desirable. The antenna of the transponder could be either integrated on chip or in the package as shown in [45–48]. However, the costs and the complexity of such an integration are very high, and limit the flexibility of the transponder implementation. An alternative to an integrated solution, the transponder was built on a PCB. In this approach, the manufacturing process is a critical part of the design phase. As the board carries several resonant structures such as the mm-wave antenna and the matching network between the antenna and the mm-wave detector/modulator circuitry, the tolerances of the manufacturing process have to be considered. Another important impact factor are the losses of transmission lines on the PCB.

2.4 System Simulations

The aim of the system simulations is to provide a platform for the development of the specifications of the MMID demonstrator. To accomplish this goal, a virtual system demonstrator is implemented in an electronic aided automation software suite. To reduce the complexity of the virtual system and the simulation efforts, the MMID system is modeled for two scenarios. The first scenario simulates the communication from
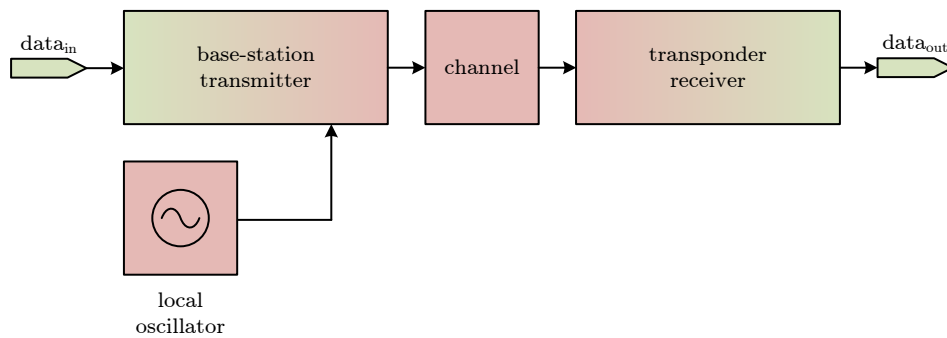
FIGURE 2.9: Structure of the downlink simulation
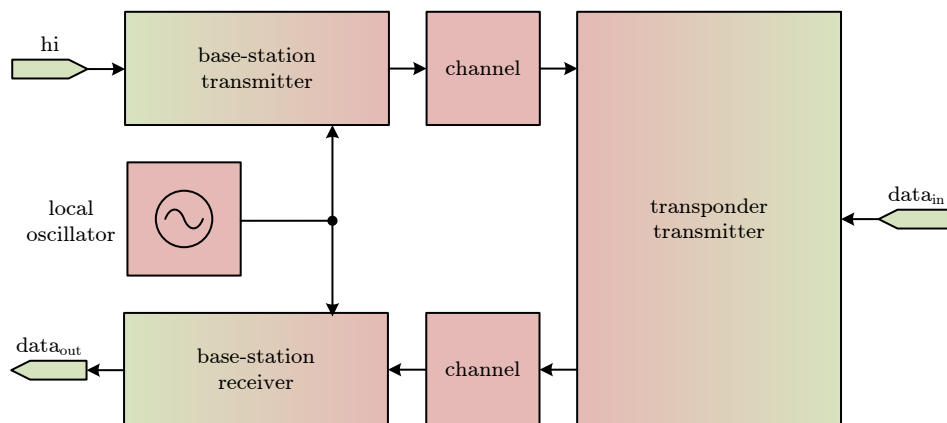
FIGURE 2.10: Structure of the uplink simulation

the base-station to the transponder (downlink) utilizing the transmitter of the base-station, a model of the transmission channel, and the receiver of the transponder as depicted in Figure 2.9. The more complex setup of the backscatter communication between the transponder and the base-station, is presented in Figure 2.10. It includes the base-station transmitter which provides the continuous wave carrier signal, the forward channel model, the transmitter of the transponder, the backward channel model, and the receiver of the base-station. In order to simplify the simulation, the crosstalk between transmitter and receiver as shown in Section 2.2 is neglected. The influence of the crosstalk can be modeled by a DC offset of the direct conversion baseband signal.

Additionally to the derivation of the system specifications, these two models allow the verification of the performance of single components within the virtual prototype during the design phase.

The virtual prototype is implemented in the Visual System Simulator$^{\text{TM}}$ (VSS) of National Instruments' AWR Design Environment$^{\text{TM}}$ [49]. This software environment analyzes RF and microwave systems from a system level point of view. It models the subsystems of the virtual prototype, such as the base-station and transponder transmitters and receivers and the transmission channel, at a component level (i.e. amplifier, mixer, filter, ...). To be able to analyze a communication system like the MMID virtual prototype on a symbol level, the VSS performs its system analysis in the time domain.

The following simulation results show the functional behavior of each block and not an in-depth study of the influence of each parameter on the overall system performance.

The base-station transmitter subsystem is used in both communication scenarios. The block diagram including the input and output ports of the transmitter subsystem of the base-station is shown in Figure 2.11. In the downlink scenario, the digital modulated data at the digital input port ($data_{in}$) is used to generate an analogue baseband signal via the digital-analog converter (DAC). The baseband signal is then fed to a reconstruction low-pass filter and an amplifier, which adapts the signal to the needs of the mixer. The mixer performs a direct up-conversion of the baseband signal to the RF regime utilizing the local oscillator as the carrier frequency. After the up-conversion, the RF signal is filtered to remove unwanted spurious elements. The last stage of the transmitter is the power amplifier, which boosts the transmit signal to the desired power level and delivers the signal to the transmit antenna – which is included in the channel model – via the RF output port (RF_{out}). In the uplink scenario, the base-station transmitter provides a constant carrier signal. This is achieved by providing a constant high level at the data input of the the subsystem.

The simulated signals of the base-station transmitter are shown in Figure 2.12. The first graph presents the analogue baseband signal after the level adoption. The second graph shows the output of the power amplifier. The small signal during the off time of the baseband input indicates the feed-through of the local oscillator signal. By increasing this effect, the AM modulation depth of the base-station transmitter can be adapted. For the first investigations, the AM depth is set to nearly $100\,\%$

The base-station receiver subsystem depicted in Figure 2.13 is only used in the uplink scenario. It implements a direct down-conversion receiver architecture. The incoming mm-wave signal is pre-selected by a bandpass filter, then fed into a low noise amplifier,
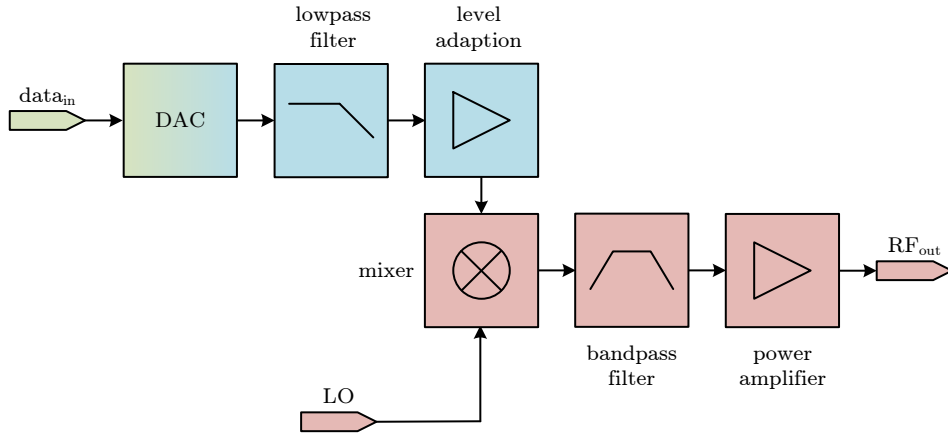
FIGURE 2.11: Block diagram of the base-station transmitter subsystem

and transformed into the base-band by the down-conversion mixer. In the base-band regime, a low-pass filter and a level adoption amplifier prepare the signal to be sampled and digitally processed.

Figure 2.14 shows the RF input (upper chart) and the baseband (lower chart) signals. Since transmitter and receiver of the base-station utilize the same LO, its non-ideal effects such as phase noise and drift, can be neglected, resulting in a very clean baseband signal.

The transmission channel is implemented with two different approaches: The first one, shown in Figure 2.15, implements the free space path loss model. The RF signal coming from the base-station (RF_{in}) is amplified by the antenna gain. Then the signal is attenuated according to by the free space path loss [50], which is represented by its inverted as the path gain ($L_{TX,Tr}$ and $L_{RX,Tr}$) in (2.14) where λ_0 is the free space wavelength of the carrier frequency and r is the distance between the base-station and the transponder. In the end, noise is added to the signal. Before feeding the signal into the transponder block, the signal is amplified by the gain of the transponder antenna.

$$L_{TX,Tr} = L_{RX,Tr} = \left(\frac{\lambda_0}{4\pi r} \right)^2 \tag{2.14}$$

Figure 2.16 presents the frequency domain (upper chart) and time domain (lower chart) analysis of the simulation output of the transmission channel model. One can notice the decrease of the carriers peak power according to the attenuation of the channel. Additionally, the noise floor at RF_{out} is increasing due to the Additive White Gaussian
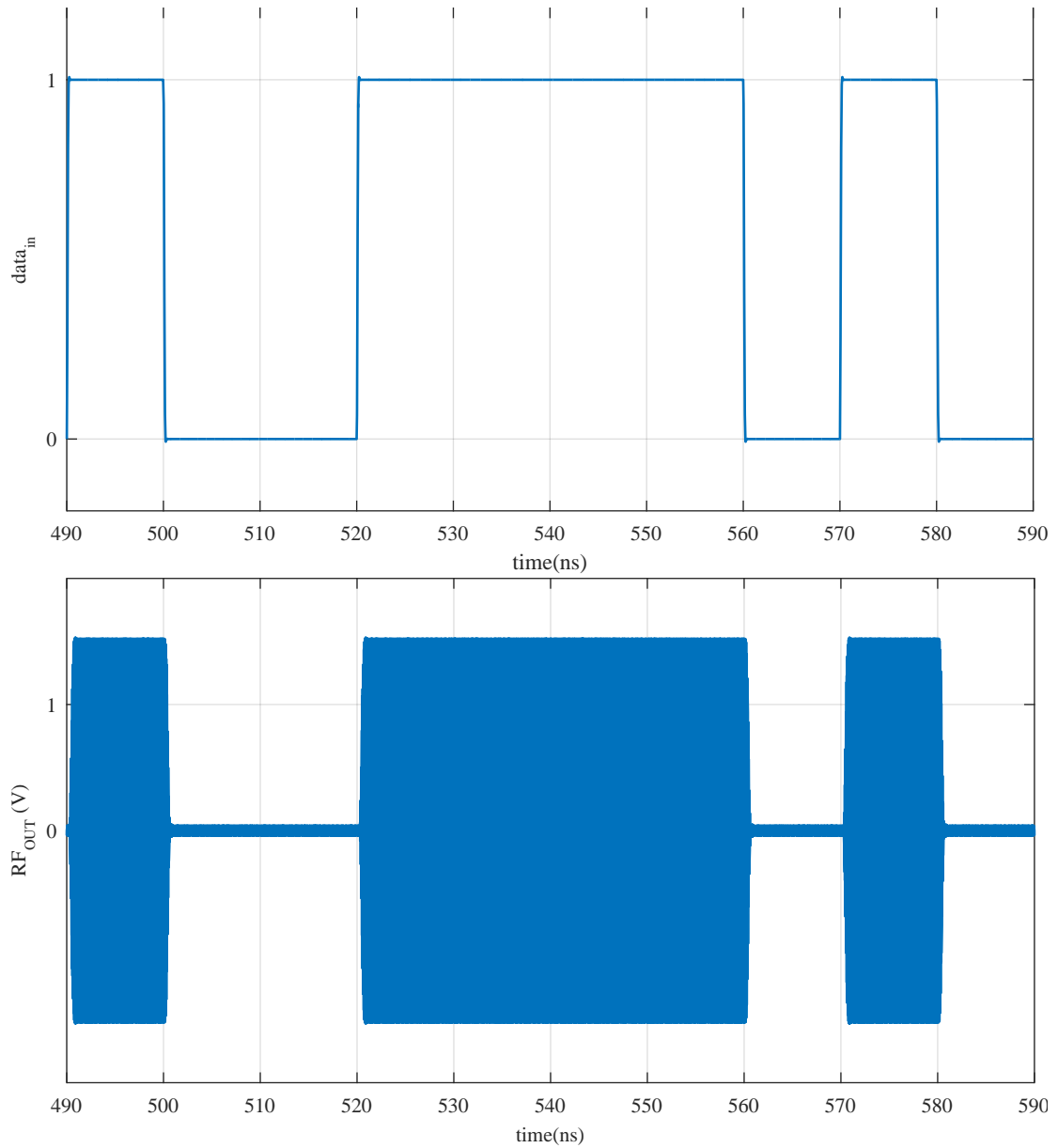
FIGURE 2.12: Simulation baseband (upper) and RF signal (lower) of the base-station transmitter subsystem

Noise (AWGN) source. In the time domain representation, the same effects can be observed. The attenuation and the additional noise cause a reduced peak amplitude during the on-time and an increase of the amplitude during the off-time of the base-station, respectively.

In the second approach, the behavior of the channel is modeled by a S-parameter block as depicted in Figure 2.17. This block can be either derived by mathematical equations, simulation, or by measurements (see Chapter 3). As these S-parameter models already include the the transmit and receive antennas, the additive noise is shaped separately
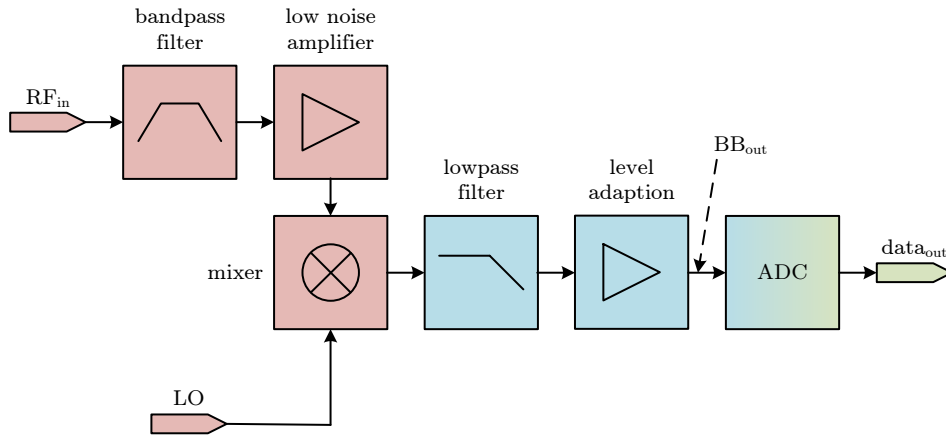
FIGURE 2.13: Block diagram of the base-station receiver subsystem

with the antenna gain to keep the comparability between the two different channel implementations.

The receiver of the MMID transponder demodulates the signal coming from the base-station using an envelope detector. The subsystem which models the receiver is shown in Figure 2.18. It comprises two of the core components discussed in Section 2.3: the mm-wave detector and the losses of the mm-wave PCB. The PCB losses are applied in the mm-wave domain of the receiver directly after the input port (RF_{in}). The mm-wave detector transforms the mm-wave signal into the base-band domain via envelope detection. In the baseband domain, a low-pass filter removes unwanted higher frequencies. Then a level adoption amplifier adjusts the amplitude of the received baseband signal, which is then transformed into the digital domain and available at the output port ($data_{out}$).

Figure 2.19 shows the simulated performance of the envelope receiver. While the mm-wave input signal (upper chart) is relatively noisy, leaving only a small signal to noise ration, the filtered baseband signal (lower chart) allows a good differentiation between high and low signal states, thus enabling the decoding of the data.

The transmitter subsystem of the transponder implements the backscatter modulation of a MMID system. The modulation is usually achieved by switching between two different reflection coefficients at the antenna feed port. As the simulation environment does not support time-variant reflection coefficients, this modulation technique cannot be directly analyzed. To circumvent this limitation, the two different reflecting states of the mm-wave modulating circuitry (Γ_1 and Γ_2) are transformed into two-port S-parameter
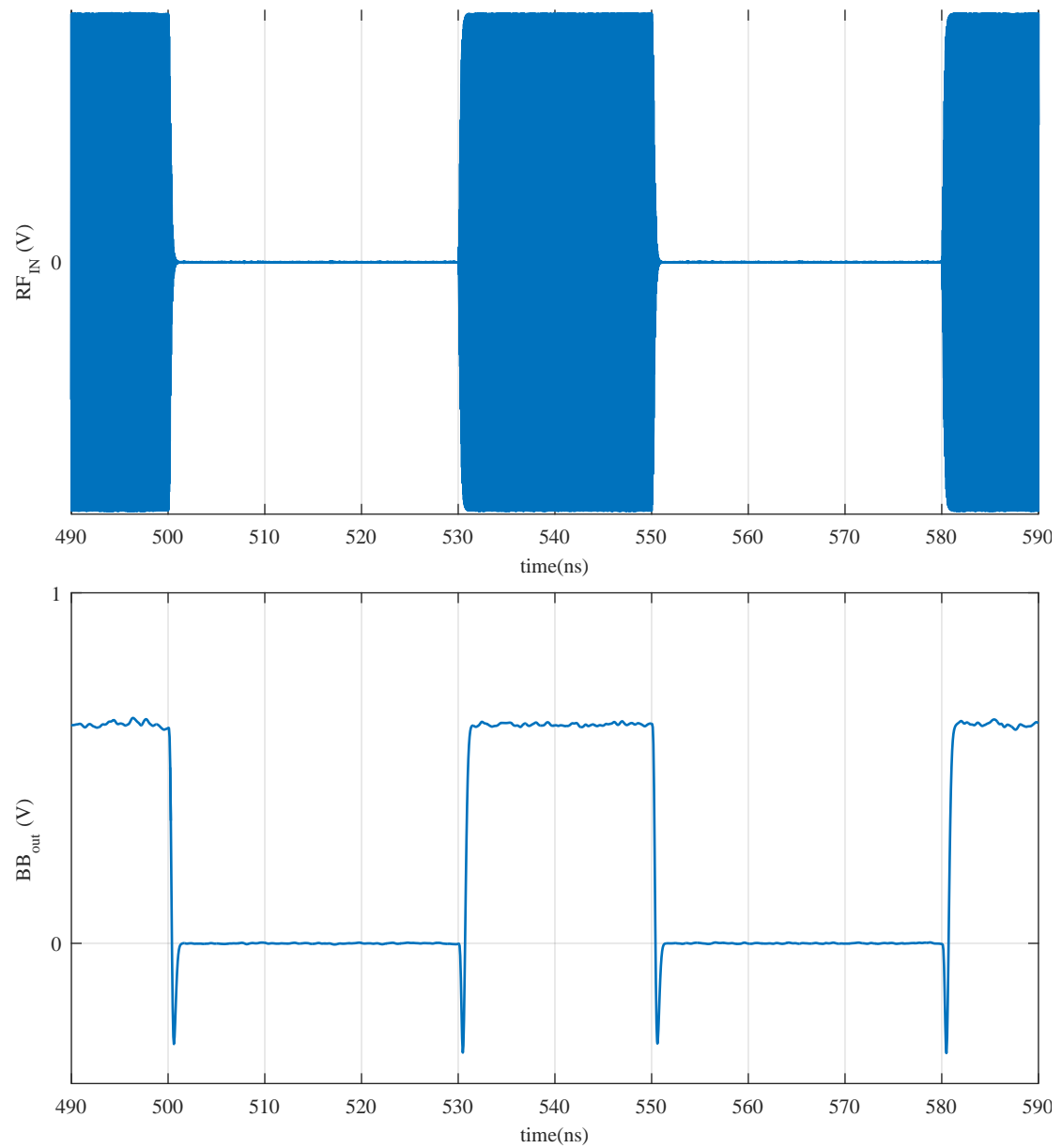
FIGURE 2.14: Simulation of the base-station receiver subsystem
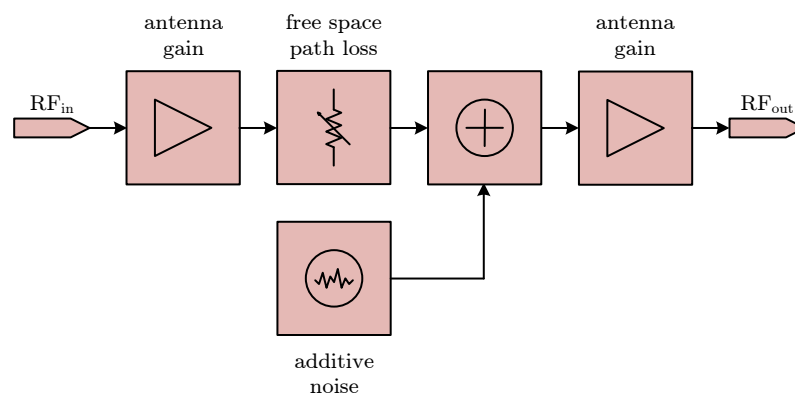
FIGURE 2.15: Block diagram of the transmission channel subsystem utilising the free space path loss model
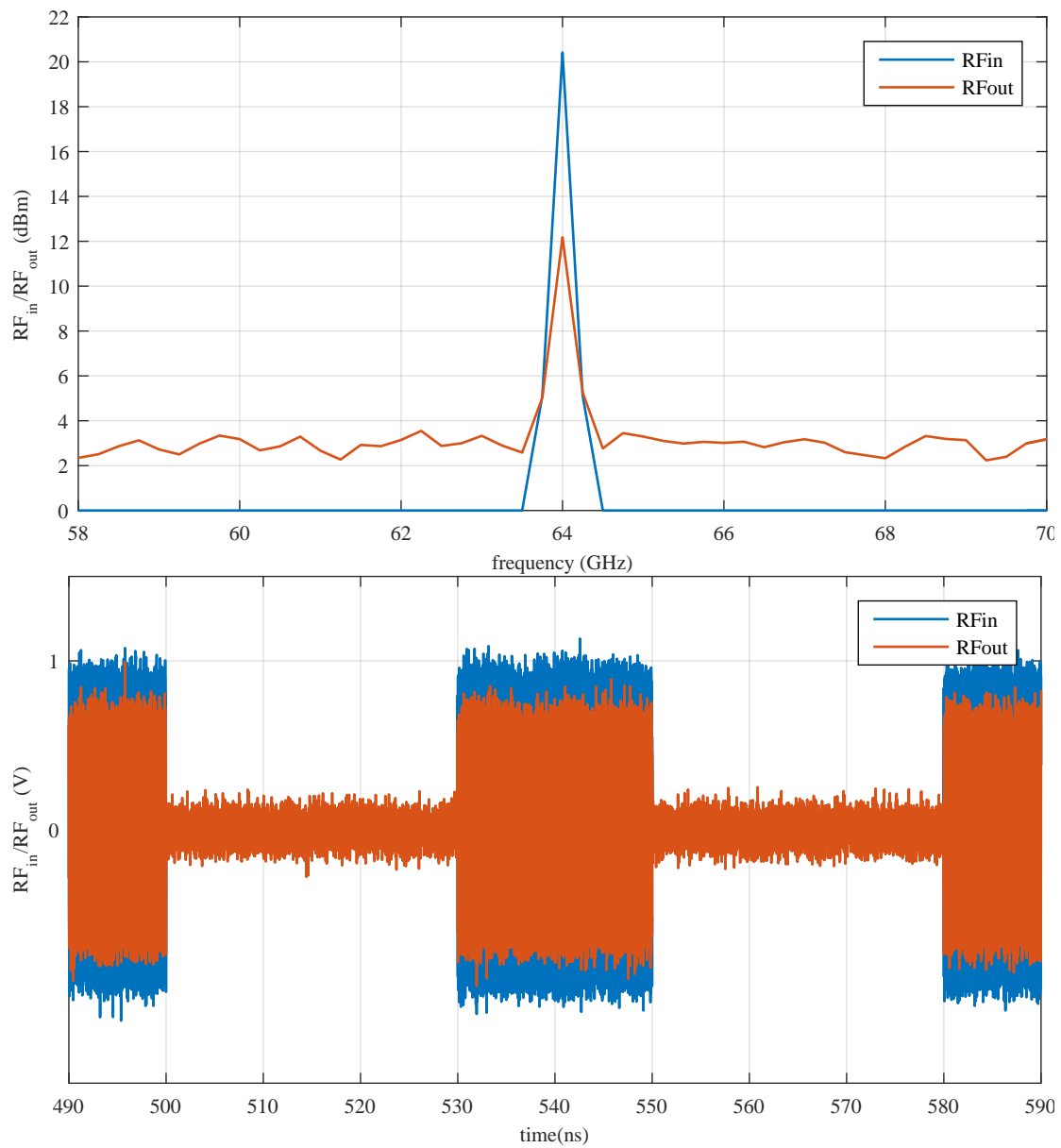
FIGURE 2.16: Simulation of the free space path loss model
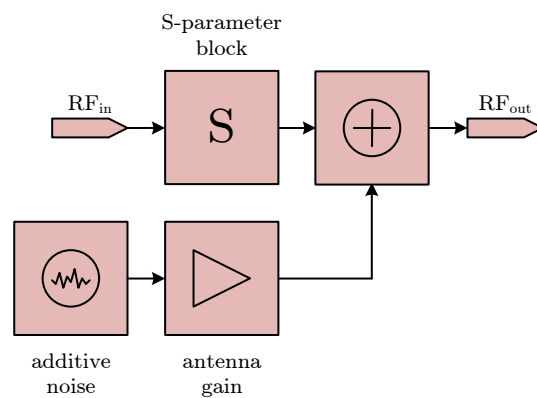
FIGURE 2.17: Block diagram of the transmission channel subsystem utilizing measurement data
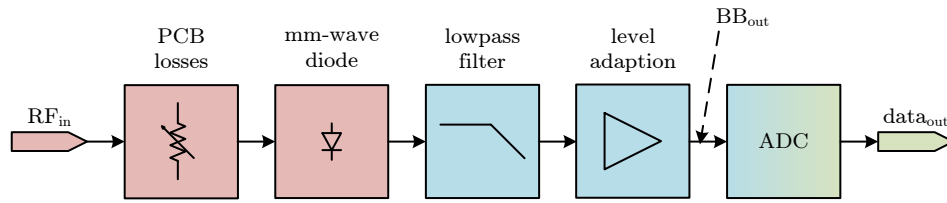
FIGURE 2.18: Block diagram of the transponder envelope detection subsystem
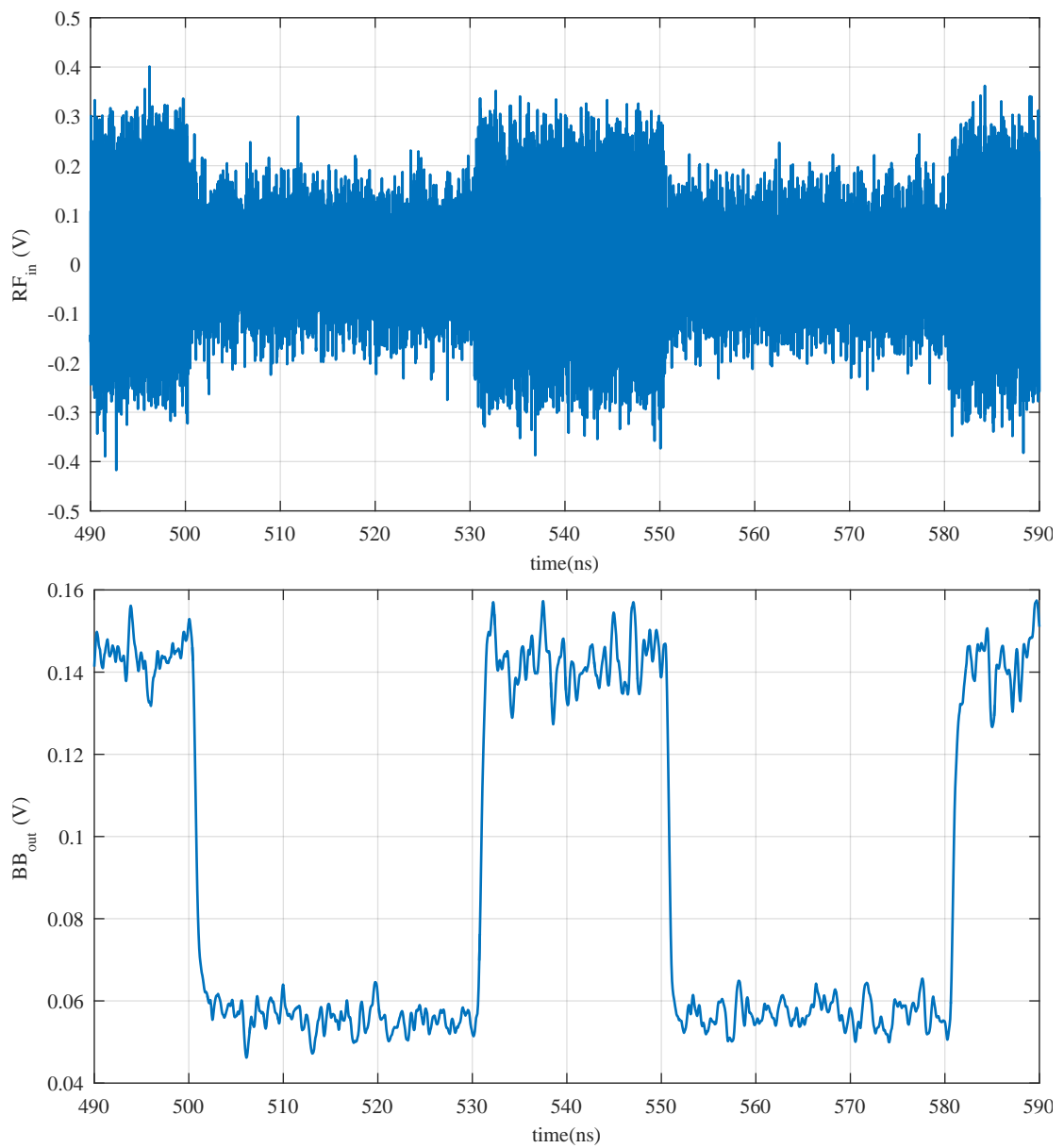
FIGURE 2.19: Simulation of the transponder envelope detection subsystem
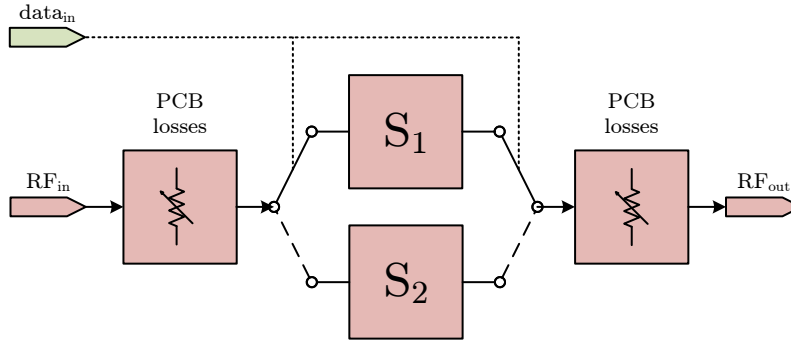
FIGURE 2.20: Block diagram of the base-station backscatter modulation subsystem

blocks (S_1 and S_2) by (2.15). The forward transmission coefficient (S_{21}) has the same amplitude and phase as the original reflection coefficient. The reflection coefficients and the backward transmission coefficient are set to 0.

$$S_{1,2} = \begin{pmatrix} 0 & \Gamma_{1,2} \\ 0 & 0 \end{pmatrix} \tag{2.15}$$

The block diagram of the transmitter of the transponder is presented in (Figure 2.20). The CW mm-wave signal from the base-station is applied at the RF input port (RF_{in}). Then, the signal is attenuated by the substrate losses of the antenna and the transmission lines. To modulate the data onto the CW signal, the model switches between the two S-parameter blocks according to the signal level applied at the digital data input ($data_{in}$). After the modulation, the signal experiences again an attenuation by the substrate losses before it is fed back into the the transmission channel via the RF output port (RF_{out}).

Figure 2.21 shows the simulation of the backscatter modulation block. The upper graph represents the digital modulation input ($data_{in}$). In the lower graph, RF_{in} depicts the CW carrier of the base-station and RF_{out} the modulated signal reflected by the transponder.

2.5 System Specification

The MMID demonstrator should operate in the E-band (60–90 GHz) with a reading range of at least up to 1 m. To enable an easy integration with existing IoT applications, it should implement the EPC Gen2 functionality. The base-station and the transponder
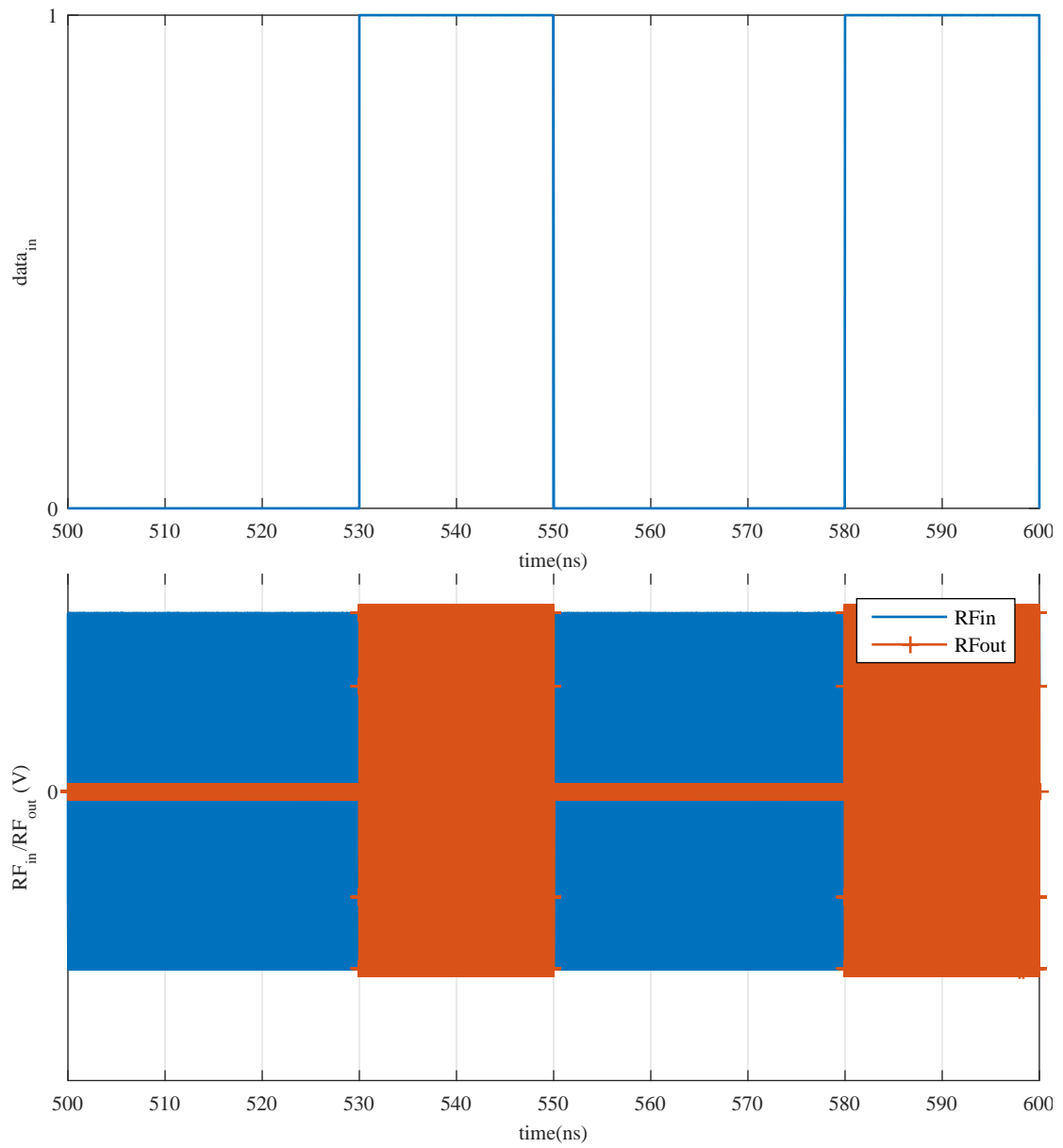
FIGURE 2.21: Output of the block simulation of the backscatter modulation

should be build in a flexible way, In order to enable additional functionalities such as localization.

Chapter 3

Transmission Channel

For the first design considerations for the MMID system (Sections 2.2 and 2.4), a simple free space path loss model with AWGN for the transmission channel was considered. To increase the accuracy of the presented system simulations more comprehensive channel descriptions are required [31].

One of the most mentioned propagation effects at mm-wave frequencies is the atmospheric attenuation, which is significantly higher compared to common microwave systems such as UHF RFID. Figure 3.1 shows the atmospheric attenuation as a function of the carrier frequency [51]. It can be seen that for both, a standard atmosphere and dry air, that the attenuation at $60\,\text{GHz}$ with $20\,\text{dB/km}$ surpasses the adjacent frequency bands. This distinct peak can be ascribed to the resonant frequency of the oxygen molecule. For a MMID system, this effect can be mainly neglected as the expected reading distances of one to several meters result in an additional loss due to the atmospheric absorption of less than a tenth of a dB.

Another effect of mm-wave propagation the reflection and scattering on obstacles. While these effects are of low importance for microwave channels, the impact on mm-wave channels is significant [31, 52]. [53, 54] show that at mm-wave frequencies, reflection coefficients between 0.5 and 1 are possible for many obstacles in indoor as well as outdoor scenarios, while the penetration losses are relatively high. Taking this into account [55, 56] conclude that a first-order reflections play a significant role in the modeling of mm-wave channels.
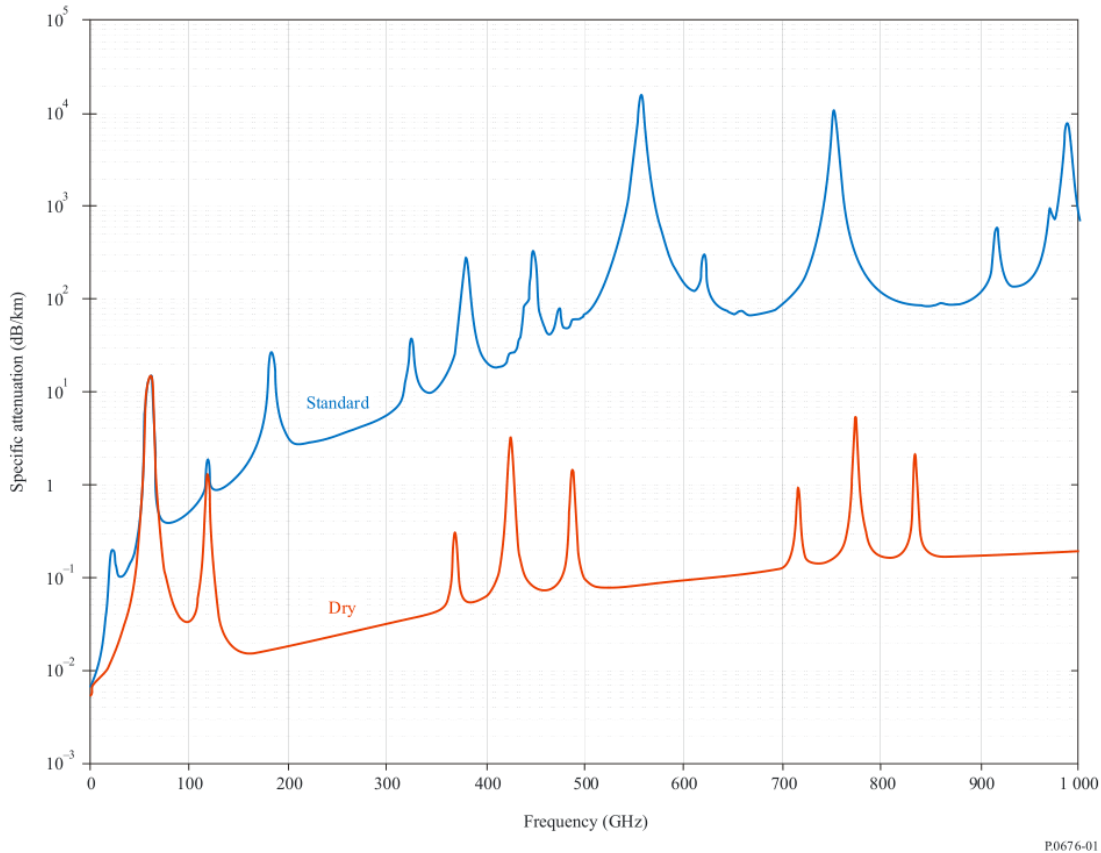
FIGURE 3.1: Atmospheric attenuation in (dB/km)

There are several indoor channel measurements campaigns at mm-wave frequencies reported in the literature. These articles can be divided into two main categories: The first category is using a vector network analyzer (VNA) to probe the transmission channel in the frequency domain [57–59]. In [60] a combination of a signal generator and a signal analyzer is used instead of the VNA, thus limiting the measurements to the magnitude of the channel transfer function. The second category relies on custom made time domain measurement systems [61–63].

The described measurement scenarios cover mid to long range indoor scenarios with a focus on multipath propagation. These scenarios do not necessarily comply with a MMID system, which operates mostly in a short range indoor setting below $1\,\mathrm{m}$. To get a more detailed view on the propagation characteristics of a MMID communication system, a characterization of the environment is necessary [31]. In order to derive a suitable channel model for the MMID system, several measurement campaigns were carried out. The results of these measurements are presented in [37] and [38].

3.1 Measurements

The measurement campaigns include three different settings: A power measurement setup, which quantifies the attenuation of the channel as a function of the frequency and enables long distance measurements. A VNA based measurement setup, which enables the characterization of the channel transfer function in magnitude and phase. Additionally to the traditional measurement setups, which are comparable to the literature presented in the previous section, a setup for an application scenario is considered for the analysis of the propagation characteristics of a MMID channel. This scenario incorporates the interaction of a user, using a hand-held reader device, interacting with a transponder attached to an object.

All measurements were performed at the RF laboratory and the RF clean room of the *Institute of Microwave and Photonic Engineering* at the *Graz University of Technology, Graz, Austria.*

3.1.1 Measurement Antennas

Due practical reasons, the antennas are included in the transmission channel. As the wave propagation is highly depended on the directivity pattern, a separation between the antenna and the propagation mechanisms is not suitable. Additionally it eases the system calibration on the transmission line ports of the antenna feeding point. Section 2.2 shows, that the characteristics of the antennas have a high impact on the overall system performance.

The gain of the antennas of the base-station and the transponder directly influences the reading range. To increase the reading range it is desired to deploy directive antennas on the base station. However, a highly directive antenna on the transponder would require a highly accurate alignment of the communication front-ends and, thus, decrease the reliability of the communication. Therefore, an antenna with lower directivity is suitable for the transponder. Derived from these requirements two different antennas are used for the channel measurement: (i) A standard gain horn antenna with a high gain and narrow main beam for the base-station. (ii) A custom made Yagi-Uda antenna, which is fabricated on a thin PCB. It provides a medium gain and rather wide main beam, similar to other PCB based directive antennas such a patch antennas.

	horn	yagi-uda
gain (dBi)	21	10.2
half power beam width (degree)	15	90
frequency range (GHz)	55–97	53–62
maximum return loss (dB)	-10	-10

TABLE 3.1: Main characteristics of the two measurement antennas

The main characteristics of both measurement antennas are listed in Table 3.1.

3.1.1.1 Standard Gain Horn Antenna

Horn antennas are one of the simplest and oldest forms of directive microwave antennas [64]. They consist of a metal waveguide which is flared from the input to a larger opening and provide typically gains up to 25 dBi. Since these antennas have no resonant elements, they provide large relative bandwidths. Horn antennas are widespread in microwave applications, such as feeding elements for reflect arrays or as element in a phased array. In the mm-wave regime, horns are often used as independent antennas or as a feeding element for lens antennas [65]. Due to its simple structure, which is easily manufacturable with high accuracy, and the well studied operation principle, horn antennas are often used in gain measurements of other high gain antennas [64].

For the channel measurements a commercial conical horn for E-band applications (QWH-ECRR00, [66]) was used. This antennas, shown in Figure 3.2, consists of a rectangular waveguide input, a transition from a rectangular to a conical waveguide, and a conical flare. The length of the flare is 52.1 mm and the maximum opening 21.6 mm. This results in a gain of 21 dBi and a half-power beam-width of roughly 15 degree. Figure 3.3 presents the input matching of the standard gain horn. It provides a minimum input matching of 18 dB for the full E-band and a 10 dB bandwidth of 55–97 GHz.

3.1.1.2 Yagi-Uda Antenna

The Yagi-Uda antenna is a well investigated antenna design [64, 67, 68]. The antenna consists of an active and several passives dipole elements. One of these is driven actively by a source, while the others behave as parasitic radiators. Yagi-Uda antennas are directional radiators with an end-fire pattern. This is achieved by placing the parasitic

FIGURE 3.2: Picture of the standard gain horn measurement antenna
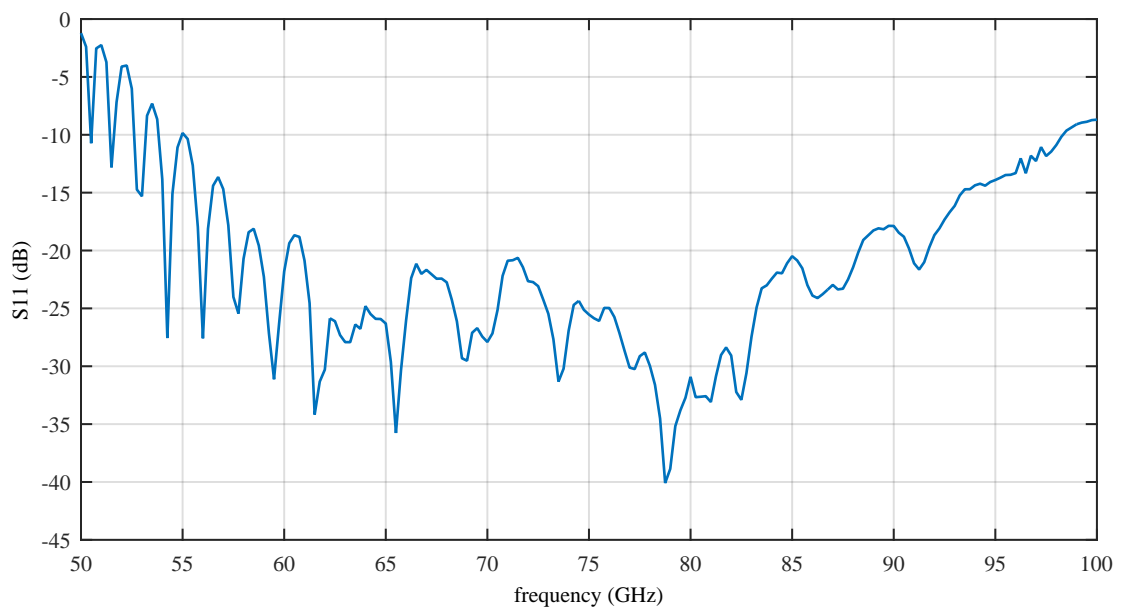
FIGURE 3.3: Measured input matching of the standard gain horn measurement antenna

elements in the main beam direction in a fashion that they act as directors, while the element in the backwards direction acts as a reflector.

Due to its low directivity, the Yagi-Uda antenna matches the requirements for the transponder antenna. Additionally, it is possible to apply relatively simple manufacturing techniques, such as the planar integration on printed circuit boards (PCB). Furthermore, several examples of Yagi-Uda antenna arrays for mm-wave applications were reported in the literature [69–73].
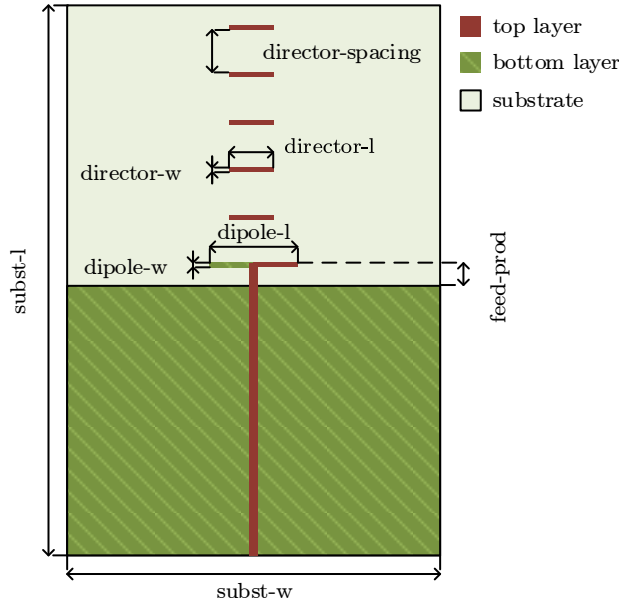
FIGURE 3.4: Geometric parameter of the Yagi-Uda measurement antenna

Parameter	Value (mm)
dipole-l	1.92
dipole-w	0.10
director-l	1.28
director-w	0.10
director-spacing	1.80
feed-l	7.00
feed-prod	1.10
subst-l	19.00
subst-w	12.70

TABLE 3.2: Dimensions of the Yagi-Uda antenna.

The original design of the custom Yagi-Uda antenna used for the channel measurements was presented by the authors of [74] for a frequency band of 22–26 GHz. To adapt the initial design to the needs for the channel measurements at mm-wave frequencies, it is transferred to a 100 um thick Rogers RO4350B ceramic substrate with a relative dielectric constant of 3.66 [75] and a frequency of 63 GHz. Figure 3.4 depicts the design of the antenna array and its geometric parameters. The active dipole is fed by a unbalanced 50 Ohms microstrip line. To achieve a good matching between the dipole and the microstrip line, a quarter-wavelength transformer was deployed. The ground plane of the microstrip line acts as the reflector. To achieve an antenna gain of roughly 10 dBi, five parasitic directors are placed in front of the active dipole. The optimum parameter set, presented in Table 3.2, for the design was derived from 3-D full-wave electromagnetic field simulations using the CST Microwave Studio software suite [76].
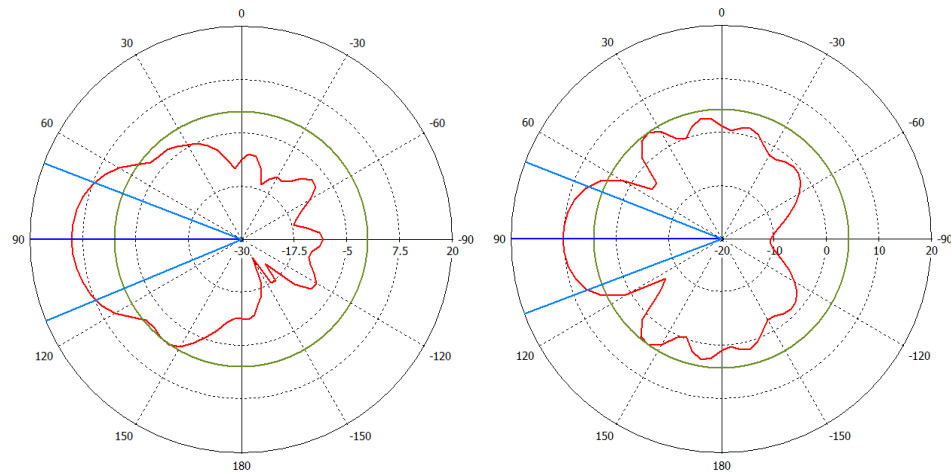
FIGURE 3.5: Simulated radiation pattern in the E-plane (left) and H-plane (right) of the Yagi-Uda measurement antenna

The simulated radiation pattern of the antenna (Figure 3.5) shows a gain of 10.2 dBi in the main beam direction and a 3 dB-beamwidth of approximately 90 degree in both, E- and H-plane. The side lobe level is 5 dB below the main beam level. Due to the unavailability of a antenna beam measurement setup in the required frequency range, only simulation data can be shown.

Figure 3.6 shows a manufactured prototypes on a PCB. To enable the connectivity between the microstrip interface of the antenna and the measurement equipment, a PC 1.85 mm end-launch connector was deployed [77]. In order to reduce the simulation efforts, the connector and its transition to the microstrip transmission line are investigated separately.

To compare the simulations with the manufactured prototypes, Figure 3.7 shows the input matching of both. One can observe a significant decrease of the center frequency between the simulations and the two prototypes from 63 GHz to 56 GHz. This shift is comparable to the observations of the authors of the original design and can be ascribed to the neglecting of the end-launch connector in the simulations. Additionally to this shift in the resonant frequency, the 10 dB bandwidth of the antenna increases from 8 GHz to 10 GHz. The variation of the resonant frequency of the two prototypes of 0.3 GHz is caused by the fabrication tolerances of the PCB manufacturer.

Despite the change of the resonant frequency, the Yagi-Uda measurement antennas are still capable of performing the channel measurements for the 60 GHz frequency band.
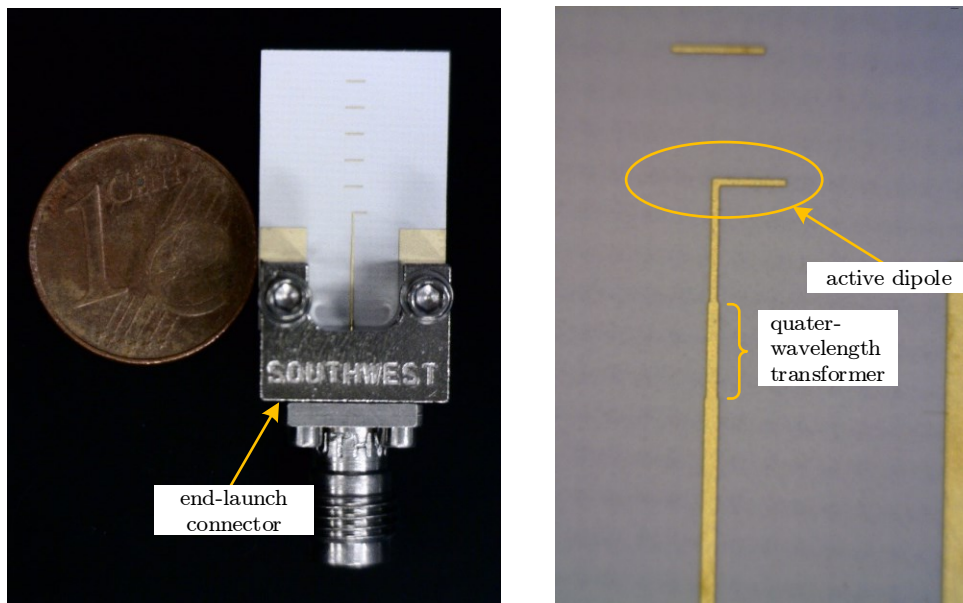
FIGURE 3.6: Picture of the Yagi-Uda measurement antenna with the end-launch connector (left) and a close-up of the feeding structure for the active dipole (right)
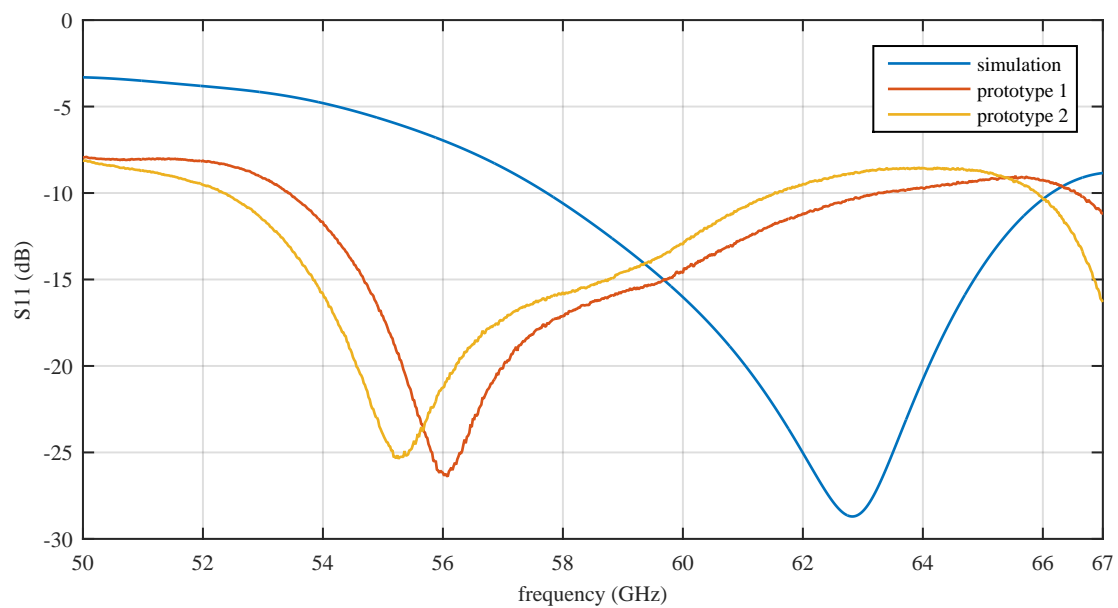
FIGURE 3.7: Input matching of the Yagi-Uda measurement antenna
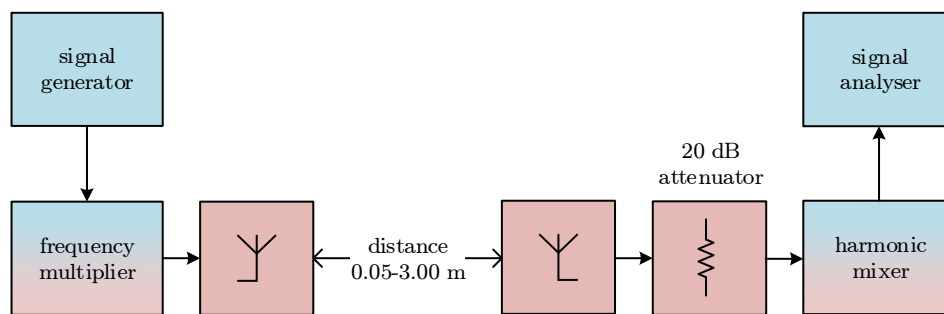
FIGURE 3.8: Setup of the power measurement.

Additionally, they provided sufficient bandwidth for an in-depth analysis of the channel behavior.

The design of the Yagi-Uda measurement antenna is presented in [37].

3.1.2 Power Measurements

The power measurement setup, as presented in Figure 3.8, utilizes a signal generator and a signal analyzer for gauging the attenuation of the transmission channel over a frequency range.

To extend the frequency range of the generator (SMF 100A, [78]) and the signal analyser (FSQ, [79]), a frequency multiplier (SMZ90, [80]) and a harmonic mixer (FS-Z90, [81]) are deployed, respectively. Table 3.3 lists the device configuration for the power measurement setup. The signal generator and its frequency multiplier are tuned to an output level of 0 dBm and sweep from 60 GHz to 70 GHz with a resolution of 50 MHz. The signal analyzers center frequency is synchronized with the generator. To reduce the measurement time, the span is limited to 100 MHz.

Since both, the multiplier and the mixer have a waveguide WR-12 mm-wave port, the E-band standard gain horn introduced in Section 3.1.1 are deployed on both, the transmitter and the receiver side. Due to the high reflectivity of the harmonic mixer, a 20 dB attenuator is used to enforce a good matching towards the receiver antenna and, therefore, reduce unwanted mismatching effects. However, this enforced matching reduces the dynamic range of the signal analyzer and therefore the maximum measurable distance.

Device	Model	Settings
signal generator	R&S SMF100A	
frequency multiplier	R&S SMZ90	output level = 0 dBm
signal analyzer	R&S FSQ	span = 100 MHz
		resolution bandwidth = 2 MHz
		video bandwidth = 5 MHz
harmonic mixer	R&S FS-Z90	LO-level = 15.5 dBm
antennas	Quinstar QWH-ECCR00	

TABLE 3.3: Measurement devices and configuration for the power measurement setup.

The advantage of this measurement setup is that there is no wired connection at high frequencies necessary between the transmitter and the receiver. Only a 10 MHz reference signal is shared between the signal generator and analyzer via an arbitrary long BNC cable. This increases the absolute achievable measurement distance to the noise floor level of the signal analyzer in an external mixer configuration (-130 dBm). Additionally, the calibration of the setup is reduced to the characterization of the 20 dB attenuator. The downside of this approach is that only the magnitude of the channel transfer function (CTF) can be measured, which limits the possibilities of the evaluation significantly.

Figure 3.9 shows a photograph of the power measurement setup. Both, the transmitter and the receiver are placed on movable tables. A laser pointer and markings on the floor ensure a satisfying alignment of the transmit and receive antennas. The measurement setup is placed in the center of the RF laboratory parallel to the longer walls, as depicted in Figure 3.10. During the measurement campaign, the separation distance between the transmitter and receiver is increased in steps of 5 cm from 5–30 cm. To reduce the measurement time, the step width between two adjacent measurement positions is increased from 30–200 cm and 200–300 cm to 10 cm and 20 cm, respectively. This results in 28 measurement positions along the main beam direction of the antennas (line of sight).

3.1.3 Vector Network Analyzer Measurements

As indicated above, the VNA is a very common tool for the characterization of transmission channels. It utilizes a vector network analyzers (ZVA67, [82]) to probe the CTF in magnitude and phase. In this setup, presented in Figure 3.11, port 1 of the VNA acts as the transmitter and port 2 as the receiver. The first port is connected to a diplexer
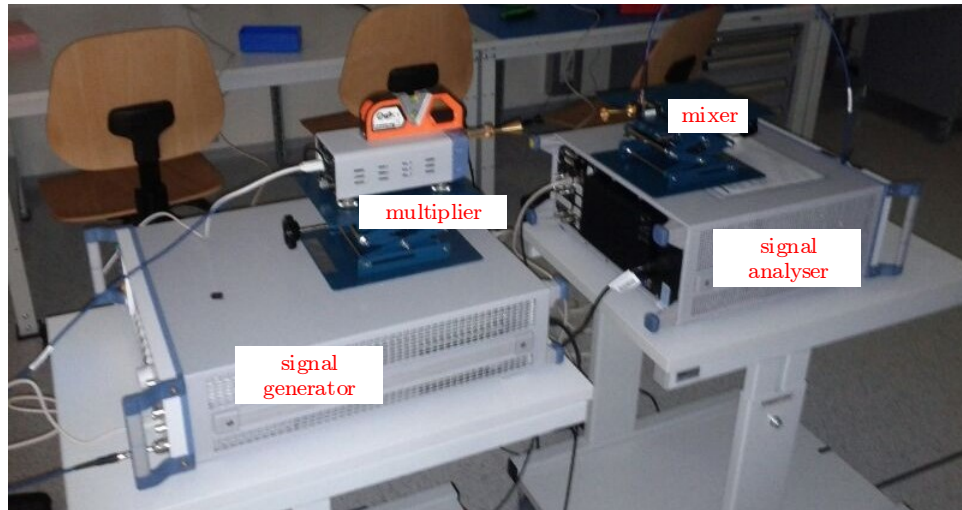
FIGURE 3.9: Picture of the power measurement setup.
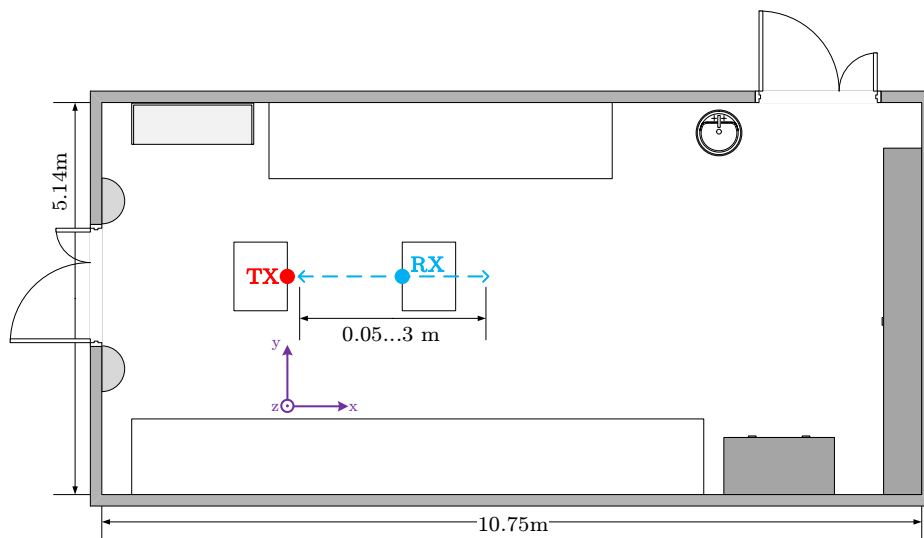
FIGURE 3.10: Floor-plan of the power measurement environment.

unit (ZV-ZD110, [83]), which serves as a mechanical support for the transmit antenna. To increase the sensitivity of the receiver, the directional coupler on the input of the second port is bypassed using the external test set. The receive antenna is connected to the VNA by cascading three precision connector (PC) 1.85 mm coaxial cables with a length of 0.9 m (36 inch) each resulting in an overall length of 2.7 m. The transmit antenna on the other side is directly mounted on the PC 1 mm of the diplexer unit. The measurement setup including the VNA is calibrated using a 1 mm PC calibration kit (ZV-Z210, [84]) and a PC 1 mm to PC 1.85 mm adapter for the receiver cable. During the measurements both antennas presented in Section 3.1.1 are deployed.

To measure the CTF, the transmission coefficient form port 1 to port 2 of the VNA
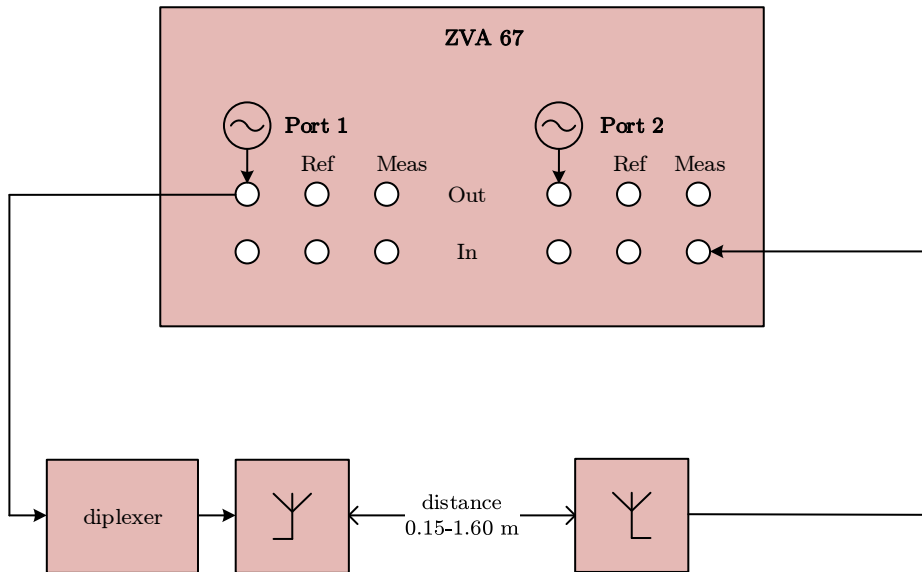
FIGURE 3.11: extended VNA measurement setup with diplexer

Device	Model	Settings
VNA	R&S ZVA67	frequency range = 50–67 GHz
		meas. points = 201
		meas. BW = 100Hz
diplexer	R&S ZVA-ZD110	output level = 5 dBm
calibration kit	R&S ZV-Z210	
antennas	Quinstar QWH-ECCR00	
	custom Yagi-Uda	

TABLE 3.4: Measurement devices and configuration for the VNA measurement setup.

(S_{12}) is used [85]. During the measurement, the VNA sweeps its signal at port 1 from 50 GHz to 67 GHz at an output level of 5 dBm. The analysis bandwidth of the VNA is set to 100 Hz to achieve a dynamic range better than 80 dB, thus limiting the maximum measurable distance only to the length of the available receiver cable. To keep the sweep time of the VNA within reasonable limits, the step width between two frequency points is set to 85 MHz which results in 201 measurement points. Table 3.4 summarizes the device configuration for this measurement setup.

The VNA and the transmit antenna on the diplexer unit are positioned approximately 1 m above ground on a stationary table. The receive unit is set up on a movable table which allows an easy variation of its position within the measurement setup. For mechanical stability and an accurate positioning, the receive antenna is supported by a
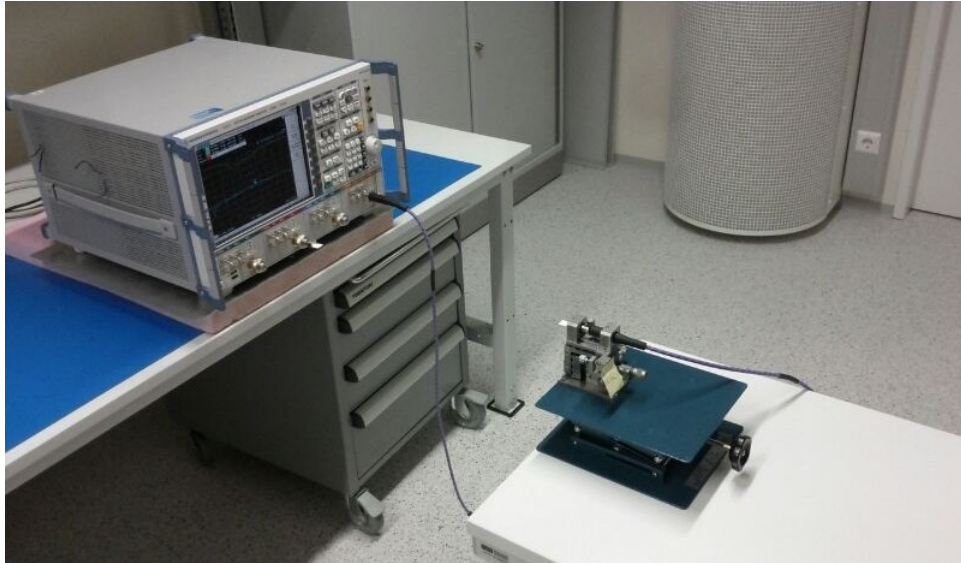
FIGURE 3.12: Picture of the VNA measurement setup.

micro-manipulator. Figure 3.12 shows a picture of the measurement setup for frequencies up to 67 GHz. In this case, the diplexer is not needed and the antenna is directly mounted on the test port of the VNA.

The measurement system is located in the clean room (Figure 3.13). The transmitter unit (TX) with the VNA and the diplexer is placed at the upper wall facing a metal probing station (green elements). The receiver unit (RX) on the movable table is aligned along the line of sight (LOS) of the transmit antenna. The separation distance between TX and RX is increased from 10 cm to 30 cm in 5 cm steps. Similar to Section 3.1.2, the step width is increased to 10 cm and 20 cm from 30 cm to 100 cm and 100 cm to 160 cm, in order to reduce the measurement efforts. This results in 15 distinct measurement points along the main beam direction of the transmit antenna.

At each of these measurement positions, the CTF is probed along a 4×4 grid (y-z plane) which is placed orthogonally to the line of sight (x-axis) as shown in Figure 3.14. The spacing between two measurement points along the grid is 1 mm in both, the y- and z-direction. This spacing is smaller than a quater wavelength of the maximum measurement frequency in the free space (67 GHz $\hat{=}$ 4.5 mm). Using this spacing, an evaluation of the small scale behaviour of the CTF around the measurement points is possible [86].

One disadvantage of this measurement concept is the cable which connects the VNA with the receiver antenna. On the one hand, these cables are rather expensive and
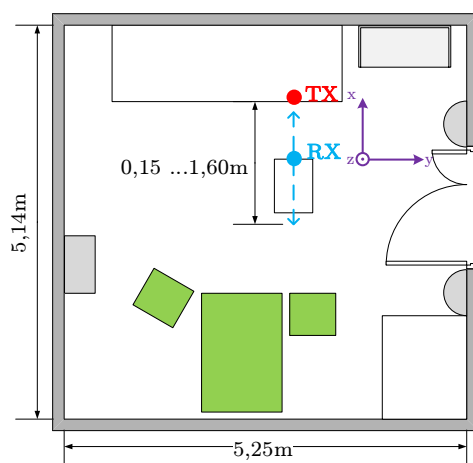
FIGURE 3.13: Floorplan of the VNA measurement environment.
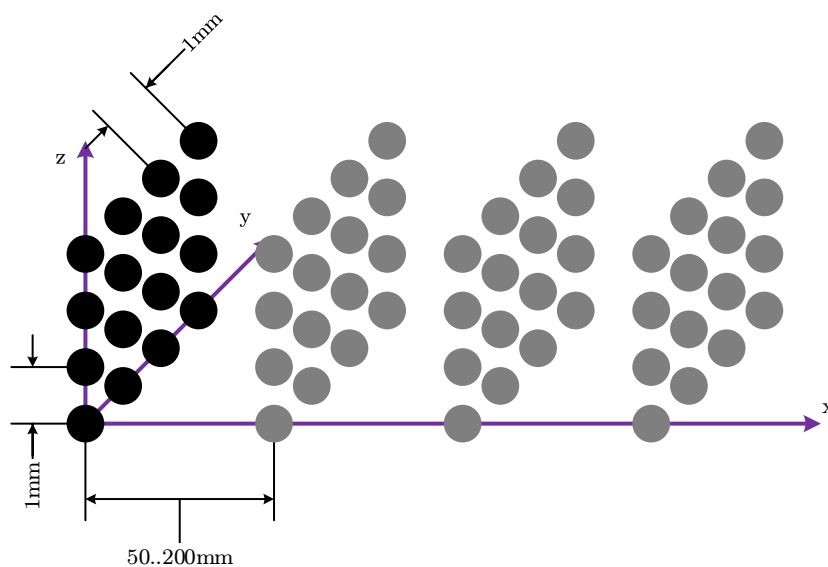
FIGURE 3.14: Spatial diversity measurement setup

usually available limited lengths, which physically limits the maximum measurement distance. On the other hand, these cables have an attenuation at mm-wave frequencies of $1.8\,\text{dB/m}$ and more at $67\,\text{GHz}$ [87]. With the additional insertion loss of the connectors, a $1\,\text{m}$ cable can have an overall insertion loss of $7\,\text{dB}$ [88]. Using three of these cables connected with adapters, this insertion limits the dynamic range of the measurement system significantly. Another issue is the phase stability of these cables. As it is inevitable to move the cable configuration of the setup after performing the calibration, a non systemic error is introduced in the measurement results. To characterize this error, a measurement series of 20 frequency sweeps were performed at a fixed RX
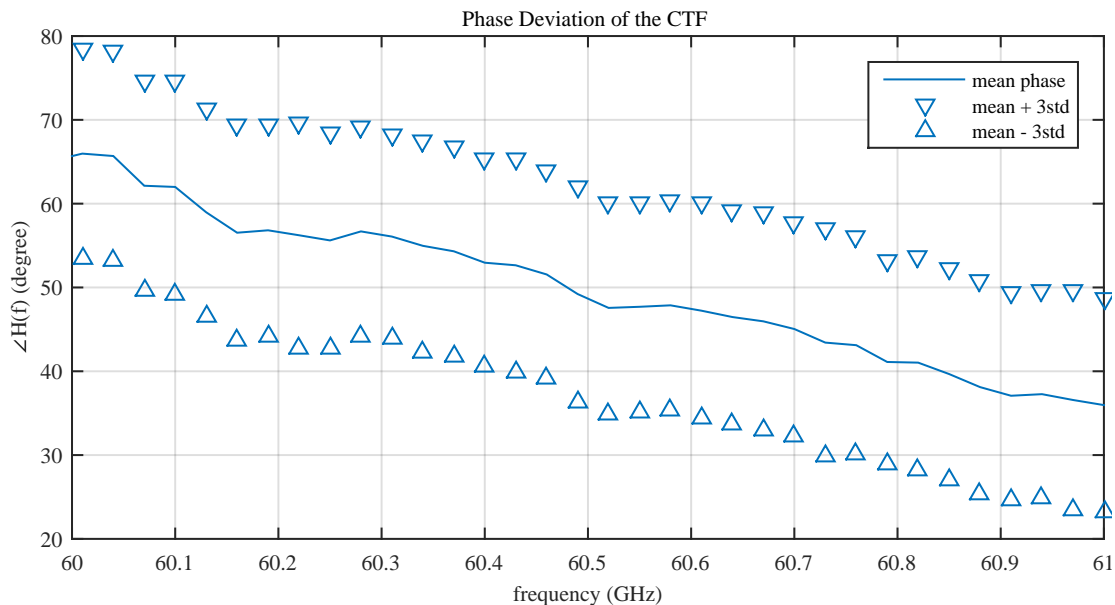
FIGURE 3.15: Phase deviation in the VNA measurement setup

position. Between the sweeps, the cable connecting the VNA and the receive antenna was moved within its bending limits. This movements are much larger than the ones which happen during the normal measurements and, therefore, provide good limits for the measurement error. Figure 3.15 shows the mean value and the three-sigma deviation of the measured phase between 60 GHz and 61 GHz. It can be seen that the standard deviation of the phase is below 10 degree. This behavior does not change over the full frequency range from 50 Ghz to 67 GHz. Additionally to the error in the phase measurement, the deviation of the magnitude was evaluated. Since this deviation is below 0.1 dB it can be safely neglected.

3.1.4 Vector Network Analyser Measurement including a User

Sections 3.1.2 and 3.1.3 describe two typical measurement setups for channel sounding. These two setups give a good insight on the behavior of the channel under the given ideal conditions. These conditions, such as the nearly perfect alignment along the LOS, or the spatial probing around the desired measurement point, allow a good description of the channel. However, they barely reflect the impact of a user interacting with the communication system. To analyze this influence, a measurement scenario including an operator who introduces realistic variations of the transmission channel into the communication system is derived. Such scenarios can include a multitude of use cases.

Device	Model	Settings
VNA	R&S ZVA67	frequency range = 50–65 GHz
		meas. points = 1001
		meas. BW = 1 kHz
		output level = 5 dBm
antennas	custom Yagi-Uda	

TABLE 3.5: Measurement devices and configuration for the user scenario

For the measurements presented in this Section, following scenario is investigated: A user with a hand-held reader device (base-station) is pointing towards a transponder. The transponder is attached to a large object which is positioned on a table in a room. The user initiates a communication with the object by pointing it with the hand-held reader. To ease the process of pointing, both, the hand-held reader and the transponder should have antennas with a relatively broad main beam. The main purpose of the scenario is to evaluate, how the non-ideal pointing process influences the propagation characteristics of the transmission channel.

To gather the CTF, a VNA setup similar to Section 3.1.3 is used. In this measurement scenario, the VNA (ZVA67, [82]) acts as the tagged object (Figure 3.16). To achieve this tagging, the RX antenna is directly attached to the output port of the external test set of the VNA. The TX antenna is held by the user and connected to the VNA via a PC 1.85 mm coaxial cables with a total length of 2.7 m. The VNA operates in a frequency range of 55–65 GHz with a spacing of 10 MHz, resulting in 1001 measurement points for a bandwidth of 10 GHz. To keep the measurement time of a frequency sweep in reasonable time limits, the measurement bandwidth is set to 1 kHz. This is necessary to reduce the influence of the movements of the user during the measurement to a negligible minimum. To calibrate the measurement setup, a direct connection between the PC 1.85 mm ports of the measurement input of the second port of the VNA, where the RX antenna is mounted, and the measurement cable connecting the source of the first port of the VNA and the TX antenna, is performed. As the use case described above requires physically small antennas on both, the transponder and the hand-held, the custom Yagi-Uda antennas with roughly 10 dBi gain and a beamwidth of 90 degree are used in this measurement campaign. Table 3.5 summarizes the devices and their respective settings.

During the measurements in the RF laboratory (Figure 3.17), the VNA is positioned at
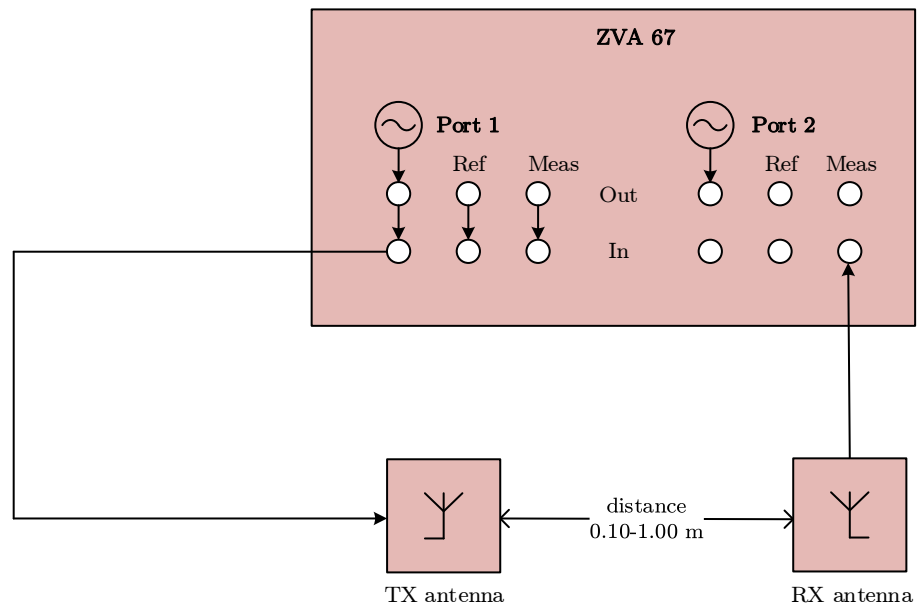
FIGURE 3.16: VNA measurement setup without diplexer
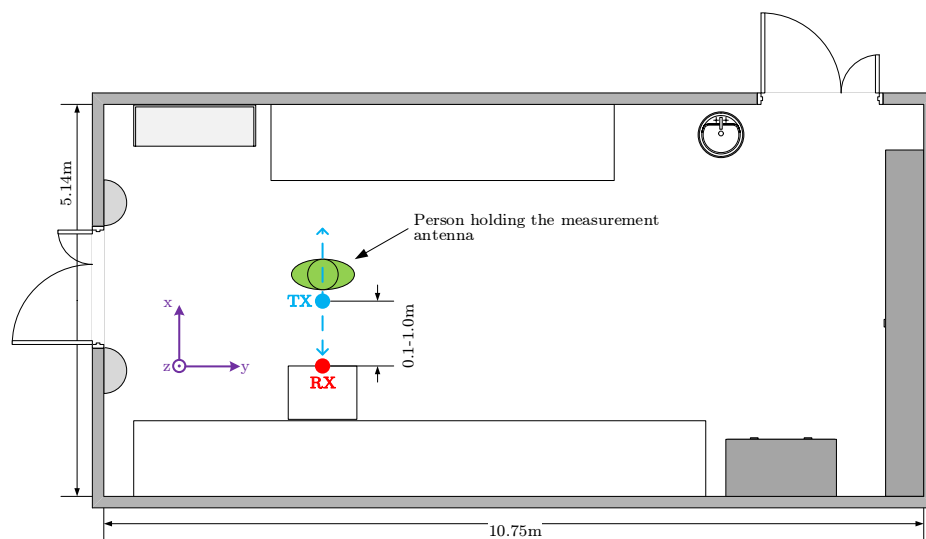
FIGURE 3.17: Floorplan of the user scenario measurement environment

a height of 1 m above the ground on a moveable table. The table is placed closely to one of the longer walls in the room. The RX antenna which is directly attached to the VNA is pointing to the center of the room. The user, who is holding the TX antenna in his hands, places himself in front of the VNA and initiates the measurement sweep using an external trigger device. For this measurement campaign, the distance between the VNA and the TX antenna held by the user is increased in 10 cm steps from 0.1 m to 1.0 m resulting in 10 different measurement positions along the main beam direction of the RX antenna.
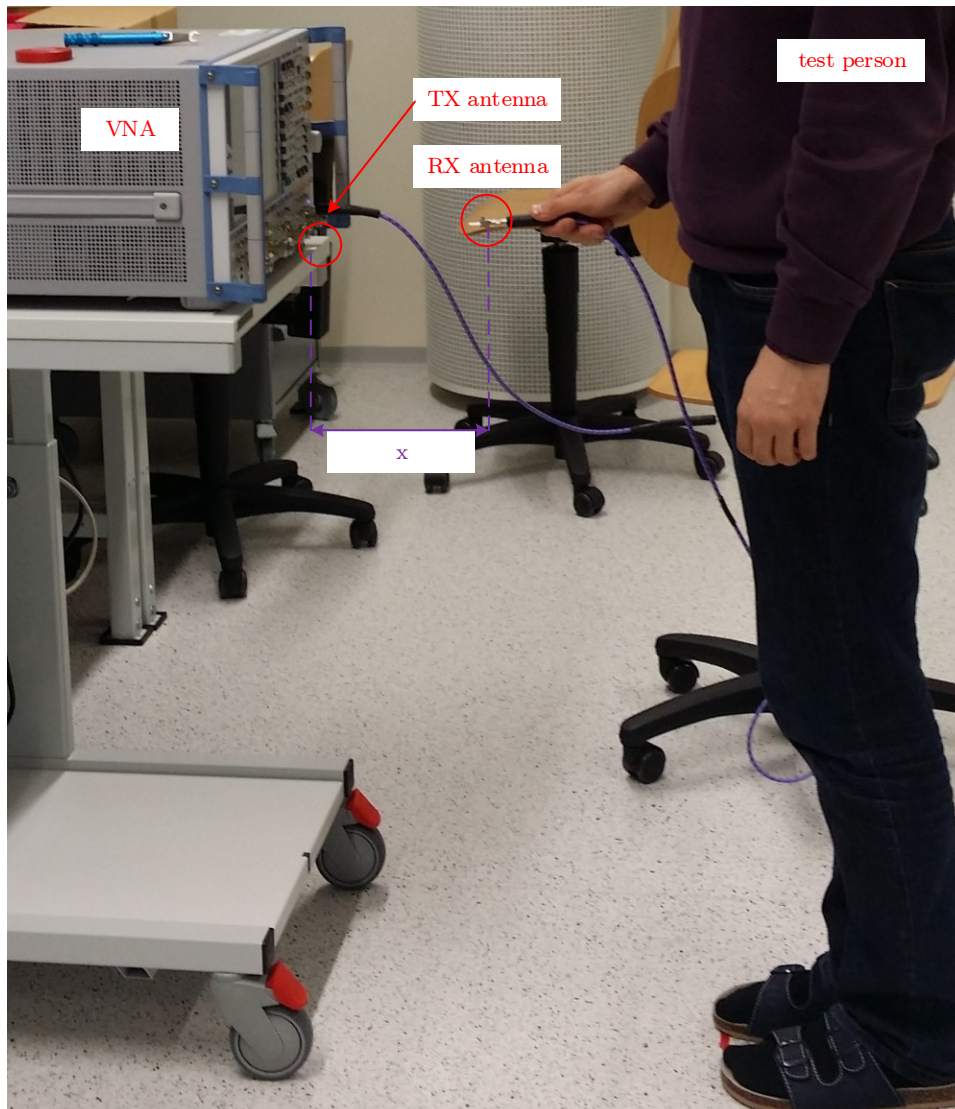
FIGURE 3.18: Picture of the user scenario measurement environment

Figure 3.18 shows a picture of the measurement setup. To achieve reproducible measurement positions, markings on the floor support the user during the alignment process. A chair in the background of the operator supports the measurement cable between the RX antenna and the VNA in order to reduce its movement and, therefore, the influence on the measured phase.

To gather enough statistical data to analyze the behavior of the channel in such a scenario, the user initiates the communication between the reader and the transponder 500 times for each of the ten measurement positions. Between the individual measurements, the user re-initiates the pointing process. This is achieved by moving the TX antenna out of the RX antennas main beam. Afterwards the TX antenna is pointed again towards the transponder. To increase the impact of the misalignment between TX and
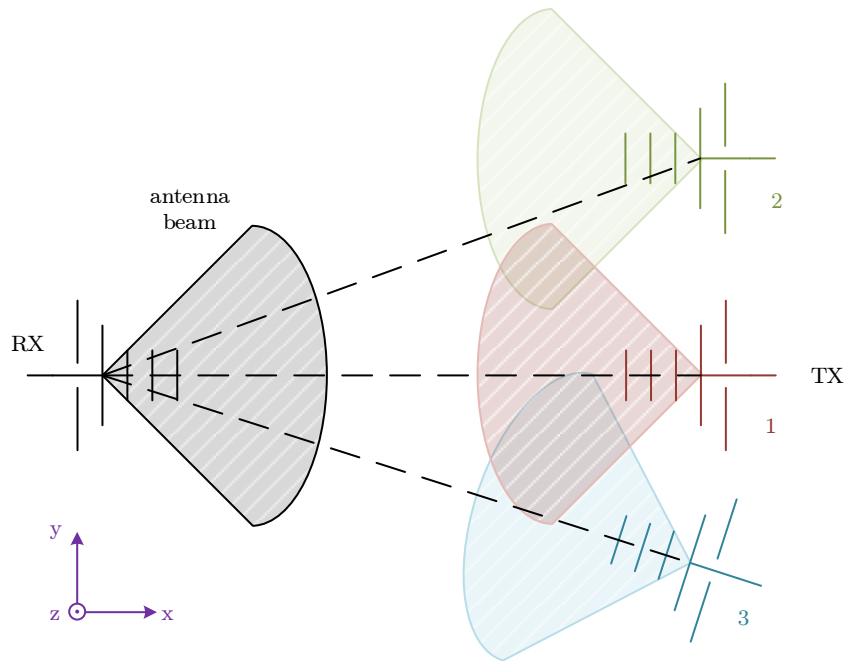
FIGURE 3.19: Intentional misalignment of the TX antenna in the user scenario measurements

RX antenna, the pointing process is exaggerated, which has to be taken into consideration when evaluating the results of this measurement campaign. The misalignment between the antennas can be divided in two main categories as shown in Figure 3.19: The position with index 1 shows a perfect alignment along the x-axis, which represents the main beam direction of the RX antenna. Index 2 represents an antenna position where the TX antenna has an offset in the y-z-plane. In this configuration, both main beam directions are parallel to each other. This results in a lower gain for both, the RX and the TX antenna. The antenna at index 3 has a similar offset in the y-z-plane but its main beam points directly at the TX antenna. In that case, the transmission channel benefits from the maximum gain of the TX antenna, while the gain of the RX antenna is decreased. Additionally to these two displacement configurations, the position of the TX antenna also varies slightly in the x-direction which generates an additional path loss.

During the measurement campaign, a ripple in the CTF of roughly 750 MHz can be observed at all measurement positions, as shown in Figure 3.20. The tendency of decreasing channel loss with increasing frequency can be explained with a larger ripple which is not seen in the represented frequency band. Experiments such as increasing the distance between the user and the TX antenna, or introducing an obstacle which
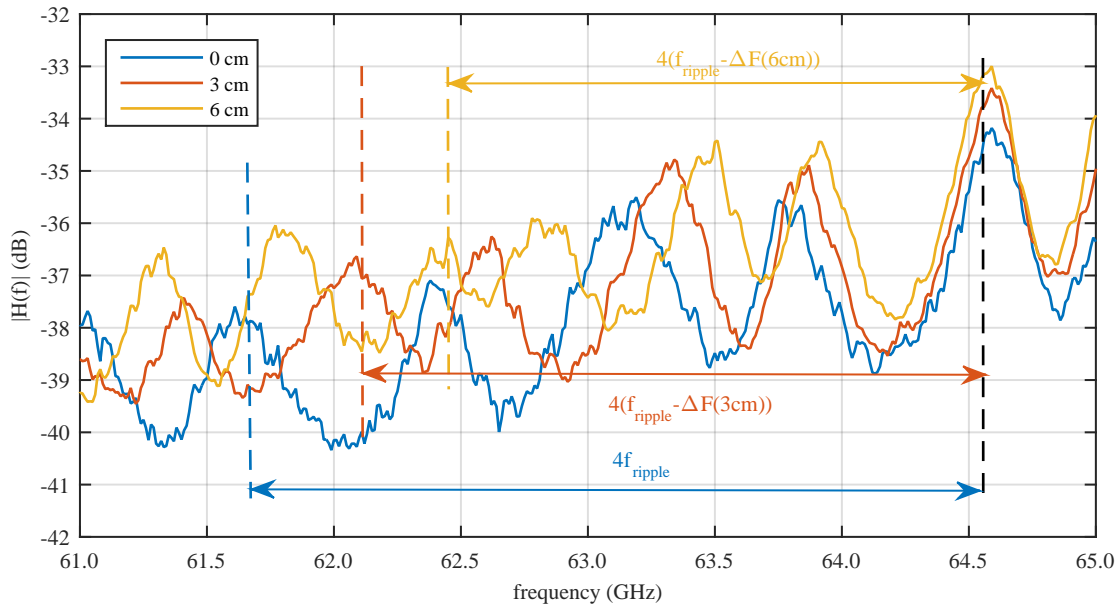
FIGURE 3.20: Ripple in the CTF of the VNA user setup for different distances between the RX antenna and the VNA

mimics a ground plane with a different height does not change the frequency of the ripple. However, by increasing the distance between the RX antenna and the VNA, the frequency of the ripple decreases according to the free space propagation [85, 89]. This ripple can therefore be ascribed to a reflection of the backward lobe of the RX antenna on or within the VNA.

3.2 Evaluation

The results of the measurement campaigns, presented in Section 3.1, are evaluated in different domains. On the one side, the channel transfer function gives a good overview on the behaviour of the channel for different frequencies. As the presented measurement systems are sounding the channel in the frequency domain, the data can be directly evaluated without any further post-processing. On the other side, the time domain parameters such as the power delay profile (PDP) and the delay spread require a transformation of the frequency domain CTF into the time domain channel impulse response (CIR). Since this transformation requires knowledge of the CTF in both, the magnitude and phase, this evaluation can only be performed for the VNA based measurements.

3.2.1 Channel Transfer Function

The CTF ($H(f)$) represents the propagation characteristics of the communication channel in magnitude and phase for distinct frequency points [85]. Classic EPC Gen2 RFID systems have an absolute occupied bandwidth of less than $1\,\mathrm{MHz}$. This translates into a negligible small relative bandwidth at mm-wave frequencies (less than two-hundredth of a percent). For such small bandwidths, the CTF can be assumed to be constant. Therefore, it is sufficient to consider only the frequency point of interest in order to estimate the influence of the channel on the MMID system.

As mentioned above, the CTF is directly gathered from the deployed measurement systems. The power measurements based on a signal analyser return only the magnitude of the CTF, while the VNA based systems probe the CTF in magnitude and phase as the transmission coefficient between the transmit and the receive port. Therefore, the post-processing of the measurement data is limited to averaging multiple independent measurements at a single point. The average CTF ($\bar{H}(f)$) for N measurements ($H_i(f)$) is given by (3.1)

$$\bar{H}(f) = \frac{1}{N} \sum_{i=1}^{N} H_i(f) \tag{3.1}$$

Assuming that the behavior of the channel is constant over the time in which the measurements are taken, and that the noise is statistically independent, the signal to noise ratio can be enhanced by $10 \cdot \log_{10}(N)$ dB. This assumption can be safely made for the power measurements. The presented measurements based on the VNA setup are sounding the channel with intentionally varying the alignment of the antennas at a given measurement position. Therefore the channel is not constant over time and this assumption does not hold true anymore. However, the averaged CTF of the VNA based measurements gives a good measure for the channel attenuation for the system design. Additionally the variation of the CTF can be taken into consideration for evaluating the performance of the MMID system using worst and best case scenarios.

In the following sections, the CTF is evaluated along two different domains: Section 3.2.1.1 assesses the measurements from the three different setups in the frequency domain for given measurement positions. Section 3.2.1.2 investigates the behavior of the CTF for a given frequency point along different measurement positions.
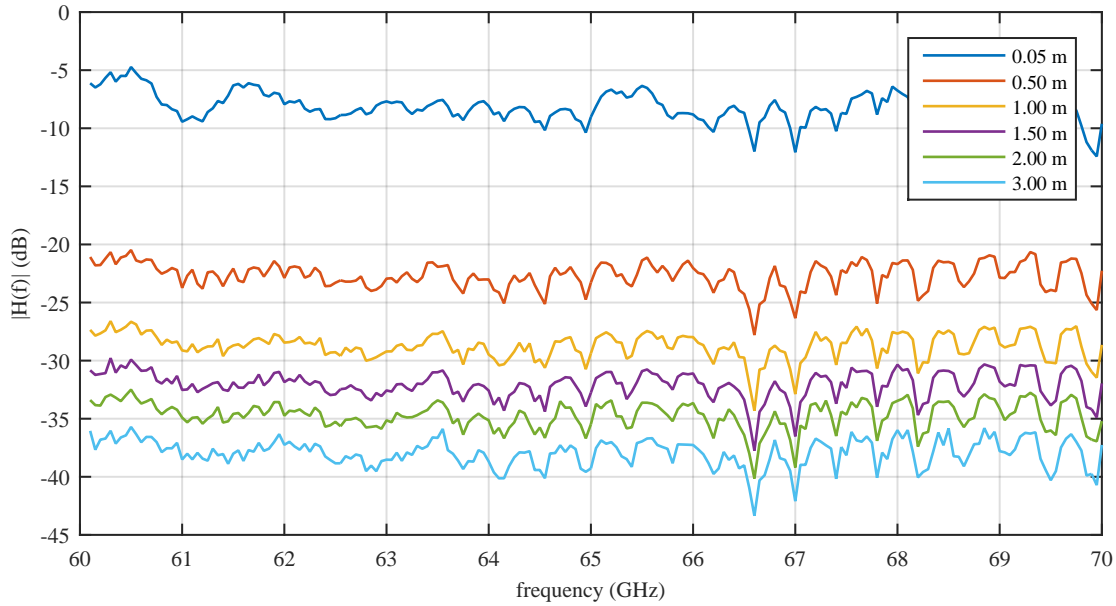
FIGURE 3.21: Channel attenuation versus frequency for different distances using the power measurement setup.

3.2.1.1 Frequency domain

Figure 3.21 shows the magnitude of the CTF for the horn-horn configuration of the power measurements at six different positions from 0.05 m to 3.0 m. The attenuation of the channel shows a very constant behavior over the whole frequency range with a maximum variation of 5 dB. The main part of this variation can be ascribed to a ripple of 400 MHz. This ripple remains constant over all measurement positions and is very pronounced starting from 63.5 GHz. Due to this invariance over different measurement distances, the cause of the ripple is either a mismatch between the multiplier of the signal generator and the TX antenna (Figure 3.8). Later investigations showed, that the WR12 to PC 1 mm adapter used in the calibration of the frequency multipliers output power showed an unexpected frequency dependent behavior, which introduces a ripple in the calibration data, which can be seen in the final measurements. Unfortunately, there was no possibility to characterize this mismatch during the time of the measurements in order to compensate for this error.

The same antenna configuration in the VNA setup is depicted in Figure 3.22. The frequency response for this setup can be divided into two parts: One below 56 GHz, in which the attenuation of the CTF heavily increases. This can be explained by the waveguide feed of the horn antenna (WR12) with an operating range of 60–90 GHz and a hard cut-off frequency around 50 GHz. The second part of the response above 56 GHz
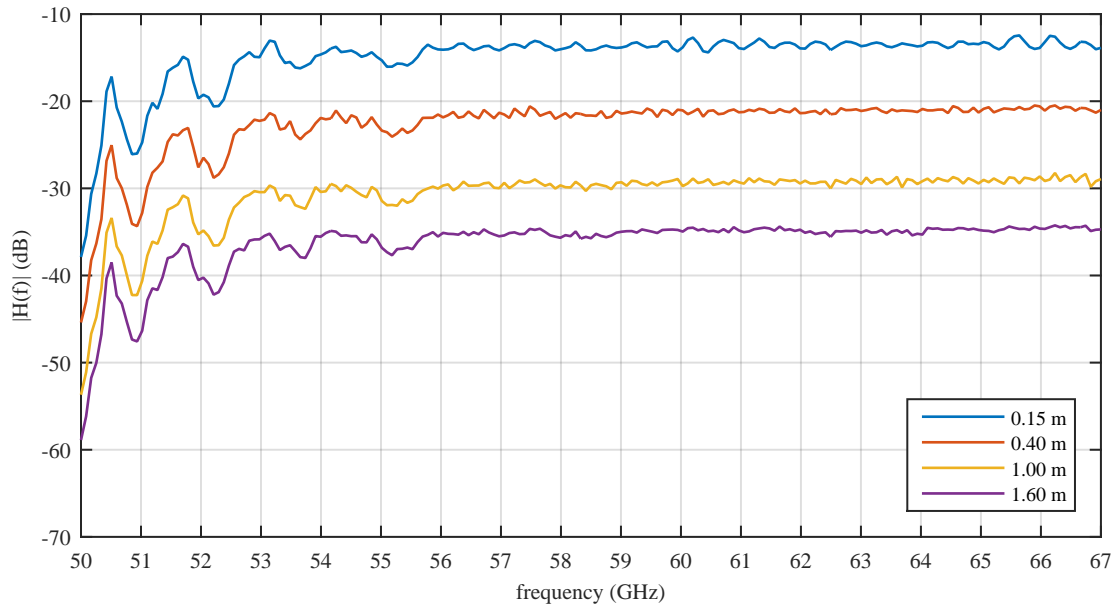
FIGURE 3.22: Averaged magnitude of the CTF for the horn-horn antenna configuration

is characterized by a very stable behavior with a very minimal ripple. This ripple is most pronounced at the measurement distance of 0.15 m and decreases significantly for increasing distances. This property suggests that the ripple is caused by a reflection between the two antennas, which are positioned in each others radiating near-field at this measurement position [64].

While comparing the measurement position of 1.00 m in Figures 3.21 and 3.22, one can observe that the attenuation between 60 GHz and 67 GHz is slightly lower in the power measurement setup. This deviation for the same antenna configuration is caused by the 1 mm PC to waveguide adapters which are deployed in the VNA setup. These adapters enable a transition between the calibrated coaxial connectors of the measurement system and the waveguide input of the horn antennas and introduce an additional attenuation to the measurements. To eliminate this deviation, a calibration of the VNA setup using a WR12 waveguide calibration kit has to be performed, which was not available at the time of the measurements.

The yagi-horn configuration in Figure 3.23 shows a similar behavior as the horn-horn configuration below 56 GHz, although the effects become distinct for frequencies below 53 GHz. Also the ripple which can be observed at the measurement position of 0.17 m is comparable to the one of the horn-horn setup and can be explained in a similar way. At the measurement points starting from 1.00 m a new ripple with a frequency of 3 GHz
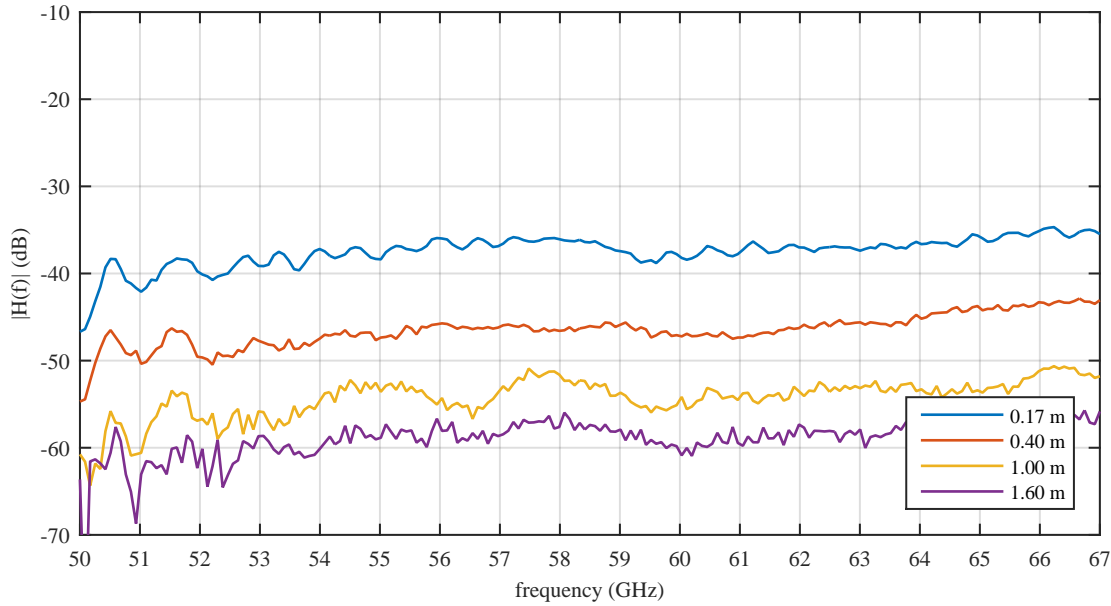
FIGURE 3.23: Averaged magnitude of the CTF for the yagi-horn antenna configuration

can be observed. This effect can be explained by a multipath propagation, such as a ground reflection [31, 85].

The last antenna configuration of the VNA setup is shown in Figure 3.24. The frequency ripple at the measurement position of 0.15 m is similar to the one observed at the other two configurations. Contrary to the previous configurations, the yagi-yagi configuration does not show a relatively constant attenuation over the investigated frequency band. The frequency response shows a maximum between 57 and 62 GHz and a stronger attenuation at the lower and upper limit of the frequency band. This behavior can be explained by the operating frequency range of the antenna as shown in Figure 3.7.

Figure 3.25 compares the three antenna configurations for the VNA setup at a measurementn distance of 1.00 m. It can be seen, that the horn-horn configuration has the lowest attenuation of about 30 dB starting from 56 GHz. The other two configurations show a very similar attenuation between 50 and 55 dB. The the comparable path loss of the yagi-yagi setup in comparison with the horn-yagi setup, despite the much higher gain of the horn antenna is caused by a polarization mismatch between the two antennas.

While the previous Figures show the averaged CTF $\bar{H}(f)$ for different measurement positions, Figures 3.26 and 3.27 show the variation of the channel in the VNA and user scenario measurements at 0.5 m. In both graphs, the solid blue line indicates the average CTF while the gray crosses represent single measurements on a sparse frequency grid.

FIGURE 3.24: Averaged magnitude of the CTF for the yagi-yagi antenna configuration
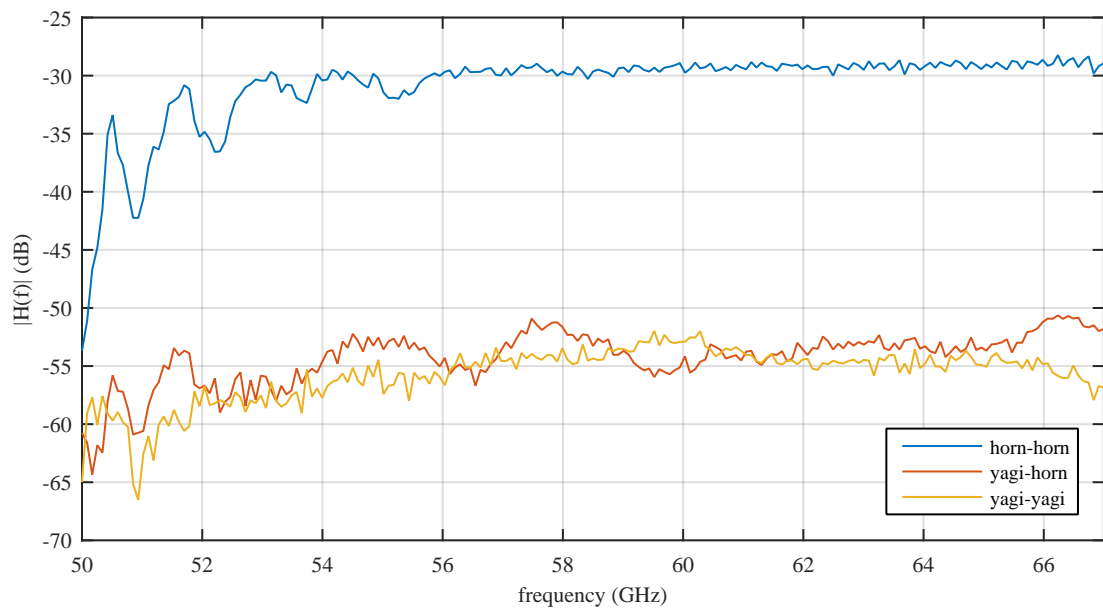
FIGURE 3.25: Averaged magnitude of the CTF for different antenna configurations at a measurement distance of 1.0 m
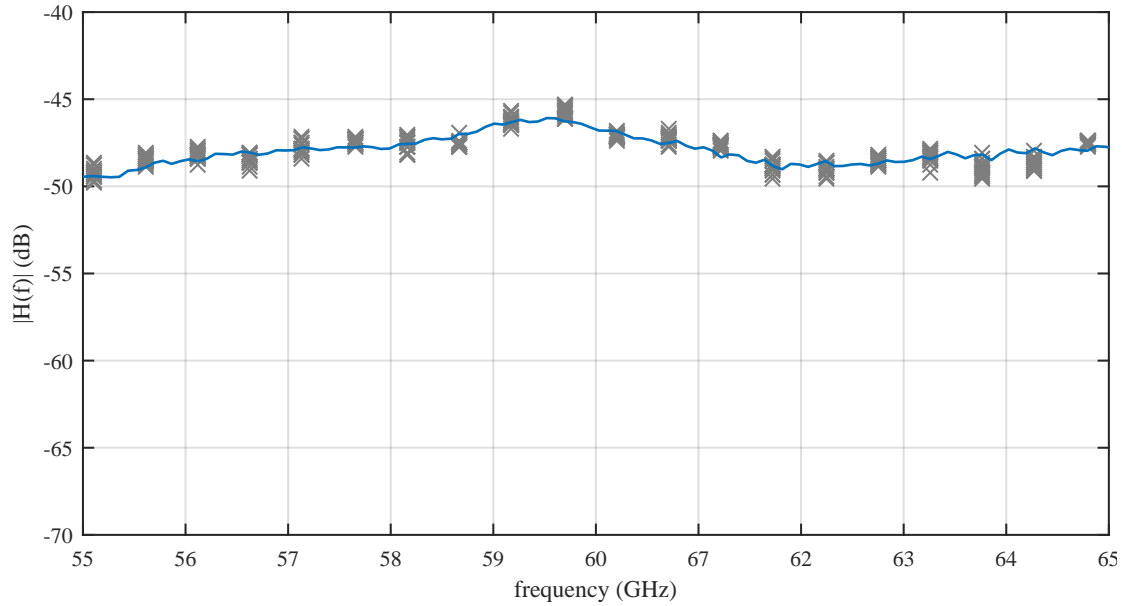
FIGURE 3.26: Averaged magnitude of the CTF for the yagi-yagi antenna configuration
from the VNA measurements at a distance of 0.5 m

The variation of the channel attenuation differs highly between the two measurement setups. For the VNA based setup in which the measurement position is varied only slightly around the LOS, the deviation from the average CTF does not excceed 1 dB over the whole investigated frequency range. The user scenario however shows a variation between 5 and 10 dB with some exceptions between 56 and 58 GHz. In this frequency range, a single measurement shows a significant anomaly, which can be neglected for further investigations.

3.2.1.2 Distance domain

Another perspective to examine the CTF is the distance domain. In this domain, the attenuation of the channel for a fixed frequency point is plotted along the different measurement points. This gives a good insight on the behavior of the channel for increasing distances and, therefore, on the expected reading range of the MMID system.

Figure 3.28 provides a comparison between the measurements of the power measurement setup and the FSPL model at 63.5 GHz. The additional gray lines depict measurements from 60–70 GHz. To parametrize the FSPL model given in (3.2), both the gain of the TX antenna (G_{TX}) and the RX antenna (G_{RX}) are assumed to be 21 dB as mentioned
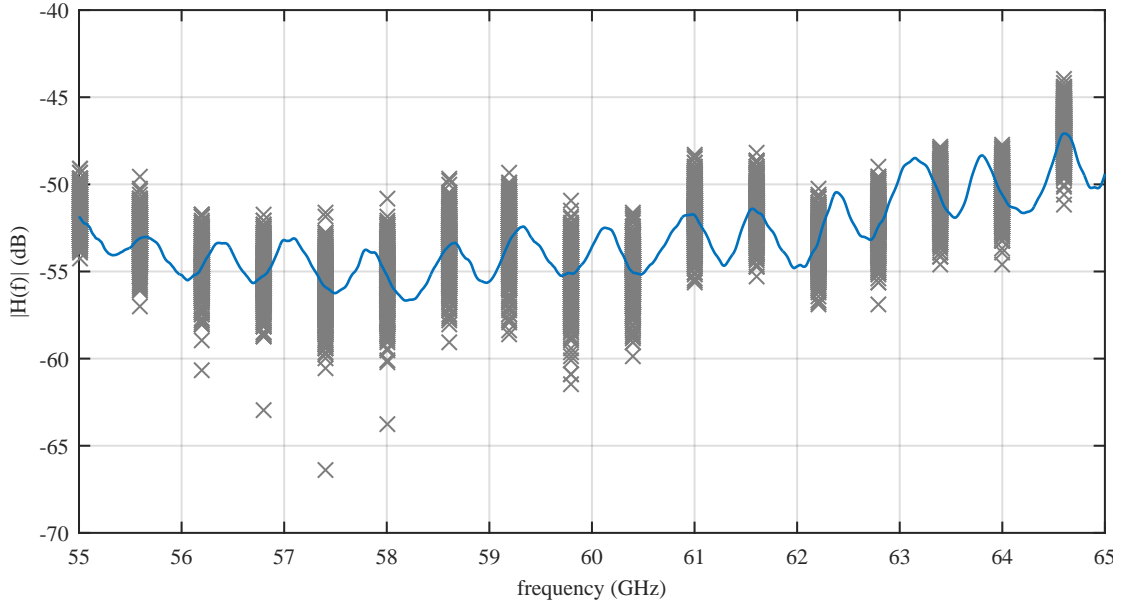
FIGURE 3.27: Averaged magnitude of the CTF for the yagi-yagi antenna configuration
from the user scenario measurements at a distance of 0.5 m

in Section 3.1.1. The path loss is calculated for a free space wave length of $4.8 \, \text{mm}$ (λ_0)
and a distance of $1.0 \, \text{m}$ (r) according to (2.14).

$$\frac{P_{RX}}{P_{TX}} = G_{TX} \cdot L_{Path} \cdot G_{RX} \tag{3.2}$$

Looking at Figure 3.28 a good agreement of the measurements and the FSPL model
can be seen. The difference between both is below $1 \, \text{dB}$ for most of the measurement
points. Only for distances below $0.5 \, \text{m}$ the deviation increases slightly. This effect can
be explained by the nature of the FSPL model which requires both antennas to be in
the far-field of each other.

Similar to Figure 3.28, Figure 3.29 shows a comparison of the horn-horn antenna config-
uration in the VNA setup with the FSPL model. The solid blue line shows the average
of the measurements at $60 \, \text{GHz}$. The FSPL model calculated by (3.2) is represented by
the solid orange line and shows an underestimation of the channel attenuation. This
constant offset can be again explained by the waveguide adapters. The influence of
these transitions can also be seen in Figure 3.30, which compares the power and VNA
measurements of the horn-horn antenna configuration over the measurement distance.
Both measurements show a very similar behavior over the investigated distances. They
only differ in a rather constant offset between 2 and $3 \, \text{dB}$. To compensate for the losses
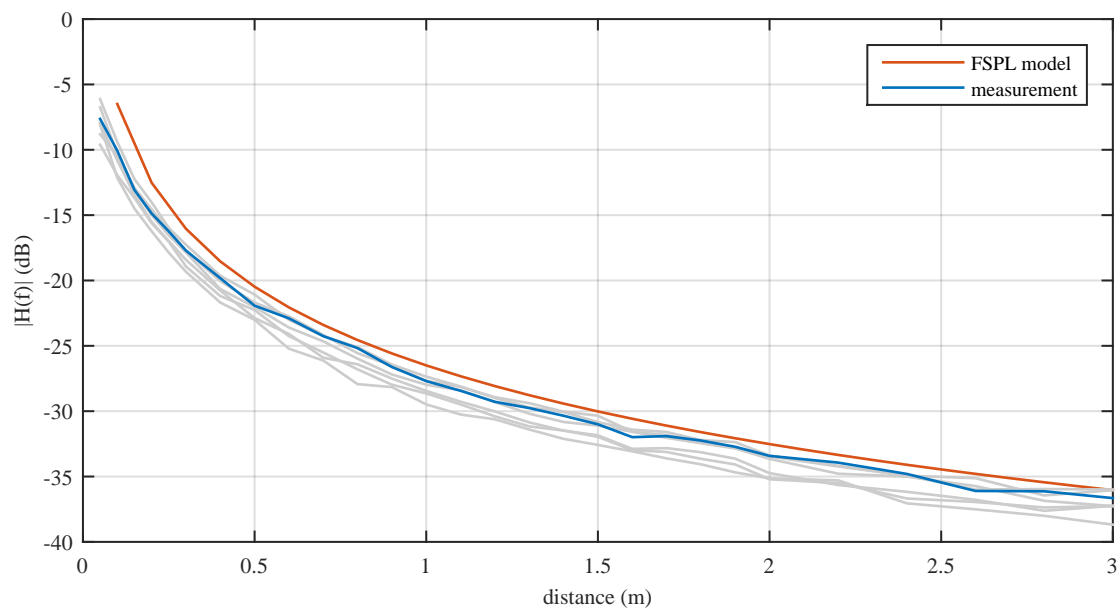
FIGURE 3.28: Comparison between the measurements of the power measurement setup and the FSPL model.
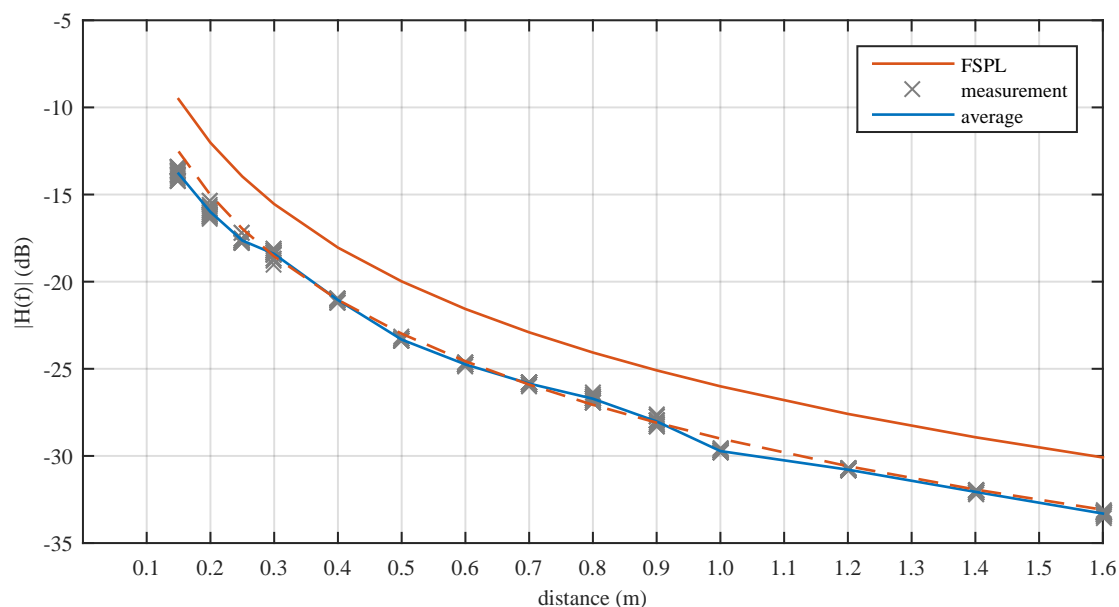
FIGURE 3.29: Averaged magnitude of the CTF for the horn-horn antenna configuration at 60 GHz

of the transitions, the gain of each horn antenna in the FSPL is reduced by 1.5 dB. This adapted FSPL model, which is depicted by the dashed orange line shows again a good agreement with the measurements. The single measurements at a measurement position (grey crosses) show a low variation which increases slightly for measurement distances below 0.3 m

The yagi-horn antenna configuration of the VNA setup is shown in Figure 3.31. Similar
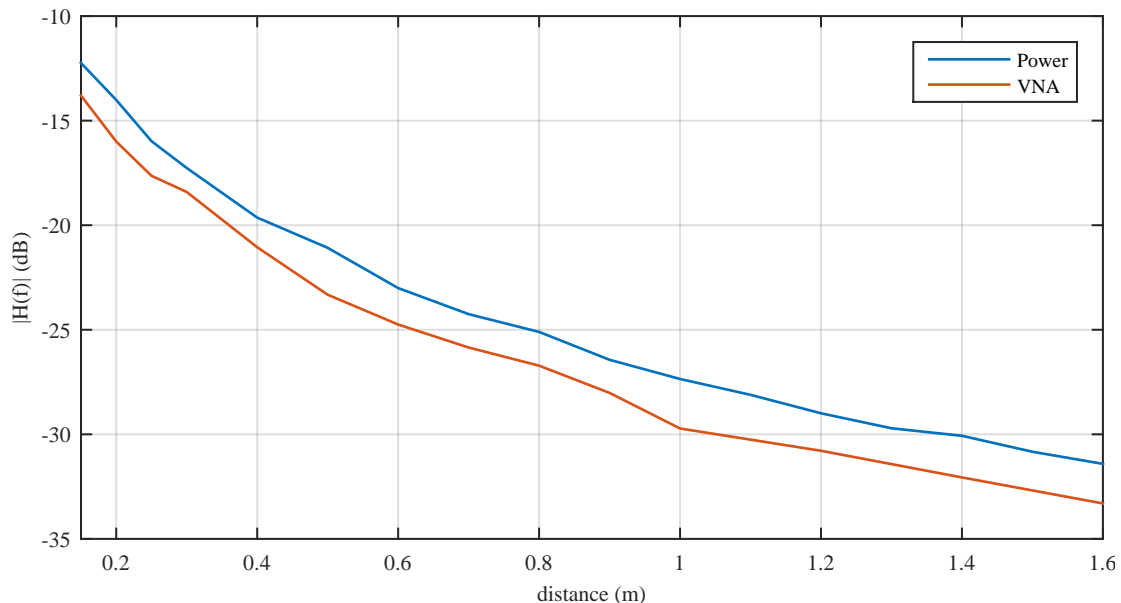
FIGURE 3.30: Comparison between the power measurement setup and the vna setup versus the measurement distance at 60 GHz

to the horn-horn configuration, the measurements show a good agreement for distances above 0.3 m. For lower distances however, the FSPL model overestimates the channel attenuation slightly. The variation of the single measurements along the grid orthogonal to the LOS show a higher variation than the previous antenna configuration. This effect can be ascribed to the wider beam width of the Yagi-Uda antenna which enables the propagation of additional paths along with the LOS. At 1.4 m the variation around the average CTF shows a maximum of approximately 5 dB. This suggests that a second propagation path such as a ground reflection interferes with the LOS.

For the yagi-yagi antenna configuration in Figure 3.32, the FSPL model shows significant deviations compared to the previous two antenna configurations. Below 0.3 m the FSPL model overestimates the channel attenuation more severe than in the yagi-horn case. This can be explained by the usage of two Yagi-Uda antennas which doubles the over-estimation and is not partly cancelled by the underestimation of the horn antenna. For increasing distances, one can observe a ripple in the CTF. This fading can be ascribed to the multipath propagation and is extensively investigated in the literature [85, 90–94].

The evaluation of the user scenario measurements is shown in Figure 3.33. As expected, these measurements show the highest variation around the average measured CTF which is constantly between 8 and 10 dB. Contrary to the systematic evaluation of the channel in the yagi-yagi antenna configuration, the FSPL model does not overestimate the
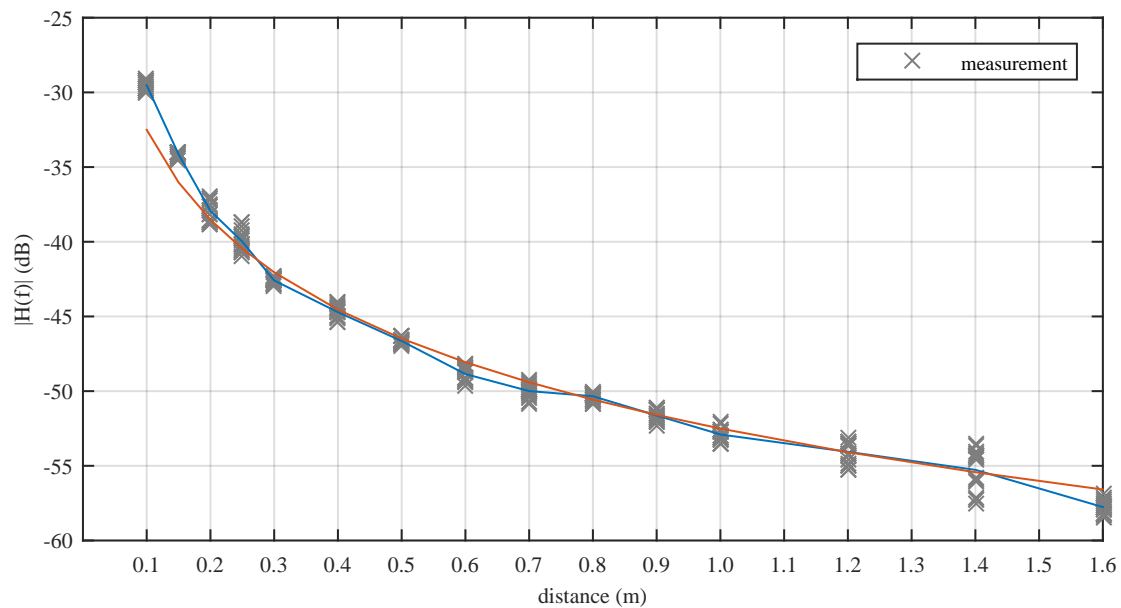
FIGURE 3.31: Averaged magnitude of the CTF for the yagi-horn antenna configuration at 60 GHz
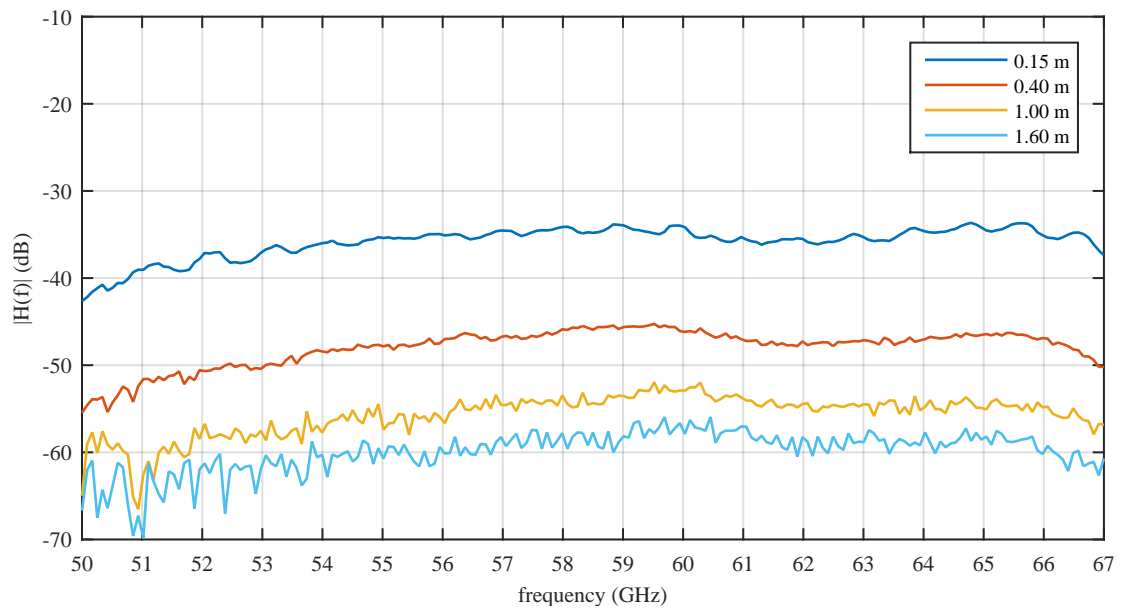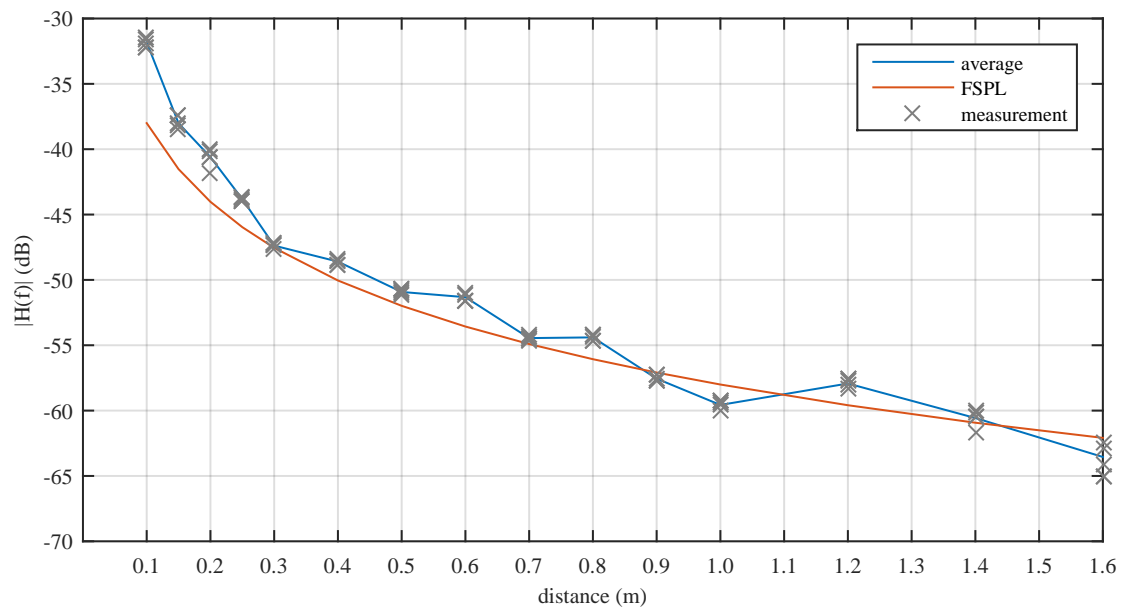

FIGURE 3.32: Averaged magnitude of the CTF for the yagi-yagi antenna configuration at 60 GHz
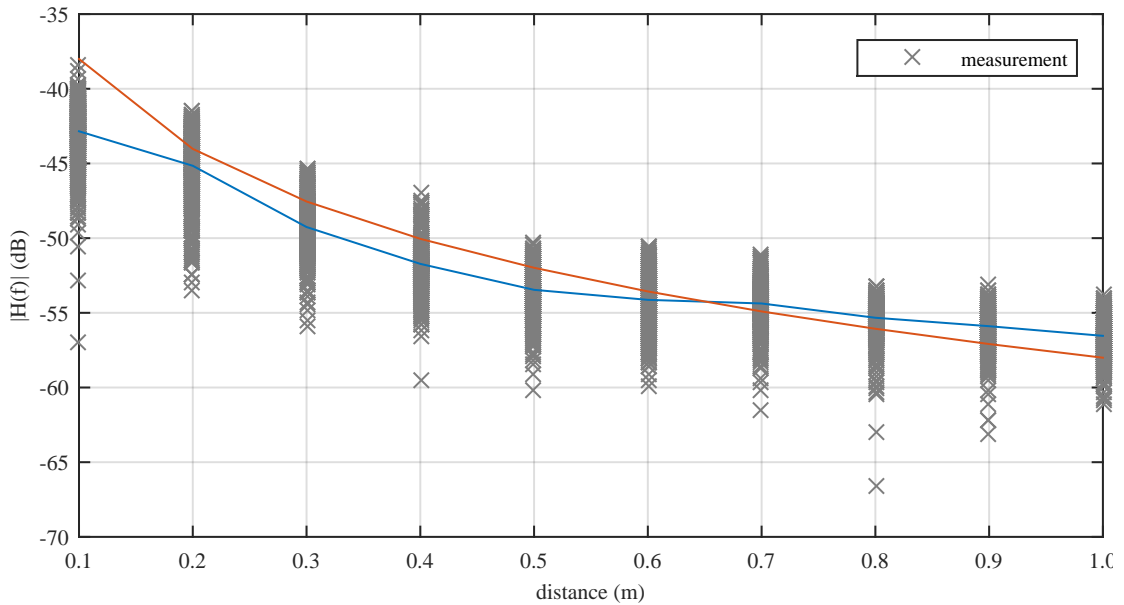
FIGURE 3.33: Averaged magnitude of the CTF for the yagi-yagi antenna configuration
in the user scenario at 60 GHz

attenuation in the near field of the antennas. Also the effect of fading due to multipath propagation is as distinct as for the previous measurements. This difference towards the systematic measurements is caused by the design of the user case measurement scenario. In the first measurements, the two Yagi-Uda antennas are perfectly aligned along the LOS and the channel is probed in its close neighborhood. In the second measurements, the user intentionally misaligns the transmit and receive antennas as described in Section 3.1.4. This covers the impact of distinct propagation mechanisms and results in an average CTF which can be well described by the FSPL model.

3.2.2 Power Delay Profile

The frequency domain based evaluation of the channel presented in Section 3.2.1 gives a good insight for continuous wave and very narrow band signals. While this characterization is valid for a MMID communication system with an occupied bandwidth of several kHz, application scenarios like the localization of a MMID transponder benefits from much higher bandwidths. The time-domain based channel impulse response (CIR) gives a good insight on the impact of the channel onto such systems [85].

To obtain a real valued CIR ($h_i(\tau)$) from the complex CTF ($H_i(f)$) is extended to the negative frequencies by mirroring the complex conjugated CTF ($H_i(f)^*$) as shown in

(3.3). The index i denotes the individual measurements. The extended CTF is then translated into the excess delay domain using the inverse Fourier transformation (3.4).

$$H_i(-f) = H_i^*(f) \tag{3.3}$$

$$h_i(\tau) = \mathcal{F}^{-1}\{H_i(f)\} \tag{3.4}$$

A way to describe the CIR in a condensed form is the power delay profile (PDP, $P_h(\tau)$) [95, 96]. The PDP or delay power spectral density gives an insight about how much power arrives at the receiver at a given time bin $(\tau, \tau + d\tau)$ and provides a good insight on the multipath propagation components of the channel [97, 98]. To obtained from the time variant CIR $(h(t,\tau))$ is computed by integrating over a quasi-stationary time interval $(2T)$ [85]:

$$P_h(\tau) = \lim_{T \to \infty} \frac{1}{2T} \int_{-T}^{T} |h(t,\tau)|^2 dt \tag{3.5}$$

Assuming that the CIR is constant for a single measurement, the calculation of the PDP can be simplified to:

$$P_{h,i}(\tau) = |h_i(\tau)|^2 \tag{3.6}$$

To further condense the PDPs of the individual measurements (16 in the case of the VNA setup and 500 for the user scenario) an average PDP (APDP, $\overline{P_h}(\tau)$) is introduced:

$$\overline{P_h}(\tau) = \frac{1}{N} \sum_{i=1}^{N} P_{h,i}(\tau) \tag{3.7}$$

Figure 3.34 shows the normalised APDP for the three antenna configurations of the VNA measurement setup at a distance of 1 m. The horn-horn configuration shows a strong LOS component with only a few negligible multi path components (MPC). The yagi-horn configuration has a strong MPC 15 dB below the LOS at an excess delay of 0.4 ns and a second minor MPC (32 dB below the LOS) shared with the yagi-yagi setup at 5.3 ns. The yagi-yagi configuration shows the highest multi path behaviour. Besides the aforementioned MPC at 5.2 ns it shows two additional MPC above 30 dB below the LOS at 3.2 and 6.8 ns. These MPC identified by the APDP correspond with the ripples which are described in the CTF in Section 3.2.1.1.
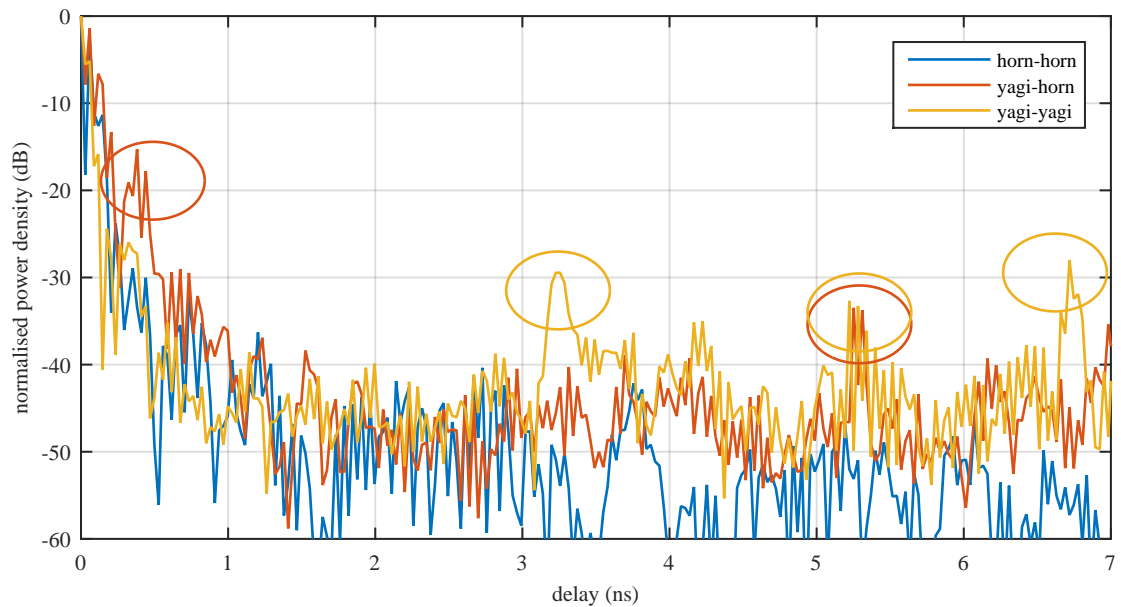
FIGURE 3.34: Comparison of the average PDP for the three different antenna combinations for the VNA measurement setup at 1 m

To examine the LOS component of the APDP, Figure 3.35 shows a close-up of the first ns of the APDP. The yagi-yagi configuration shows the narrowest LOS component with a 20 dB width of 0.12 ns. The horn-horn and yagi-horn setups show a higher dispersion with 0.18 and 0.45 ns respectively. This very high value for the yagi-horn setup can be explained by the first MPC which exceeds the 20 dB limit. This component can also be seen in the yagi-yagi configuration for with a level of 38 dB below the LOS. When disregarding the first MPC of the yagi-horn setup, the dispersion of the LOS component reduces to 0.22 ns, which is still the highest level among the three antenna configurations.

Figure 3.36 depicts the APDP of the user scenario measurements for three positions at 0.2, 0.6 and 1.0 m. At 0.2 and 0.6 m, the frequency ripple seen in Figure 3.20 is indicated clearly. For the measurement position at 1.0 m, this component is hidden by the dispersion of the LOS. At 7–10 ns a distinct MPC can be seen for all three measurement positions. This component can be ascribed to a reflection on the ground. Between 18 and 27 ns, the two higher measurement distances show several MPC which are almost negligible at the measurement at 0.2 m. These components are caused by objects in the proximity of the measurement setup such as the ventilation outlets shown in Figure 3.17.
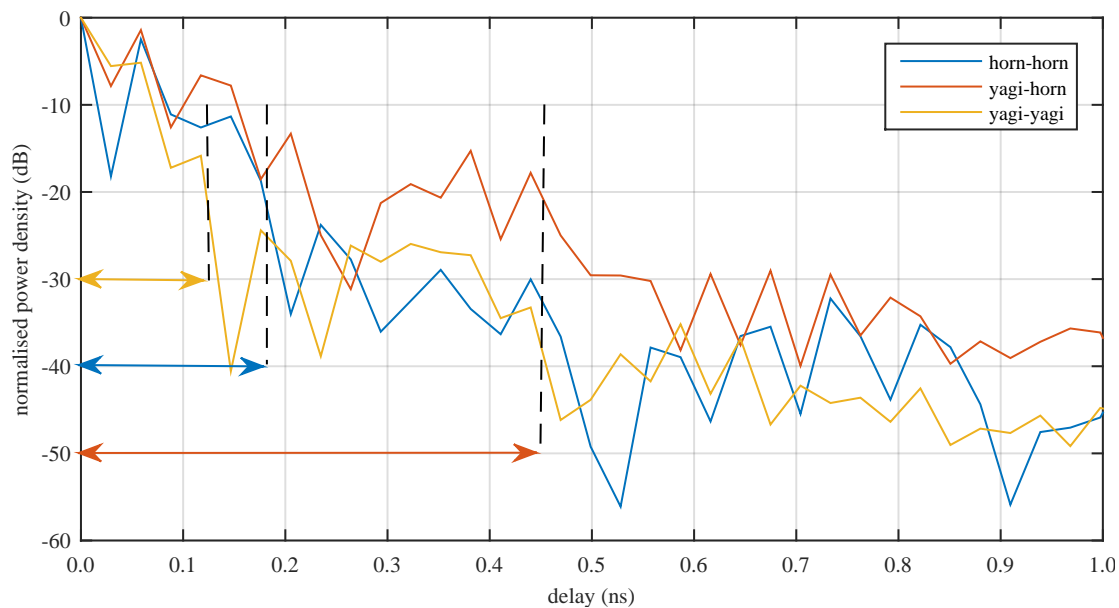
FIGURE 3.35: Comparison of the LOS component of the average PDP for the three different antenna combinations for the VNA measurement setup at 1 m
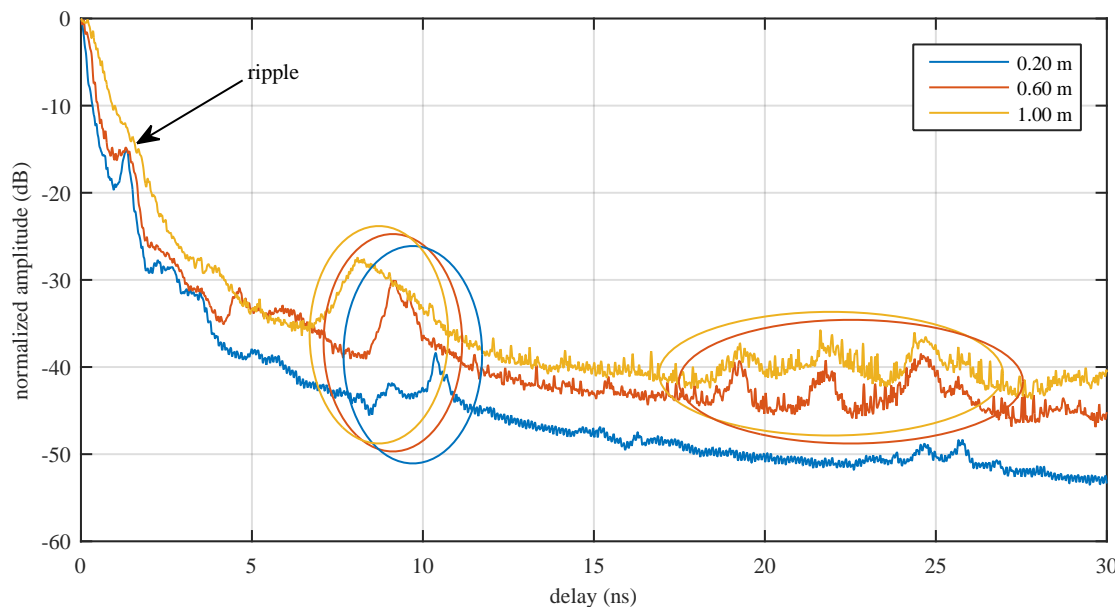
FIGURE 3.36: Comparison of the average PDP for the three different distances for the VNA user measurement setup

3.2.3 Delay Spread

To provide an even more condensed overview on the time-domain characteristics of a channel, the root-mean square delay spread (RMSDS) can be used [85]. This figure of merit gives a good insight on the performance of high data-rate communication systems for a given channel [99]. To calculate the RMSDS, the zeroth and first-order moments have to be calculated. The zeroth-order moment of the PDP is the time-integrated power (P_m):

$$P_m = \int_{-\infty}^{\infty} P_h(\tau) \ d\tau \tag{3.8}$$

The first order moment is the mean delay, normalized by the time-integrated power. and calculated by:

$$T_m = \frac{\int_{-\infty}^{\infty} P_h(\tau) \cdot \tau \ d\tau}{P_m} \tag{3.9}$$

The second-order moment of the PDP, i.e. the RMS delay spread is given by:

$$S_\tau = \sqrt{\frac{\int_{-\infty}^{\infty} P_h(\tau) \cdot \tau^2 \ d\tau}{P_m} - T_m^2} \tag{3.10}$$

As the (A)PDP is only known for a limited amount discrete points of the excess delay, the infinite integrals of (3.8) to (3.10) are reduced to finite sums (3.11).

$$S_\tau = \sqrt{\frac{\left(\sum_\tau P_h\left[\tau\right] \cdot \tau^2\right) - \left(\sum_\tau P_h\left[\tau\right] \cdot \tau\right)^2}{\sum_\tau P_h \tau\left[\tau\right]}} \tag{3.11}$$

To reduce the impact of the measurement noise, all values below the noise floor of the measurement system are filtered out before calculating the delay spread parameters. [100]. The noise floor threshold is determined visually for each measurement distance (around 45 dB below the LOS) as shown in Figure 3.37.

The RMSDS for the three antenna configurations of the VNA setup and for the user scenario are shown in Figure 3.38. Over all measurement positions, the horn-horn configuration shows the best performance with a constant level of 0.06 ns. The yagi-horn setup has a comparable performance, only significantly deviating at 0.5 m. For lower distances up to 1.0 m, the yagi-yagi configuration has the best performance, depsite some outliers at 0.3 and 0.6 m. For higher distances the delay spread increases significantly
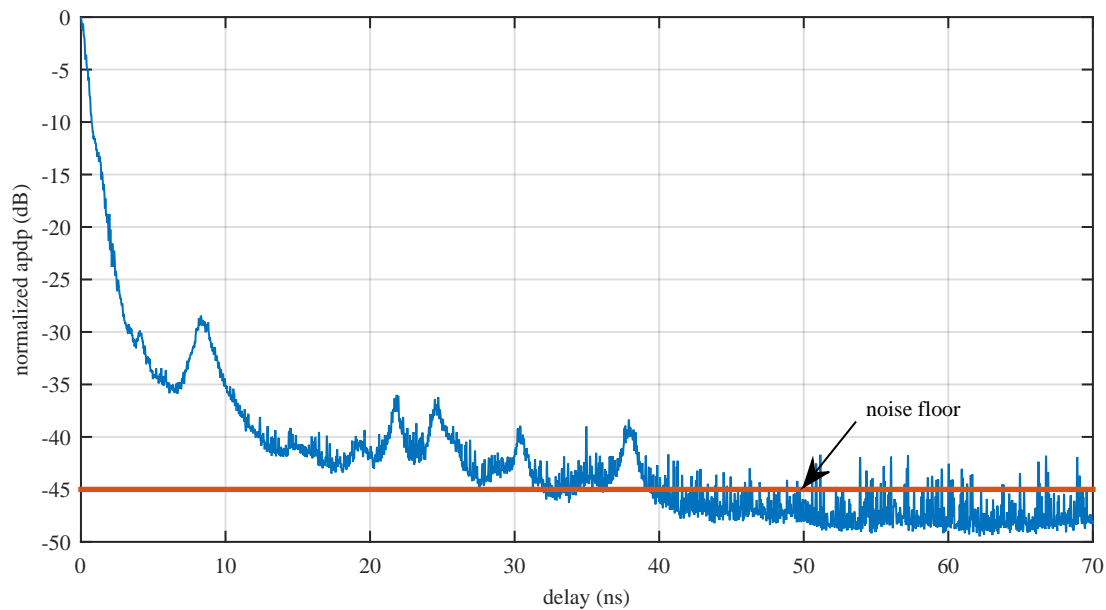
FIGURE 3.37: Visual determination of the noise floor of the APDP.
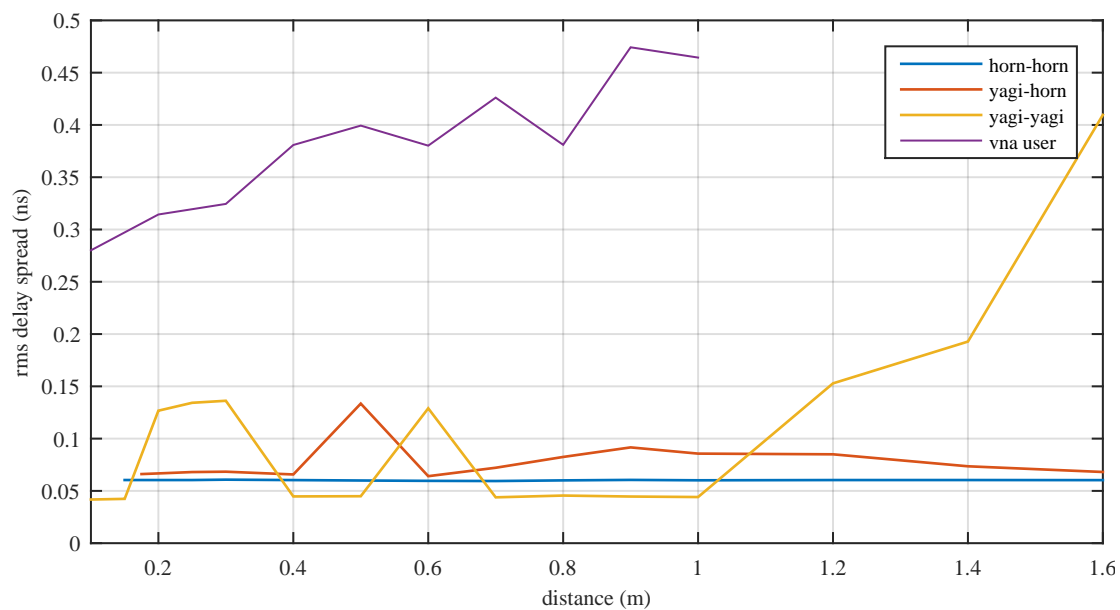
FIGURE 3.38: Variation of the rms delay spread over an increasing distance for the VNA and the VNA user measurement setup

and reaches 0.4 ns at 1.6 m. This is a good indication, that the MPC increase for the yagi-yagi setup at these measurement positions.

The RMSDS of the user scenario is a magnitude higher compared to the VNA setup. Starting from 0.3 ns at 0.1 m, the RMSDS rises steadily up to 0.45 ns at 1 m. However, indoor measurement campaigns at a similar frequency band, show a much higher delay spread of 1 ns and more [101–103].

3.3 Conclusions

In this Chapter, three different measurement setups for sounding the propagation channel are developed. The measurement campaigns using these setups are evaluated in the frequency, distance, and time domain. The frequency domain evaluation in Section 3.2.1.1 show a very flat behavior over the investigated frequency range. The distance domain results indicate that the free space propagation loss model is a good estimator for the channel in the system simulations of Section 2.4. Finally, the time domain evaluation shows that the multipath propagation of the MMID channel has a low impact on the system performance, thus enabling high data-rate and high bandwidth applications such as localization.

3.4 Contributions

The main contribution of this chapter is the investigation on the channel behavior of an MMID system in the E-band. This includes near range channel measurements up to 1 m distance between the base-station and the transponder, as well as a use-case scenario, which incorporates a user interacting with the base-station. The results of these investigations are published in [37, 38].

Chapter 4

Base-Station

The base-station of a RFID or MMID system connects an object equipped with a transponder to a larger network such as an IoT application. It responds the requests coming from the application and handles the communication with the transponders in its reading range [23]. Within the MMID system, the base-station has two main tasks: During the downlink communication, it sends amplitude modulated commands to the transponder in order to access the data required by the requesting application. During the uplink communication, the base-station provides a CW carrier for the backscatter modulation of the transponder. Due to this communication technique the requirements of the receiver are similar to the ones of a frequency modulated continuous wave (FMCW) radar system.

The MMID base-stations reported in the literature can be divided according to their RF frontend into two main categories: heterodyne and direct conversion transceivers:

A heterodyne base-station demonstrator with operating frequency of 10 GHz and an effective isotropically radiated power (EIRP) of 25.15 dBm is presented in [104]. The authors in this article utilize a standard UHF RFID base-station with an operating frequency of 850–950 MHZ as a baseband and IF unit. Two double side-band mixers are deployed to convert the output frequency of the UHF base-station into the 10 GHz frequency domain and back. This concept allows an easy integration of the full EPC Gen2 protocol in the base-station.

Direct conversion transceiver base-stations are presented in [105–107]. [105] presents a 60 GHz base-station for the uplink of an MMID system. Its active components, such

as a mm-wave voltage controlled oscillator (VCO) and a direct conversion quadrature mixer are integrated on a CMOS process. The passive elements, such as the TX and RX antenna arrays, transmission lines and power splitter are realized on a low-temperature co-fired ceramic (LTCC). The base-station module provides an output power of 11.6 dBm EIRP and an isolation between the transmit and receive channel of 43 dB. In [106, 107], the authors present a MMID base-station for localization of active transponders. The system architecture is based on a FMCW radar. The presented demonstrator provides a usable bandwidth of 500 MHz at a center frequency of 34.5 GHz.

Differently to the implementations presented in the literature, the base-station for the MMID demonstrator is designed to provide a full EPC-Gen2 functionality at E-band frequencies. Furthermore, the design is very flexible in terms of baseband modulation and analysis to support additional functionality such as different modulation schemes or localization.

4.1 Specifications

The specifications for the MMID base-station are derived from the system specifications in Section 2.5 and the concept of the base-station in Section 4.2. The targeted E-band frequency range requires the mm-wave transceiver to operate at a carrier frequency (f_c) somewhere within 60 to 90 GHz. The base-station needs to provide a sufficiently high power level at the transponder antenna (P_{Tr}) of at least 10 μW [108]. With an expected FSPL of 68–72 dB at 1 m reading range in the downlink, an EIRP of 30 dBm is required at the transmitter ($EIRP_{TX} = P_{TX} \cdot G_{TX}$) in order to provide sufficient power to the transponder. In the uplink, the receiver needs to be able to detect signals 120 dB below the carrier. In order to provide enough flexibility for different modulation schemes or other applications such as localization, the modulation bandwidth (B_m) of the base-station should exceed 100 MHz. Table 4.1 summarizes the specifications for the MMID base-station.

Parameter	Symbol	Value	Unit
carrier frequency	f_c	60–90	GHz
minimum EIRP	$EIRP_{TX}$	30	dBm
sensitivity	P_{RX}^m	-120	dBc
modulation bandwidth	B_m	100	MHz

TABLE 4.1: Specification of the MMID base-station
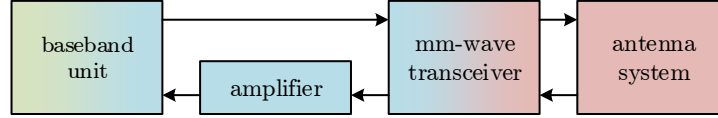
FIGURE 4.1: Concept of the MMID base-station

4.2 Concept

The MMID base-station is shown in Figure 4.1. It consists of four main blocks: a digital baseband unit, an analogue baseband amplifier, a mm-wave transceiver front-end, and the antenna system.

The core component of this concept, which influences the design of all other components is the mm-wave transceiver. It defines both, the operating range at mm-wave frequencies, as well as the baseband bandwidth and its center frequency. As the presented concept does not involve an external mm-wave amplifier, the output power (P_{TX}) and the sensitivity ($P_{RX,min}$) of the mm-wave frontend also directly influence the maximum reading range of the MMID demonstrator.

The antenna system is attached to the mm-wave ports of the transceiver. It provides the transition between the transmission lines at the output of the frontend and the free space. The directivity of the antenna (G_{TX} and G_{RX}) directly increases the reading range of the MMID system. On the other side, the crosstalk between the transmitted continuous wave signal to the receiver path of the mm-wave frontend is mainly determined by the antenna system. A high isolation between the transmitter input and the receiver output of the system improves the performance of the mm-wave demonstrator significantly.

On the baseband side, the transceiver interacts with the baseband unit. This unit is responsible for generating the commands for the transponder and analyzing its response. The influence of the baseband unit on the overall RF performance of the MMID demonstrator cannot directly be seen. However, the ability to balance out the imperfections of the mm-wave transceiver can improve some of the parameters in (2.12) and (2.13). In
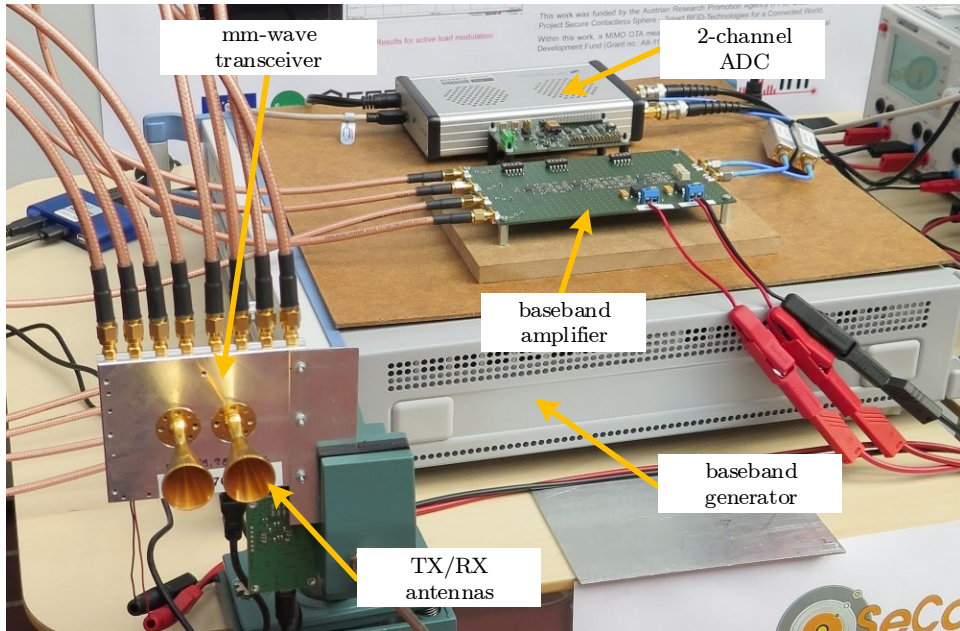
FIGURE 4.2: Picture of the MMID base-station

the transmit path, the usage of pre-distortion on the complex baseband signals mitigates the IQ imbalance of the mm-wave transmitter and improves the output power of the transmit signal (P_{TX}). In the receive path, algorithms which can deal with low signal to noise or signal to interferer ratios improve the overall sensitivity of the system, which can in turn deal with lower minimum receiver input powers ($P_{RX,min}$).

Between the mm-wave transceiver and the receiver path of the baseband unit, an amplifier is placed. The variable gain of this amplifier ensures that the inputs of the baseband unit are always fed with a constant power level. This allows to exploit the full dynamic range of the digitizers independently of the signal level from the transponder. In order to allow a maximum flexibility of the MMID system, the amplifier should cover the full bandwidth of both, the mm-wave transceiver and the baseband unit, while maintaining a large dynamic range in the adjustable gain.

4.3   mm-Wave Frontend

The mm-wave frontend is an early demonstrator board of a Silicon-Germanium based transceiver chipset for E-band backhaul applications from Infineon Technologies (BGT70, [109]). This transceiver provides a sufficiently high output power (14.5 dBm and a good receiver noise figure (8 dB) at a frequency range of 71 to 76 GHz, thus providing a good
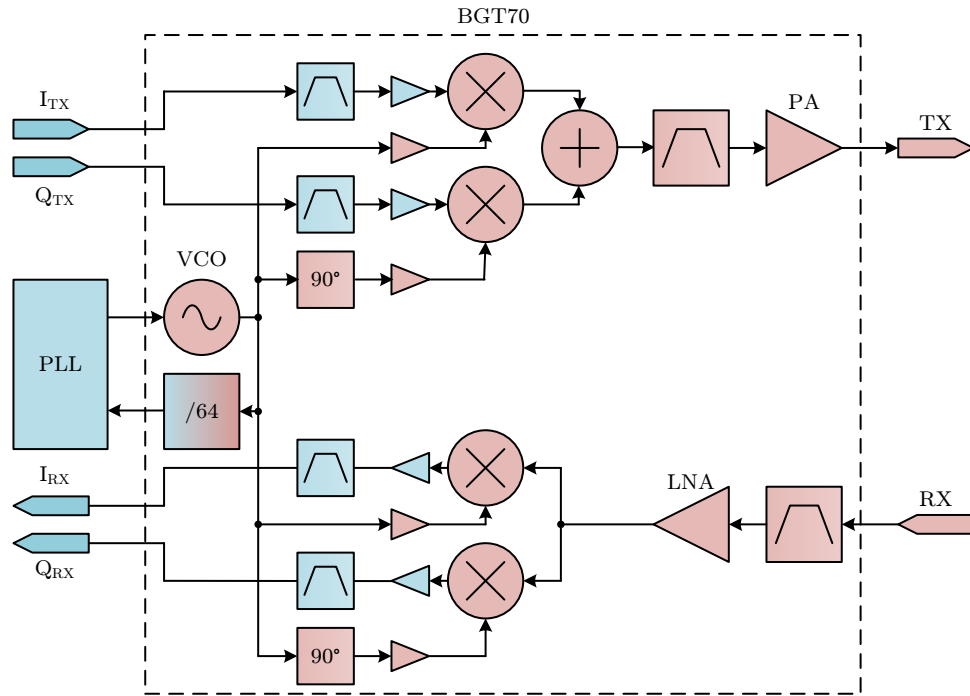
FIGURE 4.3: Concept of the direct conversion mm-wave transceiver

and flexible platform for the MMID base-station. The transceiver performs a direct conversion of complex baseband signals to a carrier frequency and vice versa. Figure 4.3 shows a high level block diagram of the chipset, which is derived from articles published by the manufacturer [110, 111].

The transceiver generates its carrier frequency of 71 to 76 GHZ using a VCO which is embedded in an off-chip phase locked loop (PLL). The PLL operates between 1.1 and 1.2 GHz and consists of an external fractional-N frequency synthesizer (Analog Devices ADF4158, [112]), the VCO and an integrated frequency divider with a factor of 64. In the transmit path, the in-phase (I_{TX}) and quadrature (Q_{TX}) baseband signals are multiplied with the carrier and its 90 degree phase shifted representation, respectively. The two mm-wave signals are then combined and out-of-band emissions are suppressed by a bandpass filter. The final signal is then amplified with a variable gain power amplifier providing an output power of up to 14.5 dBm available at the output port (TX). In the receive path, the incident mm-wave signal (RX) is boosted by a low noise amplifier and fed into the mixing stage. In this stage the in-phase (I_{RX}) and quadrature (Q_{RX}) baseband signals are separated by multiplying the RX signal with the carrier frequency and its 90 degree phase-shifted representative.
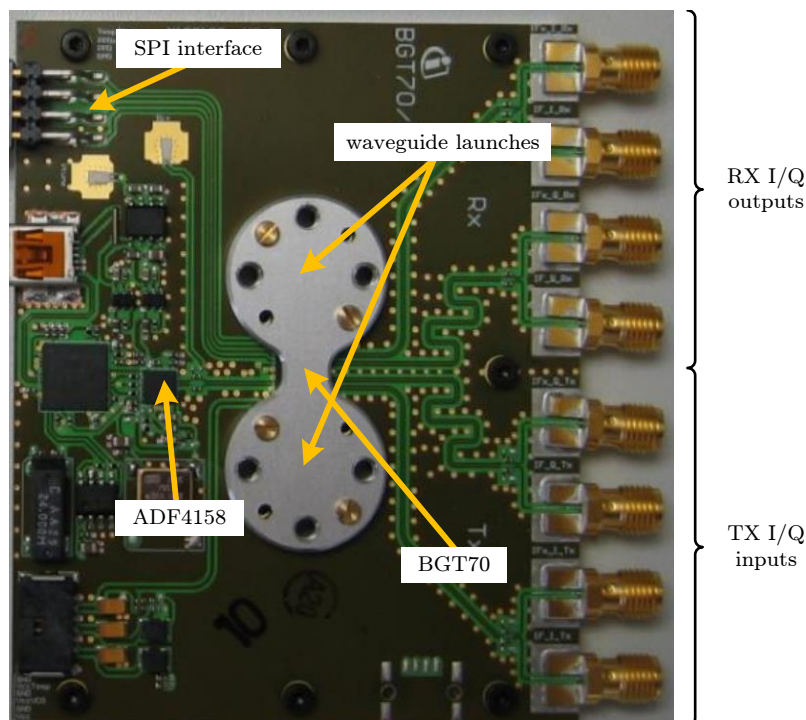
FIGURE 4.4: Concept of the direct conversion mm-wave transceiver

The transceiver provides a SPI interface for its configuration. This allows to enable or disable separate blocks of the front-end, such as the transmitter or the receiver. Additionally, there are registers available for modifying the gain of the transmitter PA and for the DC offset fed to the I/Q mixer input in order to suppress the carrier feed-through. For the configuration of the carrier frequency, the fractional-N frequency synthesizer provides a separate SPI interface. The firmware of the synthesizer does not only allow the generation of single tones within the specified frequency range, but also supports the generation of frequency ramps. This functionality can be used for generating wideband FMCW for localization applications.

Figure 4.4 shows a picture of the evaluation board, which integrates the mm-wave front-end chip. The MMIC itself is hidden under the metal back-plane of the two waveguide launches for the mm-wave RX (top) and TX (bottom) ports which are located at the backside of the board. The external PLL component (ADF4158) are placed on the left side of the chip. The interfaces for programming the BGT70 and the ADF4158 are placed on the left edge of the board. The SMA connectors for the differential I/Q inputs and outputs can be found on the right edge.
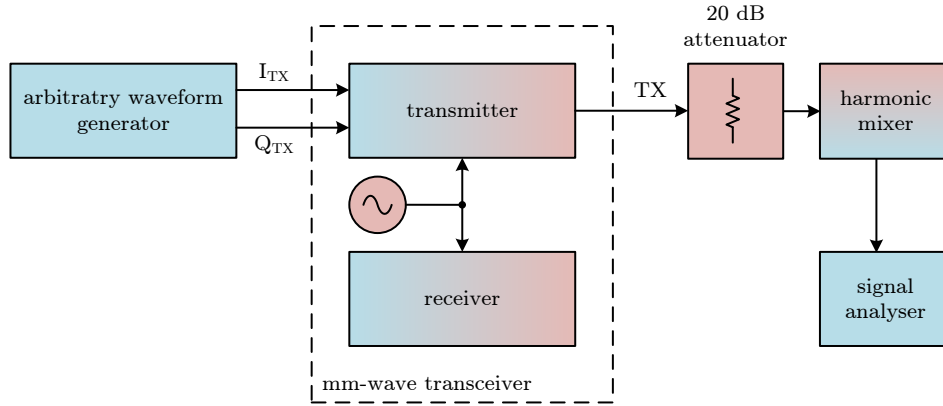
FIGURE 4.5: Concept of the transmitter measurement

4.3.1 Characterisation

To characterize the transmitter of the mm-wave front-end, a signal analyzer (FSQ26, [79]) equipped with an external harmonic mixer (Rohde&Schwarz FS-Z90, [81]) is attached to the waveguide port of the evaluation board. As shown in Figure 4.5 a 20 dB waveguide attenuator (Flann 26081-20 [113]) is placed between the transmitter output and the harmonic mixer in order to ensure a good matching and lower the power level to a range which does not overdrive the mixer input. An arbitrary waveform generator (AWG) creates the in-phase and quadrature baseband signals for the characterization routines. In order to ensure that AWG does not introduce additional artifacts into the measurement, the same model as in the final base-station setup is used (AFQ100A, [114]). Figure 4.6 shows a photograph of the measurement setup. All presented measurements are performed at a carrier frequency (f_c) of 74 GHz. The offset frequency (f_{offset}) denotes the distance between the carrier and the measured frequency ($f_{measured}$):

$$f_{offset} = f_{measured} - f_c \tag{4.1}$$

Furthermore, the offset frequency corresponds directly to the frequency of the complex baseband signal generated by the AWG.

The first measurement in Figure 4.7 shows the output power of the transmitter as a function of the frequency offset from the carrier. For this measurement the signal analyzer sweeps ±150 MHz around the carrier using a maximum hold detector. As the AWG and the spectrum analyzer were not synchronized to each other, the AWG sweeps in the same band with a much slower ramp. The average output power of the transmitter
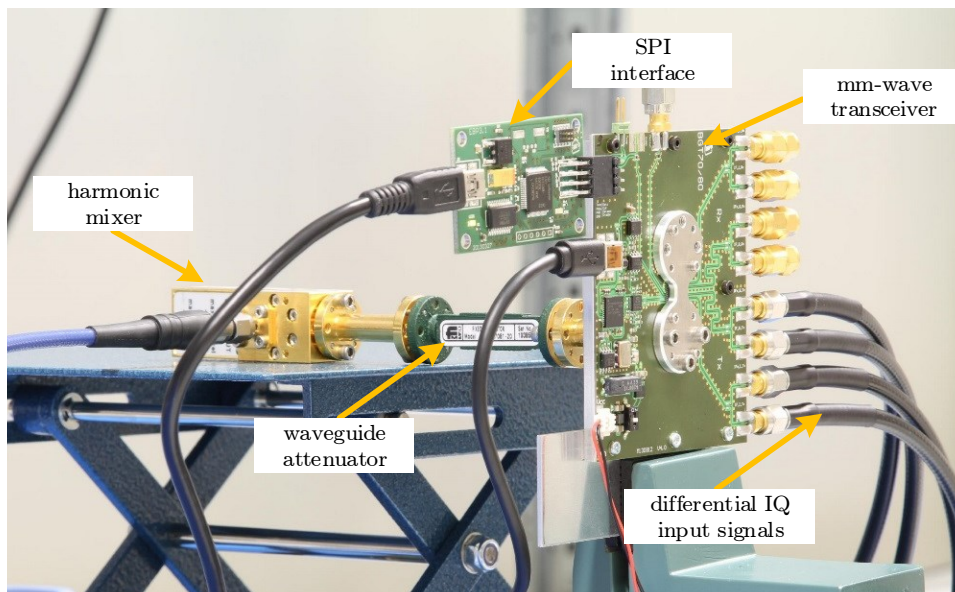
FIGURE 4.6: Photograph of the transmitter measurement
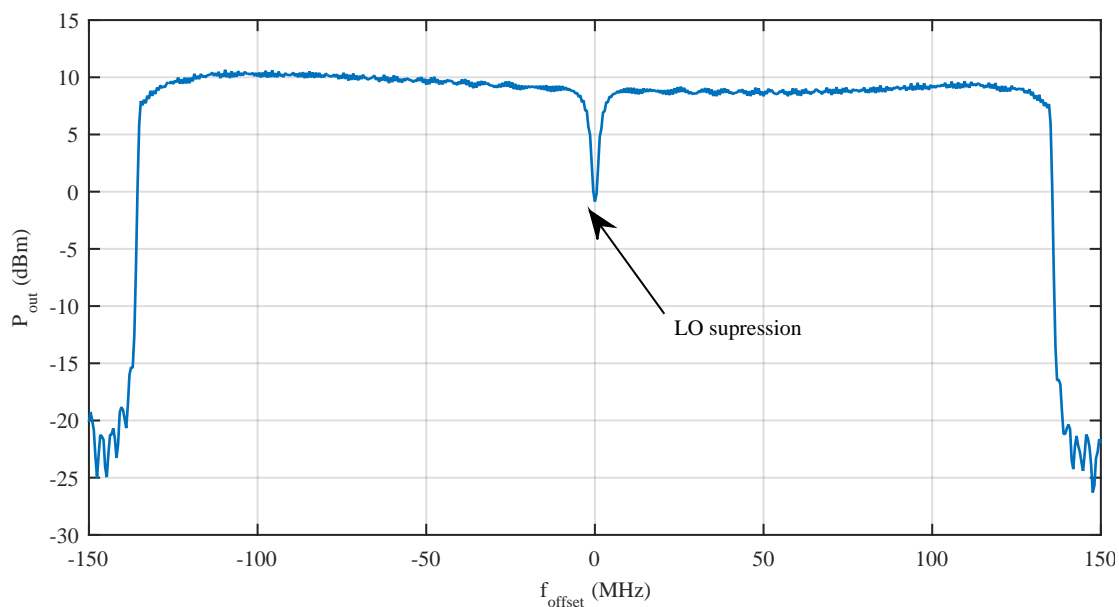
FIGURE 4.7: Output power of the transmitter over the operating frequency band

is approximately 10 dBm. Its overall variation within the frequency band of interest (±130 MHz) is below 2 dB except from a notch around the carrier frequency itself. In this area (±3 MHz) the highpass filters located at the IQ inputs of the transmitter reduce the output power by at least 10 dB to provide a sufficiently high carrier suppression. The steep drops of the output power at ±135 MHz indicate the maximum output frequency of the AWG.

The second measurement in Figure 4.8 shows the output spectrum for a baseband single
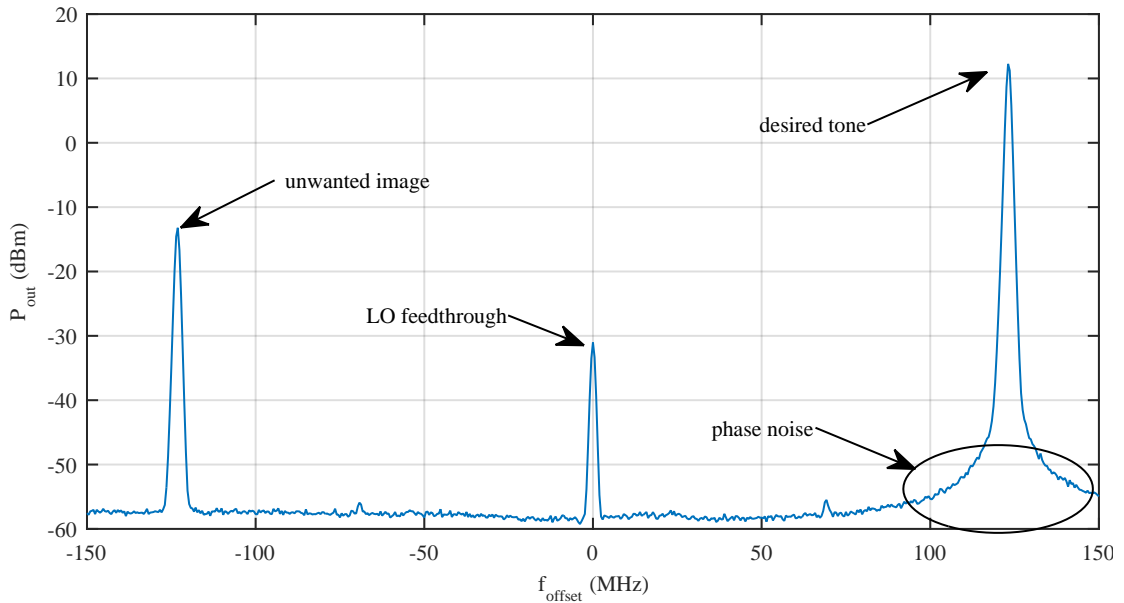
FIGURE 4.8: Single-tone measurement of the transmitter with unwanted spurious emissions

tone at 120 MHz. The desired tone at +120 MHz offset to the carrier shows an expected power level of around 10 dBm. However, additional – unwanted – spectral components are recognizable within the band of interest: The first unwanted peak is at the carrier frequency. This LO feed-through is caused by the DC offset at the in-phase and quadrature mixers. To optimize the suppression of the LO feed-through, the SPI interface of the transceiver provides two registers (DAC_MOD_I and DAC_MOD_Q) which allow to adapt the DC level of the two input signals. This optimization was done beforehand. Thus the LO feed-through of -30 dBm represents the optimum settings. At -120 MHz a second distinct peak 25 dB below the power level of the desired tone was measured. This image of the desired tone is caused by an unbalance between the up-converted in-phase and quadrature signals. To compensate this behavior, the amplitude and phase of the quadrature signal can be pre-distorted as discussed in Section 4.3.2.

4.3.2 Imbalance Compensation

As highlighted in connection with Figure 4.8, the base station generates besides the wanted signal at an offset of +120 MHz another tone at -120 MHz with an amplitude of 25 dB below the carrier. The generation of this unwanted tone can be ascribed to an imbalance between the in-phase and quadrature paths of the transmitter. Figure 4.9 shows a linear model of the transmitter including the error terms relevant to the imbalance
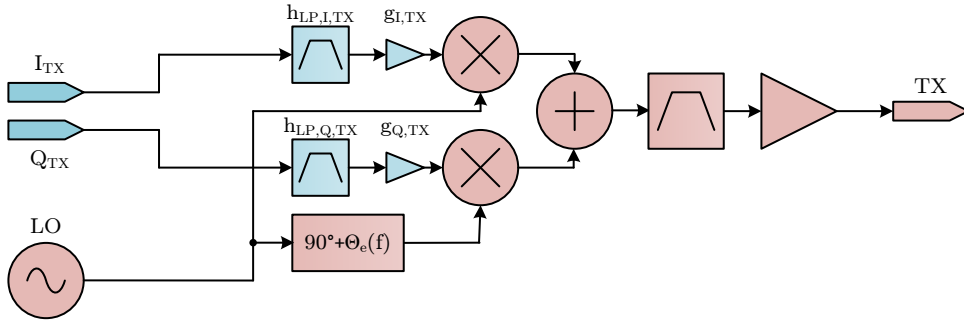
FIGURE 4.9: Model of the transmitter including imbalance error terms

analysis from [115]. For simplification the DC-offset terms both IQ paths are omitted as they are contributing only to the carrier feed through which is already compensated prior to these investigations. Overall, 5 terms can be identified: $h_{LP,TX,I}$ and $h_{LP,TX,Q}$ are the filter responses of the in-phase and quadrature path. $g_{TX,I}$ and $g_{TX,Q}$ represent the amplitudes of the two paths. $\Theta_e(f)$ is the deviation of the phase of the LO for the quadrature path from the ideal 90 degrees.

Based on this linear model, the frequency domain representation of the complex envelope transmitter signal as a function of the complex baseband signal ($BB_{TX} = I_{TX} + jQ_{TX}$) is shown in (4.2). The terms α_d and α_u model the desired signal at $+\omega$ and the unwanted mirrored signal at $-\omega$.

$$
\begin{aligned}
TX &= \left[\alpha_d(j\omega) \cdot BB_{TX}(j\omega) + \alpha_u \cdot BB_{TX}^*(-j\omega) \right] \cdot e^{j\phi_{LO}} \\
\alpha_d(j\omega) &= \frac{1}{2} \left[g_{I,TX} \cdot H_{LP,ITX}(j\omega) + g_{Q,TX} \cdot H_{LP,Q,TX}(j\omega) \cdot e^{j\Theta_e(j\omega)} \right] \\
\alpha_u(j\omega) &= \frac{1}{2} \left[g_{I,TX} \cdot H_{LP,ITX}(j\omega) - g_{Q,TX} \cdot H_{LP,Q,TX}(j\omega) \cdot e^{j\Theta_e(j\omega)} \right]
\end{aligned}
\tag{4.2}
$$

The imbalance between the quadrature and the in-phase branches of the IQ-modulator is summarized in (4.3) taking the in-phase branch as reference::

$$
\gamma_{TX}(j\omega) = \frac{\alpha_{Q,TX}}{\alpha_{I,TX}} = \frac{g_{Q,TX} \cdot H_{LP,Q,TX}(j\omega)}{g_{I,TX} \cdot H_{LP,I,TX}(j\omega)} = \left| \gamma(j\omega) \right| \cdot e^{\phi_{\gamma,TX}(j\omega)}
\tag{4.3}
$$

Substituting $\alpha_{Q,TX}(j\omega)$ with $\alpha_{I,TX}(j\omega) \cdot \gamma_{TX}(j\omega)$ in (4.2) yields to (4.4). It can be seen that the phase deviation of the LO introduces a similar error effect as the phase of the

imbalance between the IQ branches.

$$TX = \alpha_{I,TX} \cdot \Big[I_{TX}(j\omega) - \big|\gamma_{TX}(j\omega)\big| sin\big(\phi_{\gamma,TX}(j\omega) + \Theta_e(j\omega)\big) Q_{TX}(j\omega)$$
$$+ j\big|\gamma_{TX}(j\omega)\big| cos\big(\phi_{\gamma,TX}(j\omega) + \Theta_e(j\omega)\big) Q_{TX}(j\omega) \Big] \cdot e^{j\phi_{LO}} \tag{4.4}$$

To compensate the imbalance, BB_{TX} can be pre-distorted using (4.5). In this case, again the imbalance is computed with the in-phase channel as reference.

$$\widetilde{BB}_{TX}(j\omega) = I_{TX}(j\omega) + \tan(\angle\gamma_{TX}) \cdot Q_{TX}(j\omega) + j \cdot \frac{1}{|\gamma_{TX}| \cdot \cos(\angle\gamma_{TX})} \cdot Q_{TX}(j\omega) \tag{4.5}$$

In order to obtain γ_{TX} for the transmitter used in the MMID base-station a measurements using the setup presented in Figure 4.5 are carried out. During these measurements a pre-distorted single tone at a frequency ω_{offset} with an estimated $\dot{\gamma}_{TX}$ is fed into the transmitter using following definition:

$$BB_{TX}(t) = \sin(\omega_{offset} \cdot t) + \tan(\angle\dot{\gamma}_{TX}) \cdot \cos(\omega_{offset} \cdot t)$$
$$+ j \cdot \frac{1}{|\dot{\gamma}_{TX}| \cdot \cos(\angle\dot{\gamma}_{TX})} \cdot \cos(\omega_{offset} \cdot t) \tag{4.6}$$

In a first step $\dot{\gamma}_{TX}$ is set to 1. The the output level of the transmitter is observed at $-\omega_{offset}$. During the next iterations the amplitude and phase of $\dot{\gamma}_{TX}$ are varied until a minimum level of the unwanted mirror frequency is found. A detailed description of the algorithm is given in [116].

Figures 4.10 and 4.11 show the performance of the imbalance compensation for the upper and lower sideband, respectively. In both cases a suppression of at least $20\,\mathrm{dB}$ can be observed and is limited by the noise floor of the signal analyzer. At higher offsets an additional non-linearity arises which can not be seen in the un-compensated measurement. An investigation on the root cause of this distortion has not been carried out.

Figure 4.12 shows a measurement of a high power multi-tone signal for an uncompensated and a compensated baseband signal. The compensation algorithm with values for $\dot{\gamma}_{TX}$ obtained from single-tone measurements shows a similar performance as for the single-tone measurements above. In the desired band inter modulation distortions right next
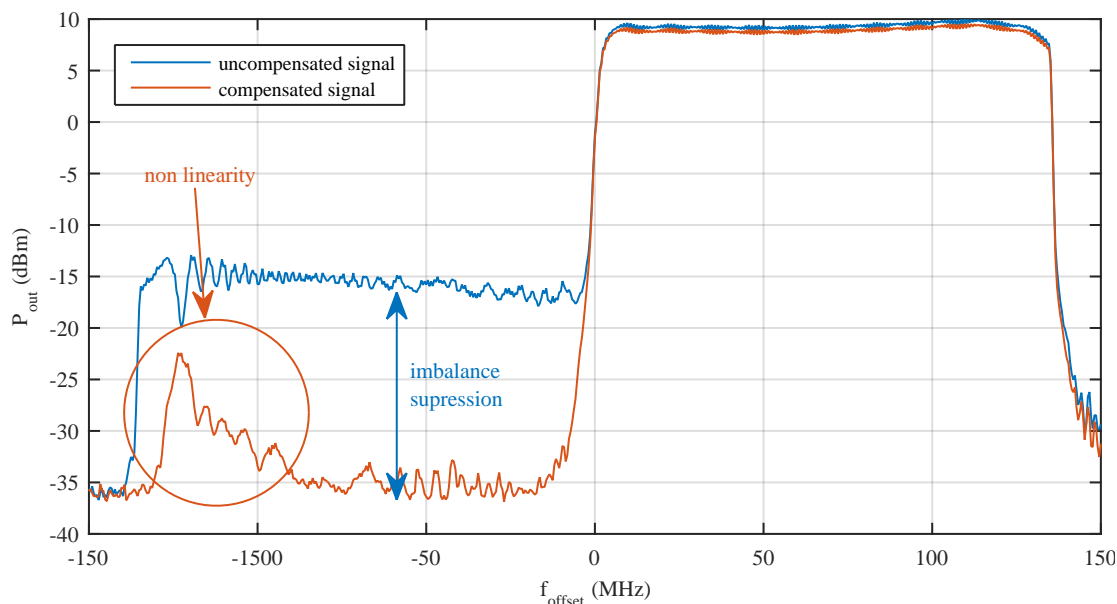
FIGURE 4.10: Imbalance compensation of the lower side band
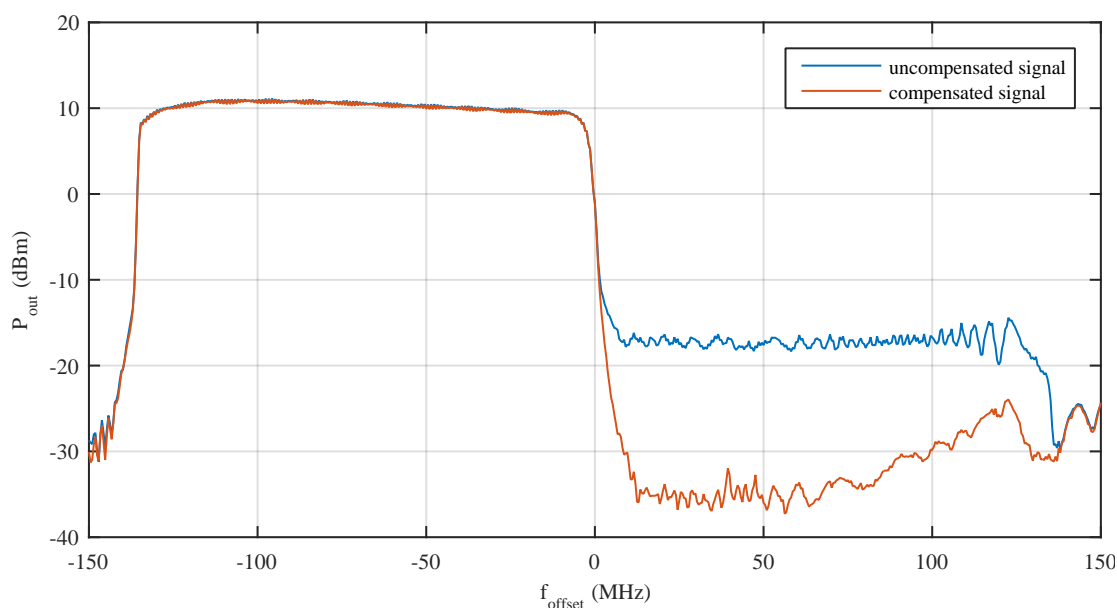
FIGURE 4.11: Imbalance compensation of the upper side band

to the desired signal can be observed. In the unwanted lower side band these distortions are almost in the noise floor for the uncompensated measurement. In the compensated measurement, neither the image signal nor its IMD are visible.

In a next step, the imbalance of the MMID base-station receiver can be investigated. However, due to the high phase noise of the LO, the measurements for estimating $\dot{\gamma}_{RX}$ were unstable. Further investigations on this topic would have been out of the scope of this thesis and remain to be carried out.
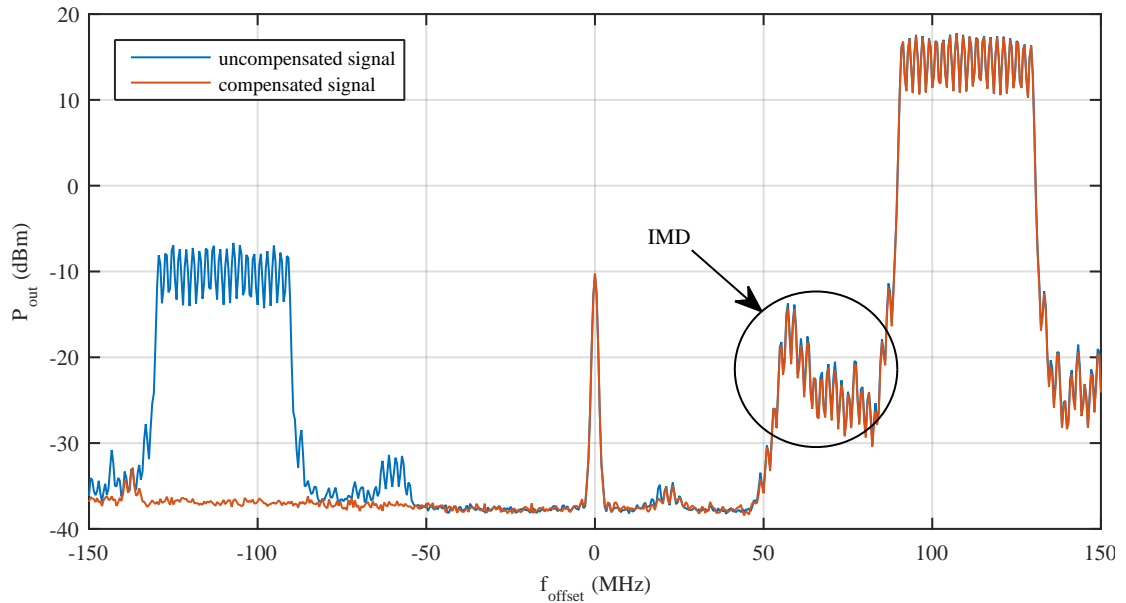
FIGURE 4.12: Imbalance compensation for a high power multi-tone signal in the upper side band

4.4 Antennas

The antenna of the MMID base-station provides the transition between the mm-wave frontend and the propagation medium – air. There are several requirements on the antenna system. It should provide a reasonably high gain to enable higher reading distances. Additionally, the isolation between the transmit and receive signal should ensure that the high power CW signal of the transmitter is not jamming the input stage of the receiver and therefore suppressing the signal of the transponder. Other desirable characteristics for a base-station antenna are reconfigurability (i.e. beam steering), small dimensions and low deployment costs.

There are several options for the antenna configuration of the base-station: (i) Two separate horn antennas as presented in Section 3.1.1, one for the transmit and one for the receive path of the base-station. This approach benefits from relative high isolation between the transmit and receive signals, thus increasing the sensitivity towards the transponder response. Additionally, the horn antennas provide a reasonably high gain at reasonable costs while maintaining a small size. (ii) An electrical large high gain antenna equipped with a circulator to separate transmit and receive signals. Such a configuration enables large maximum reading ranges due to the high gain. Furthermore, the narrow main beam width allows to pin point a single node within a group of

transponders. Due to the popularity of the E-band frequency range in automotive radar and communication applications, there is a multitude of high gain antennas available on the market. This antennas provide gains up to 45 dBi and more with HPBW as narrow as 1 degree [117]. The isolation of the transmit and receive signals in this solution is limited by the isolation of the circulator. Typical commercially available circulator provide an isolation of 20 dB [118]. An additional limit on the isolation is the matching of the antenna. (iii) Reconfigurable planar antenna arrays for transmit and receive paths as presented in [119–121]. These antennas provide a highly flexible and low-cost solution for the MMID base-station. Depending on the number of elements, antenna arrays can provide a gain of 15 dBi and more. Regarding the steer-ability of mm-wave phased arrays, deviations of more than ± 30 degree from the main beam direction are reported in the literature [122–124]. However, to achieve a steerable antenna system, the mm-wave frontend needs to provide severable transmit and receive ports which provide the ability of shifting the phase relative to each other.

As the mm-wave frontend provides WR12 waveguide interfaces for the mm-wave transmit and receive ports, the option with two horn antennas as transmit and receive antenna seems to be the natural choice. In Figure 4.2, the two antennas (QuinStar QWH-ECRR00, [66]) are mounted next to each other directly onto the mm-wave frontend. In this configuration, they both provide a gain (G_{TX} and G_{RX}) of 21 dBi at a HPBW of 15 degree.

4.5 Baseband Unit

The baseband unit is responsible for generating EPC Gen2 compatible commands for the MMID transponders and for analyzing the returning messages. The presented implementation of the baseband unit, shown in Figure 4.13, consists of a processing software and analog/digital interfaces towards the mm-wave transceiver. For the demonstrator, the processing software is implemented in a MATLAB® program. The program consists if two main parts: a transmit path and a receive path. The transmit path is responsible for the generation of the downlink signals from the base-station to the transponder. The uplink path analyzes the responds from the transponder. Additionally, a configuration and interface block allows the user to interact with the base-station. The implementation in MATLAB is very flexible and allows a quick development of additionally functionality,
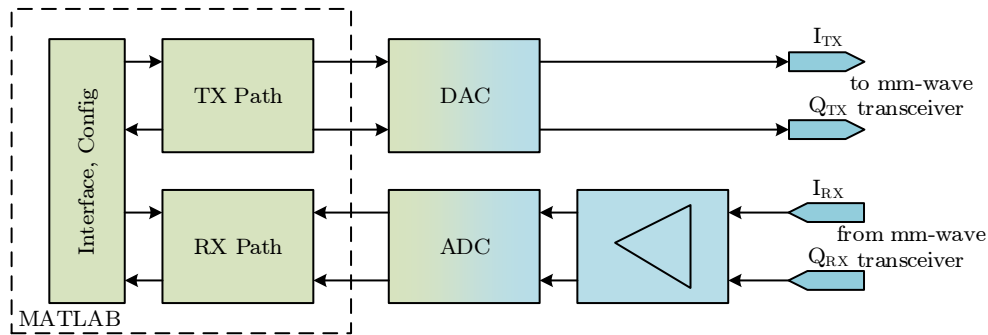
FIGURE 4.13: Concept of the of the baseband unit
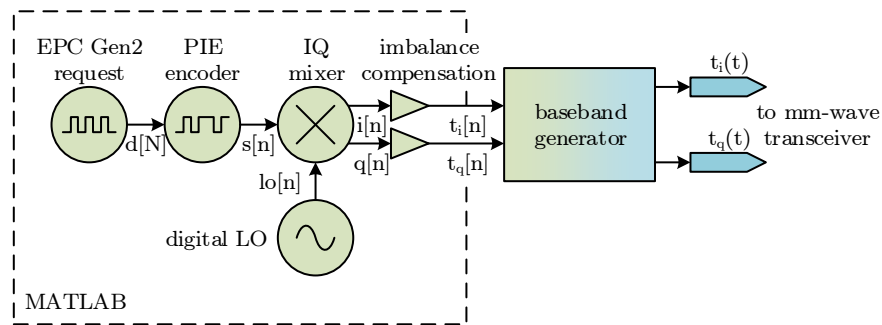
FIGURE 4.14: Concept of the transmit path of the baseband unit

such as the localization of objects using a frequency or phase modulation of the carrier signal. For a future application of the MMID system concentrating on the identification of objects, the software implementation can be moved to a FPGA system as presented in [125–127].

4.5.1 Transmit Path

The transmit path of the baseband unit consists of two major components: a computer running a custom MATLAB® software and a two-channel baseband generator (Figure 4.14).

Within the MATLAB® software, an EPC Gen2 command is generated and fed into a pulse interval encoder (PIE). To reduce the complexity of the baseband implementation, MMID demonstrator uses only the QUERY command to show a EPC Gen2 compatible RFID communication at mm-waves. The QUERY command of the EPC Gen2 Standard initiates an inventory round [9]. The bit sequence ($d[N]$) of the command used for the MMID inventory round is shown in (4.7).

$$d[N] = 1000\,0\,00\,0\,01\,01\,0\,0000\,11101 \qquad (4.7)$$

The 22 bit data word of the EPC Gen2 query is split into eight bit-fields which parametrise the request and the following inventory round:

Command The QUERY command initiates and configures the inventory round of an EPC Gen2 session.

DR The TRCAL division ration (DR) sets the link frequency to a eighth of the TRCAL length of the preamble.

M The number of subcarrier cycles per symbol (M) defines the data rate in fractions of the link frequency and the modulation scheme (FM0).

TRext The TREXT bit tells the transponder to not use a pilot tone preamble in its response.

Sel To ensure that all transponders within the reading range of the base-station respond to the QUERY, SEL addresses all transponders.

Session The session for the inventory round of the MMID demonstrator to S1.

Target Within the current inventory round, all tranponders with an inventoried flag set to A participate.

Q To ensure a 100 % probability of a transponder response, the Q parameter limits the number of slots to one.

Table 4.2 gives an overview on the values of the eight bitfields for the QUERY command and its values.

The PIE generates a standard compliant signal sequence s[n] using the sampling frequency of the BB generator and the desired value for the tari [9]. Figure 4.15 shows the two sequences used for the logical zero and one (data-0 and data-1). The data-0 sequence has a length of 1 Type A Reference Interval (tari) with equal on and off times of 0.5 tari. The data-1 sequence has a longer on time of 1 tari and the same off time of 0.5 tari which sums up to a total length of 1.5 tari. To generate the PIE baseband signal ($s[n]$) QUERY

TABLE 4.2: EPC Gen2 query command

	# of bits	value	description
Command	4	1000	query
DR	1	0	8
M	2	00	FM0 baseband
TRext	1	0	no pilot tone
Sel	2	01	all
Session	2	01	S1
Target	1	0	A
Q	4	0000	0
CRC	5	11101	CRC-5
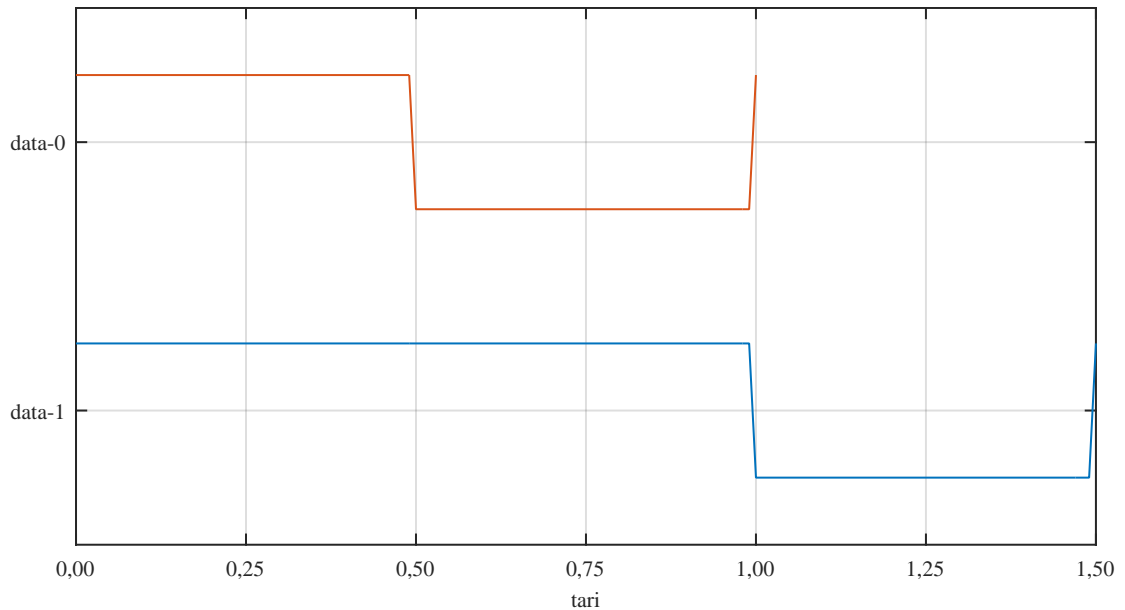
FIGURE 4.15: Sequences for logic 1 (data-1) and logic 0 (data-0) for the EPC Gen2 PIE.

command, the two sequences are stringed together according to the data word ($d[N]$) fed into the encoder. Additionally, the PIE prepends a preamble (Figure 4.16). The preamble is used to initiate the communication from the base-station to the transponder (delimiter) and defines the length of a tari (data-0), the distinction between a logical 0 and a logical 1 (RTcal) and the backscatter link frequency of the transponder (TRcal). A detailed definition of the physical layer of the EPC Gen2 downlink is given in [9].

Furthermore, an arbitrary response time for the tag is appended to the command sequence. During this response time, the output of the baseband signal is fixed to a logical 1 which allows the base-station to transmit an unmodulated carrier. Figure 4.17 shows the full PIE baseband signal with the preamble, the EPC Gen2 QUERY command. In
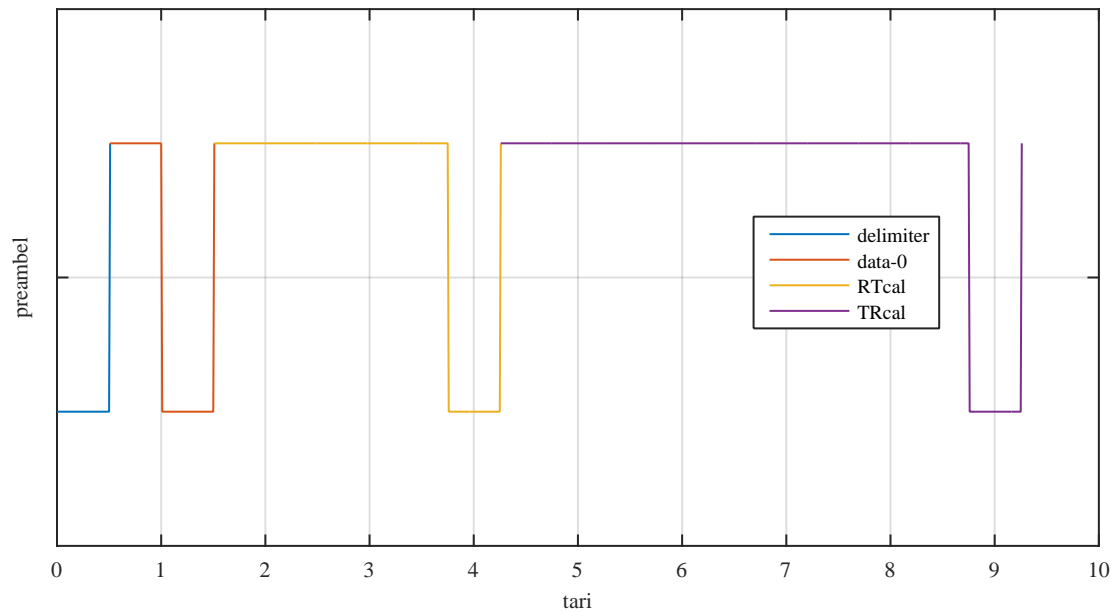
FIGURE 4.16: Preamble of the EPC Gen2 communication between base-station and transponder
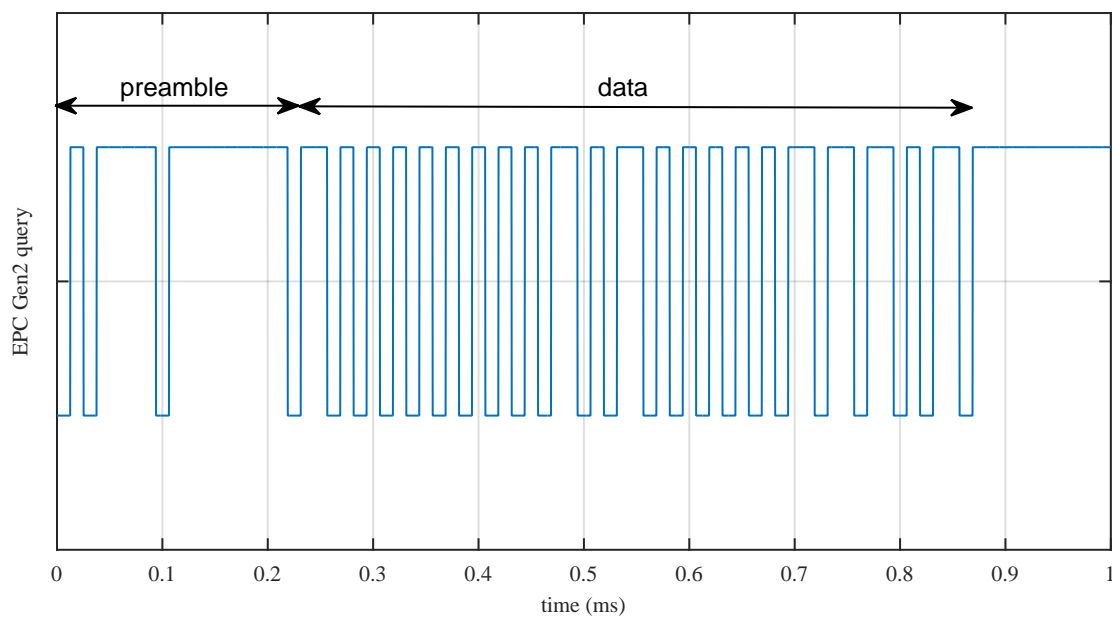
FIGURE 4.17: The baseband representation of an EPC Gen2 query

this example, the tari is set to 250 us. For a better visibility, the response time of 10 ms is truncated.

To overcome the notch filter around the carrier of the mm-wave frontend, the real valued baseband signal ($s[n]$) is then shifted to a low intermediate frequency carrier (f_{IF}) by multiplication with an ideal single tone represented by the Euler equation in (4.8). The complex valued IF signal is then separated into an in-phase ($i[n]$) and a quadrature ($q[n]$) signal.
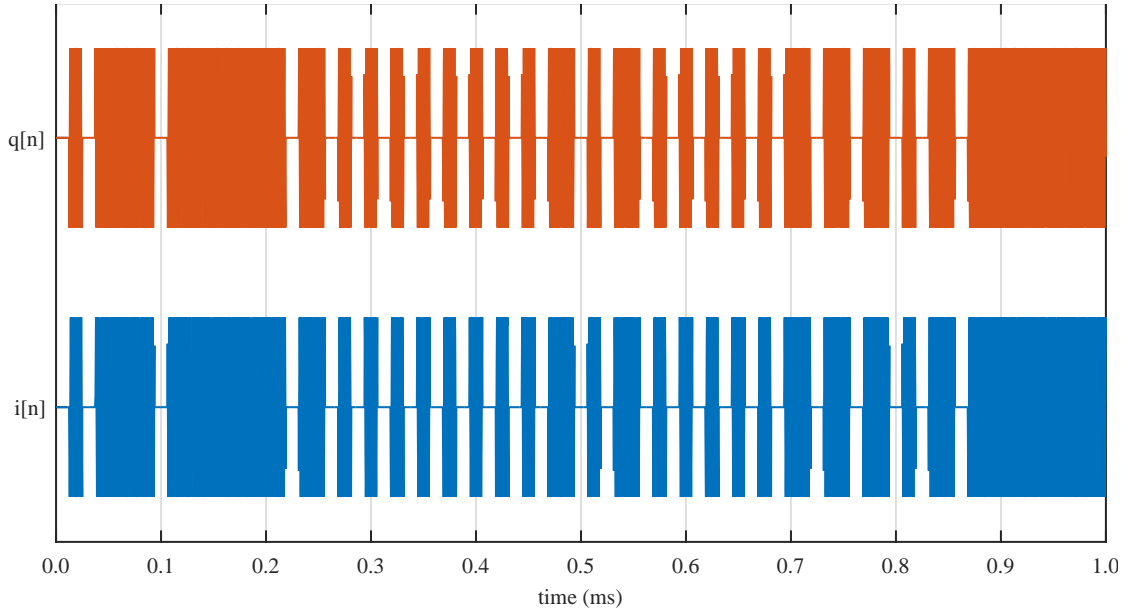
FIGURE 4.18: EPC Gen2 query in the IF domain

$$\text{lo}[n] = e^{-j \cdot 2\pi \cdot f_{IF} \cdot \frac{n}{f_s}} = \cos(2\pi \cdot f_{IF} \cdot \tfrac{n}{f_s}) + j \sin(2\pi \cdot f_{IF} \cdot \tfrac{n}{f_s}) \tag{4.8}$$

$$\text{i}[n] = \Re\Big\{ \text{s}[n] \cdot \text{lo}[n] \Big\} \tag{4.9}$$

$$\text{q}[n] = \Im\Big\{ \text{s}[n] \cdot \text{lo}[n] \Big\} \tag{4.10}$$

Figure 4.18 shows the in-phase and quadrature signals of the EPC Gen2 QUERY command. For a better visualization of the two signals, Figure 4.19 shows a close up of the off time of a data-0 sequence followed by the on time of a data-1 sequence with a reduced IF carrier of 0.5 MHz. One can easily observe the 90 degree phase shift between the two signals.

To compensate the IQ imbalance of the mm-wave frontend a compensation factor is applied to the complex valued IF signal (see Section 4.3.2).

The final transmit signal is the uploaded into the baseband generator, which converts it to the analogue domain and feeds it into the mm-wave frontend.

4.5.2 Receive Path

The concept of the receive path of the base-band unit is depicted in Figure 4.20. It consists of three parts: A baseband amplifier with variable gain a 2-channel ADC, and
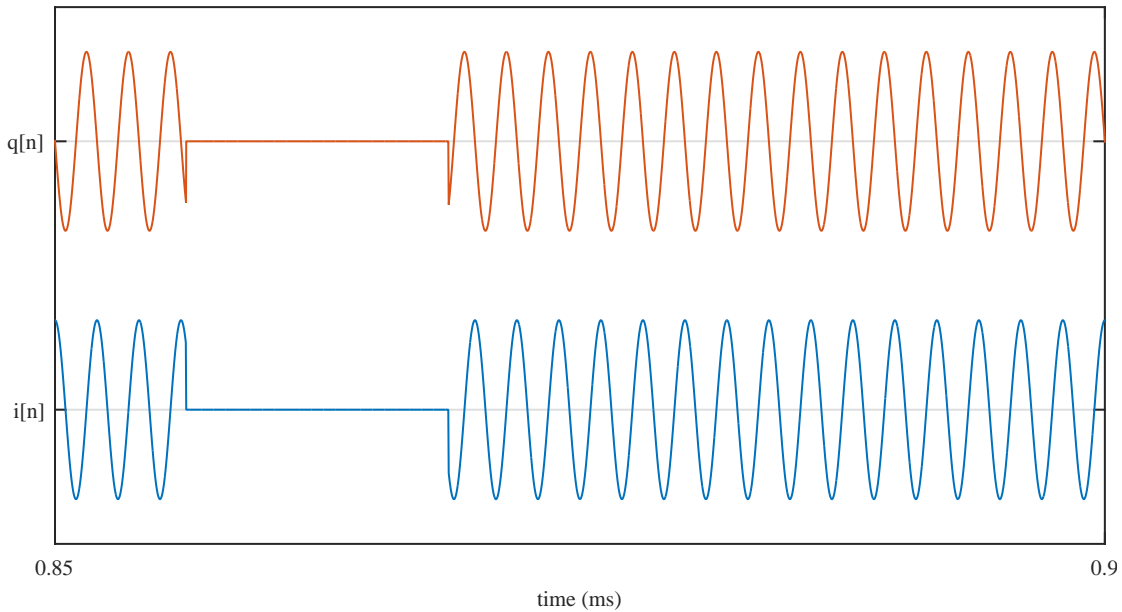
FIGURE 4.19: Detail of the EPC Gen2 query in the IF domain.
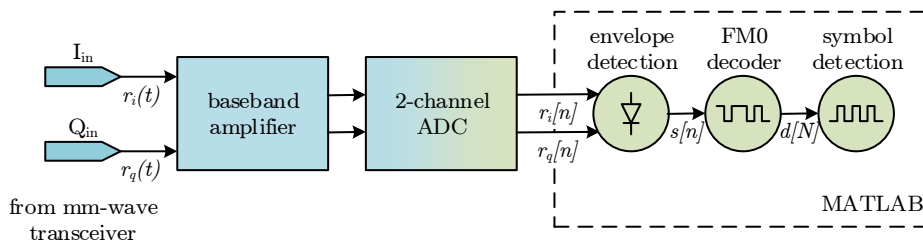
FIGURE 4.20: Concept of the receive path of the baseband unit

a digital receiver which is carried out as a MATLAB program. The custom baseband amplifier is mainly responsible for adapting the signal strength of the IQ signals coming from the mm-wave receiver in order to utilize the full dynamic range of the digitizer. The implementation of the amplifier is described in Section 4.6. The digital receiver uses an envelope detector to remove the IF carrier signal and feeds the data into an FM0 decoder.

Within this thesis, the implementation of the digital base-band receiver was not carried out in detail as it is not possible to achieve all timing constraints given by the EPC Gen2 standard using the presented MATLAB software stack. In order to master these constraints, a FPGA based implementation of the digital base-band unit is highly recommended as indicated in the introduction of Section 4.5.

4.6   Baseband Amplifier

The custom baseband amplifier is designed adjust the signal coming from the mm-wave transceiver to the input range of the ADC. Additionally it transforms the differential signal of the transceiver into a single ended signal which is compatible with the input ports of the digitiser. In order to exploit the full frequency range of the ADC, the amplifier should be able to provide a variable gain of up to 25 dB over a bandwidth of 200 MHz.

To achieve these requirements, three variable gain amplifiers (VGA) are implemented in each channel of the baseband amplifier (Figure 4.21). Each amplifying stage (Analog Devices AD8376, [128]) provides a variable gain from -4 dB to +20 dB and is controlled by a 5 bit interface. For the prototype of the MMID base-station, the 5 bit interface is controlled manually by DIP switches. In a further implementation step, the switches can be replaced by a computer interface, which allows the MATLAB program to adjust the gain as needed, or by a automatic gain control. To ensure a maximum bandwidth, resistive matching circuits are deployed at the input and output ports, as well as in between the single stages. Additionally to the matching circuits a gain compensation circuitry is deployed between the second and the last stage. After the last amplifying stage, a broadband balun converts the 100 Ohm differential signal into a 50 Ohm single-ended signal. The block diagram of the baseband amplifier is given in Figure 4.21. To improve the usability of the device, the different amplifier stages of the I and Q branch are jointly controlled (i.e. VGA I1 and VGA Q1 have the same gain setting).

In a first design step, a single stage of the baseband amplifier is realized to evaluate the performance of all components: the VGA, the matching networks, and the broad band baluns. As presented in Figure 4.22, the evaluation board is equipped with a balun on the input ports, in order to enable quick measurements utilizing a two-port VNA (Rode&Schwarz ZVL, [129]). The measurements of the two investigated amplifiers (VGA I1 and VGA Q1) in Figure 4.23 show a maximum achievable gain of 10 dB and a 3 dB-bandwidth of 200 MHz. This achieved gain differs significantly from the expected values of the amplifiers data-sheet (20 dB). This difference is caused by the resistive broadband matching circuits, which introduce a loss of approximately 5 dB at both, the input and output of the amplifier. Additionally, an imbalance of 1–1.5 dB within the targeted operating bandwidth can be noticed. This imbalance is caused by the variation
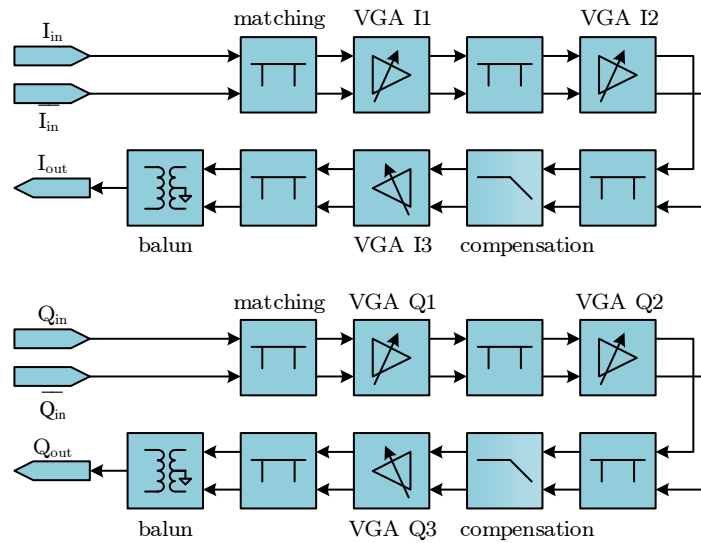
FIGURE 4.21: Concept of the three stage two channel baseband amplifier
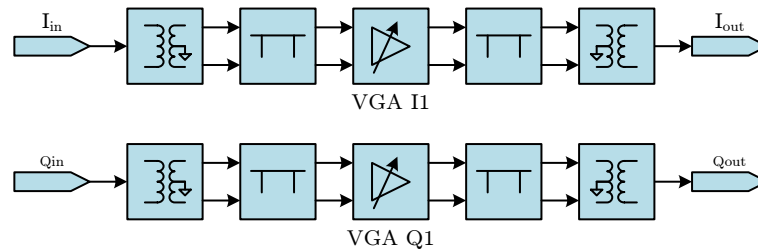
FIGURE 4.22: Concept of the single stage evaluation board.

of the components used in the interstage matching, as well as deviations in the assembly process. This mismatch can be easily reduced by introducing a higher loss in the I-branch compensation circuitry of the three stage amplifier.

In the next design step, the results from the evaluation board are incorporated into the three stage concept presented in Figure 4.21. Appendix A shows the schematics of the baseband amplifier. A photograph of the manufactured prototype is shown in Figure 4.24. For the sake of usability and simplicity of design, the I and Q branch share the 5-bit control DIP-switches for each stage.

To measure the gain of the baseband amplifier with differential input boards, an arbitrary waveform generator (AFQ 100A, [114]) is generating a differential input signal with an amplitude of $10\,mV_{pp}$. This measurement signal is fed into on of the baseband amplifier channels. The output signal of the amplifier is then captured by a signal analyzer
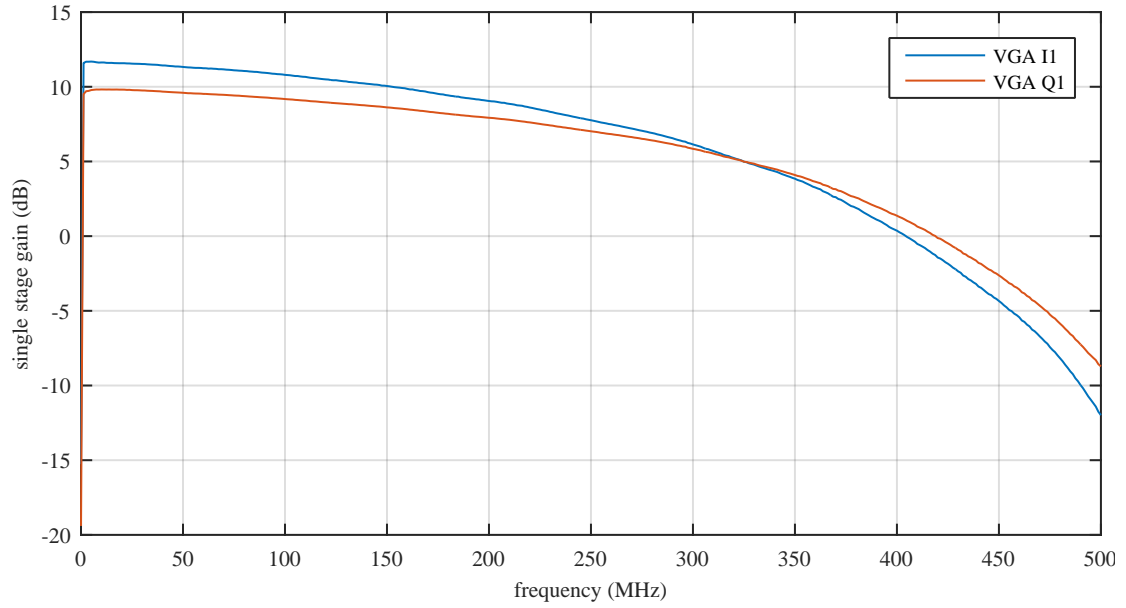
FIGURE 4.23: Gain measurement of a single VGA stage with maximum gain settings.
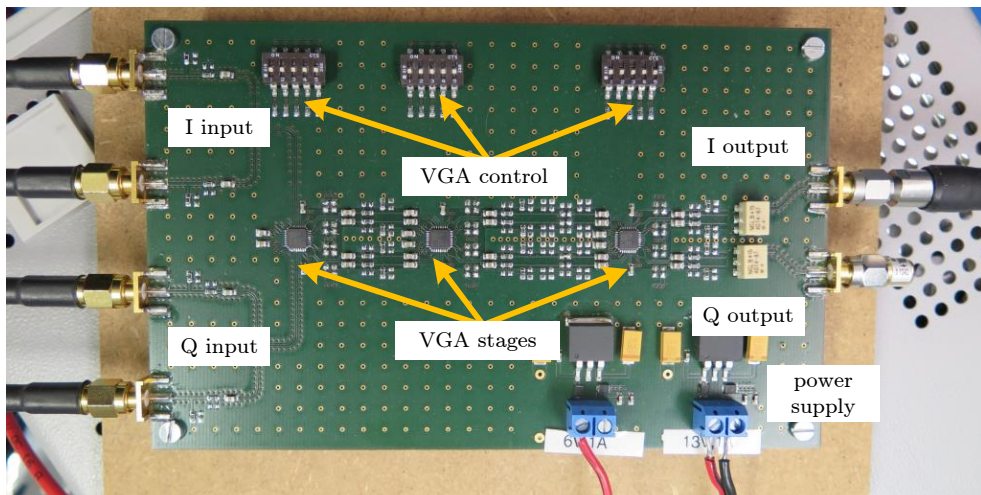
FIGURE 4.24: Picture of the manufactured baseband amplifier.
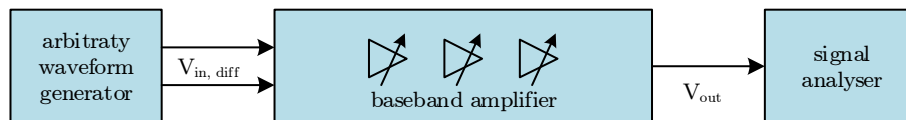
FIGURE 4.25: Gain measurement setup for the baseband amplifier.

(FSQ26, [79]). The gain of the amplifier can then be calculated by:

$$A = 20 \cdot log_{10}\left(\frac{V_{out}}{V_{in,diff}}\right) \tag{4.11}$$

Figure 4.26 presents the measurement of the baseband amplifier for which all stages are set to their maximum gain. The gain of both branches is almost identical and has a
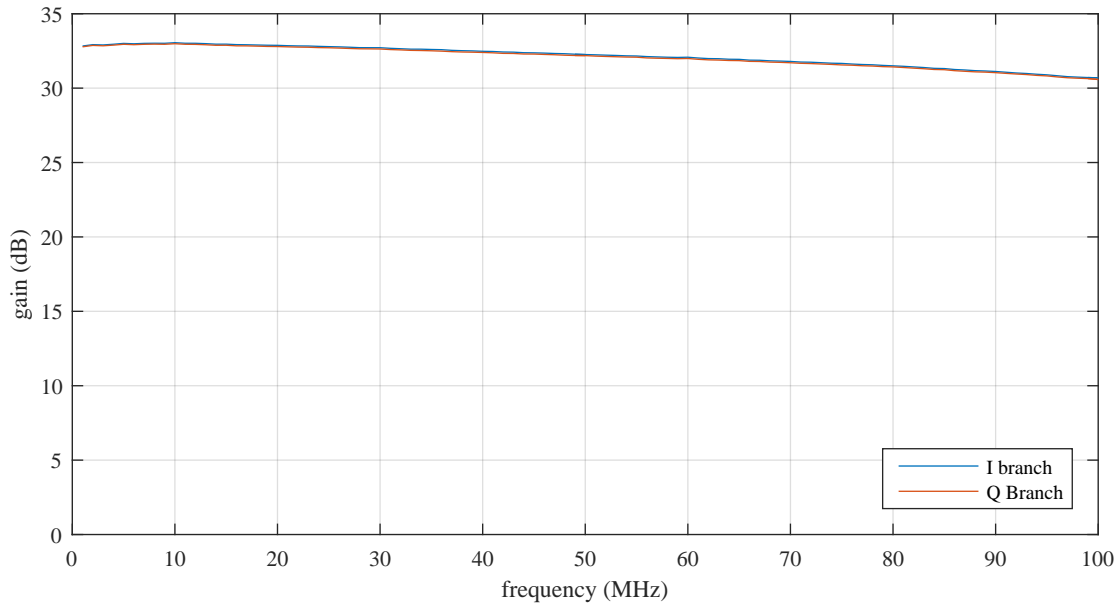
FIGURE 4.26: Gain of the baseband amplifier at maximum gain setting.

Parameter	Symbol	Value	Unit
carrier frequency	f_c	71–76	GHz
modulation bandwidth	B_m	150	MHz
EIRP	$EIRP_{TX}$	34	dBm
minimum detectable signal	P_{RX}^m	-100	dBm

TABLE 4.3: Achieved characteristics of the MMID base-station

maximum of $33.5\,\text{dB}$ at low frequenies. The $3\,\text{dB}$ bandwidth is at $100\,\text{MHZ}$.

4.7 Conclusions

In this Chapter, the concept and design of the MMID base-station was discussed. In the current stage, the base-station allows the generation and analysis of all EPC Gen2 commands and responses. However, to accomplish a full EPC Gen2 compliant communication the digital signal processing provided by a computer running MATLAB®should be replaced by a FPGA implementation. This task exceeds the scope of this thesis and remains to be carried out. The analog signal chain including the mm-wave frontend enables an in-depth analysis of potential applications for MMID, such as high data-rate communication with signal bandwidths up to $150\,\text{MHz}$, or localization of transponders using FMCW radar techniques with modulations bandwidths up to $6\,\text{GHz}$. Table 4.3 summarizes the key parameters of the MMID base-station.

Chapter 5

Transponder

The mm-wave frontend of the MMID transponder has two tasks: On the one side it is responsible for the down-conversion of the mm-wave signal from the base-station into the baseband regime. On the other side it provides the backscatter modulation functionality by modifying the impedance at its antenna port. There are several concepts and implementations of MMID transponder reported in the literature:

In [130], the authors present a micro-machined direct conversion receiver for 77 GHz with a capability to perform backscatter modulation. The antenna and microstrip structures are implemented on a silicon membrane with a flip-chip mounted GaAs Schottky diode as envelope detector. The authors obtained a signal amplitude of 40 mV at a distance of 10 cm with a radiated power of 30 dBm EIRP. Additionally, the authors demonstrated backscatter modulation capability with a carrier to signal ratio of 32 dBc.

[47] highlights the necessity of fully integrating the transponder. Additionally, it demonstrates reasonably performing mm-wave on-chip antennas on a silicon substrate, thus proofing the feasibility of fully integrated transponder chips without any I/O pins for reading ranges up to tens of centimeters.

The design of the mm-wave frontends semi-passive transponders is presented in [131]. Two different designs, one built on a low temperature co-fired ceramic (LTCC) with a backward diode, and one built on liquid crystal polymer (LCP) with a Schottky diode. Both transponders employ patch antenna arrays with 11.1 dBi and 18 dBi and show a good performance in the backscatter modulation with a reflection modulation coefficient

($\Gamma_{Tr,TX,mod}$) of approximately 0.3. However, the LTCC transponder outperforms the LCP one in the receiving sensitivity by $500\,\mathrm{mV/mW}$ to $7\,\mathrm{mV/mW}$.

A concept for a passive EPC Gen2 compatible MMID transponder was introduced in [104]. The authors are using a commercial UHF RFID transponder chip. An external mm-wave diode between the antenna and the transponder mixes the mm-waves to an IF frequency of 850-950 MHz. To enable the down-conversion at the transponder, the base station performs a single- or dual-sideband up-conversion of the RF signal of an UHF RFID Reader to mm-wave frequencies. To prove the validity, the authors implemented a demonstrator for 10 GHz, achieving a tag sensitivity of -4 dBm and a reading range of up to 30 cm.

A power harvesting integrated RFID transponder is proposed by the authors in [132]. Instead of using a backscatter communication, the transponder implements a bit-by-bit active transmission. The base-station transmits a pulsed CW to power the transponder. Between the bursts, the transponder sends one bit of data using pulse width modulation. To reduce the power consumption, the transponder uses a free running local oscillator at 60 GHz. The manufactured demonstrator achieves a reading distance of 1.3 cm and a data rate of up to 50 kb/s.

In [107] a regenerative active backscatter transponder is proposed. This concept uses a switched injection-locked oscillator (SILO) to regenerate the signal of the base station. The regenerated carrier is then pulse modulated with the response of the transponder. This increases the reading range significantly compared to backscatter modulation, at the cost of higher power consumption. The implemented demonstrator shows a reading range of up to 10 m and a data rate of up to 37.5 MB/s.

A chip-less MMID transponder is proposed by the authors in [133]. The transponder compromises two orthogonally polarized circular patch antennas loaded with resonant slots which are connected through a transmission line. The base station sends a FMCW signal through its transmit antenna, which is captured by the receive antenna of the transponder and excites the transmit antenna. The base-station receives the broadband resonant signature of the transponder. As the transponder does not employ any active components, the reading range of this concept is only determined by the base station.

Within this chapter, the design and implementation of the MMID transponder are discussed. Based on the system specifications from Section 2.5, the analysis of the transmission channel in Chapter 3, and the performance of the base-station in Chapter 4, the specifications for the MMID transponder are derived in Section 5.1. Section 5.2 presents the concept of the transponder. The building blocks of the transponder are presented in Sections 5.3 and 5.4.

5.1 Specifications

The requirements for the MMID transponder are derived from Section 2.5 and refined by Section 4.1. The transponder should integrate the EPC Gen2 protocol and operate at a center frequency within 71-76 GHz. As a fully passive operation is only feasible in a completely integrated solution, a semi-passive operation with a battery as power supply will be implemented. The antenna of the transponder should support a robust communication, thus compromising between reading distance and a wide beamwidth. Overall, the concept of the transponder should allow a very flexible setup in order to support various applications.

5.2 Concept

The transponder for the MMID demonstrator is carried out in a semi-passive fashion. While being powered by a battery, it uses backscatter modulation to communicate with the base-station. Similar to the concept proposed by the authors of [104], the transponder uses an ASIC which implements the EPC Gen2 protocol. The main difference in the concept is, that the ASIC implemented in this concept does not contain any RF circuitry, thus it is not necessary to transmit an additional high power carrier for the down-conversion of the mm-wave signal into the operating frequency range of the ASIC. The design of the transponder is published in [134].

Figure 5.1 shows a block diagram of the MMID transponder. The mm-wave front-end contains the transponder antenna, a matching network, a diode, and a low-pass filter. It is responsible for the envelope detection of the incoming signals from the base-station, as well as for performing the backscatter modulation. The baseband unit holds the ASIC
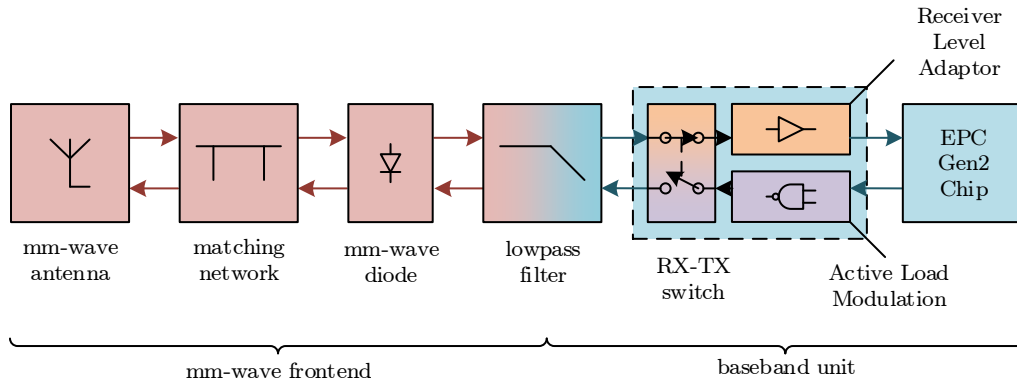
FIGURE 5.1: Building blocks of the MMID transponder.

which implements the EPC Gen2 protocol. Around the ASIC a switching circuitry separates the incoming signals from the base-station and the response. Additionally, this circuitry ensures a correct interfacing between the ASIC and the mm-wave front-end.

Figure 5.2 shows a picture of the assembled prototype of the transponder. The mm-wave front-end has much higher requirements on the performance of the substrate material compared to the baseband unit. Therefore, the two components of the transponder – the mm-wave front-end and the baseband unit – are realized on two separate PCBs. This approach allows a maximum degree of flexibility in the design. Additionally, the manufacturing costs are reduced by avoiding complex integration processes for the high performance mm-wave materials.

The operation principle of the transponder can be separated into the down- and uplink use-case. In the downlink scenario (Figure 5.3), the mm-wave antenna captures the amplitude modulated RF carrier of the base station. The mm-wave diode operates as an envelope detector and provides a low level signal to the baseband unit. The the baseband unit adapts the signal from the diode to TTL levels and feeds the data from the base station to the baseband chip. Afterwards, the switching circuitry triggers the uplink mode.

While transmitting the response (Figure 5.4) in the downlink scenario, the switching circuitry translates the response of the ASIC into two different bias voltages for the mm-wave front-end. According to the two bias levels, the mm-wave diode switches between two modes: a reflecting and an absorbing state. In the absorbing state, the
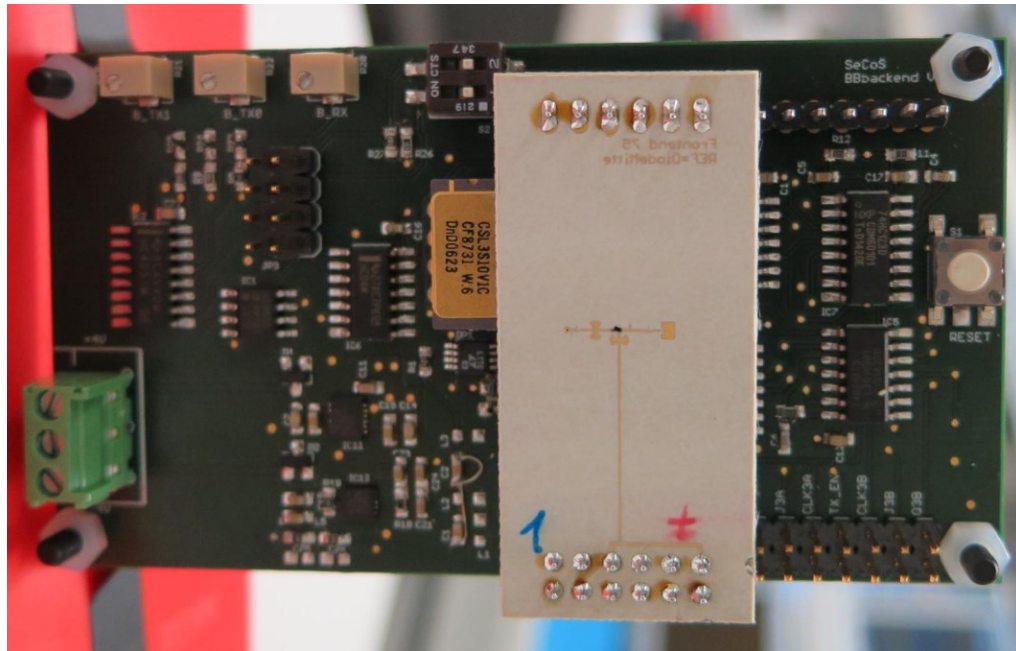
FIGURE 5.2: A photograph of the implemented transponder with the baseband PCB (green) and the mm-wave daughter board (white).
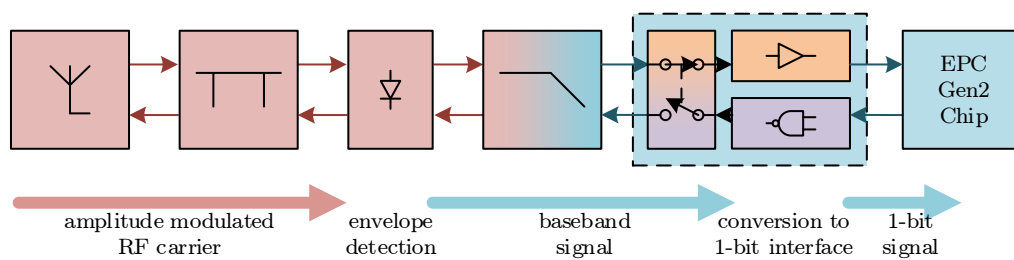
FIGURE 5.3: Receive mode of the MMID transponder.
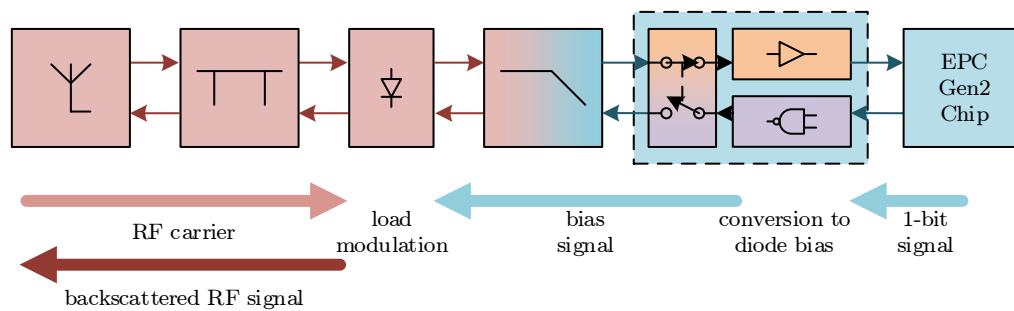
FIGURE 5.4: Transmit mode of the MMID Transponder

diode dissipates the RF carrier. In the reflecting state, most of the carrier power is reflected by the diode and sent back to the base-station.
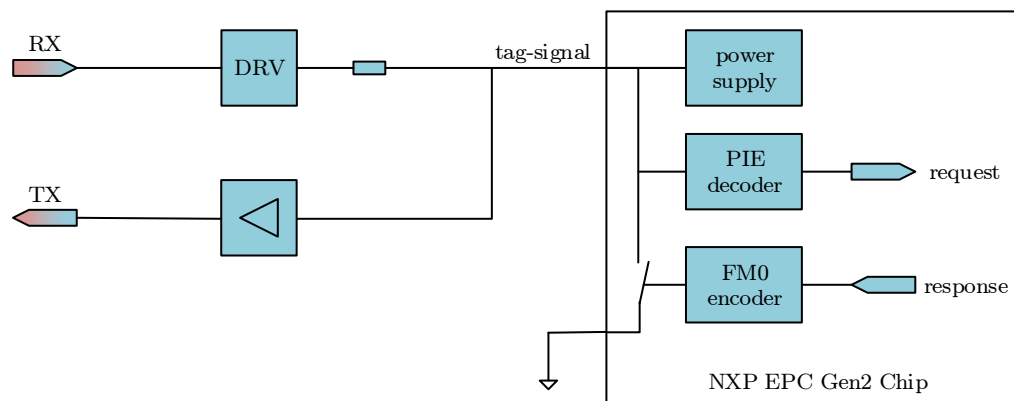
FIGURE 5.5: baseband chip.

5.3 Baseband Unit

As described in Section 5.2, the task of the baseband unit is to process the commands from the base-station and to provide a response to be sent back. Additionally, it provides the bias voltages for the mm-wave diode.

The schematics of the baseband unit can be found in Appendix B.

5.3.1 EPC Gen2 Baseband Chip

The development chip from NXP Semiconductors implements the full baseband functionality of the EPC Gen2 protocol. Similar to a standard UHF RFID chip, it provides a one-pin interface through which it receives and transmits commands and data. This pin is also used to supply the circuitry. In contrast to the commercial available UHF integrated circuits, the development chip does not comprise any RF circuitry, thus operating directly in the baseband at TTL levels.

The ASIC comprises a PIE decoder to read the commands of the base-station, a processing unit to calculate the response, and a FM0 encoder to prepare the data for the transmission. To communicate with its environment, the chip uses a switch to pull its one-pin interface to ground. During this time, the switching circuitry of the baseband unit is required to provide a constant voltage via a pull-up resistance as shown in Figure 5.5.
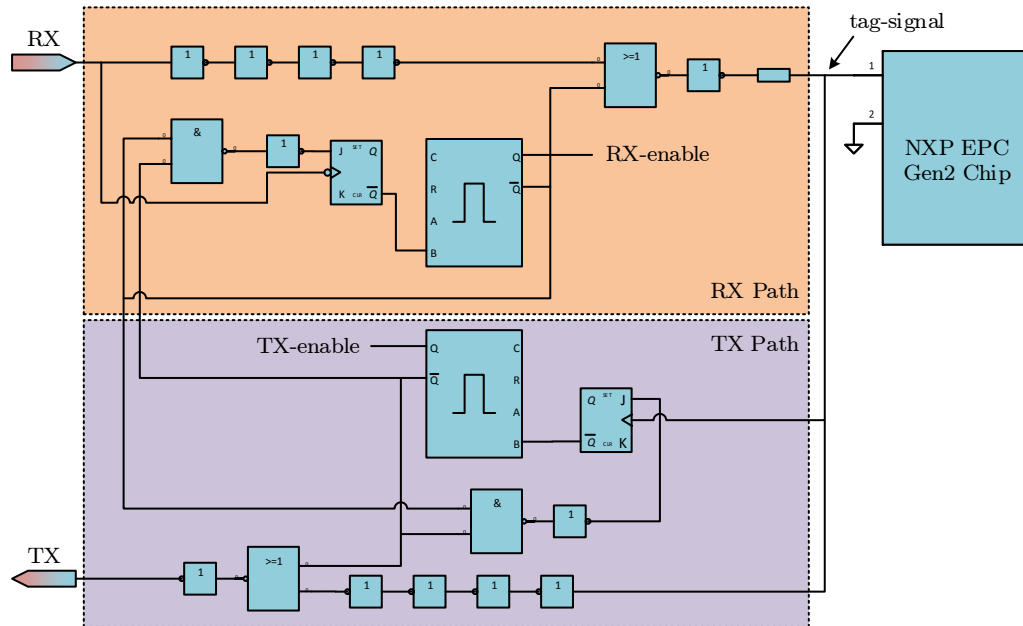
FIGURE 5.6: The RX-TX switching logic for the NXP EPC Gen2 baseband chip.

5.3.2 RX-TX Switching Logic

Figure 5.6 shows the logic circuitry of the RX-TX switch. It is used to separate the signals from the base station and the response of the transponder at the one-pin interface of the baseband chip. Additionally, it adapts the signal levels from the mm-wave front-end to the required TTL levels.

In the receive mode (which is the default mode) of the transponder, the RX mono-flop is triggered with the first falling edge of the base-station signal. After delaying the input signal, it is interconnected with the baseband chip via an OR-gate. Figure 5.7 shows the first falling edge of the input signal (RX), which is triggering RX-*enable*, and the delayed edge at *tag-signal*. At the same time, RX-*enable* signal the TX mono-flop to ensure that the base-station signal at *tag-signal* is not generating bias voltages for the backscatter modulation at *TX*. To ensure that the RX signal is not re-triggering the mono-flop, it is also disabled by RX-*enable*.

After the base station request is processed, The RX mono-flop resets itself and enables the TX mono-flop again. The next falling edge at *tag-signal* triggers the TX mono-flop, which enables the interconnection of the baseband chip with the bias voltage generation (TX). Figure 5.8 shows a simulation of the transmit mode of the switching logic. The response of the baseband chip represented by *tag-response* pulls *tag-signal* to ground.
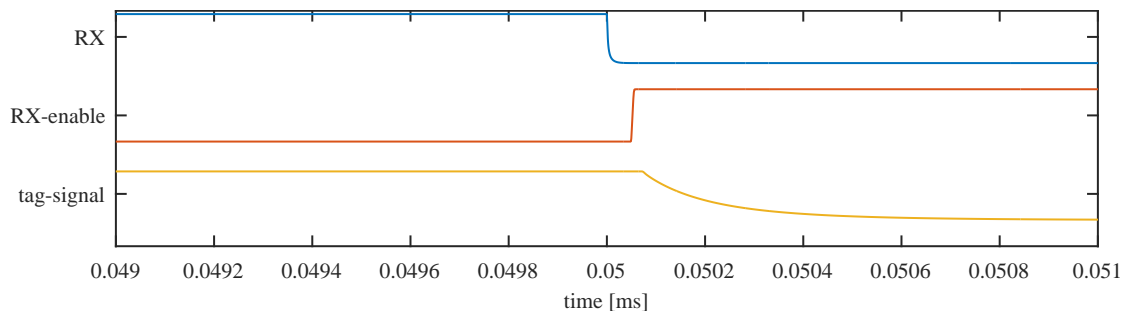
FIGURE 5.7: Functional simulation of the RX path of the switching logic.
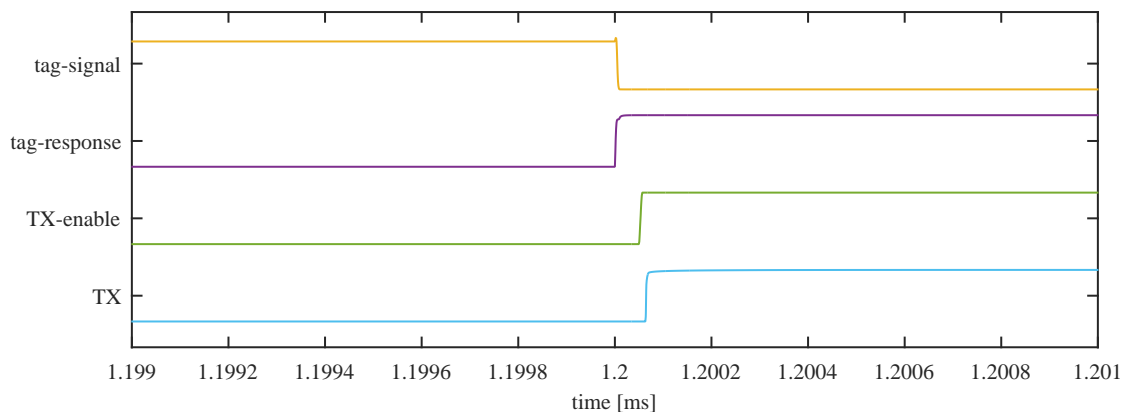
FIGURE 5.8: Functional simulation of the TX path of the switching logic.

The first falling edge of *tag-signal* triggers *TX-enable*. Additionally, *TX-enable* locks the RX mono-flop and ensures that the output of the RX path is set to high. This ensures that the baseband chip can communicate with the switching logic by pulling its interface pin to ground.

To verify the functionality of the switching logic a simulation using the setup depicted in Figure 5.10 was carried out. Pull-down switches emulate the response of the baseband chip as well as the influence of the backscatter communication on the signal level at the signal level at the RX input. Figure 5.10 shows the results for a complete communication, including both, a request from the base station and a response from the transponder.

The switching logic is implemented on the baseband board using components of the high-speed CMOS TTL level (HCT) 7400 logic family. The schematic of the implementation is presented in Appendix B.
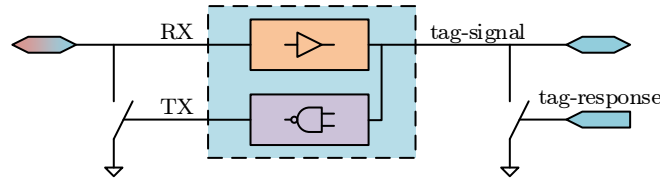
FIGURE 5.9: Setup for the functional simulation of the switching logic.
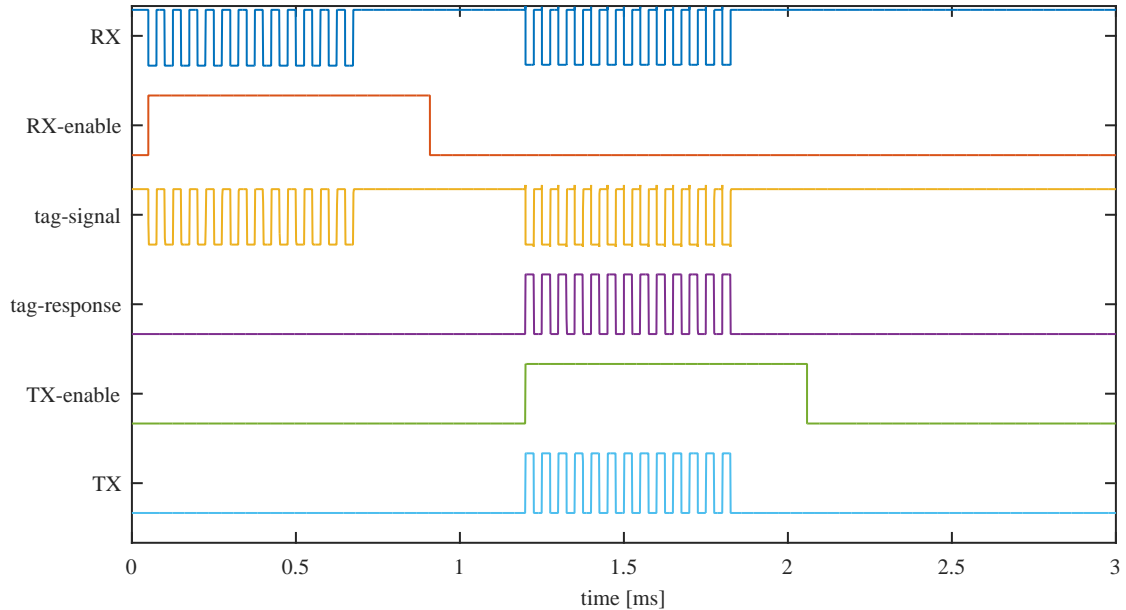
FIGURE 5.10: Functional simulation of the switching logic.

5.3.3 Bias Generation

Figure 5.11 shows the bias generation with its switching logic. It provides three different bias levels: one for the receive mode of the transponder (*Bias-RX*) to operate the mm-wave diode in an envelope detection mode, and two for the transmit mode to move the diode either in an absorb (*Bias-TX0*) or reflect (*Bias-TX1*) state. The bias voltages are generated with three adjustable voltage dividers and applied to the mm-wave diode using an analogue multiplexer (74HCT4051, [135]). Table 5.1 shows the truth table for selecting the first three input channels. *TX* and *TX-enable* control the selection of the bias voltage channel. As long as the transponder is in the receive mode and *TX-enable* is set to low, the biasing channel *A0* is selected. When the transponder switches to the transmit mode, the bias channels *A1* and *A2* are selected according to the state of *TX*. Table 5.2 shows the truth table for the control inputs of the multiplexer (*S1* and *S0*) from which Equations (5.1) and (5.2) are derived.
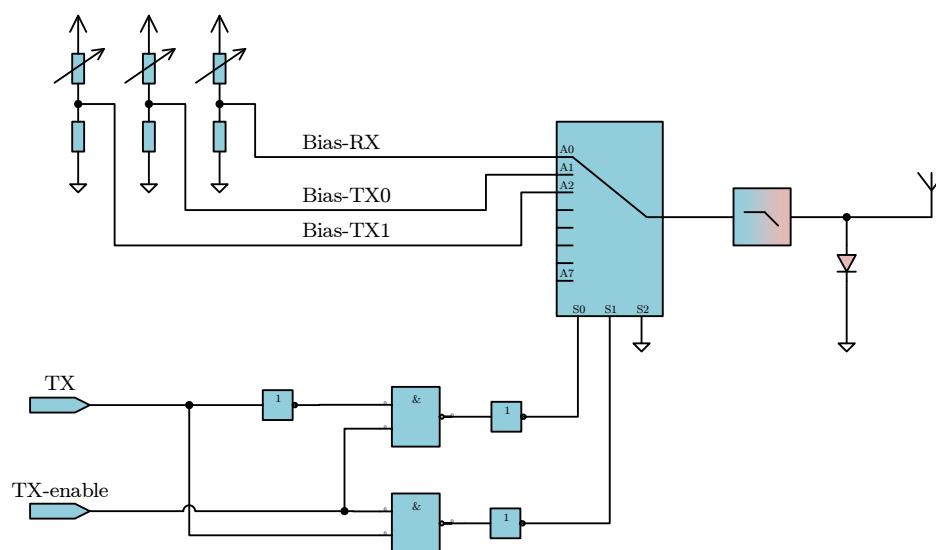
FIGURE 5.11: Switching logic for the biasing circuitry

Enable	S2	S1	S0	channel
L	L	L	L	A0
L	L	L	H	A1
L	L	H	L	A2

TABLE 5.1: Truth table of the 74HCT4051 analogue demultiplexer.

TX	TX-enable	S2	S1	S0	channel
L	L	L	L	L	A0
H	L	L	L	L	A0
L	H	L	L	H	A1
H	H	L	H	L	A2

TABLE 5.2: Truth table of the biasing logic

$$S1 = TX \land \textit{TX-enable} \tag{5.1}$$

$$S0 = \overline{TX} \land \textit{TX-enable} \tag{5.2}$$

FIGURE 5.12: Stack-up of the mm-wave PCB.

5.4 mm-Wave Frontend

5.4.1 Design of mm-wave PCB components

Figure 5.12 shows the stack-up for the mm-wave frontend PCB. To ensure a good performance of the mm-wave microstrip structures, a low-loss ceramic-filled PTFE substrate with a relative dielectric constant of 3 and a loss tangent of 0.001 (Rogers RO3003, [136]) is chosen. The 127 um thick core material is mechanically reinforced by a 1 mm thick FR4 substrate. This minimal available thickness was chosen in order to suppress additional unwanted modes in transmission lines. The copper is 25 µm thick and has a nickel-gold finish on the top layer. The PCBs were manufactured by *AT & S Austria Technologie & Systemtechnik Aktiengesellschaft*. The process, used by the manufacturer, constrains both, the minimum line width and the minimum distance between two structures to 50 um.

Overall, the mm-wave frontend PCB employs three different transmission lines architectures: coplanar waveguides (CPW), conductor backed or grounded coplanar waveguides (GCPW) and microstrip lines (Figure 5.13). All transmission lines are designed for a characteristic impedance of 75 Ω using a 3D fullwave EM simulation tool [76]. The width w and the gap g of the CPW and and the GCPW line are set to 110 um and 55 um, respectively. The conductor width w of the microstrip line is 140 um.

For the design of a transmission line it is usually assumed, that the conductors have an ideal rectangular cross-section. This however does not represent the physical reality. The etching processes used to structure the PCB produce a conductor cross section
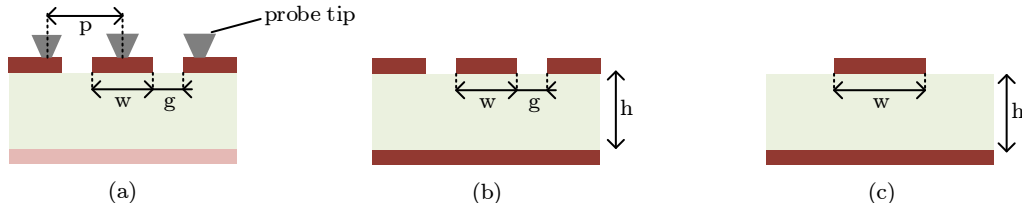
FIGURE 5.13: Transmission lines for the mm-wave PCB: (a) coplanar waveguide, (b) grounded coplanar waveguide, and (c) microstrip line.

which can be better approximated by a trapezoid. Figure 5.14 shows the influence of the etching factor on the cross-sections of a microstrip and a GCPW line. The degree of influence of the etching process on the conductor geometry can be described by an etching angle Θ (5.3), or the etching factor EF (5.4). Modern etching processes are able to achieve etching factors in the range of 4-5 which correspondents to an etching angle between 20 and 25 degree.

$$tan(\Theta) = \frac{x - y}{2 \cdot t} \tag{5.3}$$

$$EF = \frac{2t}{x - y} = \frac{1}{tan(\Theta)} \tag{5.4}$$

With increasing etching angles or decreasing etching factors, the characteristic impedance of the conductor increases by several percent [137]. Figure 5.15 shows a simulation of the characteristic impedance of a microstrip and a GCPW transmission line for increasing etching angles. The resulting impedance is plotted relative to the impedance of an ideal geometry with an etching angle of 0 degree. The deviation of the characteristic impedance increases linear with the etching angle. While the deviation of the GCPW and CPW lines is very similar with 5-7.5 % for realistic etching angles of 20-25 degree, the microstrip line shows a much more stable behavior with a deviation of 1-2 %. The better performance of the microstrip line in terms of the variation of the etching factor can be explained by the field distribution for the respective dominant modes. The electric field of CPW and GCPW modes is concentrated in the gap between the conductor and the adjacent ground planes and, therefore, more susceptible to the geometry of the conductors cross section. Whereas the electric field of the microstrip transmission line is concentrated between the conductor and the ground plane at bottom of the substrate. This shows that the microstrip is more robust towards varying etching angles and other

(a)   (b)
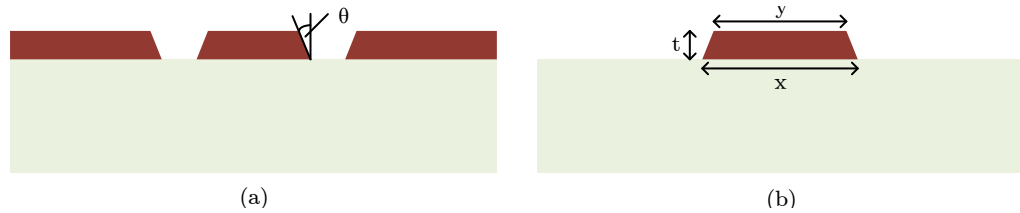
FIGURE 5.14: Influence of the etching factor on the geometry of: (a) coplanar waveguide, and (b) microstrip line.
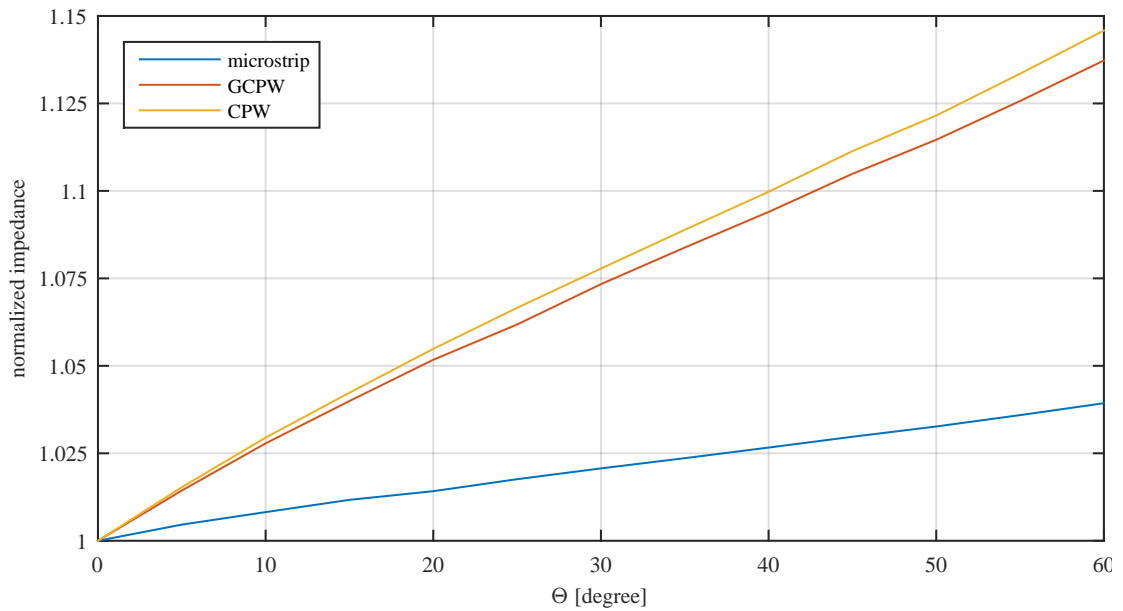
FIGURE 5.15: Simulated influence of the etching angle on the impedance of a microstrip line (blue), a GCPW (dark orange) and a CPW (light orange).

production tolerances, such as the minimum clearance between two adjacent copper areas, and therefore more suitable for the implementation of the mm-wave components of the MMID transponder.

5.4.2 Probe Launch

The characterization of the microstrip components requires a well defined transition between the co-axial interface of the measurement equipment and their planar interfaces. One solution are co-axial end-launch connectors [138]. These connectors provide a good transition, while maintaining reasonable costs. However, due to the mechanical stress, the re-usability of these components is limited. Another solution are probe station equipped with RF probes [139, 140]. While the initial costs for a probe station are significant, a single RF probe can endure several thousand touchdowns. Another advantage of this approach is the highly repeatable contacting process due to the micro
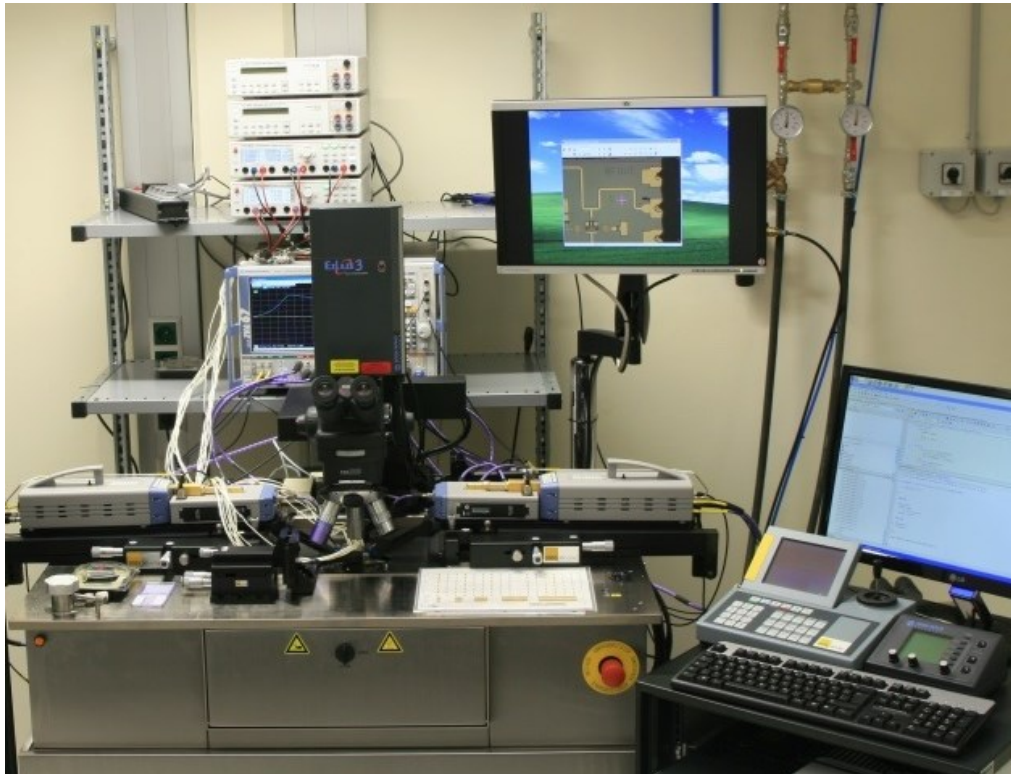
FIGURE 5.16: RF probe station equipped with a DC-110 GHz VNA

manipulators of the probe station which allow an exact positioning of the probes. To ensure a good performance of the RF probes, an appropriate launching structure has to be designed on the PCB. While the design such launching structures up to mm-wave frequencies is a well investigated for on-wafer measurements [141–145], there is – to the knowledge of the author – no literature available at the time of writing, which focuses on the design of probe launches for PCB applications.

The main challenge of designing the launching structure is to reconcile the constraints of the PCB manufacturing process with the pitch of the RF Probes while maintaining a good matching between the probe and the launching structure.

The probe launch for the mm-wave board was designed in two stages. On the first run of the PCB manufacturing, the initial design was produced. With the measurement data from this run, a second design was optimized and is presented here.

Figure 5.17 shows the design of the launching structure. It consists of three segments: a CPW area, a transition area and a microstrip. The RF probe lands on the edge of the CPW area which provides a good mode matching. Along the length of the CPW area, the mode converts from a pure CPW mode to a GCPW mode. In the transition
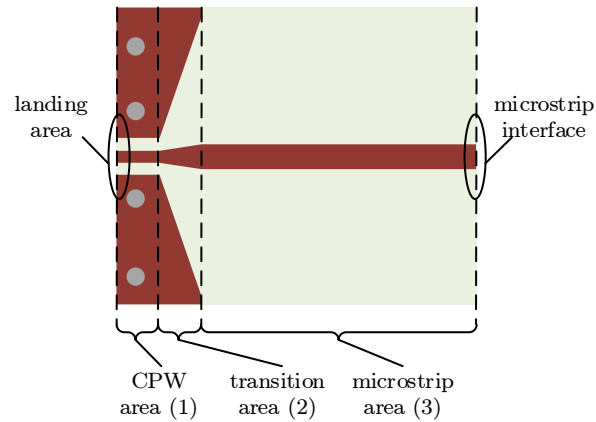
FIGURE 5.17: Probe launch and test fixture for the mm-wave PCB.

area, the ground planes of the GCPW transmission line are gradually removed while the conductor width increases to match the microstrip line. This results in a conversion of the GCPW mode into a microstrip mode. The microstrip area forms the interface to the devices to be measured.

To optimize the geometry of the launch several steps were carried out: First the ideal lengths of the CPW (cpw-l) and the transition from CPW to microstrip were determined in a 3D EM simulation by minimizing the insertion loss of the launch. During this step, the position of the grounding vias was fixed. In a second step the influence of the via position was optimized in an extensive 4-dimensional parameter sweep aiming for the best insertion loss and matching over the full frequency range. A thoroughly description of the design and optimization process can be found in [146]. The dimensions of the final launch are given in Table 5.3.

The performance of the launch is shown in Figure 5.19. The input reflection coefficient (S_{11}) and the transmission coefficient (S_{21}) show a minimum matching below -10 dB and a maximum attenuation of -2.3 dB over the full frequency range of 0-90 GHz. The design of the launch structure and the analysis of the influence of the via positioning were published in [39, 40].

5.4.3 Antenna

The transponder antenna play a key role in the link budget of the MMID system, as shown in Section 2.2. Using a high gain antenna as suggested in [130, 131], can increase the reading range of the transponder significantly. However, due to the higher gain, the
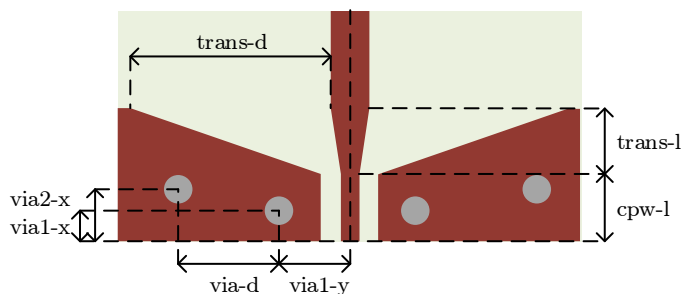
FIGURE 5.18: Dimensions of the probe launch.

variable	value [um]	description
cpw-l	300	length of the CPW area
trans-l	300	length of the transition area
trans-d	1150	distance between center conductor end ground plane at the end of the transitions
ms-l	1000	length of the microstrip area
cpw-w	110	width of the center conductor of the CPW
cpw-g	55	width of the gap between the center conductor and the ground planes
ms-w	140	width of the micro strip transmission line

TABLE 5.3: Dimensions of the probe launch.
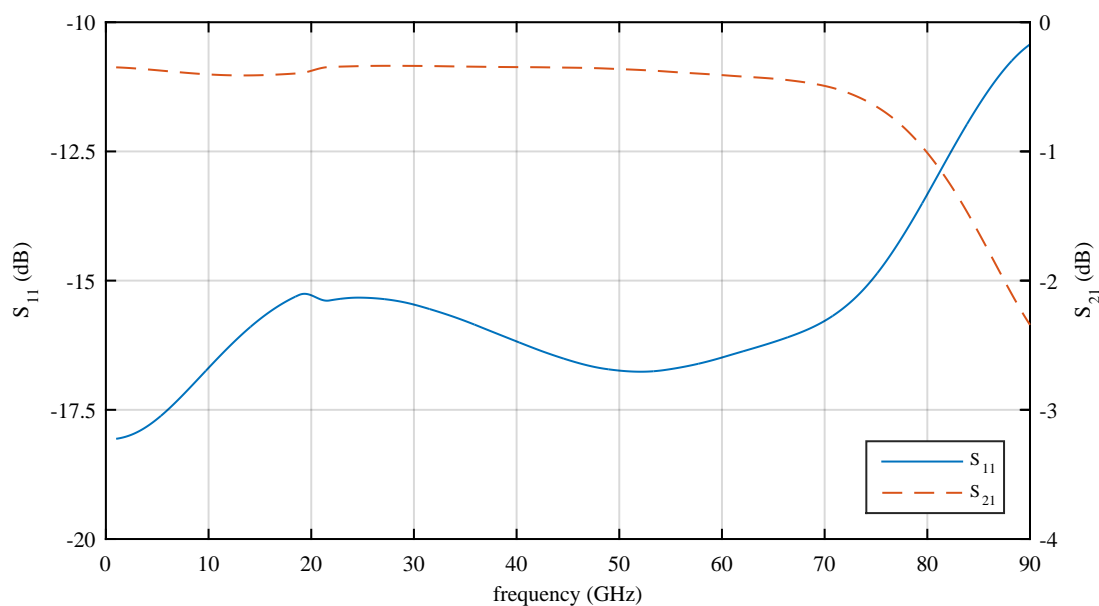
FIGURE 5.19: Simulation results of the probe launch.
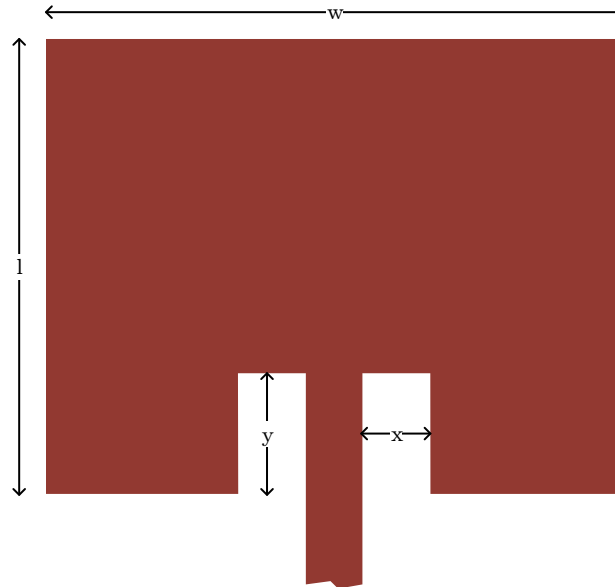
FIGURE 5.20: Dimensions of the patch antenna.

lower half-power beam-width renders the communication much more sensitive towards the alignment of the transponder and the base-station.

To compromise between reading range and a robust communication, a single patch antenna is used. The patch antenna offers a medium gain and can be easily implemented on a PCB. It consists of a rectangular conductor patch with a width w and a length l on top of a ground plane (Figure 5.20). An inset, fed with a width x and a length y, is used to match the antennas input impedance to the line impedance of $75\,\Omega$.

Using the well investigated formulas (5.5) to (5.8) from [64], seven patch antennas with resonant frequencies between 71 and $77\,\mathrm{GHz}$ were designed. To consider the etching effects of the PCB manufacturing process, a full wave 3D EM simulation as described in Section 5.4.1, was performed. The dimensions for the seven antennas are depicted in Table 5.4. The width of the inset fed is fixed to $176\,\mathrm{um}$ for all designs.

$$w = \frac{1}{2f_r\sqrt{\mu_0\epsilon_0}}\sqrt{\frac{2}{\epsilon_r + 1}} \tag{5.5}$$

$$l = \frac{1}{2f_r\sqrt{\epsilon_{eff}}\sqrt{\mu_0\epsilon_0}} - 2\Delta l \tag{5.6}$$

$$\epsilon_{eff} = \frac{\epsilon_r + 1}{2} + \frac{\epsilon_r - 1}{2}\left[1 + 12\frac{h}{W}\right]^{-1/2} \tag{5.7}$$

f_c [GHz]	w [um]	l [um]	y [um]
71	1494	1162	306
72	1473	1145	300
73	1453	1128	295
74	1433	1112	289
75	1414	1096	284
76	1396	1080	278
77	1377	1065	274

TABLE 5.4: Dimensions of the patch antenna.
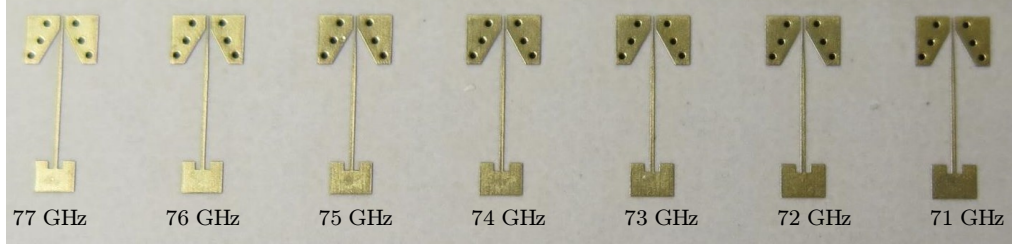
FIGURE 5.21: Picture of the manufactured patch antennas.

$$\Delta l = 0.412 h \frac{(\epsilon_{eff} + 0.3)(w/h + 0.264)}{(\epsilon_{eff} - 0.258)(w/h + 0.8)} \tag{5.8}$$

Figure 5.22 shows the simulated gain of the 73 GHz patch antenna at its resonant frequency. It shows a gain of 9.75 dBi in the main beam direction and a half-power beamwidth of 83.7 degree in the H-plane. The simulated resonant frequencies are in general lower then the desired value. However, for increasing frequencies, the actual and desired value match better (Figure 5.23). To verify the simulation results, the seven designs were manufactured and evaluated based on their input reflection coefficient, as a measurement system for antennas beam patterns at the required frequency range was not available.

The designs for 72, 73, 75, and 77 GHz show a good agreement of the resonant frequency between the simulation and measurement, while the designs for 71, 74, and 76 GHz show a shift to higher resonance frequencies. The maximum level of matching agrees with the simulations for the designs for 72 and 73 GHz. Especially for higher frequencies, the matching decreases. The mismatch between simulation and measurements can be credited to production tolerances of the PCB manufacturer with respect to the length of the patch antenna, as well as the etching factor, which deviates from the assumed value in the simulation Additionally these tolerances do not only alter the geometry of the
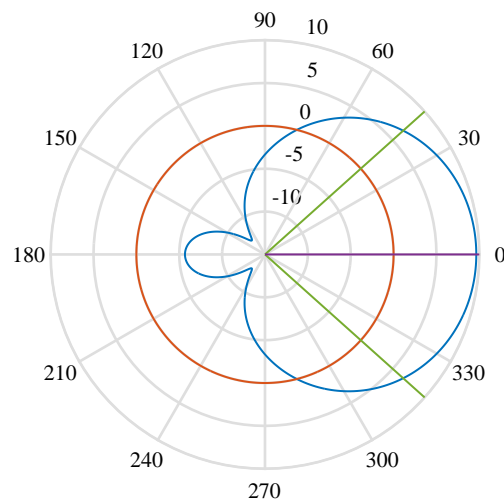
FIGURE 5.22: Gain of the 73 GHz antenna in dBi at the resonant frequency.

antenna, thus causing a shift of the resonant frequency, but also influence the behavior of the launch structure, which is used to measure the patch antenna.

Despite these production tolerances, the antennas are relatively good matched with more than -10 dB over an average absolute bandwidth of 3.13 GHz. The antenna designs for a resonance frequency of 72 and 75 GHz cover the full operational range of the base-station transmitter. Therefore, these two designs are used as a reference for the design of the other microstrip elements of the mm-wave frontend to allow a flexible setup regarding the operating frequency of the MMID system.

5.4.4 mm-Wave Diode

The mm-wave diode plays an important role in the transponder frontend. On the one side it is responsible for the demodulation of the AM commands coming from the base-station. For this task, the diode needs to provide good capabilities for envelope detection. On the other side, the diode modulates the CW carrier of the base-station in order to provide the backscatter capability for the communication from the transponder to the base-station. In this case, the diode needs to provide two very different reflection factors in order to provide a significant modulation depth.

The diode which chosen for the mm-wave frontend of the MMID transponder is an Infineon Technologies BAT14-077D [147]. This silicon-germanium single single Schottky
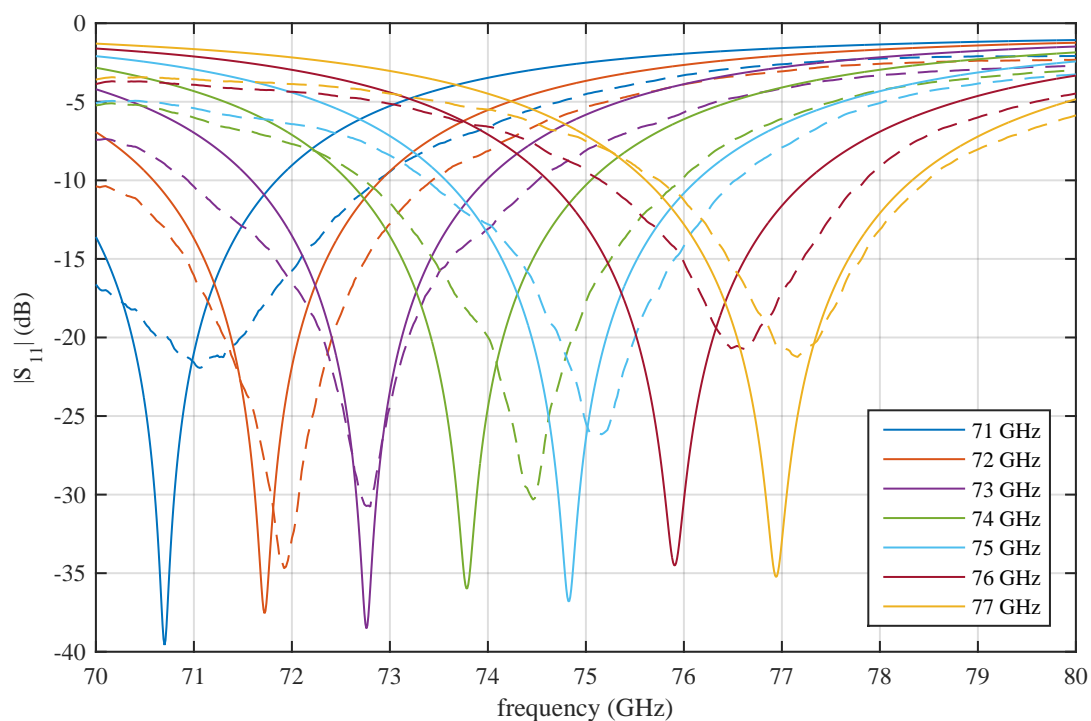
FIGURE 5.23: Simulated (solid) and measured (dashed) input matching (S_{11}) of the patch antenna.

(a)   (b)
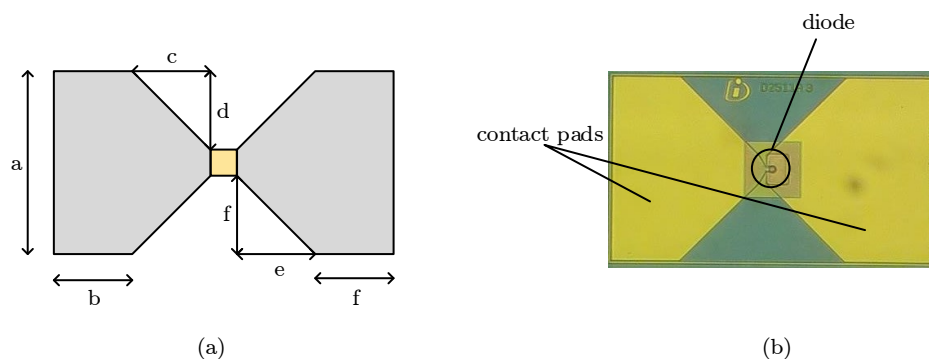
FIGURE 5.24: Dimensions (a) and a picture (b) of the mm-wave diode.

medium barrier mixer diode was originally designed for 80 GHz W-band applications, such as automotive radar. Figure 5.24 shows the layout of the diode and its contact pads for flip chip mounting (left) and a photograph (right). The parameters indicating the dimensions of the layout are given by Table 5.5.

Figure 5.25 shows the DC-characteristics of 5 different diodes which were mounted onto a test fixture. The limitation to 5.1 mA for voltages higher than 550 mV is caused by the current clamp of the utilized source measuring unit.

variable	value (um)
a	265
b	95
c	90
d	90
e	90
f	90

TABLE 5.5: Dimensions of the mm-wave diode.
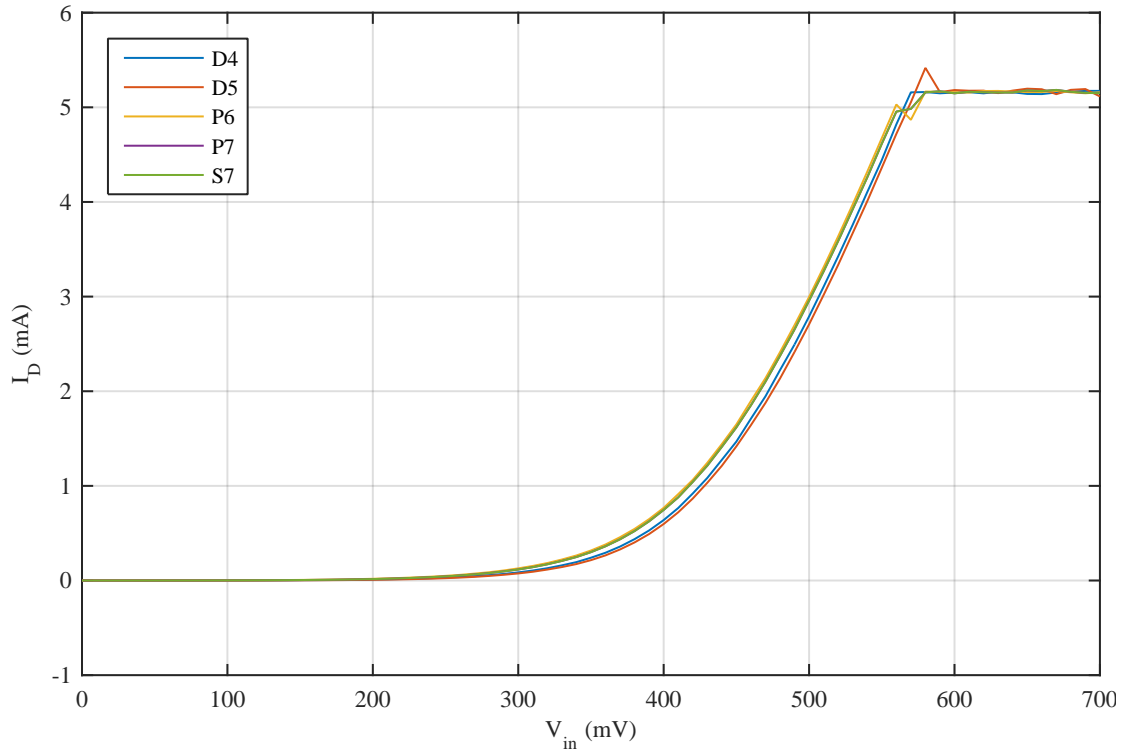
FIGURE 5.25: DC characteristics of 5 diodes on the test fixture.

Figure 5.26 presents the reflection coefficient at the anode of the mm-wave diode with a grounded cathode (Γ_{diode}) for two different bias voltages (0 and 0.5 V). The difference in magnitude between the two bias states decreases from 15 dB at 70 GHz to a negligible amount at 80 GHz. The resonance at 78.5 GHz is caused by an artifact of the de-embedding algorithm which removes the test-fixture from the measurements.

To verify the functionality and evaluate the performance of the mm-wave diode in the two aforementioned scenarios, two measurement setups, one for the downlink and one for the uplink were developed.

In the downlink measurement scenario, the envelop detection qualities of the mm-wave
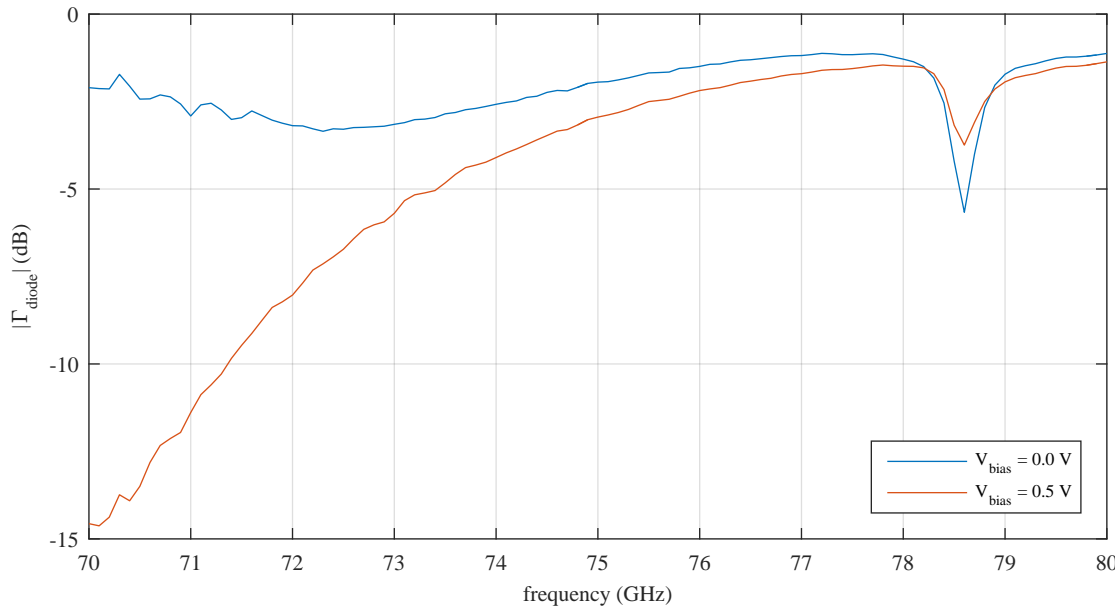
FIGURE 5.26: Reflection coefficient of the mm-wave dioode for different biasing.

diode are tested. For this scenario (shown in Figure 5.27), a diode in a shunt configuration is probed with a 110 GHz GSG probe [148]. A signal generator (SG) creates a single tone at a sixth of the desired carrier frequency and is modulated with a 100 % amplitude modulation depth by a rectangular signal with a frequency of 1 kHz. The up-converter (UC) multiplies the amplitude modulated carrier from the signal generator by the factor of six, thus simulating the base-station. The mm-wave signal is then fed into the diode via the high-pass path of a diplexer from the external testset of the VNA (Rohde&Schwarz ZVA-ZD110) and the probe. The diode performs the envelop detection and the baseband signal is sent back via the wafer probe and the low-pass path of the diplexer. A scope (OSC) with a high impedance input stage is capturing the signal for an offline analysis. Additionally, it is possible to change the biasing of the mm-wave diode via the low-pass path of the diplexer, thus allowing to find the optimum settings for the envelope detection.

Figure 5.28 shows the result of the AM-demodulation measurement. The amplitude of the demodulated signal is about 3 mV for an input signal of -3 dBm. The distorted rising edge of the demodulated signal is caused by the low cut-off frequency of the low-pass of the VNA diplexer which usually serves as a bias-tee. These results show that the chosen diode is suited for the envelope detection of the MMID system, despite the non ideal matching the the presented measurement setup.
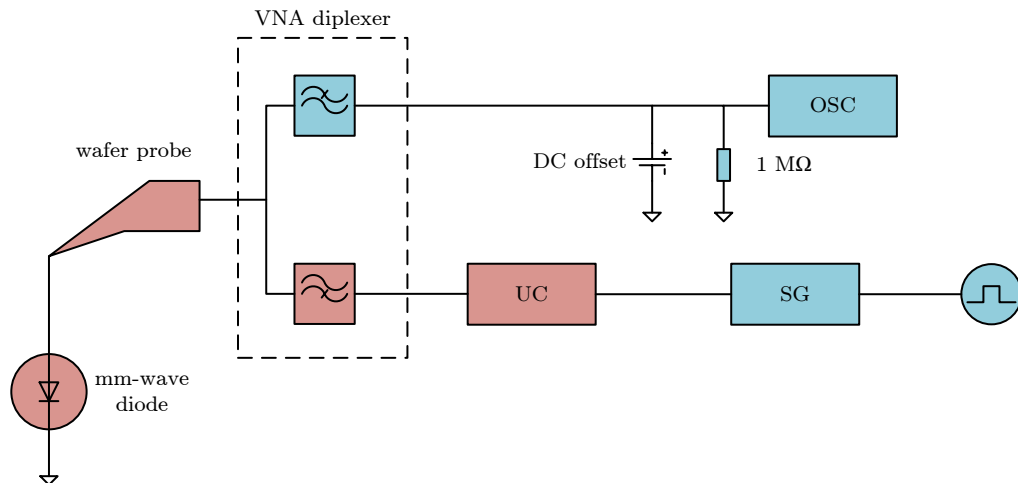
FIGURE 5.27: Measurement setup for determining the envelope detection capabilities of the mm-wave diode.
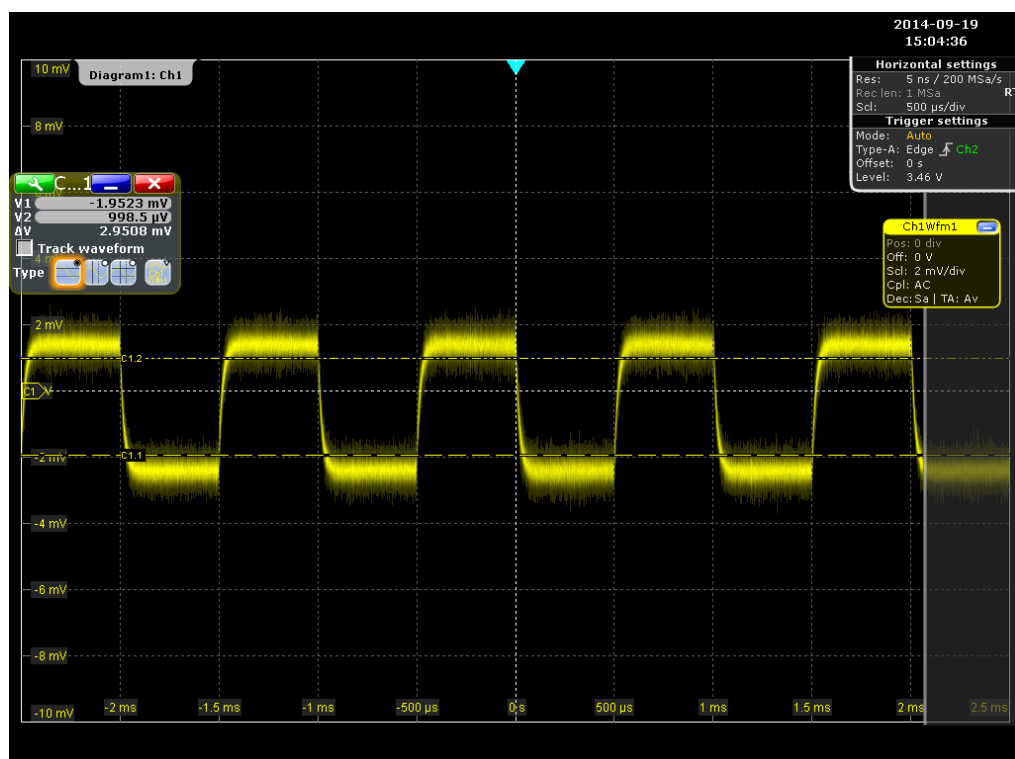
FIGURE 5.28: Measurement of the envelope detection capabilities of the mm-wave diode.
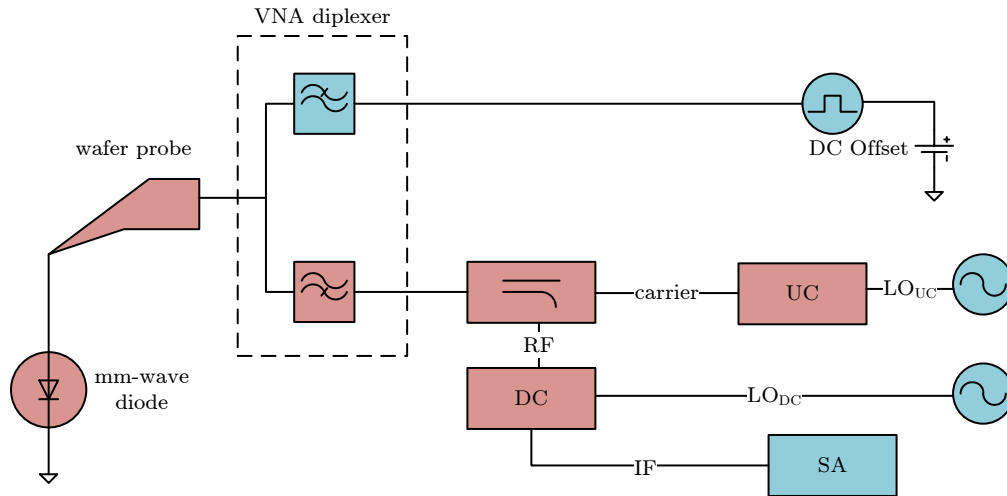
FIGURE 5.29: Measurement setup for determining the backscatter modulation capabilities of the mm-wave diode.

The measurement setup for the uplink use-case (Figure 5.29) utilizes a signal generator and an up-converter to generate the CW carrier signal for the backscatter modulation. Similar to the downlink scenario, the carrier is fed through the forward path of a directional coupler, the high-pass path of the diplexer, and the wafer probe to the mm-wave diode. An AWG in connected to the low-pass path of the diplexer switches between two biasing voltages for the diode. The reflected mm-wave carrier is then send back through the high-pass of the diplexer. The returning wave is then coupled to a down-converter (DC) which translates the modulated carrier to an intermediate frequency. The signal analyzer locks at the IF in a zero span mode and provides an insight on the modulation depth of the mm-wave front-end.

Figure 5.30 present the backscatter modulation capabilities of the mm-wave diode. Even without optimized matching of the diode towards the measurement setup, a modulation depth of about 5 dB can be achieved. This value is sufficient to ensure a good detectability of the transponder response at the MMID base-station.

5.4.5 Matching Network

The matching network between the antenna feeding port and the shunted mm-wave diode ensures an optimum performance of the MMID transponder by reducing the reflections between these two elements as noted in Section 2.2. To simplify the design process, the matching network is designed in two stages as shown in Figure 5.31: the first matches
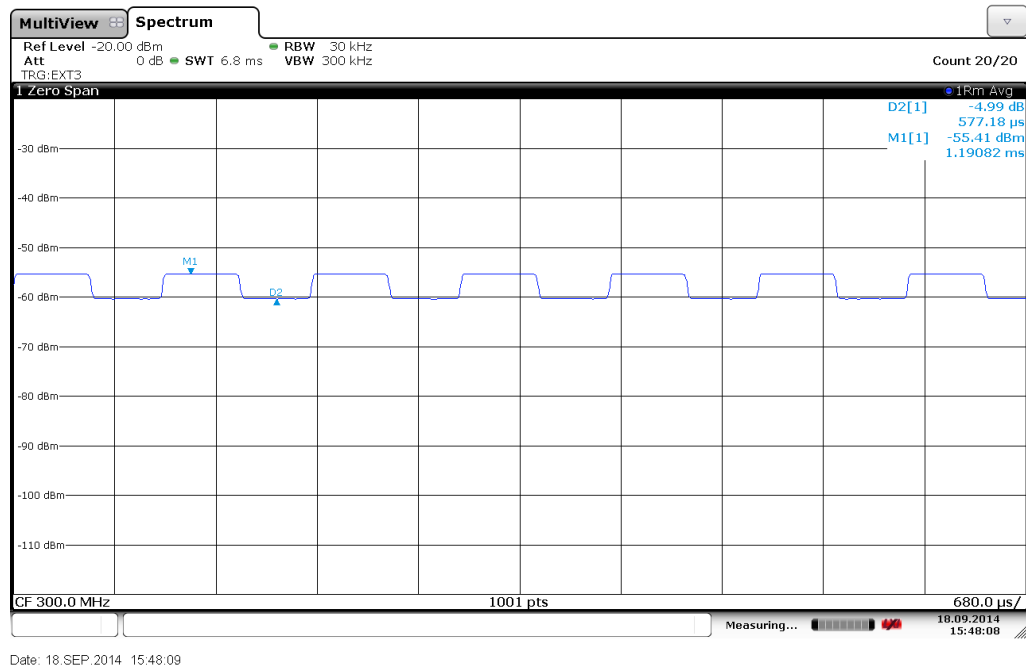
FIGURE 5.30: Measurement of the backscatter modulation capabilities of the mm-wave diode.
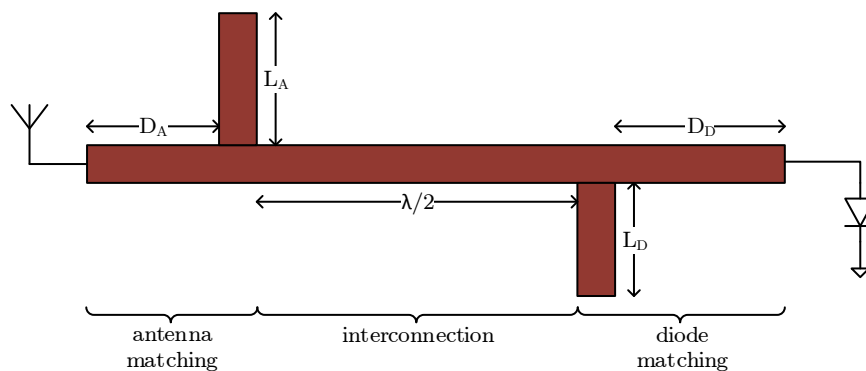
FIGURE 5.31: Dimensions of the matching network between antenna and diode.

the antenna to the characteristic impedance of the mm-wave frontends transmission line. The second stage ensures a good matching of the mm-wave diode during the downlink scenario while maintaining a high difference between the two reflection states of the transponder in the uplink scenario.

Figure 5.32 shows the reflection coefficient of the diode without and with the simulated matching network over a bias voltage sweep from 0 to 0.6 V. In both cases the reflection modulation $\Gamma_{Tr,TX,mod}$ is about 0.7 to 0.75 for bias voltages of 0 and 0.5 V. However, the magnitude of the reflection coefficient if the un-matched diode varies from 0.7 to 0.4 for different bias voltages, while the matched diode provides a similar reflection

variable	value at 72 GHz (um)	value at 75 GHz (um)
D_A	1230.0	1130.0
L_A	130.0	100.0
$\lambda/2$	1368.0	1311.5
D_D	410.0	790.0
L_D	1000.0	430.0

TABLE 5.6: Dimensions of the matching network for two different design frequencies
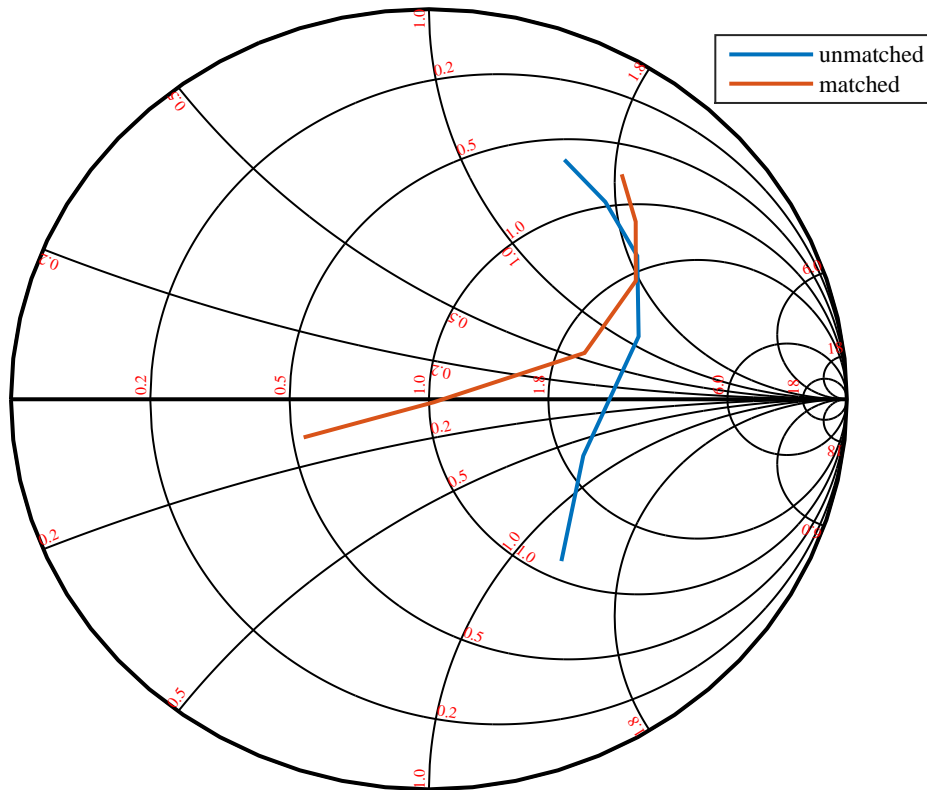
FIGURE 5.32: Reflection coefficient of the mm-wave diode at 72 GHz for different biasing voltages without and with the simulated matching network.

magnitude for an unbiased state and provides a good matching for a biasing voltage of 0.5 V. This good matching is necessary for the downlink scenario, in which a maximum of the incident signal should used in the down-conversion.

5.4.6 Radial Stubs

The radial stub is a microstrip element which provides very low impedance levels to ground for precise positions and a wide frequency range [149]. It consists of a circular conductor segment with a radius R, an enclosing angle Θ and a defined position D which can be either implemented in a serial or a shunt configuration [150]. To increase the
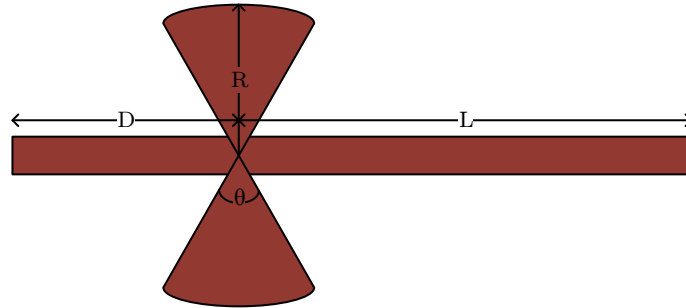
FIGURE 5.33: Geometry of a butterfly radial stub.
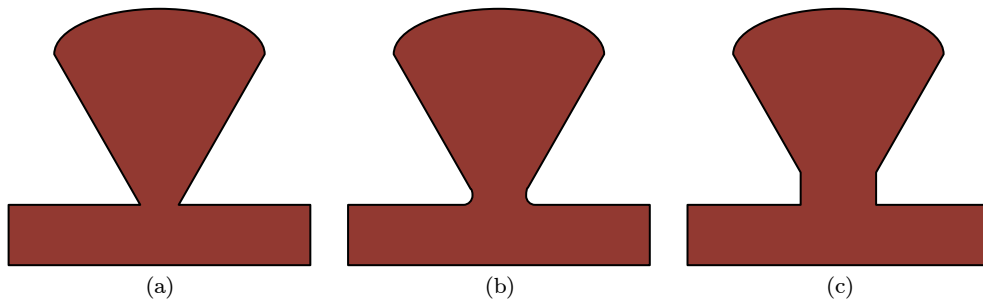
FIGURE 5.34: Influence of etching effects on the geometry of the radial stub: (a) the originally designed radial stub, (b) influences of non-perfect etching in acute angles, (c) modified geometry of the stub to avoid acute angles.

bandwidth, the shunt configuration can be extended into a butterfly configuration as shown in Figure 5.33.

There are several methods to compute analytically the impedance of these microstrip elements [149–151]. However, these formulas assume an ideal geometry. The PCB etching process can not reproduce acute angles exactly, which leads to blunt corners as shown in Figure 5.34. These remainders influence the position of the low impedance levels of the radial stub. While these can be neglected for many applications, they have to be considered for mm-wave frequencies.

To obviate this behavior, the geometry of the radial stub is modified to avoid any acute angles and, therefore, reduce the remainders of the etching process. This is achieved by inserting a rectangular conductor slab with de width W across the circular segments of the butterfly structure. The geometry of the modified radial stub is depicted in Figure 5.35.

Figures 5.36 and 5.36 compare a simulation of a radial stub with acute angles and the modified geometry. As expected, the inserted microstrip reduces the distance of the radial stub to its reference plane which decreases the reactive component. This effect
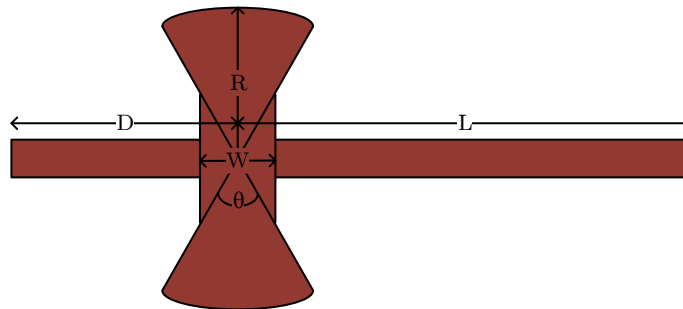
FIGURE 5.35: Dimensions of the low-pass filter with an added slab to reduce etching effects.
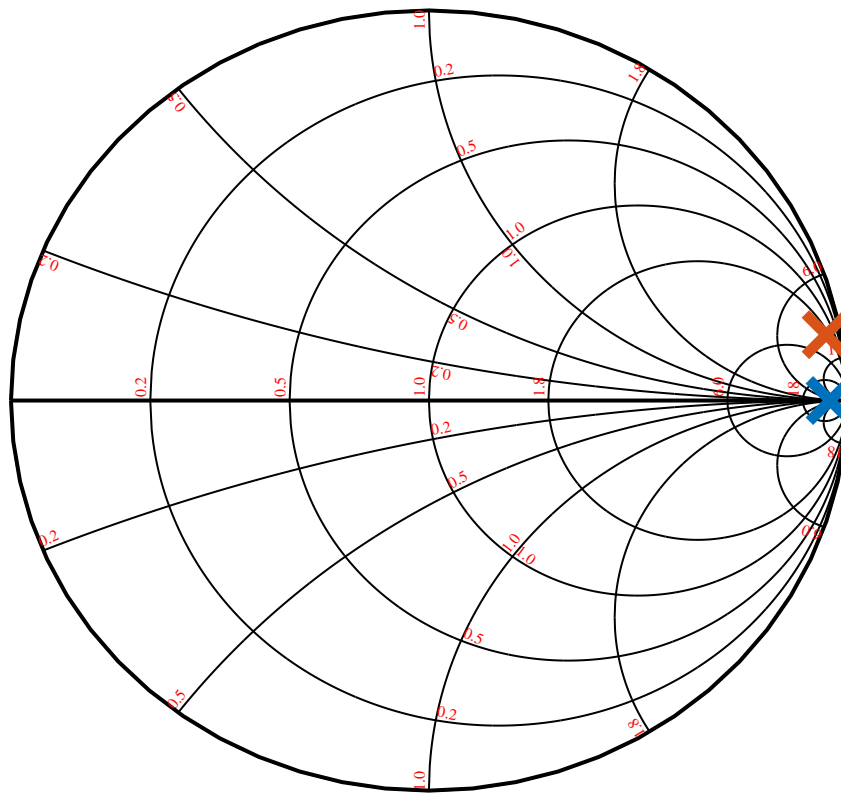
FIGURE 5.36: Reflection coefficient of a normal radial stub (blue) versus the modified version (orange).

has to be considered in the design of the open circuit by adjusting the length between the reference plane and the stub (D).

Within the mm-wave frontend, the radial stub is used at both ports of the mm-wave diode. At the anode, the radial stub provides a open circuit at mm-wave frequencies and works as a low-pass filter for the baseband signal and the biasing circuitry. At the cathode of the diode, the radial stub provides a virtual ground at mm-wave frequencies which is accompanied by a grounding via for DC and low frequencies. To provide a
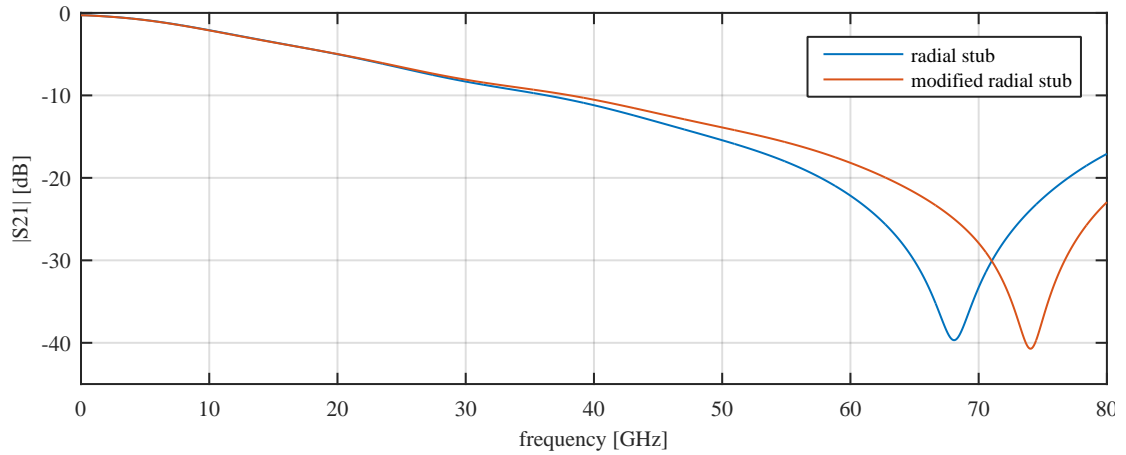
FIGURE 5.37: Simulation of the transmission coefficient of a normal radial stub versus the modified version.

variable	value for 72 GHz	value for 75 GHz
D	731 um	703 um
R	813 um	780 um
L	2000 um	2000 um
W	280 um	280 um
Θ	80 degree	80 degree

TABLE 5.7: Dimensions of the mm-wave open circuit modified radial stub.

variable	value for 72 GHz	value for 75 GHz
D	1416 um	1359.5 um
R	820 um	800 um
L	2000 um	2000 um
W	280 um	280 um
Θ	80 degree	80 degree

TABLE 5.8: Dimensions of the mm-wave virtual ground modified radial stub.

good performance for both applications, the geometry of the modified radial stub was optimized for two different oparating frequencies at 72 and 75 GHz independently using a 3D full wave simulation. The obtained values are presented in Tables 5.7 and 5.8.

Figures 5.38 and 5.39 show the measurements of the manufactured virtual ground and open on a PCB. In the reflection coefficient measurements the virtual ground shows a lower magnitude compared to the virtual open. This can be explained by the longer transmission line between the reference plane and the radial stub (D) as indicated in Tables 5.7 and 5.8. The measurement of the transmission coefficient in Figure 5.39 shows a good agreement with the simulations presented in Figure 5.37. The decrease of the matching at the resonant frequency can be again explained by the additional losses in the transmission line which have been neglected in the simulations.
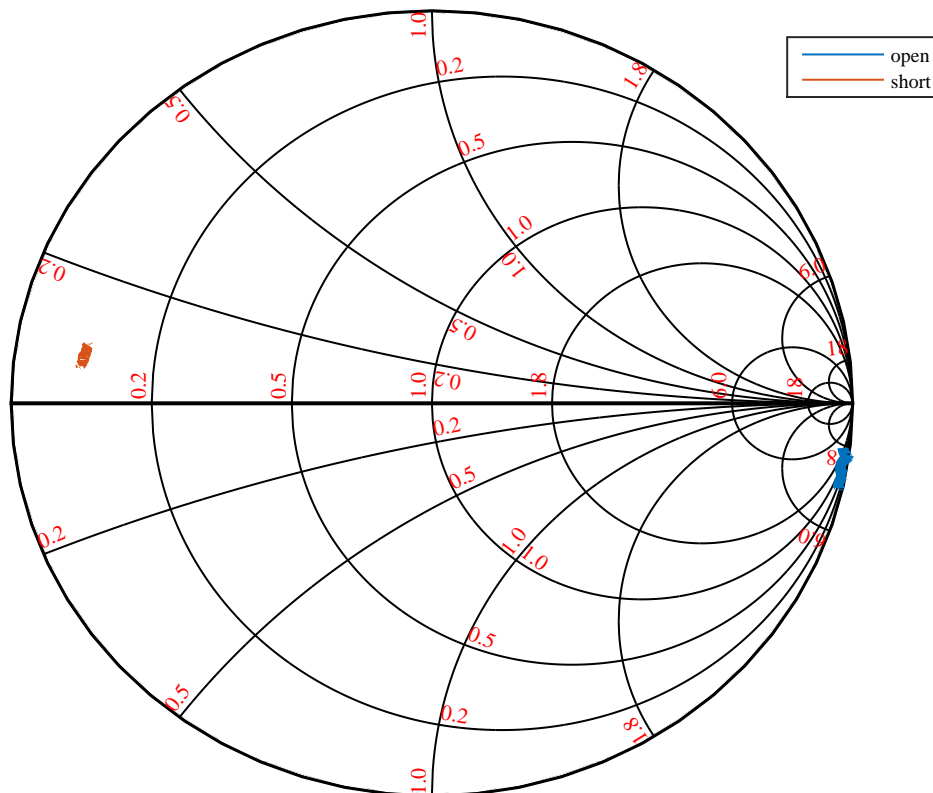
FIGURE 5.38: Measurement of the reflection coefficient of the 72 GHz virtual open (blue) and virtual ground (orange) radial stubs from 69 to 71 GHz.
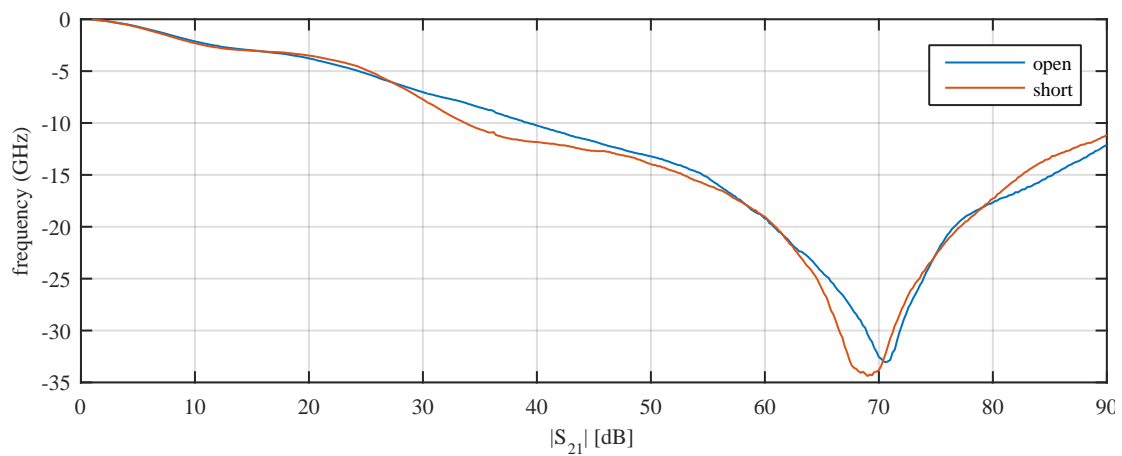
FIGURE 5.39: Measurement of the transmission coefficient of the 72 GHz open (blue) and virtual ground (orange) radial stubs.
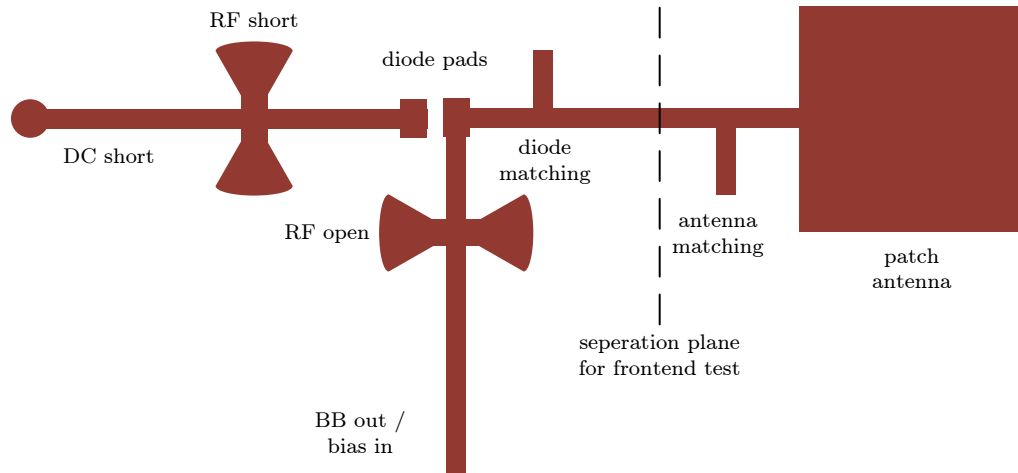
FIGURE 5.40: Assembled transponder frontend.

5.4.7 Frontend

Figure 5.40 shows the layout of mm-wave frontend of the transponder. The matching network between the antenna and the diode is connected to the anode pad of the diode. Additionally, a radial stub which is presenting an open circuit on the reference plane of the diode is connected to the same pad. This stub reflects the mm-wave signal coming from the base-station and allows only the demodulated signal to pass to the baseband module. On the cathode pad of the diode, a virtual ground connection realized by a radial stub and a via to ground provide the shunt configuration for the diode at mm-wave and baseband frequencies, respectively. The mm-wave diode is mounted on the manufactured PCB using a conductive epoxy (CW2400, [152]).

In order to evaluate the performance of the mm-wave frontend, a variation for testing has been manufactured. This variation replaces the patch antenna and its matching network by the probe launch presented in Section 5.4.2 at the separation plane shown in Figure 5.40. The measurements of the reflection modulation coefficient ($\Gamma_{Tr,TX,mod}$) on three assembled mm-wave frontends are presented in Figure 5.41. All three samples show a maximum between 72.5 and 73 GHz. The amplitude of the reflection modulation between 0.35 and 0.45, which is lower than the results expected from the simulations in Section 5.4.5. This difference can be explained by the losses on the PCB, which have not been taking into account by the simulations. The variation between the samples is caused by the manual mounting of the diodes onto the PCB, as well as through production variations of the PCB manufacturer.
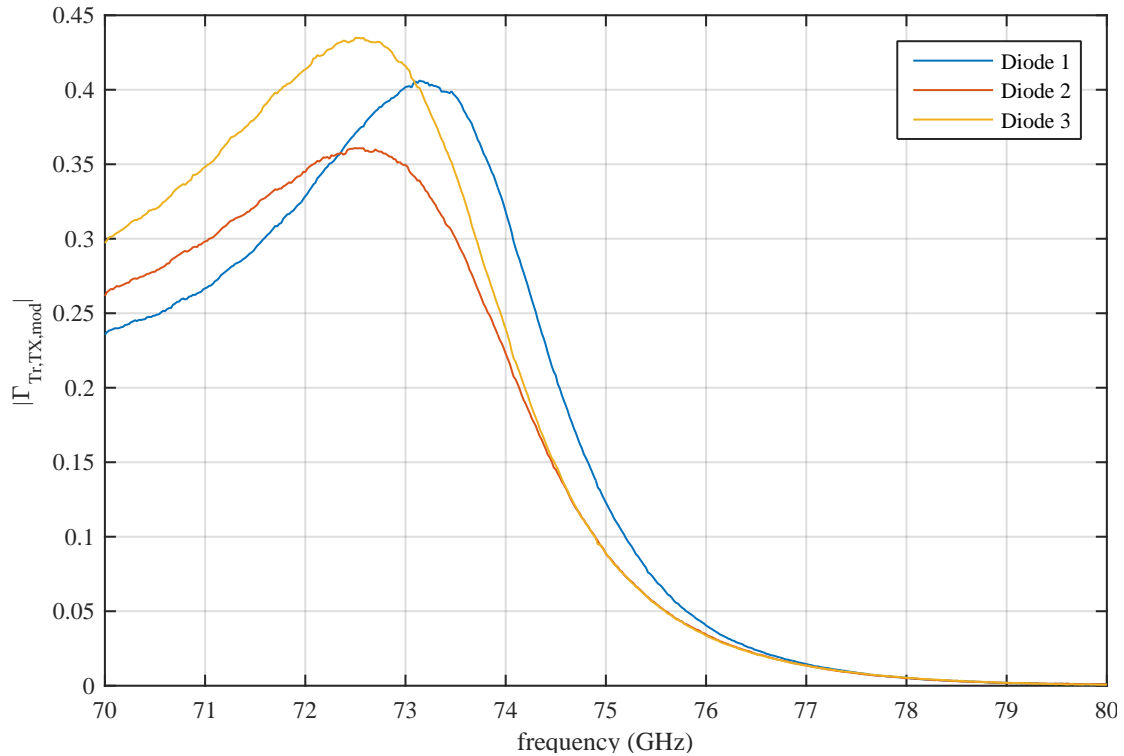
FIGURE 5.41: Results of the backscatter modulation measurements of the mm-wave frontend.

5.5 Conclusions

In this Chapter the design of a MMID transponder is discussed. The final prototype implements the full EPC-Gen2 protocol using a baseband chip from NXP Semiconductors. The mm-wave frontend of the transponder incorporates a patch antenna with a gain of 9.75 dBi and a half-power-beamwidth of 87.3 degree. This wide beamwidth ensures a robust communication while maintaining a reasonable gain which plays a significant role in the link budget of both, the down- and uplink scenario. The mm-wave diode in the frontend provides sufficient envelope detection capabilities for the downlink communication with a peak-to-peak amplitude of 3 mV for an input power of -3 dBm. In the uplink scenario, the reflection modulation coefficient up to 0.45 exceeds the performance reported in the literature [131].

Chapter 6

System Performance

In this chapter, the three distinct components of the MMID system, the transmission channel, the base-station, and the transponder, which were discussed in Chapters 3 to 5, are assembled together. To verify the performance of the complete system, two different measurements are carried out: a downlink and an uplink measurement scenario. The downlink measurement scenario, evaluates the detection capabilities of the amplitude modulated commands from the base-station at the transponder. The uplink measurement scenario focuses on the performance of the backscatter communication.

Figure 6.1 shows a photograph of the MMID System. On the table on left side, the base-station is built up. The mm-wave frontend of the base-station is mounted on a small bench vice with ball joint which allows an easy alignment of the antennas. The transponder is set on a movable support at a distance d apart from the base-station.

6.1   Downlink

To evaluate the performance of the MMID system in the downlink communication from the base-station to the transponder, an oscilloscope (OSC) was connected in parallel to the transponder baseband unit as shown in Figure 6.2. Additionally to the oscilloscope, a signal analyzer (SA) equiped with an external mixer (MIX) probes the signals coming from the base-station. During the measurements, the base-station sends every 10 ms the EPC Gen2 query command (see Figure 4.17) towards the transponder. The mm-wave frontend of the transponder demodulates the commands and passes it to its baseband
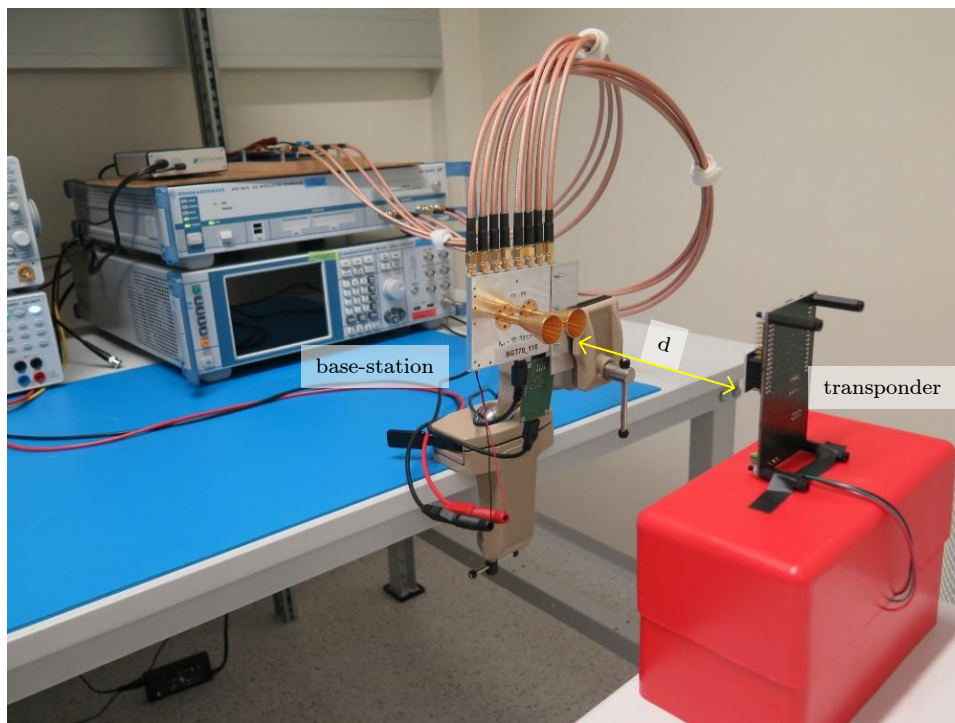
FIGURE 6.1: Picture of the MMID System.
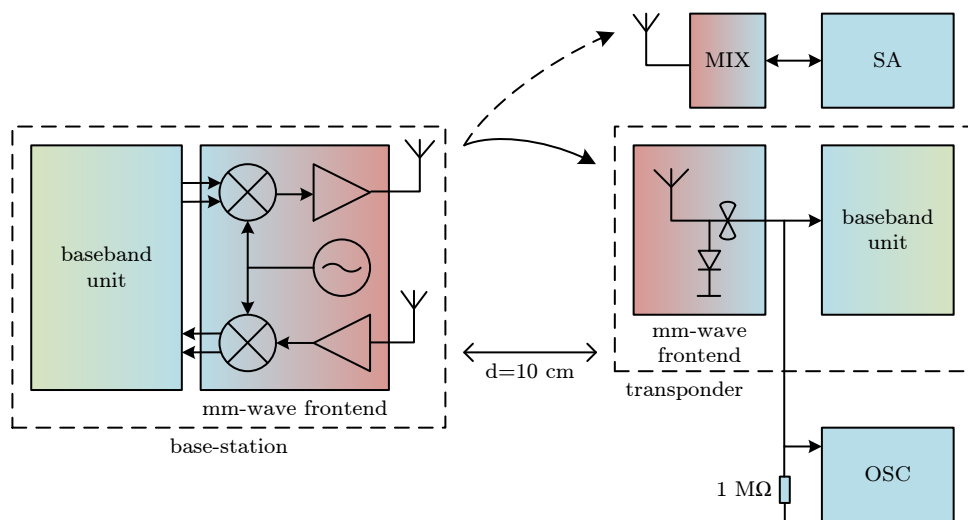
FIGURE 6.2: Setup of the downlink measurements.

unit. The demodulated response is then captured by the oscilloscope with an high-impedance probe, which ensures a minimum influence of the measurement setup onto the MMID transponder. The signal analyzer is tuned to the carrier frequency of the base-station and operated in zero-span mode.

Figures 6.3 and 6.4 show the results of the downlink measurements in the time-domain for a carrier frequency of 71.75 GHz. The signal coming from the base-station, which
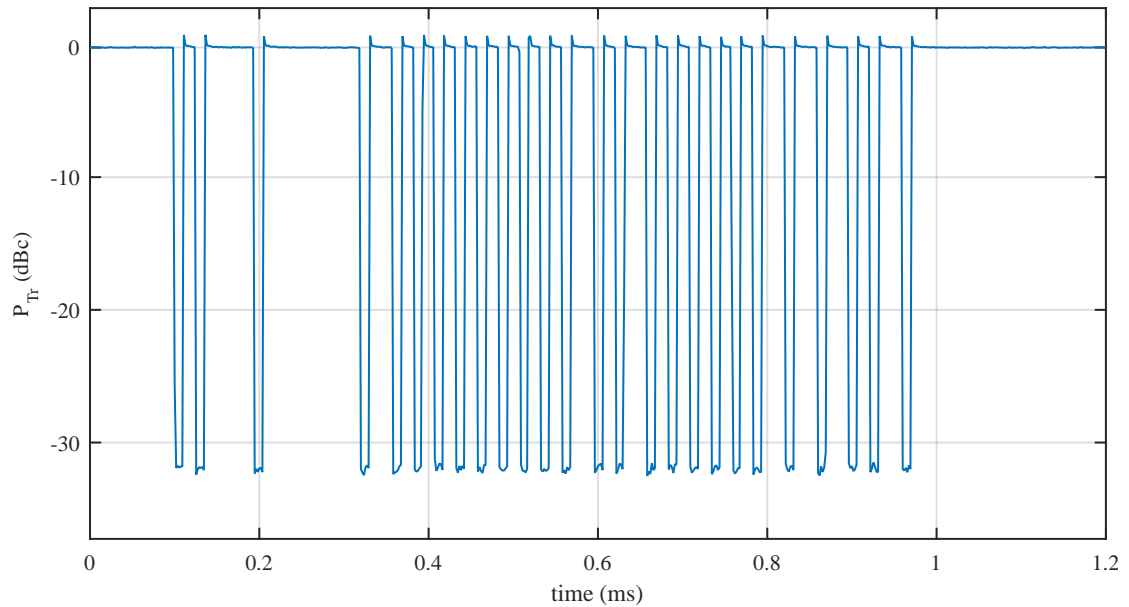
FIGURE 6.3: Time-domain results of the base-station signal at the transponder.
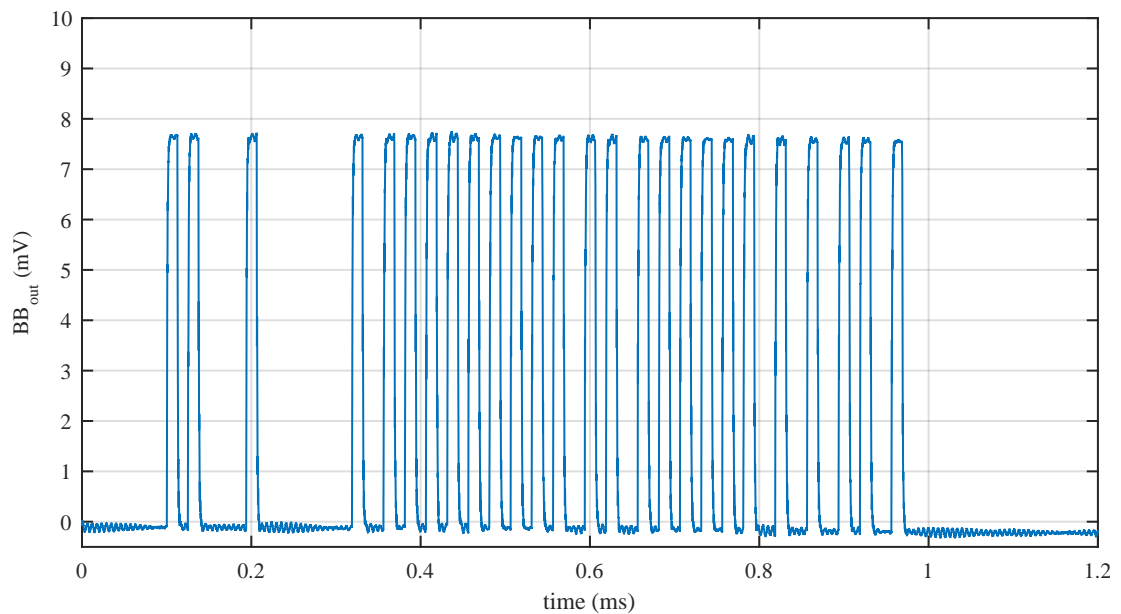
FIGURE 6.4: Time-domain results of the envelope detection in the downlink measurements.

was measured with the signal analyzer, shows a modulation depth of more than 30 dB. The demodulated base-band signal (BB_{out}) of the mm-wave diode, which is biased via a 2.5 kΩ resistor, shows a peak-to-peak amplitude of 8 mV amplitude. In order to provide a stable triggering the scope was operated with a DC coupling. The measured signal was subtracted from the the bias voltage, which results in an inverted representation inf Figure 6.4.

Figure 6.5 shows a sweep of the carrier frequency while observing the amplitude of the
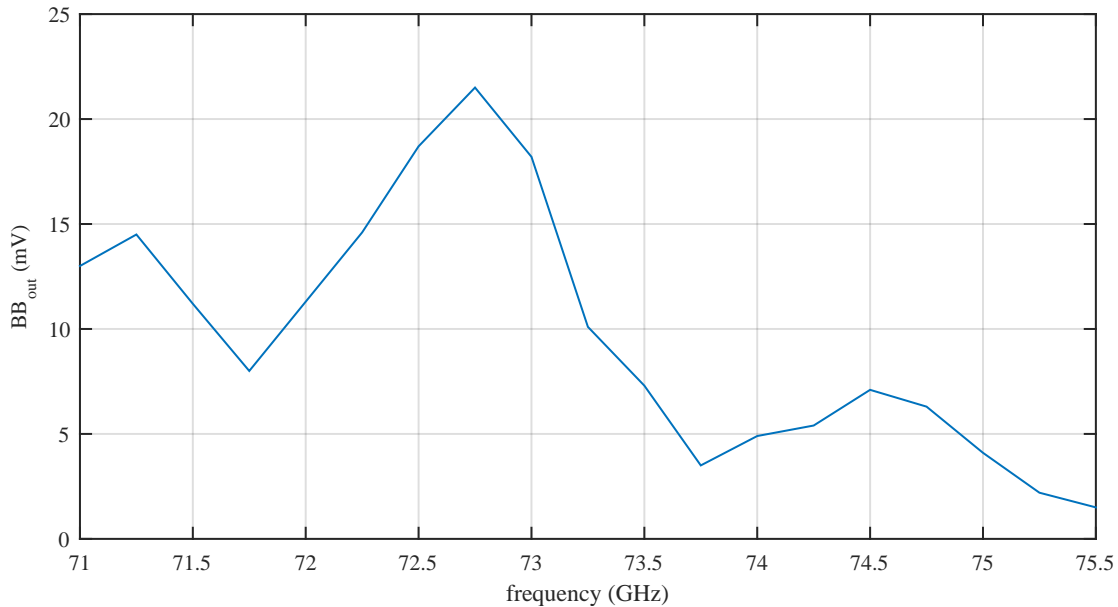
FIGURE 6.5: Results of the envelope detection in the downlink measurements for different carrier frequencies.

envelope detection. The transponders mm-wave frontend shows a maximum conversion gain at $72.75\,\mathrm{GHz}$ with a peak-to-peak amplitude of $21.5\,\mathrm{mV}$. The optimum frequency for the demodulation aligns with the results presented in Figure 5.41. Variations between different boards are caused by the manual diode mounting process.

6.2 Uplink

For the evaluation of the uplink scenario the baseband unit of the transponder is replaced by a waveform generator which biases the mm-wave diode with a square wave signal. The fundamental frequency of the signal is $160\,\mathrm{kHz}$, which is equivalent to the link frequency of the response of transponder to the EPC Gen2 query command. This modification of the MMID system allows an easier evaluation of the uplink communication by presenting an easily trigger-able and repetitive signal, as the response of the transponder to the query command includes a random number which is calculated individually for each request. During the measurements, the transmitter of the base-station constantly transmits a CW at the carrier frequency. The transponder modulates the carrier with the square-wave signal, and the base-station receiver translates the signal into the baseband. A block diagram of the uplink measurement setup is presented in Figure 6.6.
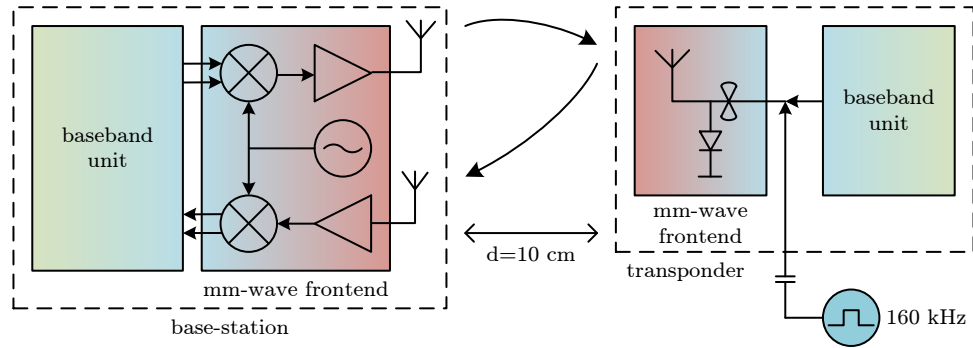
FIGURE 6.6: Setup of the uplink measurements.
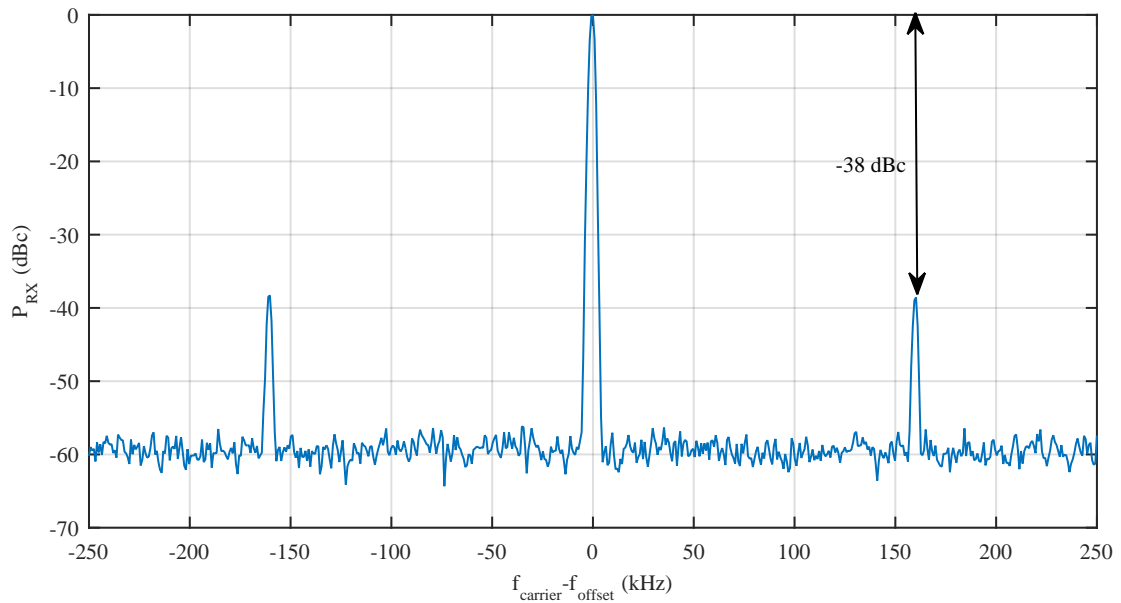
FIGURE 6.7: Results of the received power measurements of the back-scatter uplink.

Figure 6.7 shows a normalized frequency domain representation of the captured baseband signal at 10 MHz for a carrier frequency of 72.5 GHz. The sub-carrier containing the transponders response at an offset frequency of 160 kHz is at a level of -38 dBc and about 20 dB above the noise floor of the system. Using the FSPL formula which gives a loss of 50 dB for a distance of 10 cm, a maximum reading range of 1 m can be predicted before the sub-carrier is below the noise floor.

Similar to the downlink evaluation, a carrier sweep was performed to find the optimum operating frequency of the transponders backscatter modulation.

Figure 6.8 shows, that a maximum performance is achieved at 72.5 GHz which matches the measurements of the downlink.
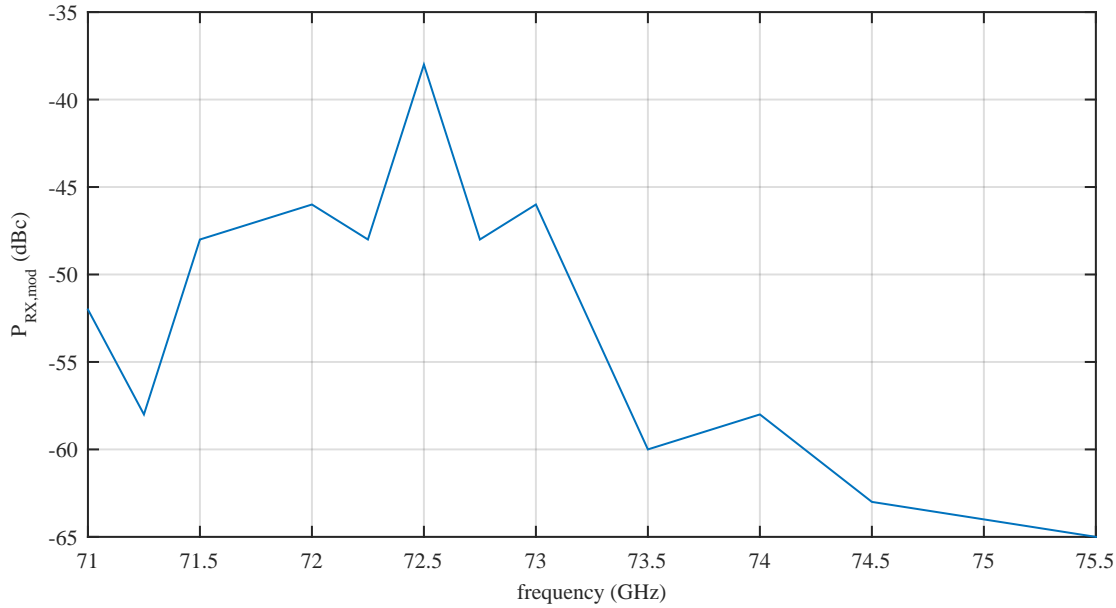
FIGURE 6.8: Results of the received power measurements of the back-scatter uplink for different carrier frequencies.

During the downlink measurements in Section 6.1, a high phase noise of the base-station transmitter was observed, which is caused by the high multiplication factor in the LO chain ($\times 64$). To evaluate the impact of the phase noise on the performance of the base-stations receiver a measurement was carried out, which compares the received signal coming from the base-stations transmitter with one from a low-noise source. Figure 6.9 shows the concept of this measurement. Both the base-station transmitter and the low-noise source Rohde&Schwarz SMF100A signal generator (SG) with a Rhode&Schwarz SMZ90 multiplier (x6) transmit their carrier signal on a metal sheet. The reflected signal is than captured by the base-station receiver and converted into the frequency domain. The resulting measurements are shown in Figure 6.10. While the low phase noise signal of the SMZ90 is convoluted with the phase noise of the LO, the signal of the base-station transmitter (BGT70) shows a much lower phase noise. This can be explained by the cancellation of the coherent phase from transmitter and receiver which share the same LO in the base-station mm-wave frontend [153]. This cancellation only works effectively for close targets with a short time of flight below the phase noise coherence time of the LO. For predicted reading ranges of the MMID system up to 1 m this requirement is met.
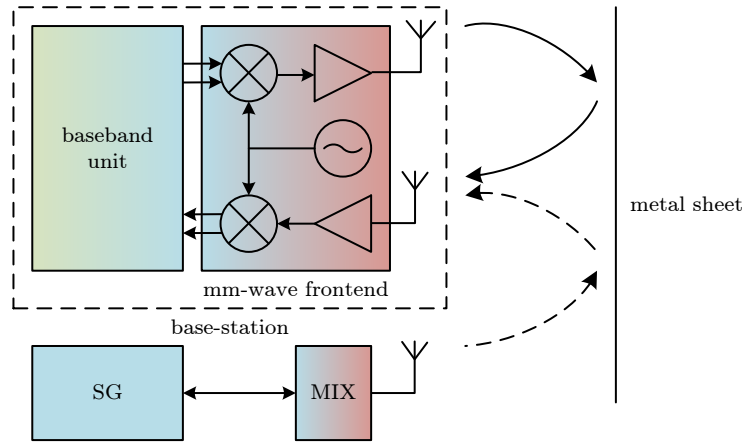
FIGURE 6.9: Measurement setup to evaluate the phase nosie performance of the MMID uplink.
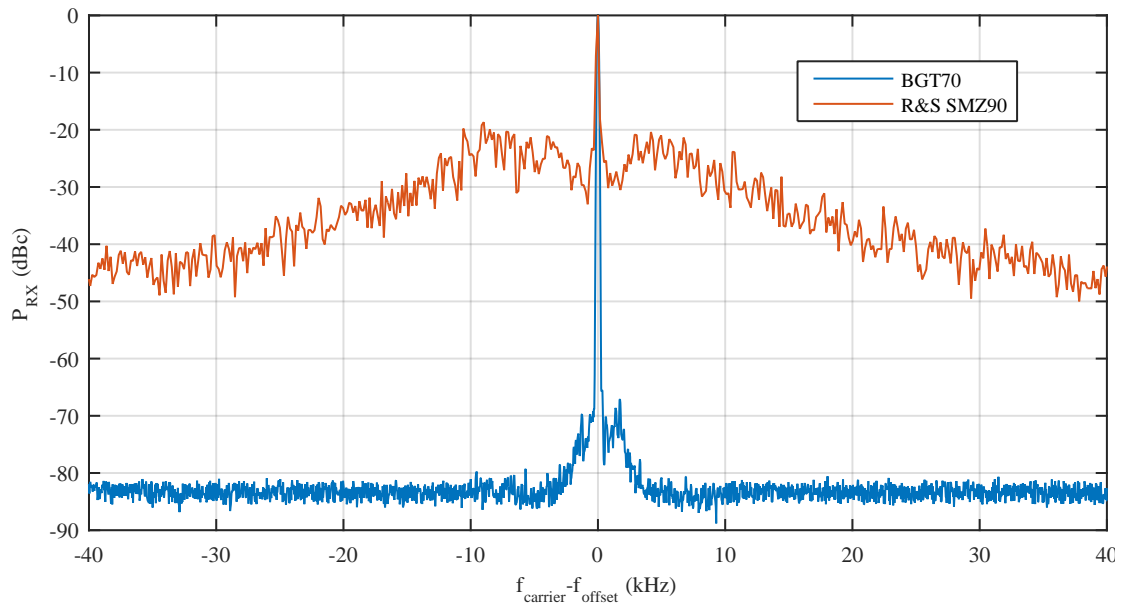
FIGURE 6.10: Results of the investigations on the phase nosie performance of the MMID uplink.

6.3   Conclusions

In this Chapter, the evaluation of the full MMID System including the base-station, the transmission channel, and the transponder is discussed. The measurements show that for both communication scenarios, the down- and the uplink, the optimum carrier frequencies match. In the downlink communication, the system provides signal levels up to $21.5\,\text{mV}$ at at a reading distance of $10\,\text{cm}$ at the baseband output of the transponders mm-wave frontend. In the uplink scenario, the backscattered signal of the transponder at a distance of $10\,\text{cm}$ is about $30\,\text{dB}$ above the noise floor of the base-station receiver.

These numbers suggest, that an operation of the presented MMID system is feasible for reading distances up to 1 m.

Chapter 7

Summary

The Internet of Things is a huge driving factor in the development of wireless communication devices, due to it's predicted economic impact. With the vision of connecting all items into a global network, new challenges to communication frontends arise. Among them are the demand for low power consumption, high data rates, and the reduction of the dimensions of the antennas. One potential candidate to cater the needs of an IoT system is radio frequency identification. This technology provides a very low power communication frontend and processing capabilities which can be operated in a battery-less transponder, which is only powered wirelessly by the base-station. However, RFID provides only low data-rates and due to its operating frequency, the antennas are rather large. A translation of RFID into the mm-wave frequency regime enables the backscatter communication technology to overcome these issues.

Within this thesis, a demonstrator for mm-wave identification (MMID) which is supporting the EPC Gen2 communication protocol was developed. The demonstrator consists of three main components: the base-station, the transponder, and the transmission channel which connects the previous ones with each other. In a first step, the operation principle of the communication system was derived from a signal flow graph in order to identify the building blocks of each component with the highest impact on the overall performance. In a second step, a simulation environment was created which allows the evaluation of the building blocks within the context of the MMID system. In order to provide realistic data for the transmission channel which connects the base-station and the transponder over the air, an extensive measurement campaign was carried out.

Three different measurement scenarios showed that the free space loss model is sufficient for a first analysis of the MMID performance. However, there are effects, such as multipath propagation, which have to be taken into account for a detailed analysis.

The presented base-station is divided into three main building blocks. A digital baseband processor, which is realized in MATLAB®, an analog baseband unit, and a mm-wave frontend. The analog baseband unit supports modulation schemes up to a bandwidth of 120 MHz and contains a variable gain amplifier which adapts the received signal level to the distance of the targeted transponder. The mm-wave frontend provides a direct-conversion IQ-modulator for the up and down conversion of the analog baseband signals to a frequency range of 71 to 76 GHz with a transmitted EIRP of 34 dBm and a minimum detectable signal of -100 dBm at the receiver. To improve the performance of the transmitter, an imbalance analysis and compensation was carried out.

The battery backed transponder consists of two building blocks: On the one hand, a mm-wave frontend, which demodulates the PIE commands from the base-station and modulates the response onto the base-station carrier using backscatter modulation. In order to ensure a good performance of the mm-wave frontend, an extensive analysis and optimization of its components was carried out. For this purpose, a custom PCB launch pad for probe tips which works up to 90 GHz was designed. This launch pad enables a reliable and consistent measurements. On the other hand, a baseband unit which employs a EPC Gen2 compatible baseband chip and additional circuitries, which interface the chip towards the mm-wave frontend. The assembled transponder shows a good performance in terms of the detection of the base-station signals and allows a backscatter modulation with a modulation depth of up to 40%.

To conclude this work, an evaluation of the system performance was performed at a distance between the base-station and the transponder of 10 cm. In this setup, the transponder shows a demodulated signal amplitude of up to 21 mV at the baseband output of the mm-wave frontend. The signal received by the base-station shows a signal level of -38 dBc. These numbers suggest that the presented demonstrator is capable to provide a EPC Gen2 compatible communication link up to distances of 1 m.

7.1   Outlook

Throughout this thesis functional MMID system, which demonstrates a EPC Gen2 compatible communication, was developed. However, there are several tasks which could not be carried out within the time-frame or which were out of the scope of this thesis:

Detailed evaluation of the MMID demonstrator performance

Within this thesis a first evaluation of the performance of the MMID demonstrator is given in Chapter 6. However, to thoroughly identify the bottlenecks of backscatter communication further measurements and analysis have to be taken. These investigations should include the full EPC Gen2 communications stack, different modulation bandwidths, various distances and angles between base-station and transponder, and various challenging environments including non-LOS communication scenarios.

Developing applications on top of the MMID demonstrator

The current implementation of the MMID demonstrator provides a flexible platform for the exploration of different applications. The software defined radio baseband unit and the versatile mm-wave frontend of the base-station allow the generation of complex modulation schemes which can be up-converted into a broad frequency range. The transponder on the other side allows an easy integration of new mm-wave frontends which incorporate different antenna topologies. With this platform, applications such as highly accurate localization and identification of items, or motion tracking could be achieved.

Implementation of the base-stations digital baseband unit in an FPGA

At the moment, the implementation of the digital baseband unit via a MATLAB$^{\circledR}$ script does not allow a EPC Gen2 compatible communication which reaches beyond a simple query command and its response. The limiting factor are the timing requirements of the standard which demand a reaction to the transponders response within 0.5 ms. In order overcome this shortcoming, the basband unit should be implemented in a field programmable gate array (FPGA). In this way it is possible to meet the EPC Gen2 link timing requirements, while maintaining a maximum degree of flexibility. There are already several implementations reported in the literature [154–157] which prove the feasibility of such an implementation.

Imbalance analysis and compensation of the base-station receiver

During the development of the MMID base-station, an in-depth analysis of the transmitter imbalance of the mm-wave frontend was conducted. An equivalent analysis of the receiver, however, was not accomplished. In order to push the limits of the MMID system, an investigation of the non-idealities of the base-station receiver should be carried out. [116] gives a detailed description on the necessary algorithms and measurements.

Implementation of a phased array at the base-station

In order to fully exploit the advantage of small sized antennas at the base station, a phased array for transmitter and receiver can be build. Such a steerable antenna would enable additional applications for MMID systems, such as angular resolution for localization. Additionally, the reading distance can be increased by pin pointing the transponder with high gain, narrow beam-width antennas.

Integration of the transponder in a single ASIC

The current implementation of the transponder does not allow a fully passive MMID system, as it requires high power in order to operate the baseband unit. Additionally, the setup with separate baseband and mm-wave frontend boards does not exploit the scalability of the transponder with the higher carrier frequency. To accomplish these goals, it is necessary to integrate the mm-wave frontend of the transponder together with its baseband unit into a single ASIC. A feasibility study on the implementation of a MMID transponder on a 65 nm CMOS process is shown in [47].

Appendix A

Implementation of the Base-Station Baseband Amplifier

On the following pages, the schematics for the baseband amplifier of the MMID base-station as presented in Section 4.6 are shown. Figure A.1 shows the interface ports of the baseband amplifier including the DIP switches for the gain control. Figures A.2 to A.4 show the three stages of the baseband amplifier including input, inter-stage and output matching as well as the equalizing network. Figure A.5 shows the power supply unit which derives all required voltage domain from a 12 V and a 5 V external power supply.
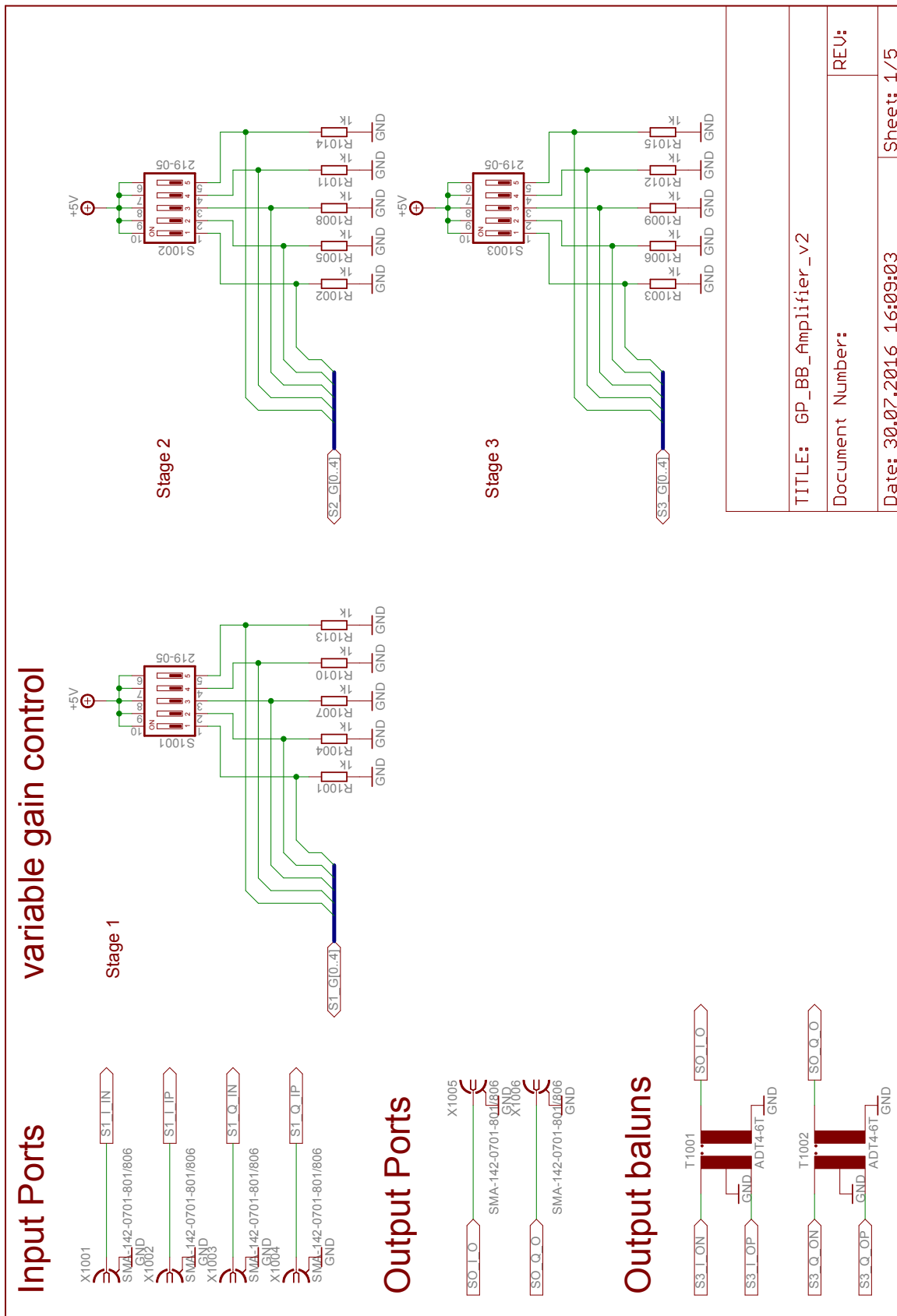
FIGURE A.1: External interfaces of the baseband amplifier
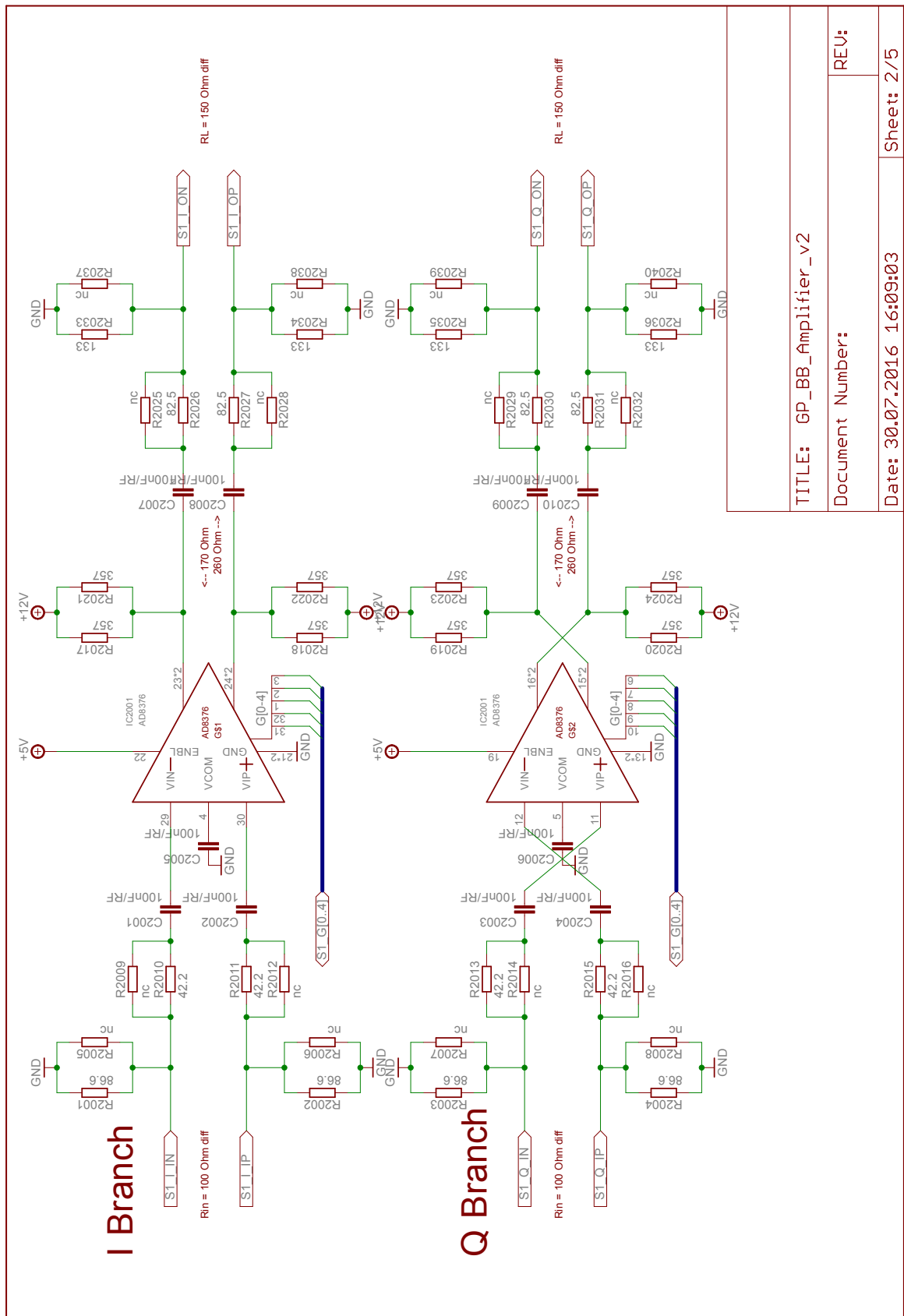
FIGURE A.2: First stage of the baseband amplifier
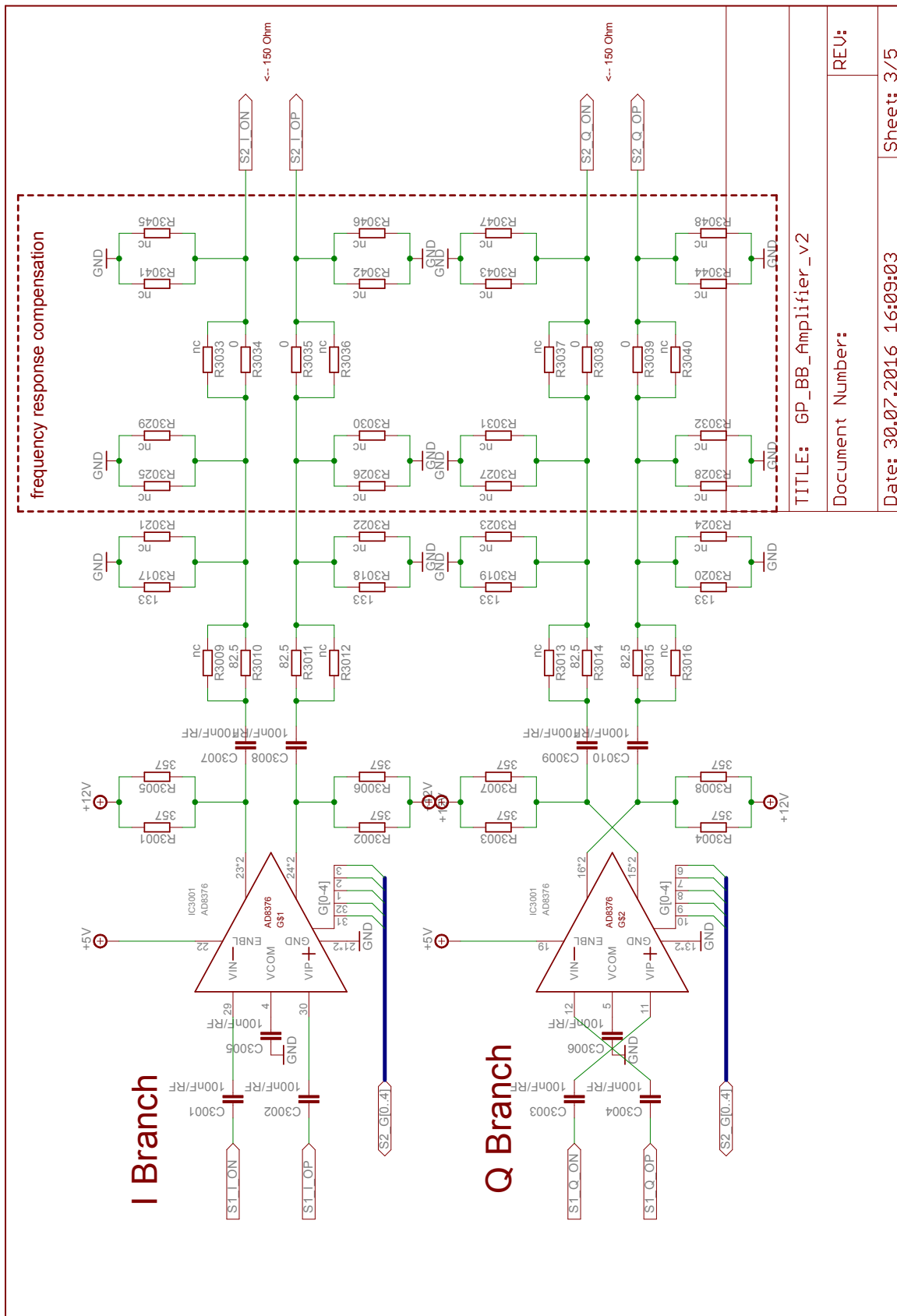
FIGURE A.3: Second stage of the baseband amplifier
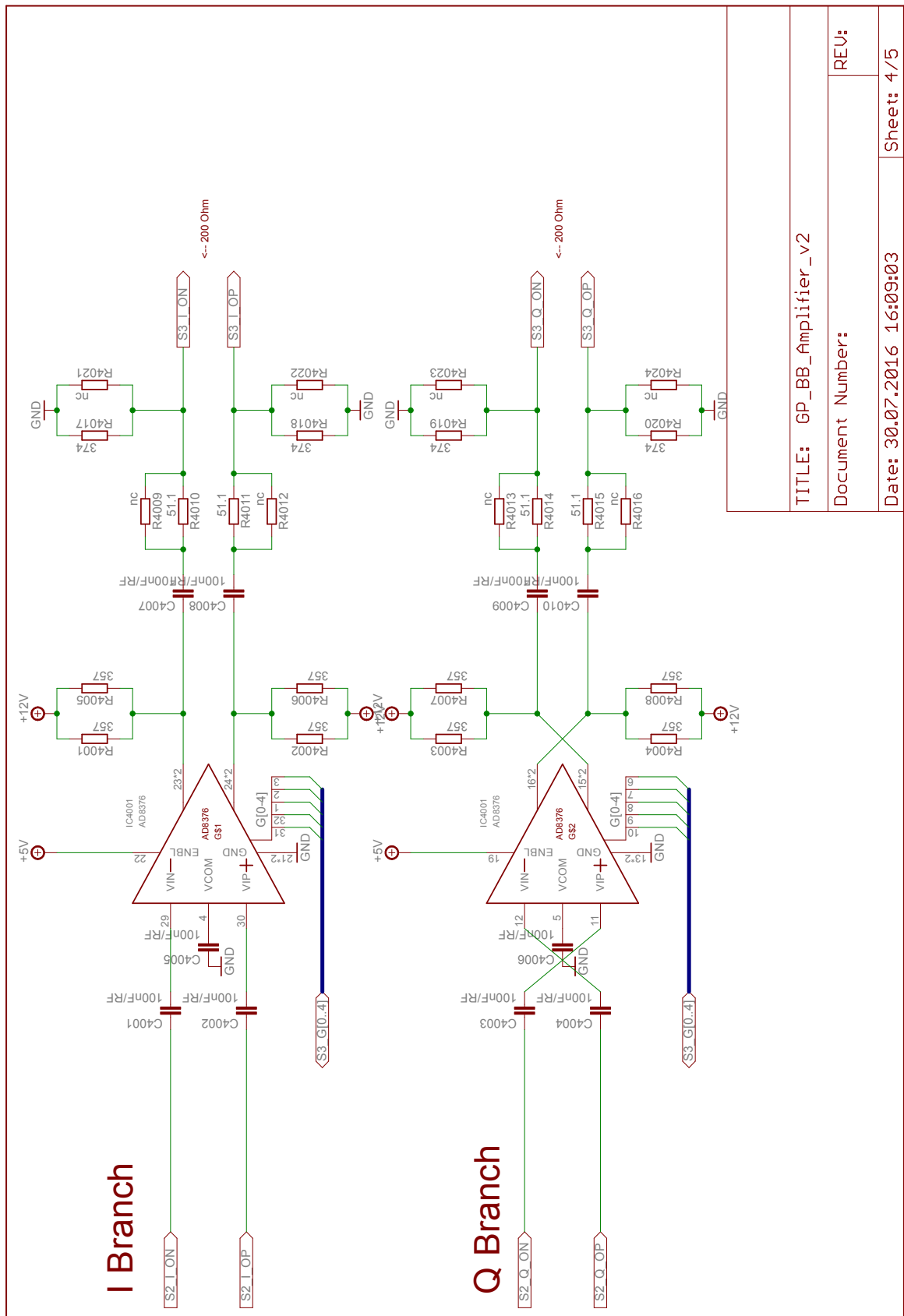
FIGURE A.4: Third stage of the baseband amplifier
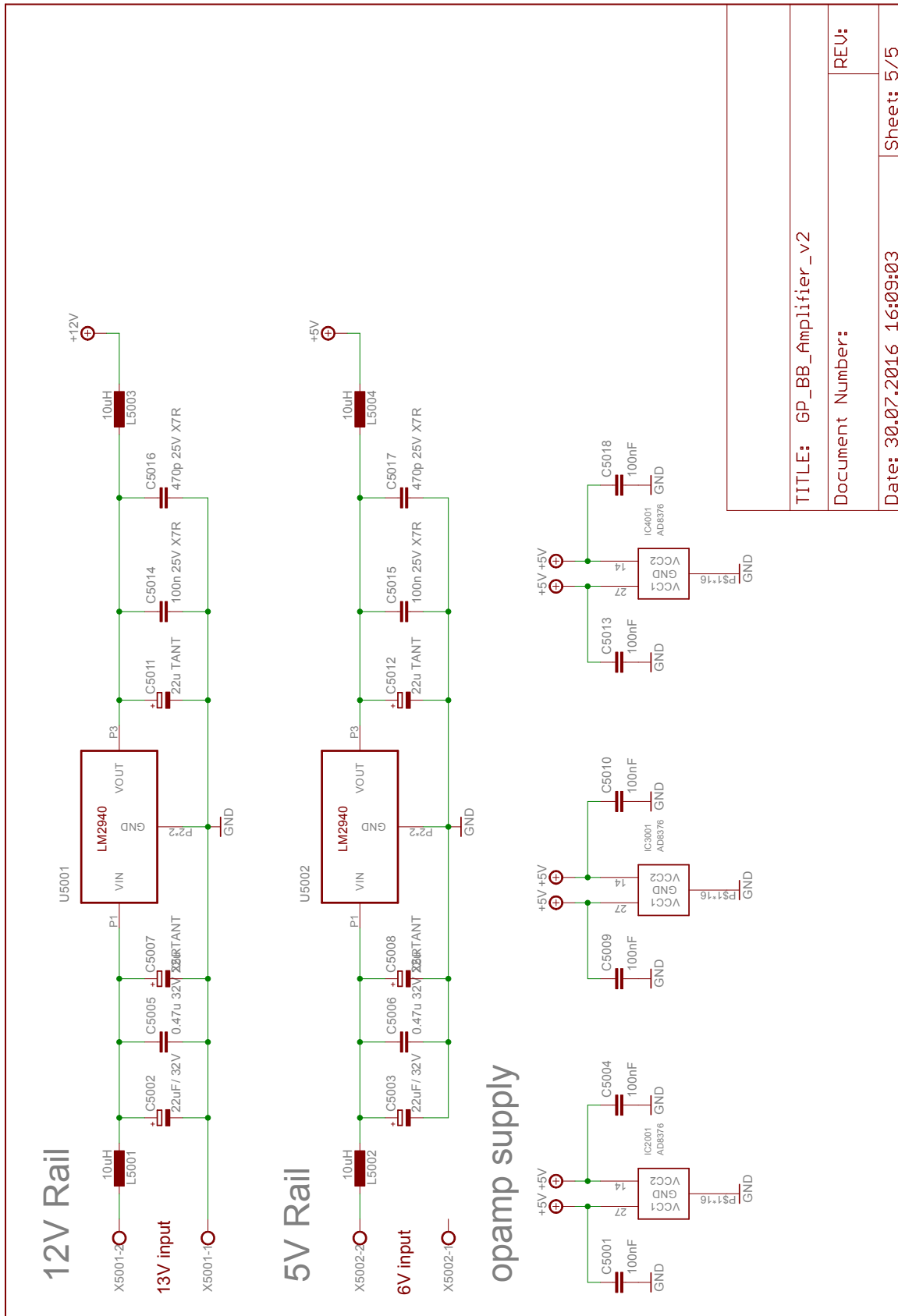
FIGURE A.5: Power supply of the baseband amplifier

Appendix B

Schematics of the Transponder Baseband Unit

The schematics of the baseband unit of the MMID transponder presented in Section 5.3 are shown in on the following pages. Figure B.1 shows the switching logic which separates the receive and transmit mode of the EPC Gen2 baseband chip from the mm-wave frontend. Figure B.2 shows the biasing circuitry for the mm-wave diode, the input stage responsible for the level adaption, and a reset functionality for the swtiching logic. Figure B.3 shows the power supply unit which derives the necessary voltages from an external ± 5 V supply.
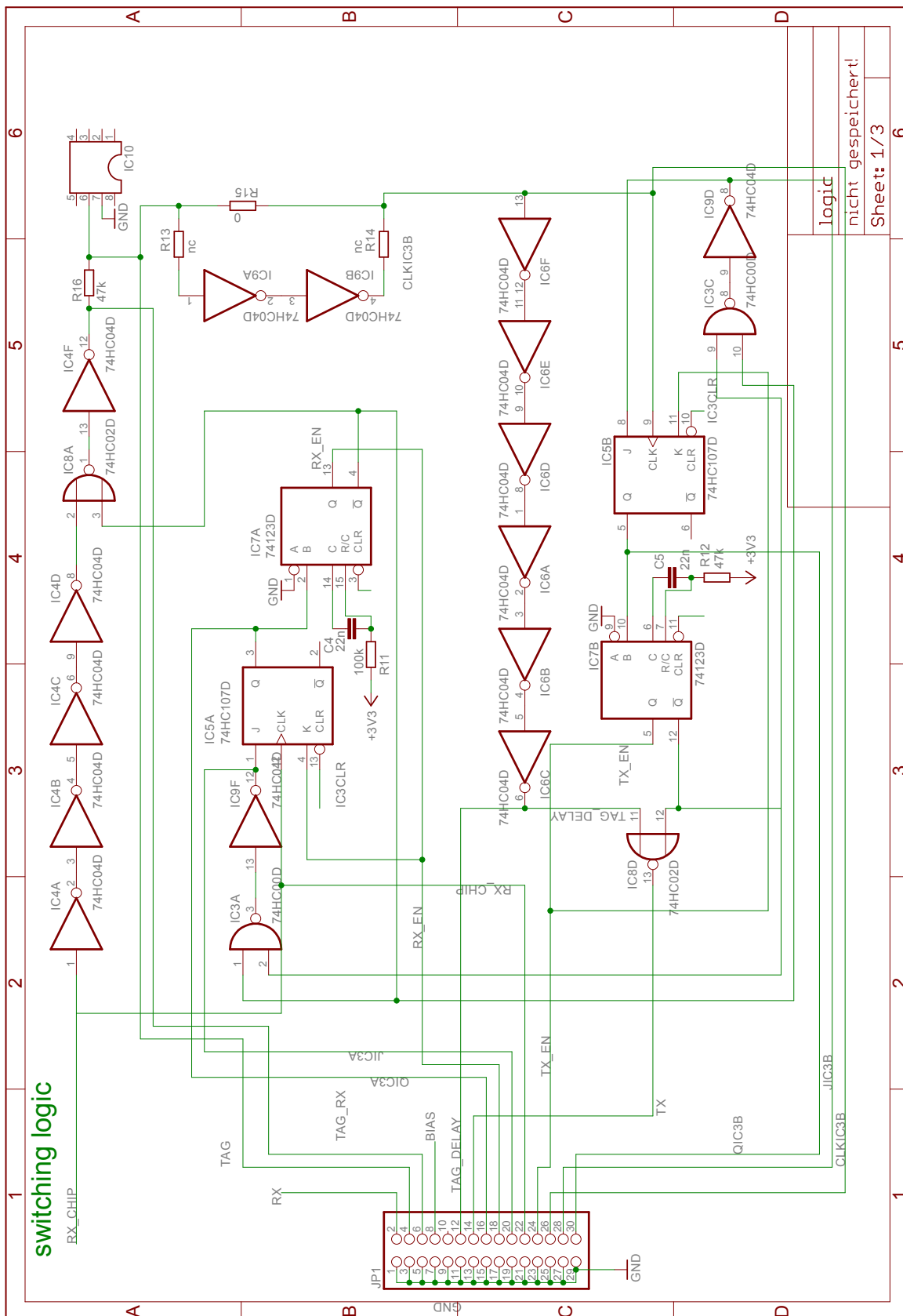
FIGURE B.1: Switching logic of the transponder baseband unit
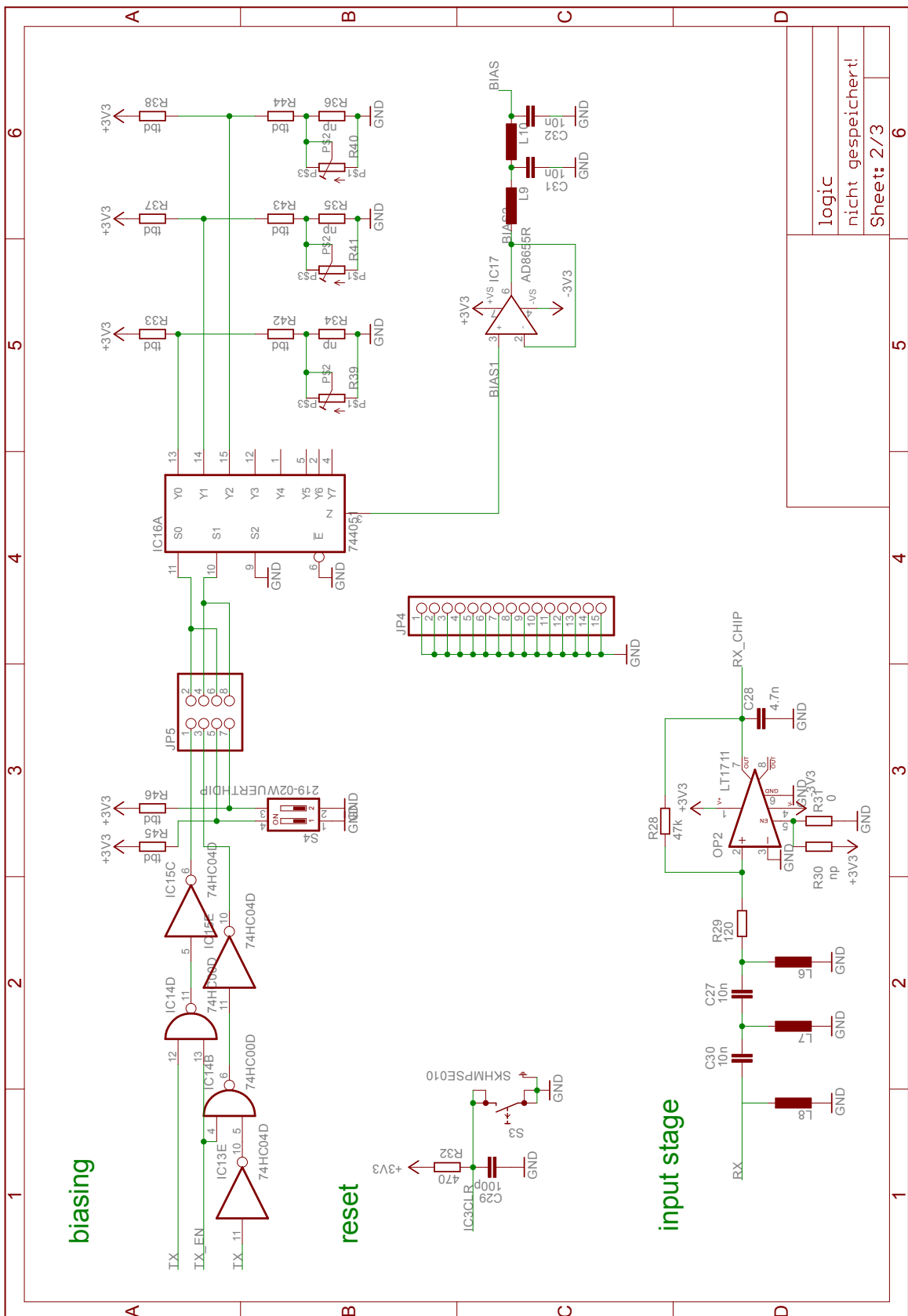
FIGURE B.2: Biasing circuitry and input stage of the transponder baseband unit

FIGURE B.3: Power supply of the transponder baseband unit

Bibliography

[1] T. Pratchett. (2005, 5) Collegiate Casting-Out of Devilish Devices. [Online]. Available: https://www.timeshighereducation.com/features/a-collegiate-casting-out-of-devilish-devices/195991.article

[2] K. Ashton. (2009, 6) That 'Internet of Things' Thing. [Online]. Available: http://www.rfidjournal.com/articles/view?4986

[3] K. Rose, S. Eldridge, and L. Chapin, "The Internet of Things: An Overview," *Internet Society*, 10 2015.

[4] J. Rivera and R. van der Meulen. (2013) Gartner Says the Internet of Things Installed Base Will Grow to 26 Billion Units By 2020. [Online]. Available: http://www.gartner.com/newsroom/id/2636073

[5] J. Greenough. (2015) How the 'Internet of Things' will impact consumers, businesses, and governments in 2016 and beyond. [Online]. Available: http://www.businessinsider.de/how-the-internet-of-things-market-will-grow-2014-10

[6] J. Manyika, M. Chui, P. Bisson, J. Woetzel, R. Dobbs, J. Bughin, and D. Aharon. (2015) Unlocking the potential of the Internet of Things. [Online]. Available: http://www.mckinsey.com/business-functions/business-technology/our-insights/the-internet-of-things-the-value-of-digitizing-the-physical-world

[7] H. Tchofenig, J. Arkko, D. Thaler, and D. McPHerson, "Architectural Considerations in Smart Object Networking," Internet Requests for Comments, Internet Architecture Board, RFC 7452, Jul. 2015. [Online]. Available: http://www.rfc-editor.org/rfc/rfc7452.txt

[8] A. Al-Fuqaha, M. Guizani, M. Mohammadi, M. Aledhari, and M. Ayyash, "Internet of Things: A Survey on Enabling Technologies, Protocols, and Applications," *IEEE Communications Surveys Tutorials*, vol. 17, no. 4, pp. 2347–2376, 2015.

[9] *EPC Radio-Frequency Identity Protocols Generation-2 UHF RFID*, GS1 Std.

[10] T. Kamina, T. Aoki, Y. Eto, N. Koshizuka, J. Yamada, and K. Sakamura, "Verifying Identifier-Authenticity in Ubiquitous Computing Environment," in *21st International Conference on Advanced Information Networking and Applications Workshops (AINAW)*, vol. 2, May 2007, pp. 403–408.

[11] S. Deering and R. Hinden, "Internet Protocol, Version 6 (IPv6) - Specification," Internet Requests for Comments, Internet Engineering Task Force , RFC 2460, Dec. 1998. [Online]. Available: http://www.rfc-editor.org/rfc/rfc2460.txt

[12] M. Gigle and S. Koo, "Internet of Things: Services and Applications Categorization," *Advances in Internet of Things*, vol. 1, no. 2, pp. 27–31, 2011.

[13] X. Xiaojiang, W. Jianli, and L. Mingdong, "Services and Key Technologies of the Internet of Things," *ZTE Communications*, vol. 8, no. 2, 2010.

[14] G. Reiter, "Wireless connectivity for the Internet of Things," Texas Instruments, White Paper, 6 2014. [Online]. Available: http://www.ti.com/lit/wp/swry010/swry010.pdf

[15] *Radio Regulations*, ITU Std., 2012.

[16] *Wireless LAN Medium Access Control (MAC) and Physical Layer (PHY) Specifications*, IEEE Std. 802.11, 2012.

[17] *Enhancements for Very High Throughput in the 60 GHz Band*, IEEE Std. 802.11ad, 2012.

[18] *Bluetooth Specification Version 4.2*, Bluetooth SIG Std., 2014.

[19] *Short range narrow-band digital radiocommunication transceivers - PHY, MAC, SAR and LLC layer specifications*, IUT Std. G.9959, 2015.

[20] *IPv6 over Low-Power Wireless Personal Area Network (6LoWPAN)*, IETF Std. 8066, 2017.

[21] *Low-Rate Wireless Personal Area Networks (LR-WPANs)*, IEEE Std. 802.15.4, 2011.

[22] H. Stockman, "Communication by means of reflected power," *Proceedings of the IRE*, vol. 36, no. 10, pp. 1196–1204, Oct 1948.

[23] K. Finkenzeller, *RFID Handbook: Fundamentals and Applications in Contactless Smart Cards, Radio Frequency Identification and Near- Field Communication*, 3rd ed.   John Wiley & Sons, L td., 2010.

[24] M. Meints, M. Gasson, P. Rotter, S. Fischer-Hübner, D. Gille, J. Strüker, S. Wohlgemuth, M. Hansen, and G. Karjoth, "D3.7 A Structured Collection on Information and Literature on Technological and Usability Aspects of Radio Frequency Identification (RFID)," FIDIS, Deliverable, 6 2007.

[25] R. Want, "Enabling ubiquitous sensing with rfid," *Computer*, vol. 37, no. 4, pp. 84–86, Apr 2004.

[26] M. Philipose, J. Smith, B. Jiang, A. Mamishev, S. Roy, and K. Sundara-Rajan, "Battery-free wireless identification and sensing," *IEEE Pervasive Computing*, vol. 4, no. 1, pp. 37–45, Jan 2005.

[27] A. Sample, D. Yeager, P. Powledge, A. Mamishev, and J. Smith, "Design of an RFID-Based Battery-Free Programmable Sensing Platform," *IEEE Transactions on Instrumentation and Measurement*, vol. 57, no. 11, pp. 2608–2615, Nov 2008.

[28] A. Vaz, A. Ubarretxena, I. Zalbide, D. Pardo, H. Solar, A. Garcia-Alonso, and R. Berenguer, "Full passive uhf tag with a temperature sesor suitable for human body temperature monitoring," *IEEE Transactions on Circuits and Systems II: Express Briefs*, vol. 57, no. 2, pp. 95–99, Deb 2010.

[29] Z.-K. Zhang, M. Cho, C.-W. Wang, C.-W. Hsu, C.-K. Chen, and S. Shieh, "IoT Security: Ongoing Challenges and Research Opportunities," in *IEEE 7th International Conference on Service-Oriented Computing and Applications (SOCA)*, 11 2014, pp. 230–234.

[30] L. D. Xu, W. He, and S. Li, "Internet of Things in Industries: A Survey," *IEEE Transactions on Industrial Informatics*, vol. 10, no. 4, pp. 2233–2243, 11 2014.

[31] T. S. Rappaport, R. W. J. Heath, R. C. Daniels, and J. N. Murdock, *Millimeter Wave Wireless Communications*, 1st ed. London: Prentice Hall, 2014.

[32] D. Liu, B. Gaucher, U. Pfeiffer, and J. Grzyb, *Advanced Millimeter-wave Technologies - Antennas, Packaging and Circuits*. New York: John Wiley & Sons, 2009.

[33] P. Pursula, T. Vaha-Heikkila, A. Muller, D. Neculoiu, G. Konstantinidis, A. Oja, and J. Tuovinen, "Millimeter-Wave Identification – A New Short-Range Radio System for Low-Power High Data-Rate Applications," *IEEE Transactions on Microwave Theory and Techniques*, vol. 56, no. 10, pp. 2221–2228, 2008.

[34] P. Freidl, M. Gadringer, U. Mühlmann, G. Holweg, and W. Bösch, "A mm-Wave RFID System based on the EPC-Gen2 Protocol," in *IEEE International Symposium of Antennas and Propagation and North American Radio Science Meeting*, 2015.

[35] P. Freidl, S. Sattler, M. Gadringer, D. Amschl, B. Auinger, U. Mühlmann, G. Holweg, and W. Bösch, "mm-Wellen RFID - Design und Implementierung eines Demonstrators," *elektrotechnik & info*, vol. 2016, no. 3, 5 2016.

[36] P. Freidl, M. Gadringer, D. Amschl, and W. Bösch, "mm-Wave RFID for IoT Applications," in *Integrated Nonlinear Microwave and Millimetre-wave Circuits Workshop (INMMiC)*, 4 2017.

[37] P. Freidl, M. Gadringer, and W. Bösch, "Measurement of MM-Wave Identification (MMID) Downlink Channels," in *Microelectronic Systems Symposium (MESS)*, 2014.

[38] P. Freidl, H. Khan, M. Gadringer, and W. Bösch, "Measurements and analysis of MM-Wave RFID channels," in *IEEE International Black Sea Conference on Communications and Networking (BlackSeaCom)*, 5 2014, pp. 88–91.

[39] P. Freidl, S. Sattler, M. Gadringer, D. Amschl, U. Mühlmann, G. Holweg, and W. Bösch, "Design of PCB RF Probe Landing Pads for Measurements up to 90 GHz," in *European Conference on Antennas and Propagation (EuCAP)*, 4 2016.

[40] M. Gadringer, P. Freidl, S. Sattler, and W. Bösch, "Landing Pads for Measuring PCBs up to mm-Wave Frequencies using a Probe Station," in *Cascade User Conference (COMPASS)*, 10 2016.

[41] M. I. Skolnik, *Radar Handbook*, 2nd ed. McGraw-Hill, 1990.

[42] D. Dardari, R. D'Errico, C. Roblin, A. Sibille, and M. Z. Win, "Ultrawide bandwidth rfid: The next generation?" *Proceedings of the IEEE*, vol. 98, no. 9, pp. 1570–1582, Sep 2010.

[43] S. Gezici, Z. Tian, G. B. Giannakis, H. Kobayashi, A. F. Molisch, H. V. Poor, and Z. Sahinoglu, "Localization via ultra-wideband radios; a look at positioning aspects of future networks," *IEEE Signal Processing Magazine*, vol. 22, no. 4, pp. 70–84, Jul 2005.

[44] *IEEE Standard Definitions of Terms for Antennas*, IEEE Std. 145, 2013.

[45] A. Natarajan, A. Komijani, X. Guan, A. Babakhani, and A. Hajimiri, "A 77-ghz phased-array transceiver with on-chip antennas in silicon: Transmitter and local lo-path phase shifting," *IEEE Journal of Solid-State Circuits*, vol. 41, no. 12, pp. 2807–2819, Dec 2006.

[46] T. S. Rappaport, J. N. Murdock, and F. Gutierrez, "State of the art in 60-ghz integrated circuits and systems for wireless communications," *Proceedings of the IEEE*, vol. 99, no. 8, pp. 1390–1436, Aug 2011.

[47] A. Fonte, S. Saponara, G. Pinto, and B. Neri, "Feasibility study and on-chip antenna for fully integrated uRFID tag at 60 GHz in 65 nm CMOS SOI," in *2011 IEEE International Conference on RFID-Technologies and Applications (RFID-TA)*, 9 2011, pp. 457–462.

[48] M. Wojnowski, R. Lachner, J. Böck, C. Wagner, F. Starzer, G. Sommer, K. Pressel, and R. Weigel, "Embedded wafer level ball grid array (ewlb) technology for millimeter-wave applications," in *2011 IEEE 13th Electronics Packaging Technology Conference*, Dec 2011, pp. 423–429.

[49] National Intruments, "NI AWR Design Environment," 1999–2016. [Online]. Available: http://http://www.awrcorp.com/

[50] H. T. Friis, "A Note on a Simple Transmission Formula," *Proceedings of the IRE*, vol. 34, no. 5, pp. 254–256, May 1946.

[51] *Attenuation by atmospheric gases*, ITU Std. P.676-10, 2013.

[52] T. Rappaport, *Wireless Communications: Principles and Practice*, 2nd ed. Prentice Hall PTR, 2002.

[53] K. Sato, T. Manabe, T. Ihara, H. Saito, S. Ito, T. Tanaka, K. Sugai, N. Ohmi, Y. Murakami, M. Shibayama, Y. Konishi, and T. Kimura, "Measurements of reflection and transmission characteristics of interior structures of office building in the 60-GHz band," *IEEE Transactions on Antennas and Propagation*, vol. 45, no. 12, pp. 1783–1792, Dec 1997.

[54] H. Zhao, R. Mayzus, S. Sun, M. Samimi, J. K. Schulz, Y. Azar, K. Wang, G. N. Wong, F. Gutierrez, and T. S. Rappaport, "28 GHz millimeter wave cellular communication measurements for reflection and penetration loss in and around buildings in New York city," in *2013 IEEE International Conference on Communications (ICC)*, June 2013, pp. 5163–5167.

[55] A. V. Räisänen, J. Ala-Laurinaho, K. Haneda, J. Järveläinen, A. Karttunen, M. Kyrö, V. Semkin, A. Lamminen, and J. Säily, "Studies on E-band antennas and propagation," in *Loughborough Antennas and Propagation Conference (LAPC)*, Nov 2013, pp. 176–180.

[56] L. Wang, J. Chen, X. Wei, J. Cui, and B. Zheng, "First-order-reflection MIMO channel model for 60 GHz NLOS indoor WLAN systems," in *IEEE International Conference on Communication Systems (ICCS)*, Nov 2014, pp. 298–302.

[57] M. Bensebti, J. McGeehan, and M. Beach, "Indoor Multipath Radio Propagation Measurements and Characterisation at 60 GHz," in *1st EuropeanMicrowave Conference*, vol. 2, 1991, pp. 1217–1222.

[58] V. Guillet, "Narrowband and wideband characteristics of 60 GHz radio propagation in residential environment," *Electronics Letters*, vol. 37, no. 21, pp. 1310–1311, Oct 2001.

[59] H. Xu, V. Kukshya, and T. S. Rappaport, "Spatial and temporal characteristics of 60-GHz indoor channels," *IEEE Journal on Selected Areas in Communications*, vol. 20, no. 3, pp. 620–630, Apr 2002.

[60] J. Purwaha, A. Mank, D. Matic, K. Witrisal, and R. Prasad, "Wide-band Channel Measurements at 60 GHz in Indoor Environments," in *IEEE Symposium on Communications and Vehicular Technology in the Benelux*, Brussels, Belgium, Oct 1998.

[61] A. Pekou, V. Nastos, N. Moraitis, and P. Constantitiou, "Time delay and coherence bandwidth measurements at 60 GHz in an indoor environment for WLANs," in *IEEE 59th Vehicular Technology Conference*, vol. 1, May 2004, pp. 93–97.

[62] P. Karadimas, B. Allen, and E. Okon, "60 GHz time-domain propagation measurement system," in *Loughborough Antennas and Propagation Conference (LAPC)*, Nov 2012, pp. 1–4.

[63] P. B. Papazian, K. A. Remley, C. Gentile, and N. Golmie, "Radio channel sounders for modeling mobile communications at 28 GHz, 60 GHz and 83 GHz," in *2015 Global Symposium On Millimeter Waves (GSMM)*, May 2015, pp. 1–3.

[64] C. A. Balanis, *Antenna Theory: Analysis and Design*, 3rd ed. Wiley India Pvt. Limited, 2005.

[65] T. Teshirogi and T. Yoneyama, *Modern Millimeter-wave Technologies*. IOS Press, 2000.

[66] QuinStar Technology, Inc., *Standard Gain Horn Antennas (QWH series)*, 2013.

[67] D. M. Pozar, "Beam Transmission Of Ultra Short Waves: An Introduction To The Classic Paper By H. Yagi," *Proceedings of the IEEE*, vol. 85, no. 11, pp. 1857–1863, Nov 1997.

[68] J. D. Kraus and R. J. Marhefka, *Antennas - For All Applications*, 3rd ed. New York: McGraw-Hill Education, 2002.

[69] D. Neculoiu, G. Konstantinidis, L. Bary, A. Muller, D. Vasilache, A. Stavinidris, P. Pons, and R. Plana, "Membrane-supported Yagi-Uda MM-Wave antennas," in *First European Conference on Antennas and Propagation*, Nov 2006, pp. 1–5.

[70] G. R. DeJean and M. M. Tentzeris, "A New High-Gain Microstrip Yagi Array Antenna With a High Front-to-Back (F/B) Ratio for WLAN and Millimeter-Wave Applications," *IEEE Transactions on Antennas and Propagation*, vol. 55, no. 2, pp. 298–304, Feb 2007.

[71] A. Amadjikpe, D. Choudhury, G. Ponchak, and J. Papapolymerou, "High gain quasi-Yagi planar antenna evaluation in platform material environment for 60 GHz wireless applications," in *IEEE MTT-S International Microwave Symposium Digest*, 2009, pp. 385–388.

[72] R. Alhalabi, Y.-C. Chiou, and G. Rebeiz, "Self-Shielded High-Efficiency Yagi-Uda Antennas for 60 GHz Communications," *IEEE Transactions on Antennas and Propagation*, vol. 59, no. 3, pp. 742–750, 2011.

[73] O. Kramer, T. Djerafi, and K. Wu, "Very Small Footprint 60 GHz Stacked Yagi Antenna Array," *IEEE Transactions on Antennas and Propagation*, vol. 59, no. 9, pp. 3204–3210, 2011.

[74] R. Alhalabi and G. Rebeiz, "High-Gain Yagi-Uda Antennas for Millimeter-Wave Switched-Beam Systems," *IEEE Transactions on Antennas and Propagation*, vol. 57, no. 11, pp. 3672–3676, 2009.

[75] Rogers Corporation, *RO4000 Series High Frequency Circuit Materials*, 2015.

[76] CST - Computer Simulation Technology, "CST MWS, CST Microwave Studio," 1998–2016. [Online]. Available: http://www.cst.com

[77] Southwest Microwave, *1.85mm Jack (Female) End Launch Connector*, 2013.

[78] Rhode&Schwarz GmbH & Co. KG, *R&S$^{®}$SMF100A Microwave Signal Generator*, 2016.

[79] ——, *R&S$^{®}$FSQ Signal Analyzer*, 2016.

[80] ——, *R&S$^{®}$SMZ Frequency Multiplier*, 2016.

[81] ——, *R&S$^{®}$FS-Z90 Harmonic Mixer*, 2013.

[82] ——, *R&S$^{®}$ZVA Vector Network Analyzer*, 2015.

[83] ——, *R&S$^{®}$ZVA110 Vector Network Analyzer*, 2015.

[84] ——, *R&S® ZV-Z2xx Calibration Kits*, 2013.

[85] A. F. Molisch, *Wireless Communications*, 2nd ed. West Sussex: John Wiley & Sons, Ltd., 2011.

[86] D. Cassioli, "60 ghz uwb channel measurement and model," in *2012 IEEE International Conference on Ultra-Wideband (ICUWB)*, 2012, pp. 145–149.

[87] W. L. Gore & Associates , *Gore 4F*, 2013.

[88] ——, *Gore 4F0BB0BB0394*, 2013.

[89] D. M. Pozar, *Microwave Engineering*, 4th ed. New York: John Wiley & Sons, 2012.

[90] P. F. M. Smulders and A. G. Wagemans, "A statistical model for the MM-wave indoor radio channel," in *Third IEEE International Symposium on Personal, Indoor and Mobile Radio Communications*, Oct 1992, pp. 303–307.

[91] D. S. Polydorou, P. G. Babalis, and C. N. Capsalis, "Statistical Characterization of Fading in LOS Wireless Channels with a Finite Number of Dominant Paths. Application in Millimeter Frequencies," *International Journal of Infrared and Millimeter Waves*, vol. 20, no. 3, pp. 461–472, 1999. [Online]. Available: http://dx.doi.org/10.1023/A:1021721600307

[92] Z. Zhou, L. Qi, and Y. Tan, "Spatial and Temporal CM Equalization for Broadband Wireless Indoor Networks at Millimeter Waves," *International Journal of Infrared and Millimeter Waves*, vol. 22, no. 2, pp. 255–263, 2001. [Online]. Available: http://dx.doi.org/10.1023/A:1010792119960

[93] J. Blumenstein, T. Mikulasek, T. Zemen, C. Mecklenbrauker, R. Marsalek, and A. Prokes, "In-Vehicle mm-Wave Channel Model and Measurement," in *IEEE 80th Vehicular Technology Conference (VTC2014-Fall)*, Sept 2014, pp. 1–5.

[94] T. S. Rappaport, G. R. MacCartney, M. K. Samimi, and S. Sun, "Wideband Millimeter-Wave Propagation Measurements and Channel Models for Future Wireless Communication System Design," *IEEE Transactions on Communications*, vol. 63, no. 9, pp. 3029–3056, Sept 2015.

[95] G. Turin, F. Clapp, T. Johnston, S. Fine, and D. Lavry, "A statistical model of urban multipath propagation," *Vehicular Technology, IEEE Transactions on*, vol. 21, no. 1, pp. 1–9, Feb 1972.

[96] H. Suzuki, "A Statistical Model for Urban Radio Propogation," *IEEE Transactions on Communications*, vol. 25, no. 7, pp. 673–680, Jul 1977.

[97] P. Bello, "Characterization of Randomly Time-Variant Linear Channels," *IEEE Transactions on Communications Systems*, vol. 11, no. 4, pp. 360–393, Dec 1963.

[98] D. Cox and R. Leck, "Correlation Bandwidth and Delay Spread Multipath Propagation Statistics for 910-MHz Urban Mobile Radio Channels," *IEEE Transactions on Communications*, vol. 23, no. 11, pp. 1271–1280, Nov 1975.

[99] J.-P. de Weck, P. Merki, and R. Lorenz, "Power delay profiles measured in mountainous terrain [radiowave propagation]," in *Vehicular Technology Conference, 1988, IEEE 38th*, Jun 1988, pp. 105–112.

[100] S. Salous, *Radio Propagation Measurement and Channel Modelling.* New York: John Wiley & Sons, 2013.

[101] A. G. Siamarou and M. O. Al-Nuaimi, "Wideband propagation measurements for future millimetre 60 GHz wireless LANs," *Electronics Letters*, vol. 38, no. 16, pp. 918–920, Aug 2002.

[102] A. G. Siamarou, "Broadband wireless local-area networks at millimeter waves around 60 GHz," *IEEE Antennas and Propagation Magazine*, vol. 45, no. 1, pp. 177–181, Feb 2003.

[103] E. Ben-Dor, T. S. Rappaport, Y. Qiao, and S. J. Lauffenburger, "Millimeter-Wave 60 GHz Outdoor and Vehicle AOA Propagation Measurements Using a Broadband Channel Sounder," in *IEEE Global Telecommunications Conference (GLOBECOM)*, Dec 2011, pp. 1–6.

[104] P. Pursula, F. Donzelli, and H. Seppa, "Passive RFID at Millimeter Waves," *IEEE Transactions on Microwave Theory and Techniques*, vol. 59, no. 8, pp. 2151–2157, Aug 2011.

[105] P. Pursula, T. Karttaavi, M. Kantanen, A. Lamminen, J. Holmberg, M. Lahdes, I. Marttila, M. Lahti, A. Luukanen, and T. Vaha-Heikkila, "60-GHz Millimeter-Wave Identification Reader on 90-nm CMOS and LTCC," *IEEE Transactions on Microwave Theory and Techniques*, vol. 59, no. 4, pp. 1166–1173, Apr 2011.

[106] C. Carlowitz, A. Strobel, T. Schäfer, F. Ellinger, and M. Vossiek, "A mm-wave rfid system with locatable active backscatter tag," in *Wireless Information Technology and Systems (ICWITS), 2012 IEEE International Conference on*, Nov 2012, pp. 1–4.

[107] C. Carlowitz, M. Vossiek, A. Strobel, and F. Ellinger, "Precise ranging and simultaneous high speed data transfer using mm-wave regenerative active backscatter tags," in *2013 IEEE International Conference on RFID (RFID)*, 4 2013, pp. 253–260.

[108] NXP Semiconductors, *SL3S1204 UCODE 7*, 2017.

[109] Infineon Technologies, *Single-Chip SiGe Transceiver Chipset for E-band Backhaul Applications from 71 to 76 GHz*, 2014.

[110] Infineon Technologies AG, "Millimeter Wave Technology and Test Instrumentation for V-E Band Applications," Infineon Technologies, Tech. Rep., 2012.

[111] Infineon Technologies, "Single-Chip Packaged RF Transceivers for Mobile Backhaul," *Microwave Journal*, vol. 56, no. 8, pp. 108–110, Aug 2013.

[112] Analog Devices, Inc., *Direct Modulation/Waveform Generating, 6.1 GHz Fractional-N Frequency Synthesizer ADF4158*, 2016.

[113] Flann Microwave Ltd, *Fixed Attenuators Series 081*, 2015.

[114] Rhode&Schwarz GmbH & Co. KG, *R&S® AFQ100A I/Q Modulation Generator*, 2014.

[115] M. E. Gadringer, T. Faseth, and G. Magerl, "Comparison of the Imbalance effects in Direct Conversion Transmitters and Receivers," in *2011 Workshop on Integrated Nonlinear Microwave and Millimetre-Wave Circuits (INMMIC)*, 4 2011.

[116] M. E. Gadringe, "Modeling and Compensation of Direct Conversion Transmitters and Receivers," Ph.D. dissertation, Vienna University of Technology, 2011.

[117] Radio Gigabit LLC. Lens Antennas. [Online]. Available: http://radiogigabit. com/en/lensantennas/

[118] Millitech, Inc., *Series JFD (junction ferrite devices)*, 2009.

[119] Y.-H. Suh and K. Chang, "A new millimeter-wave printed dipole phased array antenna using microstrip-fed coplanar stripline tee junctions," in *IEEE MTT-S International Microwave Symposium Digest*, vol. 2, June 2002, pp. 1321–1324 vol.2.

[120] H. K. Pan, B. D. Horine, M. Ruberto, and S. Ravid, "Mm-wave phased array antenna and system integration on semi-flex packaging," in *IEEE International Symposium on Antennas and Propagation (APSURSI)*, July 2011, pp. 2059–2062.

[121] N. Ghassemi and K. Wu, "High-efficient patch antenna array for e-band gigabyte point-to-point wireless services," *IEEE Antennas and Wireless Propagation Letters*, vol. 11, pp. 1261–1264, 2012.

[122] H. K. Pan, "Dual-polarized mm-wave phased array antenna for multi-gb/s 60ghz communication," in *2011 IEEE International Symposium on Antennas and Propagation (APSURSI)*, July 2011, pp. 3279–3282.

[123] M. Khalily, R. Tafazolli, T. A. Rahman, and M. R. Kamarudin, "Design of phased arrays of series-fed patch antennas with reduced number of the controllers for 28-ghz mm-wave applications," *IEEE Antennas and Wireless Propagation Letters*, vol. 15, pp. 1305–1308, 2016.

[124] J. H. Kim, J. H. Han, J. S. Park, and J. G. Kim, "Design of phased array antenna for 5g mm-wave beamforming system," in *2016 IEEE 5th Asia-Pacific Conference on Antennas and Propagation (APCAP)*, July 2016, pp. 201–202.

[125] C. Angerer, "A digital receiver architecture for rfid readers," in *International Symposium on Industrial Embedded Systems*, Jun 2008, pp. 89–94.

[126] X. Li and C. Wang, "Design and fpga verification of uhf rfid reader digital baseband," in *International Conference on Electrical and Control Engineering (ICECE)*, Sept 2011, pp. 2100–2103.

[127] M. Winkler, T. Faseth, J. Steininger, and H. Arthaber, "Implementation of a receiver for an epc tag emulator for performance evaluation," in *41st European Microwave Conference (EuMC)*, Oct 2011, pp. 119–122.

[128] Analog Devices, Inc., *Ultralow Distortion IF Dual VGA AD8376*, 2013.

[129] Rhode&Schwarz GmbH & Co. KG, *R&S®ZVL Vector Network Analyzer*, 2009.

[130] A. Müller, D. Neculoiu, P. Pursula, T. Vaha-Heikkila, F. Giacomozzi, and J. Tuovinen, "Hybrid integrated micromachined receiver for 77 GHz millimeter wave identification systems," in *10th European Microwave Conference*, 10 2007, pp. 1034–1037.

[131] P. Pursula and F. Donzelli, "Transponders for millimeter wave identification," in *IEEE-APS Topical Conference on Antennas and Propagation in Wireless Communications (APWC)*, Sep 2011, pp. 1221–1224.

[132] S. Pellerano, J. Alvarado, and Y. Palaskas, "A mm-wave power harvesting RFID tag in 90nm CMOS," in *IEEE Custom Integrated Circuits Conference, 2009.*, 9 2009, pp. 677–680.

[133] N. Karmakar and C. K. Pern, "Mm-wave chipless RFID tag for low-cost item tagging," in *Asia-Pacific Microwave Conference Proceedings (APMC)*, 12 2011, pp. 1462–1465.

[134] P. Freidl, S. Sattler, B. Auinger, M. Gadringer, U. Mühlmann, G. Holweg, and W. Bösch, "Design of a mm-Wave RFID transponder based on the EPC-Gen2 Protocol," in *4th Management Commitee / Working Group Meeting and Workshop of COST ICT1301*, 3 2014.

[135] NXP Semiconductors, *74HC4051; 74HCT4051 8-channel analog multiplexer/demultiplexer*, 2012.

[136] Rogers Corporation, *RO3000 Series Circuit Materials*, 2015.

[137] B. C. Wadell, *Transmission Line Design Handbook*. Norwood: Artech House, 1991.

[138] B. Rosas, "The Design and Test of Broadband Launches up to 50 GHz on Thin and Thick Substrates," Southwest Microwave, Inc., Tech. Rep., 2011.

[139] S. Wartenberg, "RF Coplanar Probe Basics," *Microwave Journal*, 3 2003.

[140] A. Rumiantsev and R. Doerner, "RF Probe Technology: History and Selected Topics," *IEEE Microwave Magazine*, vol. 14, no. 7, pp. 46–58, 11 2013.

[141] D. Williams and T. Miers, "A coplanar probe to microstrip transition," *IEEE Transactions on Microwave Theory and Techniques*, vol. 36, no. 7, pp. 1219–1223, 7 1988.

[142] A. Pham, J. Laskar, and J. Schappacher, "Development of On-Wafer Microstrip Characterization Techniques," in *ARFTG Conference Digest-Spring, 47th*, vol. 29, 6 1996, pp. 85–94.

[143] G. Zheng, P. Kirby, A. Rodriguez, J. Papapolymerou, M. Tentzeris, and L. Dunleavy, "Design and on-wafer measurement of a W-Band via-less CPW RF probe pad to microstrip transition," in *Microwave Conference, 2003. 33rd European*, vol. 1, 10 2003, pp. 443–446.

[144] Z. Zhou and K. Melde, "Development of a Broadband Coplanar Waveguide-to-Microstrip Transition With Vias," *IEEE Transactions on Advanced Packaging*, vol. 31, no. 4, pp. 861–872, Nov 2008.

[145] K. Jung and J. Ebner, "Via-adjusted microstrip launch for sub-terahertz wafer probing," in *Microwave Measurement Conference (ARFTG)*, 12 2014, pp. 1–4.

[146] S. W. Sattler, "Design and Characterization of Microstrip Structures at mm-wave Frequencies," Master's thesis, Graz University of Technology, 11 2015.

[147] Infineon Technologies, *Silicon Single Flip Chip Schottky Diode BAT14-077D*, 2014.

[148] Cascade Microtech, Inc., *Infinity Probe®High-frequency performance with low, stable contact resistance*, 2010.

[149] R. Sorrentino and L. Roselli, "A new simple and accurate formula for microstrip radial stub," *IEEE Microwave and Guided Wave Letters*, vol. 2, no. 12, pp. 480–482, 12 1992.

[150] B. Syrett, "A Broad-Band Element for Microstrip Bias or Tuning Circuits (Short Papers)," *IEEE Transactions on Microwave Theory and Techniques*, vol. 28, no. 8, pp. 925–927, 8 1980.

[151] F. Giannini, R. Sorrentino, and J. Vrba, "Planar Circuit Analysis of Microstrip Radial Stub," *IEEE Transactions on Microwave Theory and Techniques*, vol. 32, no. 12, pp. 1652–1655, 12 1984.

[152] Chemtronics, *CircuitWorks®Conductive Epoxy*, 2013.

[153] K. Siddiq, R. J. Watson, S. R. Pennock, P. Avery, R. Poulton, and B. Dakin-Norris, "Phase noise analysis in fmcw radar systems," in *2015 European Radar Conference (EuRAD)*, Sept 2015, pp. 501–504.

[154] S. K. Kim, S. S. Nam, and S. H. Cho, "A fpga design of the i/q signal combining for uhf rfid reader receiver," in *2010 2nd IEEE InternationalConference on Network Infrastructure and Digital Content*, Sept 2010, pp. 556–560.

[155] X. Li and C. Wang, "Design and fpga verification of uhf rfid reader digital baseband," in *2011 International Conference on Electrical and Control Engineering*, Sept 2011, pp. 2100–2103.

[156] A. Ibrahim, I. Ismail, and A. T. Abdullah, "Development and simulation of pie encoder architecture for uhf rfid reader based on fpga," in *2012 IEEE Business, Engineering Industrial Applications Colloquium (BEIAC)*, April 2012, pp. 58–63.

[157] F. Galler, S. Grebien, T. Faseth, K. Witrisal, G. Magerl, and H. Arthaber, "Extension of an sdr uhf rfid testbed for mimo and monostatic time of flight based ranging," *IEEE Journal of Radio Frequency Identification*, vol. PP, no. 99, pp. 1–1, 2017.